X-ray telescope mirrors
From surface profile to Point Spread Function: a new approach

UNIVERSITÀ DEGLI STUDI DELL'INSUBRIA

Dottorato di Ricerca in Astronomia e Astrofisica
XXIV Ciclo

Lorenzo Raimondi

Relatore: Dr. Daniele Spiga

Commissione: Prof. Marco Barbera
Prof. Andrea Biviano
Prof. Filippo Frontera

Facoltà di Fisica e Matematica

The research reported in this thesis was carried out at the Osservatorio Astronomico di Brera-Merate, Italia.

I'm so fast that last night I turned off the light switch in my hotel room and was in bed before the room was dark.

Muhammad Ali

Contents

1 Abstract

'A vita, è 'na muntagna
'e niente...

Livia Soprano

X-ray astronomy was born on 1962 when Giacconi decided to put a Geiger counter onto a rocket, in hope of measuring the X-ray emission from the Sun. Even if the Sun emission was disappointing, he made the discovery that changed our view on the Universe. An unknown background of X-ray emission that later turned out to contain millions of X-ray sources, both galactic and extra-galactic. Owing to the development of increasingly sophisticated instruments, the sensitivity and the resolution to detect X-ray sources has improved significantly over the last 50 years.

One of the major technological improvement was the development of focusing telescope, which allowed to enhance the angular resolution and sensitivity of several orders of magnitude. The angular resolution of an X-ray imaging telescope is mainly determined by the quality of its focusing optics. These generally consist of a number of nested shells of *grazing incidence mirrors*. The typical configuration used, which minimizes the effect of coma aberration and reduces the focal length, is the so-called Wolter-I (paraboloid-hyperboloid mirror configuration). In order to keep the mass to levels comparable with the launcher (because X-ray absorption in the atmosphere prevents observation from ground) the optics have to be lightweight, hence the mirrors have to be thin.

The final performance of a mirror module is always subject to degradation, provided in the realization phase. During the different stages of production (under construction and integration) there may be distortions. In addition, the mirror surface is not ideally smooth but is characterized by a certain roughness topography. Both these types of imperfections combine to determine the degradation of the Point Spread Function (PSF), i.e. the annular integral of focused intensity around the focal spot, which generally characterizes the quality of the optics.

Regarding the characterization of an X-ray mirror, one of the basic objectives is to *establish the relationship between the imperfections of the mirrors and their PSF as a function of the incident wave energy*. The aim is to predict the angular resolution of a mirror, given measurements of profiles and microroughness, or to establish the level of tolerable imperfections of a mirror given a certain angular resolution required by the project specifications.

The study of the topography of the mirror surface is done through several methods. It is generally divided into two different kinds of analysis: the study of the profile, i.e. large spatial wavelengths (comparable with the mirror length) and the study of microroughness, i.e. short spatial wavelengths.

The first ones, also called the figure errors, are often due to deformation of the mirror that occurs during construction and integration and are responsible for the degradation of the PSF and can be treated by *geometrical optics*. The second ones are due, for example, to the limits of the polishing mandrel methods, from which the shells are replicated, and the deposition technology of the reflective coating. These imperfections are responsible for a diffusion (called scattering), which degrades the PSF at increasing energy and can not be treated by geometrical optics, but using *physical optics* under some assumptions. This problem is much more important in X-ray than in optical astronomy, because X-ray have a 1000 times smaller wavelengths and are sensitive to surface defects 1000 times smaller. The surface polishing is thereby a fundamental point in X-ray mirrors.

The characterization of the microroughness is made in terms of power spectrum as a function of the spatial frequency on the surface (PSD - Power Spectral Density). The PSD is a fundamental quantity in the characterization of X-ray telescope optics because is proportional to the scattering. The measure of roughness is done with different instruments in order to have a range of spatial frequencies as more wide as possible, from a few millimetres to a few tens of nanometres.

There is also a range of *intermediate frequencies*, at the limit of microroughness, which generates a degradation of the PSF that *can neither be predicted by geometrical optics and nor by the scattering theory*. For this reason, it is difficult in general to predict accurately its effect on the PSF.

My PhD activity is included in the mission project *NHXM* financed by ASI and in the development of X-ray mirrors for *ATHENA* mission project financed by ESA. The first part of my PhD project has been therefore aimed at the *characterization of microroughness and reflectivity of the mirrors*, at INAF/OAB, in order to determine the topography of the surface and to support the industry (Media Lario Technology, leader company of manufacturing optical components) in setting the process. The second part of the project was instead dedicated to the *development of a self-consistent general method*, based on physical optics, to compute the PSF of X-ray

mirrors from their profile metrology. The third part, which is the merging of these two parts of the project, consist in the applications to real cases through verifications with calibration tests.

My research work can be divided into three phases:

- **First phase** - I performed measurements of mirror profiles and roughness of several samples of mirrors for the missions NHXM and ATHENA, using different instruments available at INAF/OAB. The roughness measurements, at spatial scales smaller than 1 mm, can be achieved with different instruments that have different spatial wavelength ranges (i.e. optical interferometer WYKO and Atomic Force Microscope). However, the effects of roughness can also be directly observed by performing X-ray reflectivity measurements using an X-ray diffractometer. I used the X-ray diffractometer available at INAF/OAB for scattering measurements, with particular attention to the effects in large angle scattering and modulation interference introduced by the multilayer. By merging these different data I derived the complete roughness surface PSD.

  By means of the X-ray diffractometer I made reflectivity measurements of samples of mirrors with multilayer coating, obtaining the reflectivity curve as a function of the angle of incidence and as a function of the energy. Using a program to fit the reflectivity curves (PPM), I estimated the thickness of the layers and their uniformity, then assessing the compliance with design specifications. In summary, from one hand surface roughness (from direct topography measurements and scattering measurements) to obtain the PSD, on the other hand, measurements of reflectivity (as a function of both the incidence angle and the energy) for the characterization of the structure of the multilayer. The feedback provided to the industry in a commons way and the isolation of the critical points has lead to the deposition of coatings with excellent reflectivity.

  I performed reflectivity measurements also within the study of the crystallization of gold during the evaporation process, which contributes to worsen the surface roughness. The gold layer is deposited on the mandrel, which is then electroformed a Nickel-Cobalt shell (the mirror). The gold layer serves to detach the shell from mandrel and it should minimize the microroughness increasing. In this regard, I performed diffraction measurements of different gold deposits with different thickness. Studying the Bragg peaks I obtained an estimation of the size of the gold crystallites as a function of the thickness. Larger are the crystallites, higher is the value of the microroughness. The conclusion is that more the gold layer is thick, larger are the crystallites and *larger crystallites means microroughness increasing*.

- **Second phase** - I developed a new method to calculate the PSF of an X-ray mirror (e.g. Wolter-I configuration, in double reflection) at any energy by ap-

plying the principle of Huygens-Fresnel from real profile and roughness data. In other words, the X-ray reflection is treated by the undulatory theory, building the wavefront deformed by the mirror imperfections. In this interpretation, even the deformed geometry are treated by the physical optics. *This allows to obtain the PSF determined from both contributions (figure error and scattering) at any energy in a self-consistent way, without considering different separated energy regimes treated with different methods. This method, never used before, ultimately solves the problem of PSF computation, starting from the complete surface topography of an X-ray mirror.*

- **Third phase** - I performed several calibrations over mirror shells in different configurations as demonstrator for the NHXM hard X-ray imaging telescope (0.3 - 80 keV). Prototypes of NHXM mirror modules with a few mirror shells were manufactured, aiming at demonstrating the feasibility of mirrors. I made the direct performance verification by measuring the X-ray PSF (Point Spread Function) up to 50 keV in full-illumination setup at PANTER (MPE, Germany) and in pencil-beam set up at monochromatic X-ray energies from 15 to 63 keV at the BL20B2 beamline of the SPring-8 synchrotron radiation facility. Moreover, I simulated PSF from the metrology profile of mirror shell using Fresnel diffraction method. *The calibration measured data and the simulated data (obtained with my Fresnel method) match perfectly. This provide the experimental proof of the correctness of the method, that therefore will represent, from now on, a powerful prediction tool in X-ray optics.*

The Fresnel diffraction method is easily extendible to other optical systems, also out of astrophysical applications, even with a number of more than two reflections, e.g Syncrotron and FEL facilities.

For the future, I plan to implement the Fresnel diffraction method improving the simulations of mirrors coated with multilayer. In this case in order to increase the prediction accuracy, we have to taking into account the scattering from multilayer interfaces.

2 Introduction

2.1 Astronomy in X−ray band

The possibility of studying astrophysical sources in X-rays has had a profound significance for all astronomy. X-rays can reveal to us the existence of high energy events in the cosmos: events in which the total energy is extremely high (supernova explosions, emissions by active galactic nuclei, etc.) or in which the energy per nucleon or the temperature of the matter involved is extremely high (infall onto collapsed objects, high temperature plasmas, interaction of relativistic electrons with magnetic or photon fields).

The study of astronomical objects at X-rays (and gamma rays) began in the early 1960s. Many rocket flights carried out by several groups in the 60's were able to find new stellar sources and the first extragalactic sources. The first rocket flight to successfully detect a cosmic source of X-ray emission was launched in 1962. This rocket flight used a small X-ray detector, which found a very bright source they named Scorpius X-1 (Giacconi et al., 1962). The truly extraordinary aspect of the discovery was its extraordinary properties: in Sco X-1, the X-ray luminosity is 10^3 times the visible light intensity and it was later determined that the intrinsic luminosity is 10^3 the entire luminosity of the Sun. A new type of celestial object was discovered.

In the 1970s, dedicated X-ray astronomy satellites, such as UHURU, Ariel 5, SAS-3, OSO-8 and HEAO-1, enabled a fast development of this field of science. The next step which led to discoveries of great astrophysical relevance occurred on December 12, 1970, when UHURU (an observatory entirely dedicated to X-ray astronomy, the first of the Small Astronomy Satellite series), was launched. It extended the time of observation from minutes to years. In three months all the sky could be studied systematically and many new sources could be localized with a precision of about 1 arc minute, often permitting the identification of the X-ray sources with a optical or radio counterpart. This in turn leads to an evaluation of the distance, the intrinsic luminosity, and the physical characteristics of the celestial object from which the X-

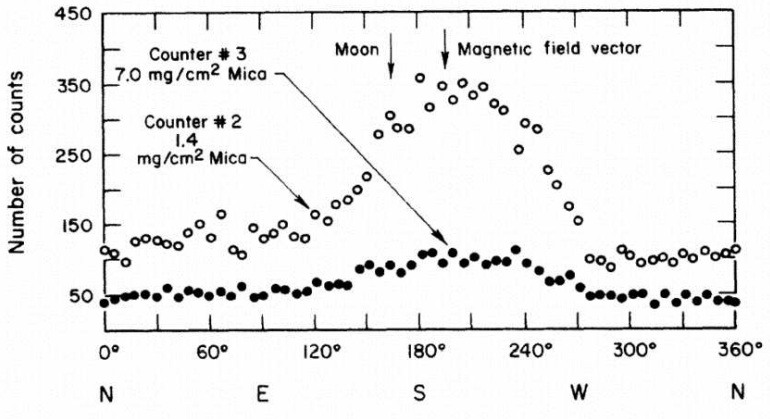

Figure 2.1: Discovery of the first X-ray source outside the solar system: Sco X-1. The spike that was seen over and over again as the rocket X-ray detectors swept over the sky, was not from the Moon, but actually came from another part of the sky, about 25 degrees away. The Moon would have produced a maximum in the graph at about 160 degrees, whereas the peak occurs at about 185 degrees. It turned out that the Moon's X-ray brightness contributes virtually nothing to the count rate we see. Credit: Giacconi et al. (1962).

rays originated. Among the 300 new sources which were discovered, it was possible to identify binary X-ray sources, supernovæ, galaxies, active galaxies, quasars, and clusters of galaxies. These observations proved the existence of binary systems containing a neutron star and of systems containing a black hole. Black holes of solar mass size existed. A new source of energy for celestial objects was revealed: the infall of accreting material in a strong gravitation field.

A very important discovery of UHURU, both because of its intrinsic interest and for its consequences in the field of cosmology, was the detection of emission from clusters of galaxies. This emission is not simply due to the sum of the emission from individual galaxies, but originates in a thin gas which pervades the space between galaxies. This gas was heated in the past during the gravitational contraction of the cluster to a temperature of millions of degrees and contains as much mass as that in the galaxies themselves. In one stroke the mass of baryons contained in the clusters was more than doubled.

These first findings with UHURU, which could detect only the three richest and closest galaxy clusters and with a poor angular resolution of 1/2 a degree, were confirmed and expanded by the introduction of a new and powerful X-ray observatory, Einstein, which first utilized a completely new technology in extrasolar X-ray astronomy: grazing incidence telescopes. This substantial technical improvement made

possible the detection of all types of astrophysical phenomena. Main sequence stars of all types, novae and supernovae were detected. Binary X-ray sources could be studied anywhere in our own galaxy as well as in external galaxies. Normal galaxies as well as galaxies with active galactic nuclei, such as Seyferts and BLac, could be detected at very great distances. The sources of the isotropic extragalactic background could begin to be resolved. It is in the study of X-ray emissions from clusters of galaxies that the Einstein observations have had some of the most profound impact.

From the 1980s to the early 2000s, the study of X-ray astronomy has been carried out using data from different satellites: the HEAO series, EXOSAT, Ginga, RXTE, ROSAT, ASCA, as well as BeppoSAX, which detected the first afterglow of a gamma-ray burst. One X-ray mission that continues to contribute to the data available to researchers is the Chandra X-ray Observatory (CXO), NASA's current flagship mission for X-ray astronomy. It was launched in July 1999, and is designed to detect X-rays from very hot, high energy regions of the Universe, such as galaxy clusters, matter surrounding black holes and stars that have exploded. Owing to the great sensitivity and angular resolution of Chandra, it has been possible to resolve the apparently diffused emission of the X-ray background into millions of individual sources. They are active galactic nuclei, quasars, and normal galaxies.

The European Space Agency's (ESA) X-ray Multi-Mirror Mission, called XMM-Newton, was launched in 1999, like Chandra. It has recently been used to observe ultraluminous X-ray sources and find evidence of intermediate-mass black holes.

Data from these satellites continues to aid our further understanding of the nature of these sources and the mechanisms by which the X-rays and gamma rays are emitted. Understanding these mechanisms can in turn shed light on the fundamental physics of our Universe. By looking at the sky with X-ray and gamma-ray instruments, it is possible to collect important informations and to address questions such as how the Universe began and how it evolves, and gain some insight into its eventual fate.

All categories of celestial objects, from planets to normal stars, from ordinary galaxies to quasars, from small groups of galaxies to the furthest known clusters, have been observed. As a result of these studies it has become apparent that high energy phenomena play a fundamental role in the formation and in the chemical and dynamical evolution of structures on all scales. X-ray observations have proved of crucial importance in discovering important aspects of these phenomena.

X-ray astronomy is important since this radiation reveals the existence of astrophysical processes where matter has been heated to temperatures of millions of degrees or where particles have been accelerated to relativistic energies. The X-ray photons are particularly suited to study these processes because they are numerous, because they penetrate cosmological distances, and because they can be focused by telescopes. However, in a more fundamental way, high energy astronomy has great

importance in the study of the Universe, because high energy phenomena play a crucial role in the dynamics of the Universe.

2.2 X-ray emission processes and astrophysical sources

Several types of astrophysical objects emit, fluoresce, or reflect X-rays, from galaxy clusters, through black holes in active galactic nuclei to galactic objects such as supernova remnants, stars, and binary stars containing a white dwarf (cataclysmic variable stars and super soft X-ray sources), neutron star or black hole (X-ray binaries). Some solar system bodies emit X-rays, the most notable being the Moon, although most of the X-ray brightness of the Moon arises from reflected solar X-rays. A combination of many unresolved X-ray sources is thought to produce the observed X-ray background. The X-ray continuum can arise from bremsstrahlung, black-body radiation, synchrotron radiation, or what is called inverse Compton scattering of lower-energy photons by relativistic electrons.

The next sections present in more detail the origin and the properties of the emission arising from the most important X-ray astrophysical sources.

2.2.1 Physics of accretion flows onto solar mass and super massive Black Holes

Black Holes (BHs) are known to accrete matter from a stellar companion in Galactic Black Hole Binaries (GBHB, where the BH have masses of the order of 10 $M_{\odot}$) and maybe in Ultraluminous X-ray sources (where the BHs may have masses as high as about a thousand solar masses) and from the ISM in AGNs, which host at their center supermassive ($10^6 - 10^9$ $M_{\odot}$) BHs. Many similarities exist between the X-ray properties of these systems as the basic process is the same, even if differences do also exist, related to the dependence of the maximum disc temperature on the BH mass and to the different environments. The existence of fundamental similarities between accreting BH across the range of masses is proved by the existence of scaling relationships, like the fundamental plane for BH (Merloni et al., 2003) and the *break frequency*-BH mass-m relation (McHardy et al., 2006).

Accreting BH systems emit in X-rays over a broad band, with significant emission above 10 keV (at least in GBHB and AGN). While the soft X-ray emission is due to thermal disc emission in GBHB, and is of unknown origin in AGN, the hard X-ray emission is likely due to Comptonization of soft disc photons by T=10^9 K electrons. The resulting spectrum is usually very complex, including also the Compton reflection component, peaking at about 30 keV (George & Fabian 1991, Matt et al. 1991). This component arises from the reprocessing of the primary continuum by circumnuclear matter, and is accompanied by fluorescent lines, the most prominent of

them being the iron Kα fluorescent line. This representation of the spectrum is much simplified, not including further absorption and emission components often present, especially in AGN (e.g. the warm absorber). The presence of all these components makes already clear the need for broad band coverage, to disentangle the various components.

X-ray binaries

X-ray binaries are a special class of binary stars. They are formed by a low mass (Low Mass X-ray Binaries, LMXBs) or a high mass (High Mass X-ray Binaries) donor star transferring matter onto a black hole or a neutron star (NS). The binary nature of the system allows astronomers to measure the mass of the compact object. In some systems, the inferred mass of the X-ray emitting object supported the idea of the existence of black holes, as they were too massive to be neutron stars.

The binary system produces X-rays if the stars are in close enough proximity that material is pulled off the normal star by the gravity of the dense, collapsed star. The material accreted onto the surface must go through a transition region called the boundary layer. In the boundary layer, friction within the disk heats up the accreting material to temperatures exceeding a million degrees, and forces the material to spiral down gradually onto the compact object. Close to the compact object, the accreting plasma emits in the X-ray band and can reach very high luminosities. This region, located at few kilometers from the compact object, constitutes an ideal laboratory for studying the effects of General Relativity in the strong field regime. At the same time, it is important to study the properties of the accretion flow itself, as its different physical components and emission mechanisms are very complex and not yet fully understood. In addition, the possible relation between the accretion properties and the ejection of powerful relativistic jets from the systems must be investigated in more detail.

Ultra-Luminous X-ray Sources

Recent X-ray observations of galaxies have uncovered a populations of sources that have high X-ray luminosities but are not coincident with the nucleus of the galaxy. The luminosities are too high for a BH which has a mass a few times that of the Sun to be powering these sources. Moreover, these sources are long-lived, and so they cannot be special types of supernovae, for example. There are two main ideas which could explain these sources. In the assumption that they are BHs accreting from a companion star, the masses required are in the region of 100 $M_{\odot}$ or more, suggesting the existence of intermediate mass black holes (IMBH). The problem with this explanation is that there is no clear way to create BH of this mass. What could occur is that the emission from these objects is not isotropic, but concentrated into jets.

This reduces the necessity for the most massive BHs, and means that ULXs could just be special X-ray Binaries. Why some X-ray binaries have emission concentrated into particular directions and others do not is another matter. The other explanation is that the maximum luminosity limit is temporarily over-stepped for a few years or decades.

X-ray images of interacting galaxies show that in such a systems there are large numbers of ULXs present. When galaxies collide the stars very rarely hit each other as most of space is empty, but the gas that exists between the stars does interact and the collision causes shock waves. These cause the collapse of gas clouds and new stars form. Interacting galaxies tend to have large amounts of star formation, and appear blue as the light is dominated by young massive stars. These objects show large amounts of star formation and contain many ULXs, suggesting a link between the two. This apparent connection is difficult to reconcile with the IMBH model, as the formation of IMBHs is uncertain and there is no clear reason why there should be a connection to recent star formation.

ULXs may just be a special stage in X-ray Binary evolution which are easier to form and could be expected to be connected to recent star formation as the most massive star, which forms the BH, does not last for very long. Then either the emission is concentrated into particular directions or the luminosities are just very bright.

This is still an ongoing topic of research as these sources have only been discovered since the launch of Chandra and XMM-NEWTON.

Active Galactic Nuclei

Most large galaxies have $\sim 10^{11} M_{\odot}$ of stars, $\sim 10^{9} - 10^{10} M_{\odot}$ of interstellar gas, and $\sim 10^{12} M_{\odot}$ of dark matter. In some galaxies the central region is observed to outshine all the billions of stars in the galaxy itself. The spectrum is not like that observed from stars and the emission is observed to be bright at all wavelengths. The luminosity varies on very short timescales, less than a day, and this means that the size of the central region is less than one light-day across. The most efficient conversion of matter to energy is the accretion by a BH, which works around 10%, and so we infer that it is a Super Massive Black Hole (SMBH) which is causing the emission.

The picture invoked to explain the existence of such objects is the following. When galaxies were young, the stars in the central regions of the galaxies were very closely packed. Star collisions and mergers occurred, giving rise to a single massive black hole with perhaps 10^6 to 10^9 $M_{\odot}$.

Gas from the galaxy's interstellar medium, from a cannibalized galaxy, or from a star that strays too close, falls onto the SMBH. As in X-ray binary star systems, an accretion disk forms, emitting huge amounts of light across the electromagnetic spectrum (infrared to gamma rays). The SMBH plus accretion disk produces the phe-

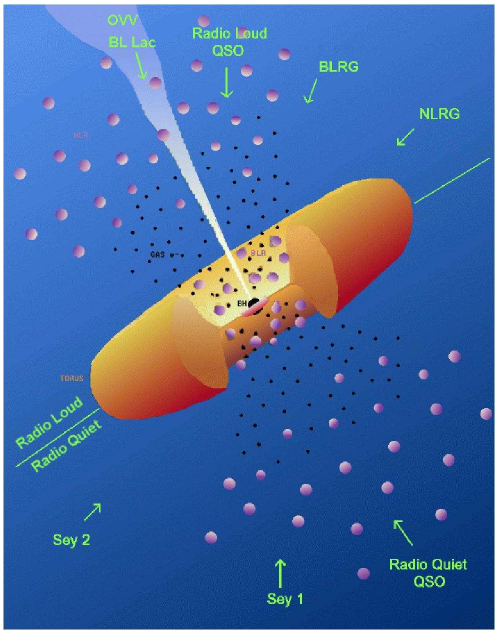

Figure 2.2: It is thought that the different properties of AGN can be attributed to differences in the observer's viewing angle, i.e. looking at an AGN through the dusty torus, it can look very different from viewing an AGN along the axis of its jet. This schematic diagram illustrates these differences. Credits: Urry & Padovani, 1995.

nomena seen in active galactic nuclei (AGN). The central object, accretion disk and lobes are all visible. The high energy and radio emission is direct, coming from the central regions around the black hole itself. In the optical and infrared wavebands the emission is not direct - the light has been absorbed and then is re-radiated (possibly at a new wavelength) by clouds of gas and dust which surround the central engine.

The different types of AGN are variations on this theme. The lower luminosity AGN are called Seyfert Galaxies (and there are two types of these) and Radio Galaxies. The more luminous AGN are called Quasars (from Quasi Stellar Objects or QSO as they looked like stars in early telescopes), blazars and BL Lac's.

Another distinctive feature of AGN is that some of them (approximately 10%) are observed to have jets. By some unknown mechanism the BH produces jets of material which are linear and remain collimated over thousands of light years. These jets emit radio waves which imply that they contain charged particles, most probably electrons, and magnetic fields. Radio galaxies, quasars, and blazars are AGN with strong jets that can travel outward into large regions of intergalactic space. The whole family of AGN may be unified by using one model, which is then viewed at different

angles (Fig. 2.2). The BH is surrounded by an accretion disc and is producing jets. In the same plane as the disc there are clouds of material in orbit around the BH, those closer in move faster and so their spectral lines have greater Doppler broadening. The brightest objects are those which are aligned such that we are looking straight down the jet. The emission from the core becomes less and less as the angle from the jet axis increases. Many of the apparent differences between types of AGN are due to our orientation with respect to the disk. With blazars and quasars, we are looking down the jet. For Seyferts, we are viewing the jet broadside.

X-ray astronomy has helped to confirm that SMBHs exist and are present at the centers of AGNs. Some spectral lines occur in the X-ray realm of the electromagnetic spectrum, the Iron K line at 6.4 keV is one of the most used. The line is no longer a sharp peak but spread out in a distinctive shape which results from the relativistic effects which are expected to occur close to the black hole. The extent of the line to low energies, the "red-wing", depends on from how close to the black hole there is emission from the accretion disc. If there is a "blue-wing" then the disc is more edge-on.

Considerable uncertainties remain. Exactly how are jets produced and accelerated? Where do the clouds producing the broad emission lines come from? Can we empirically confirm that a SMBH is actually present?

2.2.2 Supernova Remnants

In a Supernova explosion the outer layers of the star are expelled into space and form a Supernova Remnant. What is left of the centre of the star is either a NS or a BH. X-ray observations are one of the most important means to study the many aspects of SNRs.

The outer layers of the star travel outwards much faster the speed of sound; they form a blast (or shock) wave. This compresses the tenuous gas in between the stars (the Inter Stellar Medium, ISM) which causes the emission of X-rays. X-ray observations of supernova remnants have been a valuable source of information on the interactions between the explosion and the surrounding gas, and have been used to create our present understanding of the supernova explosion.

X-ray spectroscopy is essential to obtain abundances of the prime nucleosynthesis products of supernovae, which are the so-called alpha-elements (O, Ne, Mg, Si, S, Ar, Ca) and iron-group elements (chiefly Fe, Ni, and some trace elements with $20 < Z < 28$). All these elements have prominent emission lines in the 0.5-10 keV band for temperatures between 0.2-5 keV, which happens to be the typical electron temperatures of plasma heated by SNR shocks.

If the core of the star forms a NS, then this can also be a source of X-rays. NS can have intense magnetic fields associated with them, and they can also rotate very fast. As it is the naked core of the star it is initially very hot and emits X-rays;

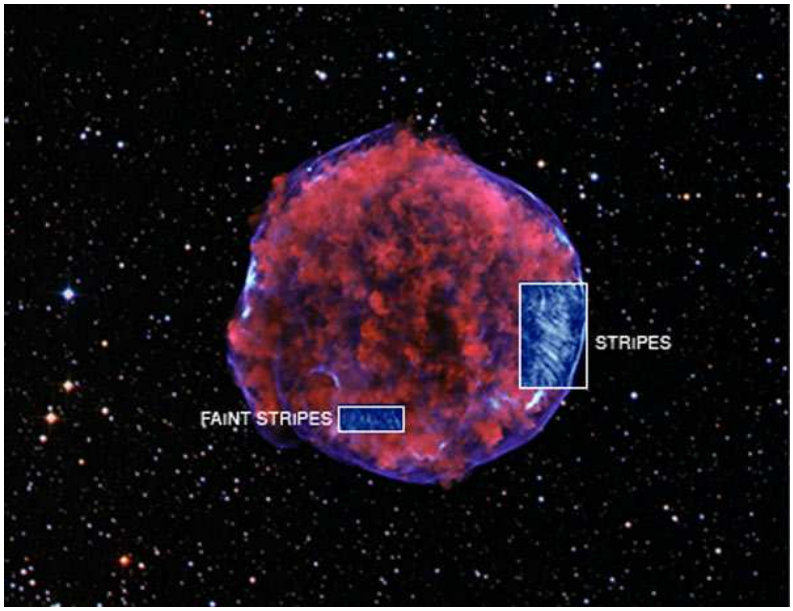

Figure 2.3: Tycho's supernova remnant: the expanding debris from the explosion is shown in low-energy (1.6-2.15 keV) X-rays (red), while the blast wave shines in high-energy (4-6 keV) X-rays (blue). X-ray stripes, which have never been seen before in any supernova remnant, have been spotted lurking in X-ray observations of its high-energy blast wave. The stripes are believed to be regions where magnetic fields in the blast wave are more tangled than in surrounding areas. (credit: X-ray: NASA/CXC/Rutgers/K.Eriksen et al.; Optical: DSS)

however they cool over many years. Once it has cooled down it can only be seen if the magnetic axis is not aligned to its rotation axis. As the magnetic fields are so strong radiation and particles are channelled down the magnetic poles and the stars can only be "seen" when a pole points towards the Earth - this is then known as a pulsar (pulsating star) as a set of regular pulses are observed, like a lighthouse. The X-rays that come from the central remnant of the Supernova cause the elements in the expanding gas shell to fluoresce. Different elements show up at different energies, which allows the composition of the gas shell and also the star to be estimated.

Recent very deep Chandra observation of the Tycho supernova remnant (Eriksen et al., 2011) revealed that high-energy X-rays show a pattern of X-ray "stripes" never previously seen in a supernova remnant (Fig. 2.3). These stripes may provide the first direct evidence that SNRs can accelerate cosmic rays and they provide support for a theory about how magnetic fields can be dramatically amplified in such blast waves.

2.2.3 Clusters of Galaxies

Galaxy clusters contain from several hundred to several thousand galaxies in a volume of around 1 Mpc. These galaxies are bound together by their mutual gravitational attraction. The amount of mass tied up in these systems is generally between 10^{14} to 10^{15} solar masses. Galaxy clusters, however, are not just composed of galaxies, for they also contain hot gas. The temperature of the gas is very high, ranging from 0.2 keV to 10 keV. With such a high temperature, the gas is almost fully ionized. The dominant radiative process is bremsstrahlung emission, which is the emission of electromagnetic radiation by a free electron passing by an ion. This radiation has a characteristic energy that is set by the temperature of the electrons. For a temperature of several keV, this energy is in the X-ray band. Galaxy clusters are therefore X-ray sources.

The first issue in observing galactic clusters with the current imaging X-ray telescopes is to accurately model this gas cloud. Already these telescopes have shown the structure of the hot gas to be spatially more complicated than a simple sphere. The gas can have two central concentrations, and it can have a somewhat complicated structure.

Because clusters of galaxies emit X-rays, they can be found by their X-ray emission. For this reason, current X-ray telescopes are conducting surveys to find clusters. The value of these surveys is that they tell us how much of the Universe's mass is tied up in galaxy clusters, and it gives us a measure of how clumped matter is on the 10 Mpc length. These measurements therefore can improve our understanding of cosmology.

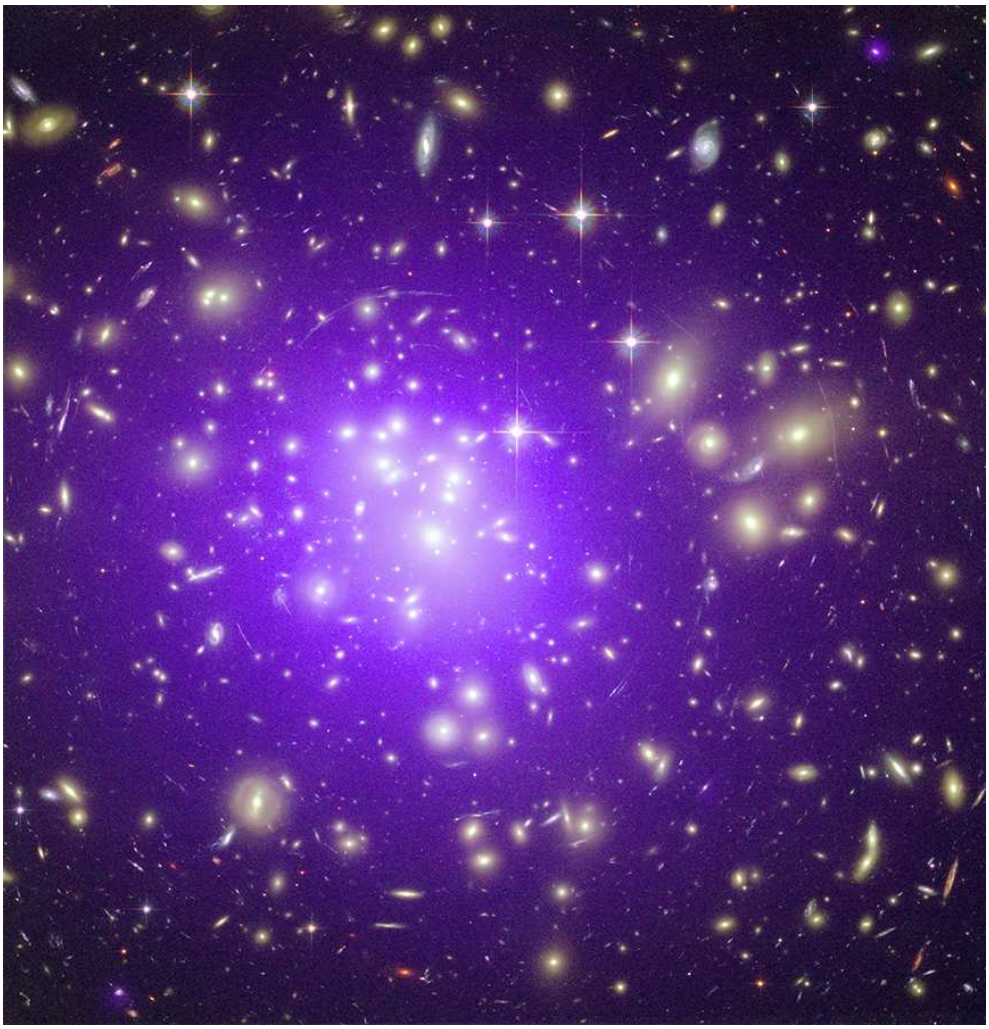

Figure 2.4: Abell 1689, shown in this composite image, is a massive cluster of galaxies located about 2.3 billion light years away that shows signs of merging activity. Hundred-million-degree gas detected by NASA's Chandra X-ray Observatory is shown as purple in this image, while galaxies from optical data from the Hubble Space Telescope are colored yellow. Credit: X-ray: NASA/CXC/MIT/E.-H Peng et al; Optical: NASA/STScI

2.2.4 Cosmic X-ray Background

The discovery of a diffuse Cosmic X-ray Background (CXB) radiation dates back to the birth of X-ray astronomy: it was a serendipitous result of the same rocket experiment that detected the first extra-solar X-ray source, Scorpius X-1 (Giacconi et al., 1962). The data showed diffuse emission of approximately constant intensity from all directions. The first all-sky X-ray survey with Uhuru and Ariel V in the 1970's revealed a high degree of CXB isotropy leading researchers to the conclusion that the CXB has to be mainly extragalactic. The problem of the nature of the CXB immediately became one of the most debated topics in astrophysics.

In the late 70 s the first broad-band measurement of the CXB spectrum was obtained with the HEAO-1 satellite. In the 3-50 keV range the data were found to follow a thermal bremsstrahlung distribution (kT$\sim$40 keV), well approximated below 15 keV by a simple power law with photon index $\sim$1.4 (Marshall et al., 1980). Several pieces of evidence led to the understanding that the bulk of the CXB above the energy of $\sim$1 keV is extragalactic in origin and is made up from the integrated emission of faint discrete sources, with a dominant contribution from AGNs (Setti & Woltjer, 1989). In particular, optically bright quasars and Seyfert galaxies dominate at low energies (up to a few keV), while obscured AGNs are thought to be responsible for the bulk of the CXB at high energies ($>$10 keV).

This picture has been confirmed by the results from imaging X-ray observatories. Starting from the early observations with the Einstein satellite (Giacconi et al., 1979), to the recent deep surveys with Chandra (Moretti et al. 2003 and references therein) and XMM-Newton (Hasinger et al., 2001), a higher and higher fraction of the CXB, up to 80-90% in the overall 0.5-10 keV range, has been resolved into discrete sources, mainly obscured and unobscured AGNs.

One of the main uncertainties involved in the problem is the CXB intensity itself. Since the HEAO-1 experiment, several measurements of the CXB spectrum have been obtained at energies below 10 keV. While the results on the spectral shape confirmed a power law with index $\sim$1.4, the normalization of the CXB remained highly uncertain as a consequence of large discrepancies (well beyond the statistical errors) among the different determinations. A difference as large as $\sim$40% is found from the highest measured value Vecchi et al. 1999 using SAX data) to the lowest one (the original HEAO-1 experiment, Marshall et al. 1980).

At low energies ($<$15 keV) many CXB measurements with both imaging and non-imaging telescopes aboard satellite missions, have been performed. At high energies ($>$15 keV), instead few measurements are available (after that with HEAO-1). Observations at these energies have been performed with INTEGRAL (Churazov et al., 2007) and Phoswich Detection System (PDS) aboard the BeppoSAX satellite (Frontera et al., 2007).

Barcons et al. (2000) pointed out two possible different causes to explain the large

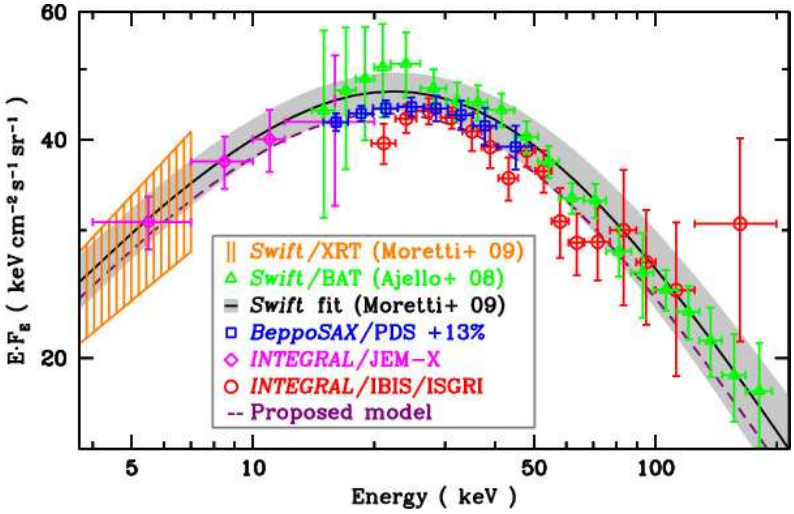

Figure 2.5: CXB spectrum (unresolved plus resolved) as observed by different missions. Credit: Frontera et al. (2007).

scatter among the different determinations of the CXB intensity. First, cosmic variance: spatial variations of the CXB intensity are expected as a consequence of its discrete nature. In this view, part of the discrepancies could be due to the amount of sky solid angle surveyed, which is very large in the case of HEAO-1 and BeppoSAX PDS, and very small in the case of BeppoSAX MECS, XMM-Newton, and Chandra, although this would imply that the sky regions surveyed by these telescopes are systematically brighter than the average sky sampled with HEAO-1 and BeppoSAX PDS. The second explanation invokes systematic errors, including cross-calibration differences.

An uncertain value of the intensity represents a very severe limitation to any understanding of the ultimate nature of the CXB. Even basic information such as the resolved fraction of the CXB cannot be firmly evaluated.

How the hard emission is produced, the exact modes in which accretion occurs, how the accreting matter is distributed, and the complex interplay between the AGN power and their host galaxies, are all still poorly known. Given the importance of this topic, one of the main goal for future X ray missions should be to resolve most of the CXB at its peak energy density, shedding light on the physics of accretion and the emission mechanisms. Only hard X-ray observations (up to 70-80 keV) with high sensitivity can allow to pinpoint and study the sources that make the bulk of the CXB.

2.3 Why we need X-ray telescopes focusing above 10 keV and with higher angular resolution

High energy phenomena are best revealed and characterized by their non thermal-emission in the low energy X-ray and hard X-ray domains, the latter probing the most energetic and violent environments. The emission from astrophysical sources, however, is by large best known at energies below 10 keV, due to a very large gap in angular resolution and sensitivity between these two domains. The main reason for this situation is purely technical since grazing incidence reflection has so far been limited to the soft X-ray band.

Below 10 keV, astrophysics missions are using X-ray mirrors based on grazing incidence reflection properties. This has allowed the study of compact accreting sources, galaxies with an active nucleus and high temperature thermal plasma sources. The use of collimated detectors on board the UHURU, Ariel-V, and HEAO1 satellites in the 1970 decade led to the discovery of <1000 X-ray sources in the whole sky, most of which with a redshift $z < 0.5$. Imaging detectors, first on board Einstein and then ROSAT, produced the first systematic observations of AGNs up to z = 2–3, and systematic mapping of galaxies, clusters of galaxies and supernova remnants. The superior image quality of Chandra and the high throughput of XMM-Newton have expanded the discovery space even further, resolving for example more than 80% of the CXB below 5-6 keV, and starting to probe emission of star-forming galaxies, and to resolve jets lobes and hot spots in quasars and radio galaxies.

Above 10 keV, i.e. in the so called hard X-ray band, however, the situation contrasts strikingly with this picture. The most sensitive observations so far have been performed by using only passive collimators, as those on board of the BeppoSAX and RossiXTE satellites, or coded masks as those on board of the INTEGRAL and Swift satellites. As a result less than two thousands sources are known in the whole sky in the 10-100 keV band, a situation recalling the pre-Einstein era at lower energies.

X-rays of energy greater than several hundreds of eV can penetrate the interstellar gas over distances comparable to the size of our own galaxy, with greater or lesser absorption depending on the direction of the line of sight. At energies of a few keV, X-rays can penetrate the entire column of galactic gas and in fact can reach us from distances comparable to the radius of the Universe. This demonstrates the fundamental importance of the wide band to understand in depth the physics of the variety of objects in the X-ray sky and their emission and transfer processes. These include, for instance, thermal versus non-thermal processes, particle acceleration, radiative transfer in strongly magnetized media, jet formation and evolution, absorption and scattering in Compton thick surroundings: all of these in often (highly) variable sources. Those results demand that above 10 keV, in order to match the sensitivity below 10 keV, one should go down to limits in flux three orders of magnitude better than

those reached so far, and correspondingly out to very large cosmological distances. This last point brings to the forefront the topical case of the CXB. Made of discrete sources in the soft X-rays, consisting mainly of accreting Super-massive Black Holes distributed over cosmological distances, in the spectral region where it peaks, namely between 20 and 30 keV, a fraction as large as about 98% of the CXB remains unresolved. Therefore the putative discrete sources that, according to model-dependent extrapolations, should be contributing to it are still to be identified. All this calls for focusing X ray optics at higher energies, up to 80 keV and beyond.

The advent of new and even more powerful experimental techniques, such as high resolution spectroscopy and X-ray telescopes capable of focusing increasingly higher energies over wider fields, ensures a wide opportunity for new astronomical discoveries.

Examples of new project missions with improvement in spectral resolution and angular resolution developed in the last period are listed:

Simbol-X - a new-technology hard X-ray (0.5 - 80 keV) focussing telescope that could provide order of magnitude improvement in angular resolution and sensitivity compared to the non-focussing instruments that have operated so far in this crucial energy band. The key of this project was having a long focal length (30 m) in order to increase the energy band reducing the incidence angle. Simbol-X could be the first orbiting telescope to take advantage of the emerging spacecraft formation flying technology. The Symbol-X mission was jointly supported by the French (CNES) and Italian (ASI) space agencies: it has been selected for phase-A study with a target launch at the beginning of 2014 (Ferrando et al. 2006). Unfortunately, due to budget restrictions, in March 2009, CNES unexpectedly decided to stop the project after the end of Phase A. The Simbol-X mission was therefore cancelled.

NHXM - New Hard X-ray Mission telescope was the attempt to ASI into using the technology already developed in the Simbol-X project, improving the optical system to multilayer technology. The New Hard X-ray Imaging and Polarimetric Satellite Mission had a high spatial and energy resolution over a very broad energy band, from 0.2 to 80 keV, together with a sensitive X-ray imaging polarimetric capability. It was based on four identical mirror modules that, for the first time, could extend from 0.2 keV up to 80 keV the fine imaging capability today available only at $E<10$ keV. At the focus of three telescopes there will be three identical spectro-imaging cameras, at the focus of the fourth the X-ray polarimeter. The addition of a Wide Field X-Ray Monitor, sensitive in the band 2-50 keV, could permit also to detect highly variable sources (e.g. GRB, soft-Gamma Ray repeaters, transient sources like CV, novae, binary sources, or relativistically boosted blazars, etc.). (Tagliaferri et al.

2011) Unfortunately, in June 2011, the project was cancelled because ESA did not approve the mission as medium size mission. The project will be presented in more detail in section 3.

Astro-H - ASTRO-H is an international X-ray observatory, which is the 6th in the series of the X-ray observatories from Japan. It is currently planned to be launched in 2014. ASTRO-H features two hard X-ray telescopes with depth-graded, multilayer reflectors that provide a 5-80 keV energy range (Miyazawa et al. 2010). The project will be presented in more detail in section 3.

NuSTAR - The NuSTAR mission will deploy the first focusing telescopes to image the sky in the high energy X-ray (6 - 79 keV) region of the electromagnetic spectrum. The project will be presented in more detail in section 3.

ATHENA - Advanced Telescope for High ENergy Astrophysics, is a high-throughput X-ray telescopes, based on ultra-lightweight Silicon Pore Optics (SPO) technology developed by ESA. The focal length of each telescope is approximately 12 m. ATHENA will be launched into a halo orbit at the Sun-Earth L2 after 2025. The project will be presented in more detail in section 3.

3 X-ray telescopes

3.1 Collimated telescopes

A *collimated telescope* is essentially a channel (or a system of channels) in front of the X-ray detector (CCD for X-ray imaging, gratings, crystals, photoelectric or calorimetric detectors for spectroscopy) that limits the solid angle of observation. The angular resolution of an X-ray collimated telescope almost coincides to its Field of View (FOV) unless we use coded masks (or microchannels plates) and position-sensitive detectors. Anyway, the angular resolution will be poor, unless we reduce the aperture dimensions at cost of the effective area. Also when using coded mask devices, in practical cases the angular resolution will be limited to some arcminutes. On the other side, a *X-ray focusing system* allows a real X-ray imaging, resolving the extended source details avoiding the source confusion in the same FOV, without loss of collection area. At present time the resolution limit is not dictated by the diffraction of light (unlike optical telescopes), but it depends mainly on the optics shape accuracy and design, and on their stability in orbit environmental conditions.

3.1.1 Angular resolution

The photon distribution on the focal plane may be defined in different ways. The bidimensional distribution of photons from an object located at infinity on the focal plane is in general integrated around the focal spot to obtain the radial distribution called PSF (Point Spread Function). The EE (Encircled Energy) is the fraction of focused photons as function of the angular distance from the barycentre. In practice, the angular resolution is obtained from the above definitions as the HEW (Half-Energy Width), also known as HPD (Half Power Diameter), i.e. the angular diameter in the focal plane that includes the 50% of the focused photons. The PSF FWHM is also used, even if this parameter is not very useful in X-ray optics, because the X-ray focal spot often deviates from the gaussian profile and shows relevant ”wings”: hence, the FWHM usually underestimates the photon spread unless the X-ray source is very

bright. The HEW instead allows one to estimate the fraction of photons which are effectively focused on the detector, which in turn determines the sensitivity of the telescope (see Fig. 3.1).

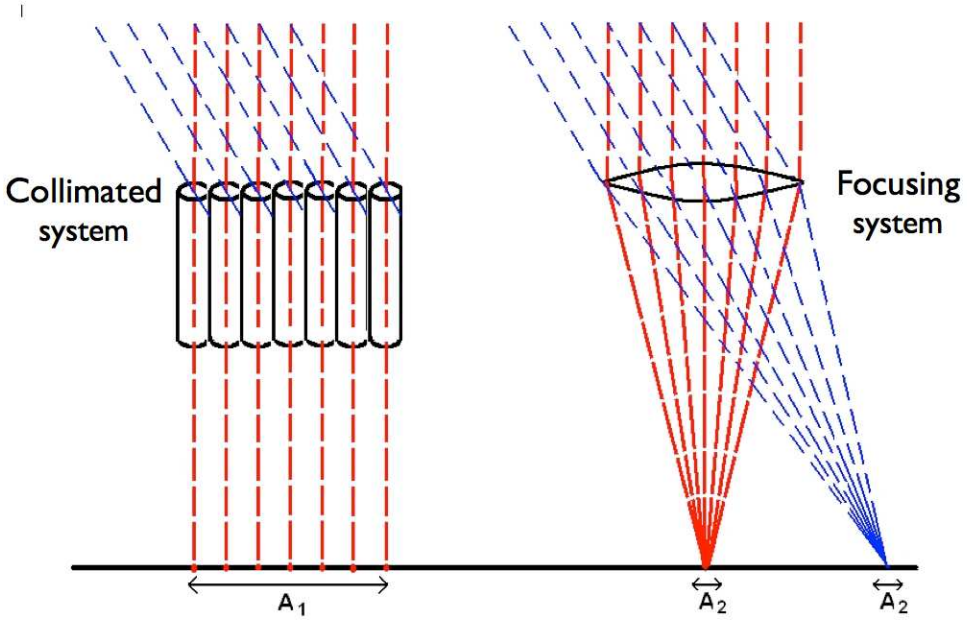

Figure 3.1: The principle of X-rays focusing. Left: in a simply collimated telescope the source is projected on the detector together with all the background B, and using a very large fraction of the detector surface. Right: in a focused telescope the image of the star is concentrated on a little surface and most of background is rejected.

3.1.2 Sensitivity

The use of focusing optics also greatly improves the telescope sensitivities. The minimum detectable flux (the telescope *sensitivity*) is limited by the *background noise* B, defined as the number of background counts per unit time, per energy band and per detector unit area, which is typical of the chosen detector (intrinsic background: dark current in the proportional counter, nuclear decays, etc.) and of the operative conditions (aperture background: cosmic background, trapped particles in Earth magnetosphere, cosmic rays, solar protons, etc.). A measurement of the average background value is obtained when the source is out of the field: the source flux is then calculated

by subtraction. However, as the background flux fluctuates according the Poisson's statistics, the source flux is known with an uncertainty depending on the fluctuation amplitude. Let us suppose to have a collimated telescope with detector area A_d and a quantum efficiency ηE at the photon energy E, sensitive in the energy band ΔE. In the time Δt the background counts will be $C_B = BA_d\Delta E\Delta t\eta_E$. In the same time, the photon count from an X-ray source with flux S_E will be $C_S = S_E\Delta t\Delta E\eta - EA_d$. During an observation, the background is superposed to the signal C and then subtracted. The measured count C_{meas} is obtained as C_{meas} = (C_S + C_B) - C_B . Since the background fluctuation is much larger than that of the signal, propagating the error on C_{meas} we obtain:

$$\sigma^2(C_{meas}) = 2\sigma^2(C_B) \tag{3.1}$$

The condition to see this source over $N\sigma$ will be $C_{meas} > N\sigma(C_{meas})$, yielding for the minimum detectable flux S:

$$S = \frac{N}{\eta_E}\sqrt{\frac{2B}{A_d\Delta t\Delta E}} \tag{3.2}$$

this is the sensitivity of a collimated X-ray telescope (of course as a function of the energy).

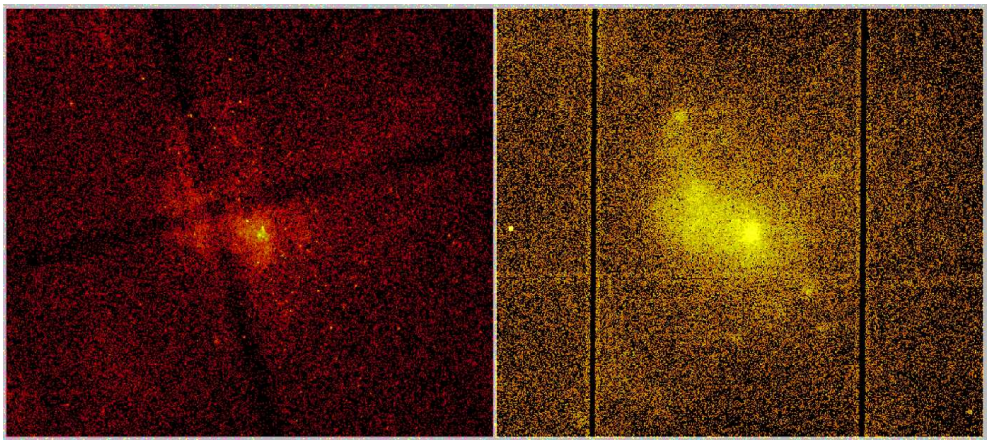

Figure 3.2: A comparison between the observation of the Galactic Centre by Chandra (left, HPD = 0.5") and XMM (right, HPD = 20"). The degradation in angular resolution is a 40-fold factor.

Let us suppose instead to have a *focusing optic* with effective area A_e which focuses the flux S on a fraction ϵ of the detector area A_d: in this case the detected signal

is $C_S = S\Delta t\Delta E\eta_E A_e$, and the noise will be $\sigma(C_{meas}) = (2BA_d\Delta E\Delta t\epsilon)^{1/2}$. The sensitivity will thus be

$$S = \frac{N}{A_e\eta_E}\sqrt{\frac{2BA_d\epsilon}{\Delta t\Delta E}} \tag{3.3}$$

The comparison between the eq. 3.2 and the eq. 3.2 show the different dependence of the sensitivity on the telescope size. In a collimated telescope the sensitivity is proportional to $A_d^{1/2}$ i.e. on the *root of the detector area*: considering the size of practically obtainable detectors, it is very difficult to reach a good sensitivity with collimated telescopes. Moreover, very large detectors (including those used with coded masks) are very difficult to be monitored and controlled in response efficiency. On the other side, a focused telescope improves the sensitivity in proportion to A_e, the *effective optics area*: moreover, in this case we should prefer to use small detectors, because in this case the photon collection is completely demanded to the optics and smaller detectors will result in a lower background noise (see Fig. 3.3).

The big *leap* of sensitivity in hard X-ray is sured by the absence in hard X-ray of focusing optics with high angular resolution (smaller values of ϵ in 3.3) and large collecting area.

3.2 Soft X-ray optics

In a telescope sensitive to extreme ultraviolet and X-ray wavelengths, a normal incidence mirror would be very inefficient because it absorbs photons. For this reason X-ray mirrors work in grazing-incidence, exploiting the total reflection principle, where incoming light is reflected off the mirror surface at very shallow angles, close to the critical angle (see next section).

3.2.1 Grazing incidence

Light waves incident on a material induce small oscillations of polarisation in the individual atoms (or oscillation of electrons, in metals), causing each particle to radiate a small secondary wave (in all directions, like a dipole antenna). All these waves coherently interfere to give specular reflection and refraction, according to the Huygens-Fresnel principle (see sect. 6.1).

We consider the amplitudes of the reflected and transmitted waves. We shall assume that the two (homogeneous and isotropic) media are both of zero conductivity and consequently perfectly transparent; their magnetic permeabilities will then in fact differ from the unity by negligible amounts, and accordingly we take $\mu_1 = \mu_2 = 1$. Let A be the amplitude of the electric vector of the incident field. We consider **p** the parallel direction and **s** the perpendicular direction with respect the incidence plane

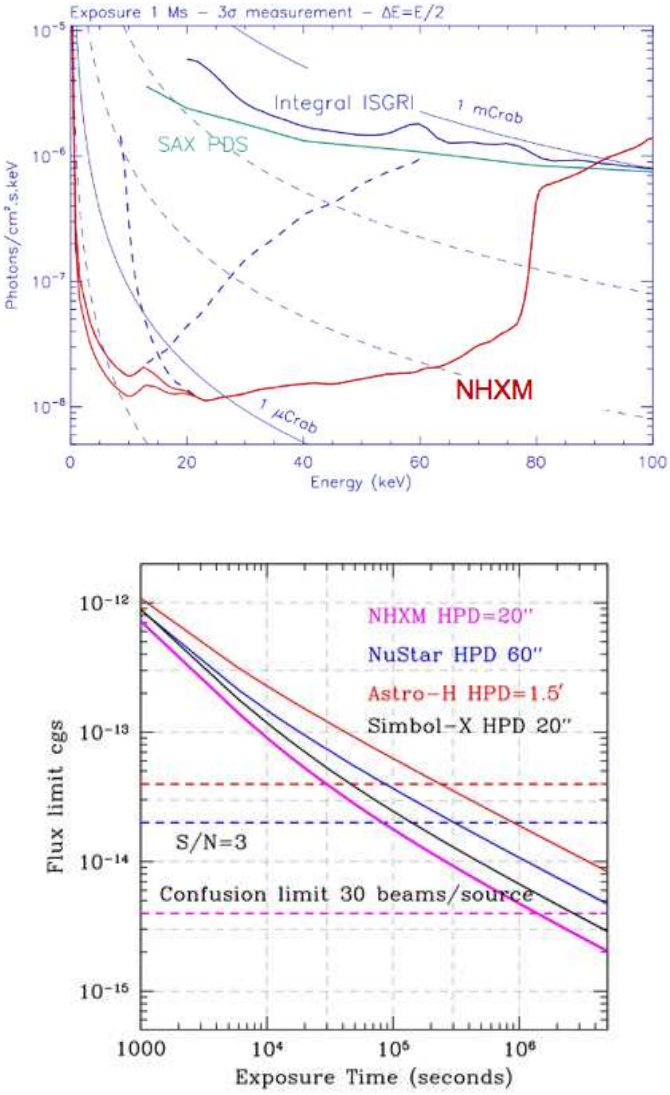

Figure 3.3: Top: NHXM sensitivity as function of the energy compared with current and previous missions. At low energies the two lines are for two different operating modes of the low energy detector. Clearly, NHXM is orders of magnitude more sensitive than non-focusing instruments. Bottom: the 10-40 keV 3sigma sensitivity of NHXM (purple curve), NuStar (blue curve) and Astro-H (red curve) as a function of the exposure time. The horizontal dashed lines represent the confusion limit for the three missions, computed assuming 30 beams per source (Tagliaferri et al., 2011).

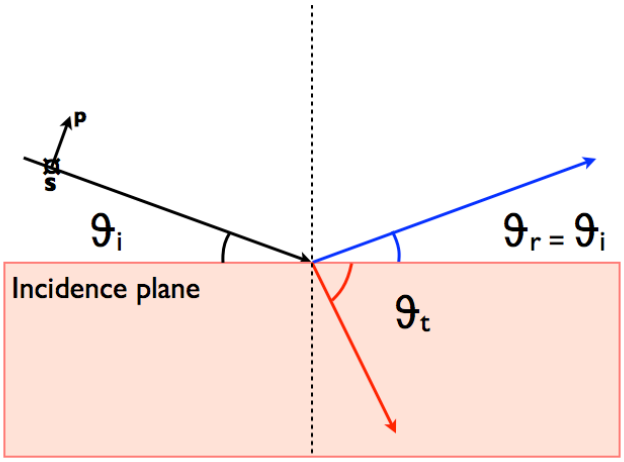

Figure 3.4: Sketch of a wavefront impinging a single dioptre.

(see Fig. 3.4). The *Fresnel formulae* provide the complex amplitudes of the transmitted and reflected waves, T and R; as functions of the incidence (θ_i) and refraction (θ_t) angles.

$$T_p = \frac{2\cos\theta_t \sin\theta_i}{\sin(\theta_i + \theta_t)\cos(\theta_i - \theta_t)} A_p \tag{3.4}$$

$$T_s = \frac{2\cos\theta_t \sin\theta_i}{\sin(\theta_i + \theta_t)} A_s \tag{3.5}$$

$$R_p = \frac{\tan(\theta_i - \theta_t)}{\tan(\theta_i + \theta_t)} A_p \tag{3.6}$$

$$R_s = \frac{\sin(\theta_i - \theta_t)}{\sin(\theta_i + \theta_t)} A_s \tag{3.7}$$

Since θ_i and θ_t are real, the trigonometrical factors on the right-hand sides of the formulae will also be real. The phase of each component of the transmitted wave is always equal to the phase of the corresponding component of the incident wave. In the case of the reflected wave, the phase is 0 or π depending on the relative magnitudes of θ_i and θ_t.

But the reflectivity of a mirror depends on its surface morphology and on its own internal structure. In order to completely understand this dependence we have to apply the optical physics laws. As visible light, the propagation of X-rays is ruled

by Maxwell's Laws and a plane wave travelling in an arbitrary direction **r** may be represented by the function:

$$\mathbf{E}(x,y,z,t) = \mathbf{E}_0 exp\left[i(\mathbf{k}\,.\,\mathbf{r} - \omega t)\right], \qquad \mathbf{k} = \frac{2\pi}{\lambda}\mathbf{n} \tag{3.8}$$

where n, the refractive index of the medium, can be written in a complex form:

$$n = 1 - \delta + i\beta \tag{3.9}$$

where β accounts for the absorption losses. The δ and β parameters are the *optical constant* of the material. The main contribution to β is given by the photoelectric effect: it becomes important especially in correspondence of the electronic energy levels, especially for the most tightly bound electrons (K-shell). Typical values are $\delta \approx 10^5 \div 10^6$ and $\beta \approx 10^6 \div 10^7$. Expressions of δ and β are:

$$\delta = \frac{N_A r_e}{2\pi A}\lambda^2 \rho f_1 \quad \beta = \frac{N_A r_e}{2\pi A}\lambda^2 \rho f_2 \tag{3.10}$$

where f_1 and f_2, the number of effective electrons/atom, are called scattering coefficients. N_A is the Avogadro number, r_e is the classical electron radius, A is atomic mass, and ρ is the density. In visible light, excepting propagation in conductors, the imaginary term is usually negligible, and n is significantly larger than 1. The incidence and the refraction angles are related by the usual Snell law:

$$n_1 \cos\theta_1 = n_2 \cos\theta_2 \tag{3.11}$$

Both δ and β contribute to the reflectivity, therefore the reflection coefficients do have an imaginary part, by assuming a phase shift of reflected rays.

In X-rays the reflection and the refraction obey the same laws as in the optical range, but because of values of refractive index they exhibit different features:

- As the real part of n is less than 1, the refracted X-ray approaches the surface, what is uncommon in the visible light.
- Being the n values so close to 1, the deflection of the refracted wave is about $\delta \cos\theta$: that is, very small; e.g. a 1 Å X-ray incident at $45°$ on Gold will have a deflection $\approx$ 10".
- For the same reason, the Fresnel equations give a reflectivity very close to 0 for both polarization at almost all incidence angles.
- After the refraction the X-ray is exponentially absorbed according to the law $e^{-(\beta/\lambda)x}$; that is, a 1Å X-ray in Gold decays of 1/e in a typical length $\lambda/\beta \approx 10^6\lambda = 0.1$ mm.

However, for very small values of θ_1, it is easy to show that the Fresnel equations for the reflected ray may be approximated by:

$$r_s = -r_p = +\frac{\delta_2 - \delta_1}{2\sin^2\theta_1} \tag{3.12}$$

and the reflectivity approaches 1 for decreasing angles down to $\theta = \theta_c$ (in the considered case $\delta_1 = 0$ and n = 1-δ_2); that is the largest possible angle of incidence which still results in a refracted ray and it is called the *critical angle*. Indeed, when light travels from a medium with a higher refractive index (e.g. a metal with high z) to one with a lower refractive index, Snell's law seems to require in some cases (whenever the angle of incidence is large enough) that the sine of the angle of refraction is greater than one. This of course is impossible, and the light in such cases is completely reflected by the boundary, a phenomenon known as *total internal reflection*. The electric field permeates the medium in a depth $\sim \lambda\sqrt{\theta_c^2 - \theta_0^2}$.

Therefore, if $\theta_i = \theta_c$, sin$\theta_t = 1$, i.e. $\theta_t = 90°$, so that the light emerges in a direction tangent to the boundary. So if θ_i exceeds the limiting value θ_c all the incident light is then reflected back into the first medium and we speak of *total reflection*. Nevertheless, the electromagnetic field in the second medium does not disappear, but there is not energy flux across the boundary.

The Snell law condition for the critical angle is $n_2 = n_1 cos\theta_1$ where n_1 and n_2 are the refractive index of the medium and of the reflective material respectively if $n_1 = 1$ (vacuum) and $n_2 = n$, the condition $\cos\theta_1 = n$ turns into $\theta_1 \simeq \sqrt{2\delta}$. If ρ is the density of the reflective material and E the energy of the incident wave we have also

$$\theta_c \propto \frac{\sqrt{\rho}}{E} \tag{3.13}$$

The critical angle increases for larger reflecting layer density but decreases in proportion to the photon energy. This implies that only X-ray energies below a cut-off value E_c can be totally reflected at a fixed incidence angle (see fig. 3.5). To increase θ_c, dense and high Z are adopted (e.g. Au, Pt, Ir). However, over 10 keV, even the critical angles of the densest coatings become too small and the mirror cross section offered to the incident flux becomes too low to return a sufficient effective area. For this reason multilayer coatings are used (see sect. 3.4.1).

Let us have an X-ray incident from vacuum on a material with refractive index n, with a grazing incidence angle θ_0. Snell law reduces to cos θ_0 = n cos θ_c. If (assuming $n = n_{12} = n_1/n_2$) we set

$$\sin\theta_t = \frac{\sin\theta_i}{n}, \qquad \cos\theta_t = \pm i\sqrt{\frac{\sin^2\theta_i}{n^2} - 1} \tag{3.14}$$

Developing the Fresnel formulae for the reflected amplitudes we obtain:

$$R_p = \frac{\sin\theta_i\cos\theta_i - \sin\theta_t\cos\theta_t}{\sin\theta_i\cos\theta_i + \sin\theta_t\cos\theta_t} A_p \tag{3.15}$$

$$R_s = -\frac{\cos\theta_i \sin\theta_t - \cos\theta_t \sin\theta_i}{\cos\theta_i \sin\theta_t + \cos\theta_t \sin\theta_i} A_s \tag{3.16}$$

and substituting into these expressions the 3.14, remembering that the upper sign is to be taken in front of the square root. We obtain the *Fresnel equations valid in any reflection regime*:

$$R_p = \frac{n^2 \sin\theta_i - i\sqrt{\cos^2\theta_i - n^2}}{n^2 \sin\theta_i + i\sqrt{\cos^2\theta_i - n^2}} A_p \tag{3.17}$$

$$R_s = \frac{\sin\theta_i - i\sqrt{\cos^2\theta_i - n^2}}{\sin\theta_i + i\sqrt{\cos^2\theta_i - n^2}} A_s \tag{3.18}$$

We note that R_p, R_s are in general complex (they reduce to the ordinary Fresnel equations in the case of usual refraction).

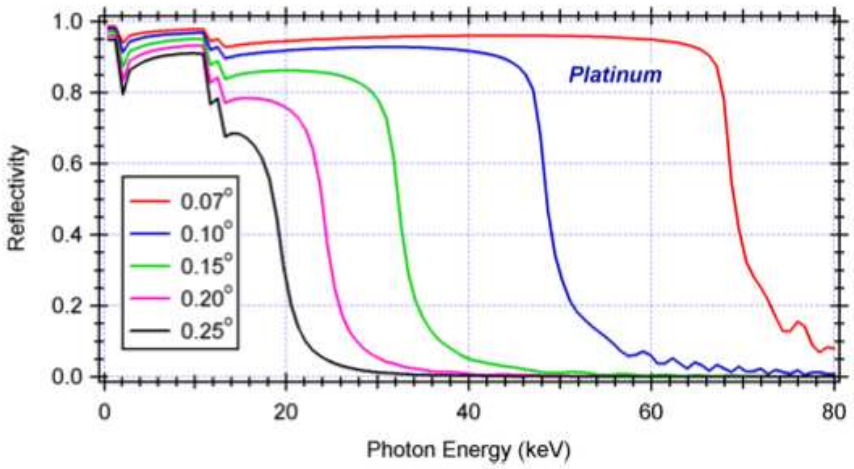

Figure 3.5: Behaviour of reflectivity with the energy of the incidence wave of a mirror coated with Platinum at several incidence angles. We note that the reflective cut-off increases as the incidence angle is decreased.

3.2.2 Mirror design

Several designs of grazing-incidence optics have been used in X-ray telescopes, including flat mirrors or combinations of parabolic and hyperbolic surfaces. In general, in order for any optical system to form a Coma-free image, it must satisfy the "Abbe sine condition", at least approximately. The Abbe sine condition states that an optical system will form Coma-free image of an infinitely distant object only if for each ray

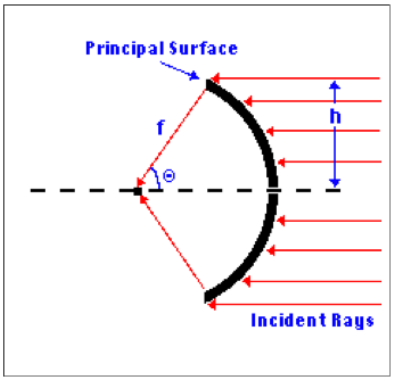

Figure 3.6: Abbe sine condition

in the parallel beam emanated from the source fullfills the condition:

$$h/\sin(\theta) = f \tag{3.19}$$

where h is the (axial) distance of the ray from the optical axis, θ is the angle of the final path of the ray relative to its initial path (and thus the optical axis) and f is a constant for all rays. In other words, an image will be formed if the principal surface, defined as the locus of intersections of the initial and final paths of rays, is a sphere. An optical system satisfying the Abbe sine condition acts as a spherical lens.

Parabolic mirror

A simple parabolic mirror was originally proposed in 1960 by Riccardo Giacconi and Bruno Rossi, the founders of extrasolar X-ray astronomy. This type of mirror is often used as primary reflector in optical telescopes where the paraboloid is well approximated by a sphere near the vertex. In an X-ray telescope the incidence has to be shallow angled, the part of the parabola must be distant from the vertex and it does not satisfy the Abbe sine condition, since the principal surface is the paraboloid itself and not a sphere (see Figure 3.7). Paraxial rays (rays impinging on the mirror parallel to the optical axis) will indeed focus to a point, but images of off-axis objects will be severely blurred. The German physicist Hans Wolter showed in 1952 that the reflection off a combination of two elements, a paraboloid, followed by a confocal and coaxial hyperboloid, will allow the Abbe sine condition to be nearly satisfied. Wolter also showed that any odd number of coaxial conic sections will not form a Coma-free image, but any even number can.

The most commonly used X-ray mirrors are the cylindrically parabola-hyperbola symmetric systems first described by Wolter.

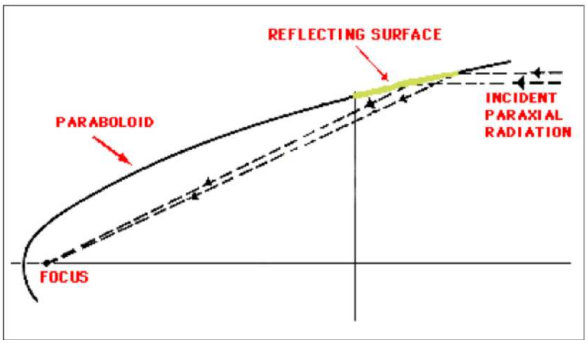

Figure 3.7: A simple parabolic mirror, Credits: van Speybroeck & Chase (1972)

Wolter-I system

Among the double reflection designs, the Wolter-I has the simplest mechanical configuration (Figure 3.8).

The equation for paraboloid-hyperboloid system (van Speybroeck & Chase 1972) coaxial and confocal (see Fig. 3.8) can be written in cylindrical coordinates as

$$r_p^2 = P^2 + 2PZ + [4e^2Pd/(e^2-1)] \qquad paraboloid \tag{3.20}$$

$$r_h^2 = e^2(d+Z)^2 - Z^2 \qquad hyperboloid \tag{3.21}$$

In the above equations the origin is at the focus for axial rays, Z is the coordinate along the axis of symmetry, and *r* is the radial coordinate. The common focus of the two surfaces is at $Z = [-2e^2d/(e^2-1)]$. There are thus three independent parameters, e, d, and P, which describe the surfaces. e is the eccentricity, P and d are two linear parameters expressing the dimension and the position of the two segments.

It is convenient to consider three other surface parameters to describe the system: Z_0 is the distance from the focus to the intersection plane of the paraboloid and hyperboloid which represents the principal plane of the optic ($Z_0 = f$), i.e. its focal length; α = 1/4 arctan (r_0/Z_0) = 1/2$(\alpha_p^* + \alpha_h^*)$, where r_0 is the radius of the surfaces at their intersection and α_p^*, α_h^* are the grazing angles between the two surfaces and the path of an axial ray that strikes at an infinitesimal distance from intersection. Note that if $\tan\theta_p^*$ and $\tan\theta_h^*$ are the slopes of the two surfaces at the intersection, α_p^* = θ_p^*, α_h^* = θ_h^* - 2θ_p^*, and α = 1/2(θ_h^* - θ_p^*); ξ = α_p^*/α_h^* = the ratio of the two grazing angles for an axial ray striking near the intersection of the two surfaces. The original parameters, e, d, and P can then be determined as follows:

$$\theta_p^* = [2\xi/(1+\xi)](\alpha) \simeq \alpha \tag{3.22}$$

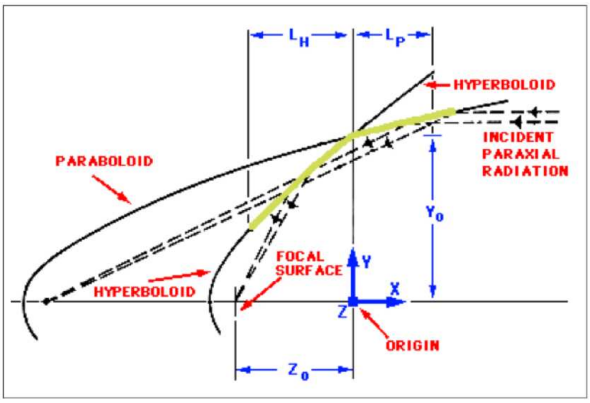

Figure 3.8: Wolter-I configuration, two element reflection image system. Credits: van Speybroeck & Chase (1972).

$$\theta_h^* = [2(1+2\xi)/(1+\xi)](\alpha) \simeq 3\alpha \tag{3.23}$$

$$P = Z_0 \tan(4\alpha) \tan(\theta_p^*) \tag{3.24}$$

$$d = \tan(4\alpha) \tan(4\alpha - \theta_h^*) \tag{3.25}$$

$$e = \cos(4\alpha)[1 + \tan(4\alpha) \tan\theta_h^*] \tag{3.26}$$

Moreover, if L_p and L_h are the lengths of the paraboloid and hyperboloid we have to consider that for every length of the paraboloid, L_h is constrained to be long enough so that axial rays striking the front of the paraboloid also strike the back of the hyperboloid. The constraint results in the following equation:

$$\frac{L_h}{L_p} = \frac{P}{ed + (e-1)L_p} \approx \frac{\xi}{1 + (\xi L_p / Z_0)} \tag{3.27}$$

In general, $\xi = 1$ and $L_p \ll Z_0$, therefore the most obvious choice is $L_h = L_p$ nevertheless, $L_h \lesssim L_p$ (see Fig. 6.4).

The radius R_0 of the mirror is determined by the focal length and the incidence angle:

$$R_0 = 4f \tan\alpha \tag{3.28}$$

as it can be seen with simple geometry considerations.

Polynomial geometry mirror

More general mirror designs than Wolter's exist in which the primary and secondary mirror surfaces are expanded as a power series (see Fig. 3.9). These polynomial solutions are well suited for optimization purposes, which may be used to increase the angular resolution at large off-axis positions, degrading the on-axis performances. The

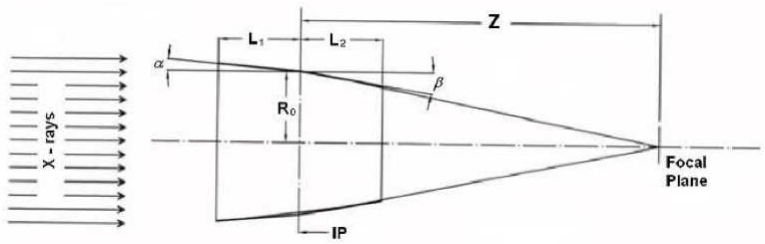

Figure 3.9: Telescope configuration and parameters. R_0 is the mirror shell radius at the intersection plane (IP); α (β) is the angle the between the primary (secondary) mirror tangent at the intersection plane and the optical axis; L_1 (L_2) is the length of the parabola (hyperbola) mirror segment; Z is the distance between the IP and the focal plane along the optical axis. For an X-ray telescope Z is very close to the focal length of the telescope F. (Conconi & Campana 2001)

idea is to transfer the principle of the Ritchey-Chretien Cassegrein telescope, widely used in optical astronomy, to grazing incidence optics. By deliberately compromising the on-axis performances, one can introduce aberrations (mainly spherical) that tend to cancel or reduce the off-axis aberrations (Conconi & Campana 2001). Such a profile is to be adopted in telescopes with large field of view like WFXT (Conconi et al. 2010).

Kirkpatrick-Baez system

Another system which forms real images consists of a set of two orthogonal parabolas of translation, off which incident X-rays reflect successively, as first proposed in 1948 by Kirkpatrick and Baez (Kirkpatrick & Baez 1948). A simplified Kirkpatrick-Baez design in shown in Figure 3.10a. In practical designs, the surface area is increased by using many approximately parallel mirrors (i.e., nesting) in each reflecting stage as in Figure 3.10b. The Kirkpatrick-Baez system offers inexpensive construction since the reflecting surfaces can be optically flat glass plates, bent to the proper curvature by mechanical stressing. On the other hand, the coalignment of many reflecting surfaces to form an optimum image is a difficult process. Since this was the first imaging telescope used for non-solar X-ray astronomy, the Kirkpatrick-Baez system is worthy of mention only for historical reasons. The typical application of the KB systems is in relation with facilities as synchrotron and electron linear accelerator (as Free Electron Laser FEL (Allaria et al. 2010)), where it is important having very small spot (on the order of a few microns) and high intensity flux for microscopy studies. It is also worth noting that a KB geometry was proposed for the XEUS optics (Ghigo 2008).

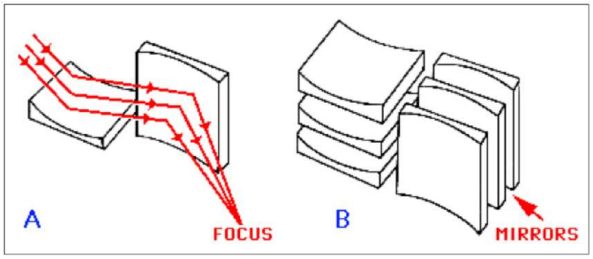

Figure 3.10: The Kirkpatrick-Baez X-ray Telescope Design

3.2.3 Effective Area

The Effective Area of an X-ray mirror is given by the ratio between the focused flux detected on the mirror focal plane and the incidence flux per unit area. For a source on-axis at infinity it is possible to show that for a Wolter I mirror the effective area A_e can be well approximated by the double cone expression:

$$A_e(E) = 8\pi f L \alpha^2 R(E)^2 \tag{3.29}$$

where f is the focal length, L the mirror length, θ the incidence angle on the reflective coating, $R(E)$ the reflectivity of the mirror at the X-ray energy E. In particular, the area depends on the squared reflectivity because the rays are reflected two times. The formula 3.29 can be applied to the Wolter-I to within L/f accuracy (Spiga et al. 2009).

For a source off axis of an angle γ at infinity (unless the f-number is small), the geometric area off-axis is reduced by a factor of

$$\frac{A(\gamma)}{A(0)} = 1 - \frac{2\gamma}{\pi\alpha_0} \tag{3.30}$$

In figure 3.11 is shown the normalized geometric area of an unobstructed mirror shell. If normalizing the result to $A_e(E, 0)$, the on-axis geometric area nesting obstruction (Eq. 3.29), can be expressed using the non-negative $S(x)$ function,

$$S(x) = \sqrt{1 - x^2} - x \arccos x, \quad with \;\; 0 \leqslant x \leqslant 1, \tag{3.31}$$

we have for a source off-axis of an angle γ

$$\frac{A_e(\gamma)}{A_e(0)} = 1 - \frac{2\gamma}{\pi\alpha}\left[1 + S\left(\frac{\Phi - \alpha}{\gamma}\right)\right] \tag{3.32}$$

where Φ is an obstruction parameter which represents the maximum angle visible from the reflective shell at the intersection plane through the entrance pupil (Spiga

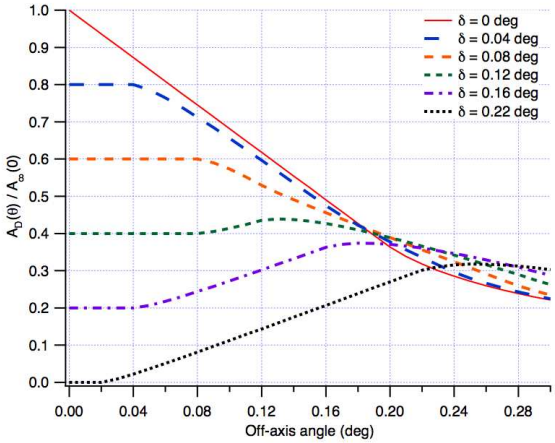

Figure 3.11: Normalized geometric area, $A(\gamma)/A(0)$, for a double cone mirror with a $\gamma_0 = 0.2$ deg, as a function of the off-axis angle, for different δ angles due to the finite distance of the source (Spiga et al. 2009).

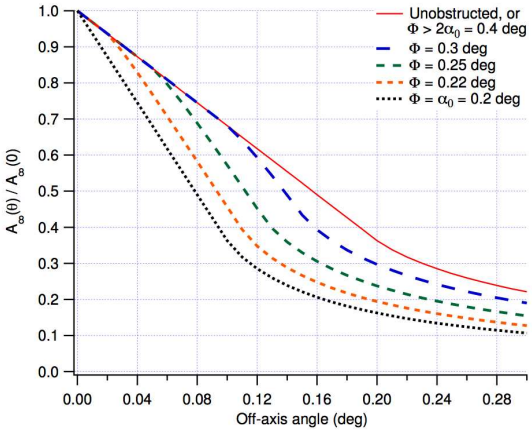

Figure 3.12: Normalized geometric area, $A_e(\gamma)/A_e(0)$ of an obstructed mirror shell with $\theta = 0.2$ deg and $L1 = L2$, as a function of the off-axis angle, for different values of the obstruction parameter Φ. The curve for the unobstructed mirror (the solid line) is also valid for any obstructed mirror with $\Phi > 2\theta$ (Spiga 2011).

2011). In Fig. 3.12 is shown the normalized geometric area of an obstructed mirror shell.

As θ has to be less than $\theta_c(E)$ in order to keep $R(E)$ at a convenient value, the incidence angles have to be very shallow, and the effective area of a single mirror is very modest. In order to increase the effective area of a telescope a number of coaxial and confocal mirrors with decreasing radii ("mirror shells") are assembled: the incidence angle decreases going from the outer to the inner shells according to Eq. 3.28. This is obtained by nesting a number of mirrors and thus filling the front aperture as far as possible. The nesting efficiency is determined by the mirror shell thickness and, in case of very low grazing angles, by the minimum radial mirror separation which is required for integration and alignment. The thinner the mirror shells the less the shells are spaced, the larger is the collecting area. However a very dense nesting results in a minor obstruction off-axis, as shown in the Eq. 3.32.

Impact on the reflectivity of surface microroughness

The high reflectivity required to an X-ray reflecting surface (and especially to the Wolter I shaped optics, which exploit a double reflection) may be seriously hampered by the microroughness of the reflecting surface. The mirror surface has to be very smooth in order to return an X-ray reflectivity near to the value predicted by the Fresnel laws. Superpolishing methods have been developed in order to reduce the surface roughness to few angstroms, but the roughness is still the main threat to the reflectivity of an X-ray mirror. A reflecting, flat surface may be described by a function $z(x, y)$, which gives the height of the surface at each point (x, y): an ideal surface would simply have $z(x, y) = z_0$, but real surfaces are never ideally smooth. The basic condition to apply the Fresnel equations is that the rms (σ) fullfills the *smooth surface condition*:

$$2\pi\sigma \sin\theta_i < \lambda \tag{3.33}$$

where θ_i is the incidence angle.

We can start to characterize the smoothness of the surface by its rms value θ,

$$\theta^2 = \frac{1}{L}\int_0^L [z(x, y) - z_0]^2 \, dx \tag{3.34}$$

which is the most important parameter for the characterization of the reflecting surface. To understand how the surface reflectivity varies with its roughness, let us suppose to have a flat surface with a Fresnel amplitude reflectivity r and transmissivity t. The surface is isotropic and (for simplicity) let a representative section profile be z(x), with $z_0 = 0$. Let L be the illuminated surface length. A ray with wavelength λ impinges with a grazing incidence angle θ_i from an ambient with refractive index n_1 and it is reflected (in the incidence plane) at the angle $\theta_s = \theta_i$. The (eventual)

transmitted beam is refracted at the angle θ_r in the reflective layer with refractive index n_2. Moreover, let us suppose that the smooth-surface condition (Eq. 3.34) is

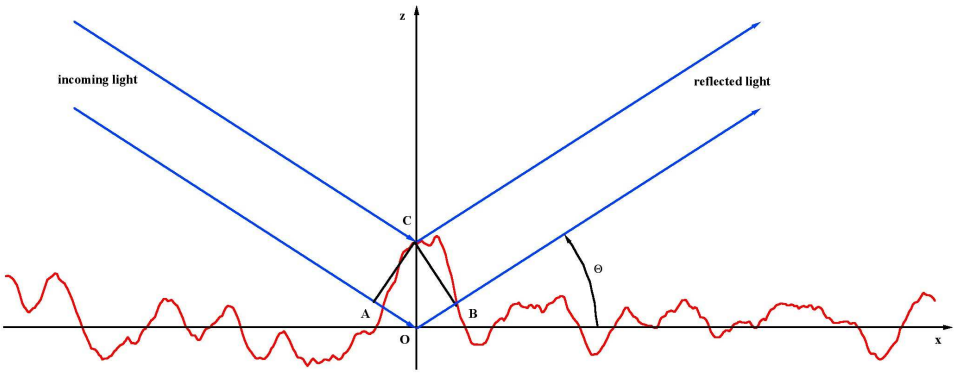

Figure 3.13: Reflection from a rough surface. The reflectivity reduction is caused by the loss of spatial coherence in the incident wavefront.

met, as usually in practical cases. If the surface were perfectly smooth, two adjacent parts of the wavefront would be reflected and would arrive to the analyser with the same phase shift they had in incidence: the secondary waves would produce a wavefront only in the θ_i direction and the reflectivity would be r, as predicted by the electromagnetic theory. As the profile shows instead a distribution of heights, it is possible to have a non-zero constructive interference in other directions than θ_i: the consequence is the scattering of the beam and the reduction of reflectivity in the θ_i direction. We observe for the moment the specular direction, the phase shift of a ray reflected in the direction θ_i by an element of surface Δx at a point x with height z will be (see fig. 3.13)

$$\Delta\phi = \frac{2\pi}{\lambda} 2z(x) n_1 \sin\theta_i \tag{3.35}$$

The reflected electric field will be the superposition of the contribution of all of the elements of the profile with amplitude rE_0 (E_0 is the incident electric field amplitude at the surface), each with its own phase shift, weighted upon the likelihood $p(x)dx = \frac{1}{L}dx$ of striking the surface element dx;

$$E_r = r\frac{E_0}{L}\int_0^L exp\left(i\frac{4\pi}{\lambda} n_i sin\theta_i\right) dx \tag{3.36}$$

This sum was possible due to the smooth-surface approximation, which guarantees the reflection of the beam in the θ_i direction. It is impossible, however, to resolve the integral in the eq. 3.36 without more information about the profile z(x). In the following, we shall suppose that the distribution p(z) of heights in z(x) is a Gaussian:

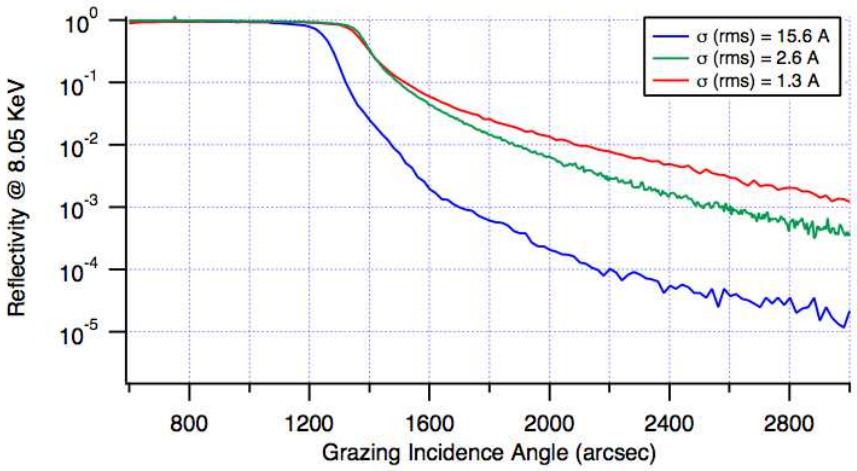

Figure 3.14: Reflectivity scans of three Ni samples, polished at different levels: the reflectivity decreases as the sample is superpolished with a lower accuracy (higher σ), in agreement with the eq. 3.39. Credits: (Spiga et al., 2006).

$$p(z)dz = \frac{1}{\sigma\sqrt{2\pi}} e^{\frac{z^2}{2\sigma^2}} dz \tag{3.37}$$

where σ is the rms of the surface. Summing on z instead of x, the eq. 3.36 becomes:

$$E_r = r\frac{E_0}{\sigma\sqrt{2\pi}} exp\left(-\frac{8\pi^2}{\lambda^2} n_1^2 \sigma^2 sin^2\theta_i\right) \int_{-\infty}^{+\infty} e^{-\left(\frac{z}{\sqrt{2}\sigma} - i\frac{2\sqrt{2}\pi}{\lambda}\sigma n_1 sin\theta_i\right)^2} dz \tag{3.38}$$

now the integral may be easily evaluated as $\sigma\sqrt{2}\pi$, and so the reflectivity of the rough surface $R\theta = |r\theta|2 = (E_r/E_0)^2$ is

$$R_\sigma = r^2 exp\left[-\left(\frac{4\pi}{\lambda}\sigma n_1 sin\theta_i\right)^2\right] \tag{3.39}$$

This basic formula (known as *Debye-Waller formula*) shows that:

- the reflectivity decreases as the exponential of the square of the roughness rms σ;
- the reflected amplitude E_r is real and positive: this means that the reflected wavefront has no phase shift caused by the superposition of scattered waves in the specular direction;

- the reflection at larger angles is more sensitive to the roughness effect, as the phase dispersion depends only on the projected roughness in the direction of incidence.

3.3 Manufacturing techniques of X-ray mirrors

The design and realization of Wolter I type X-ray optics is a challenge: other than the optics performances, the mirrors have to be as light as possible but resistant to the huge amount of stresses they will be exposed during the missions. In the traditional mirror manufacturing the first step is the choice of the mirror's substrate material and the process of giving it the right shape. There are three different approaches used for manufacturing the optics: grinding the substrate, using thin foils or mirror replication.

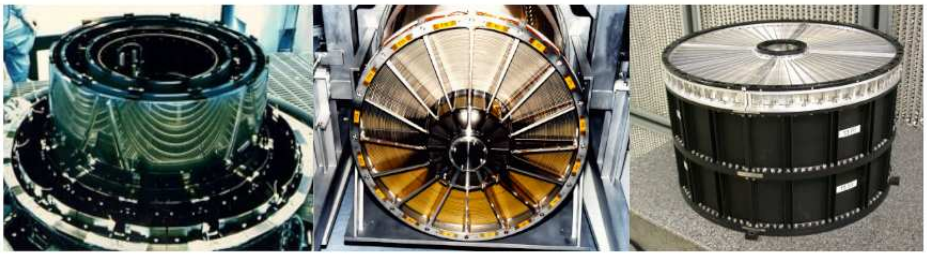

Figure 3.15: The complete optics modules of the X-ray telescopes Chandra (left), XMM-Newton (centre) and Suzaku (right). Credits: NASA, ESA, JAXA.

In the first case the paraboloid and the hyperboloid are separately ground and then figured by high precision numerically controlled machines. Afterwards the mirror inner surfaces are super-polished by lapping with ultra-thin alumina powders reaching a rms roughness on the order of few angström. The most commonly used substrate materials are Zerodur (*Rosat*, *Chandra*), Quartz (*Einstein*) and Nichel (*XMM-Newton*), since their Coefficient of Thermal Expansion (CTE) are low as well as their mass. At this point a thin coating is deposited in order to create the reflecting layer with material properly chosen (Au, Ni, Ir, Pt), even if sometimes an additional layer has to be deposited as adhesion promoter under the coating. The reached angular resolution is generally high, even if the achievable effective area is low since the number of nested shells is limited by the single shell substrate dimension ($\sim$ cm). This kind of optics is suitable for detailed observation of extended objects (SNR, galaxy clusters, XRB) where the angular resolution is a primary requirement.

The second manufacturing technique is based on mirror replication, i.e. the replication of the reflective surface grown around a super-polished mandrel which has a

negative mirror profile (named master) and acts as a mirror shell template (see Fig. 3.16). Mirrors made in such a way have several advantages: can have any cylindrical profile, are monolithic (meaning an easy assembly process) and the system is very resistant to mechanical deformations. In addition the optical shape reproduces very well the mandrel shape (with high optical performance), the obtained shells are very thin and the master mandrel may be reused after the replication to produce other identical mirror shells. This method has been used for making the SAX, Jet-X, Swift/XRT, eRosita and XMM's mirrors by INAF-OAB and Media-Lario allowing a strong reduction of production costs, manufacturing and assembly time, achieving very high performances. Technically speaking there are two ways that can be adopted in the replication technique: the Nickel electro-forming or using ceramic material. These approaches differ essentially in the growth process of the material that constitutes the mirror walls. In table 3.1 is presented an example of three X-ray telescopes (see Fig. 3.15) made with different manufacturing techniques. The third

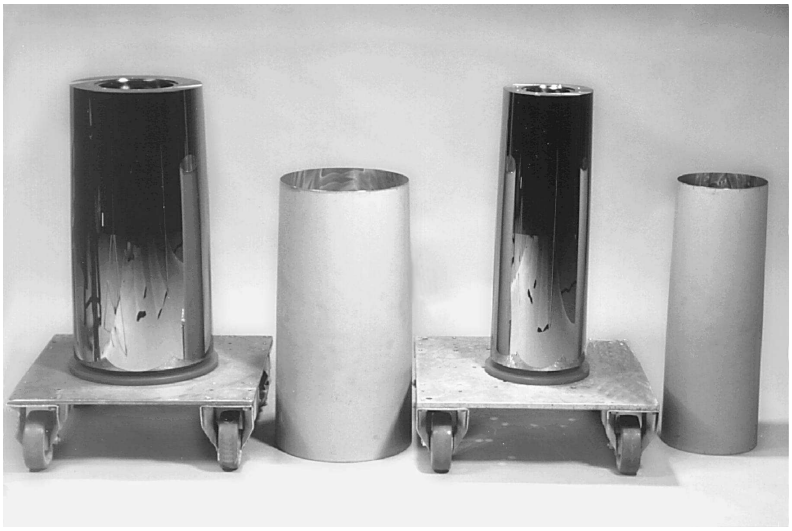

Figure 3.16: The mirror replication technique. Two mandrels and shells of the Jet-X optical module.

method approximates the Wolter-I profile with a double-cone shape: the two cones are composed by a number of mirror segments formed by thin foils (from 0.1 to 0.3 mm thick) of glass or Aluminium coated with a reflective layer (Pt or Au). Afterwards the segments are assembled in order to form the double cone structure. The correct shape of each foil is obtained by mechanically bend of a plane Aluminium foil or, in case of glass, the segments are curved after heating (ASCA, Sodart and Suzaku telescopes). The achievable angular resolution with this manufacturing tech-

nique is very limited since the composited structure of the segmented mirror is very sensitive to mechanical deformations that may take place during the satellite launch or thermal variations. Moreover this method is used by telescopes devoted to spectroscopic applications with a large collecting area and limited angular resolution (some arc minutes).

Table 3.1: Performances of some optics produced with the traditional manufacturing technique (first column), based on the thin foil technique (second column) and based on replication (third column).

	Chandra	XMM	Suzaku
Mirror profile	Wolter I	Wolter I	Double cone
Modules number	1	3	2
Shells per module	4	58	175
Energy range / keV	0.07-10	0.1-15	0.5-15
Grazing incidence angle / $'$	21 - 51	17 - 40	30
Effective area / cm^2	1150	1400 @ 1.5 keV	250 @ 7 keV
Focal length / m	10	7.5	8
HPD	0.5”	15”	2.1’

3.3.1 Currently operating X-ray telescopes

Table 3.2: Chandra Technological characteristics for Chandra telescope (Weisskopf 1999).

Geometry	**1 optical module Wolter-I**
Manufacturing	**Direct manufacturing**
Energy band	**0.1 - 10 keV**
Focal length	**10 m**
Field of view (at 3 keV)	**$\geq$17' diameter**
Substrate	**Zerodur**
Coating	**Ir**
Effective area	**$\geq$ 340 cm^2 at 1-6 keV**
Angular resolution	**$\leq$ 1" (HEW)**

Table 3.3: XMM/Newton Technological characteristics for XMM/Newton telescope (de Chambure et al. 1999).

Geometry	**3 optical moduleWolter-I**
Manufacturing	**Electroforming replica**
Energy band	**0.1 - 12 keV**
Focal length	**7.5 m**
Field of view (at 3 keV)	**$\geq$30' diameter**
Substrate	**Nichel**
Coating	**Au**
Effective area	**each module $\geq$ 900 cm^2 at 2-6 keV**
Angular resolution	**$\leq$ 15" (HEW)**

Table 3.4: Swift/XRT Technological characteristics for Swift X-ray telescope (Burrows et al. 2003).

Geometry	**1 optical module Wolter-I**
Manufacturing	**Electroforming replica**
Energy band	**0.2 - 10 keV**
Focal length	**3.5 m**
Field of view (at 3 keV)	**$\geq$24' diameter**
Substrate	**Nichel**
Coating	**Au**
Effective area	**$\geq$ 110 cm^2 at 1.5 keV**
Angular resolution	**$\leq$ 20" (HEW)**

Table 3.5: Suzaku Technological characteristics for Suzaku telescope (Soong et al. 2011).

Geometry	**4 optical module segmented conical approx.**
Manufacturing	**Bent thin foils**
Energy band	**0.1 - 10 keV**
Focal length	**4.5 m**
Field of view	**$\geq$19' diameter**
Substrate	**Al**
Coating	**Au**
Effective area	**each module $\geq$ 440 cm^2 at 1.5 keV**
Angular resolution	**$\leq$ 1.9' (HEW)**

3.4 X-ray focusing above 10 keV

Because of the excellent detection sensitivity achievable with focusing or concentrating telescopes, the development of grazing incidence optics operating at hard X-ray energies will bring about major observational advances in this wavelength band, where the X-ray sources are significantly fainter and more difficult to detect (see chapter 2).

The most obvious challenge in extend traditional grazing incidence optics to the hard X-ray band (E $>$ 10 keV) is the decrease with energy of the graze angle for which significant reflectivity can be achieved. For a Wolter-I or conical approximation mirror geometry, the on-axis graze angle, α, on a given mirror shell is related to the focal ratio by $\alpha = (r/4\ f)$, where r is the mirror shell radius and f is the focal length. Extending response to high energies therefore requires either using smaller focal ratios, or increasing the maximum graze angle over what can be achieved with standard metal coating. The former can be accomplished by employing very long focal lengths or many small diameter optics in the telescope design which entails a more complex optic assembly and alignment problems. The latter by coating the reflective surfaces with multilayer structures that can substantially increase the maximum graze angle for which significant reflectivity is achieved over a relatively broad energy range.

3.4.1 Multilayer coating

When X-rays impact an atom, they make the electronic cloud move as does any electromagnetic wave. The movement of these charges re-radiates waves with the same frequency; this phenomenon is known as Rayleigh scattering (or elastic scattering). These re-emitted wave fields interfere with each other either constructively or destructively in crystal. The regular spacing of atoms causes the constructive interference to be concentrated at precise diffraction angles, producing a diffraction pattern on a detector.

This interpretation was first proposed by William Lawrence Bragg and William Henry Bragg in 1913 in response to their discovery that crystalline solids produced regular patterns of reflected X-rays. They found that crystals, at certain specific wavelengths and incident angles, produced intense peaks of reflected radiation (now known as *Bragg peaks*). W. L. Bragg explained this result by modeling the crystal as a set of discrete parallel planes separated by a constant parameter d. In this way they obtained the clarification of the nature of X-rays. The incident X-ray radiation produces a Bragg peak if their reflections off the various planes interfere constructively. The interference is constructive when the phase shift is a multiple of 2π; this

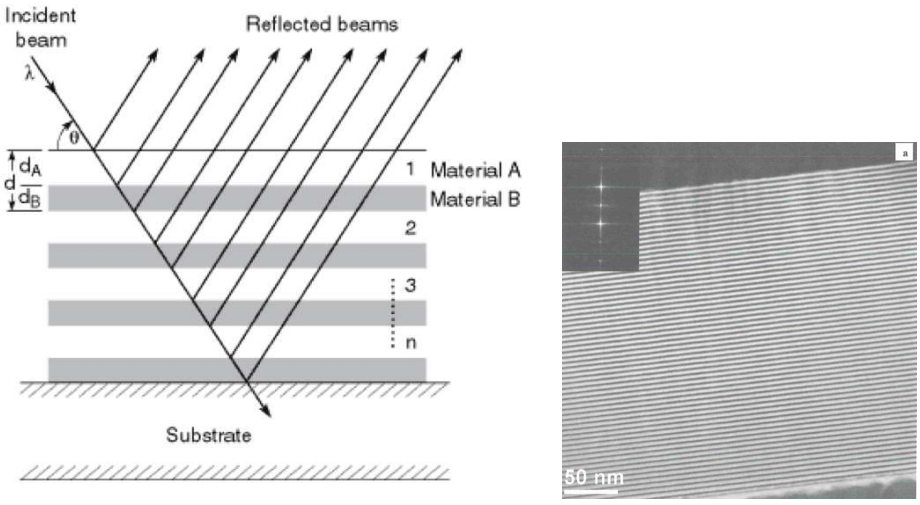

Figure 3.17: Left: scheme of a multilayer reflector of N bilayer pairs. The parameters λ, θ, and d are chosen to satisfy the familiar Bragg equation, but the relative thicknesses of the high- and low-Z materials are also critical in optimizing reflectivity. The total reflectivity is the vector sum of the complex reflection coefficients at each interface, with the different path lengths taken into account. Right: transmission electron microscope (TEM) image of a W/Si multilayer on a Silicon wafer substrate cross section. Credits: IMEM-CNR, Parma and MLT.

condition can be expressed by Bragg's law,

$$n\lambda = 2d\sin\theta \tag{3.40}$$

where n is an integer, λ is the wavelength of incident wave, d is the spacing between the planes in the atomic lattice, and θ is the angle between the incident ray and the scattering planes.

Exactly line natural crystal enhance the X-ray reflection owing to constructive interference. The same principle can be exploited by making an artificial lattice with a properly-designed spacing. This is obtained by depositing a sequence of thin films named *multilayer*, with the interfaces playing the role of crystalline planes.

A multilayer coating consists of alternating layers of high and low refractive index material (see Fig. 3.17). When all of the layer pairs in a multilayer have identical thickness, the reflectivity is concentrated at energy peaks given by the Bragg equation, where *d* is the period of the multilayer. To obtain a broadband reflector (see Fig. 3.18 left), one uses a depth graded multilayer, where the top layers have large d-spacing to reflect the lower energies and the bottom layers have small d-spacing to reflect the higher energies (see Fig. 3.18 right). This arrangement minimizes losses due to absorption because lower energy photons travel through a lower absorption thickness. The most performing bilayer thickness distribution is defined by a power law with three parameters:

$$\mathrm{d}(i) = \frac{a}{(b+i)^c} \tag{3.41}$$

where a, b, and c are the constants, and i is the bilayer index ranging from 1 to N, with i = N being the bilayer next to the substrate. This concept was introduced first for neutron mirrors by Mezei in 1988 and after developed by Joensen in 1993 for X-ray astrophysics. There are several factors to consider when choosing the materials for a multilayer. The number of layers required to achieve optimum reflectivity depends on the contrast in refractive index between the materials. Since the refractive index is a function of electron density, multilayers utilizing materials with large difference in atomic number and mass density require a smaller number of layers. This results in shorter deposition times and lower stress in the coating (which depends both on the total coating thickness and on the number of layer pairs). Interfacial roughness and interdiffusion, which depend on the choice of materials, must also be minimized. Both of these effects reduce the reflectivity of the multilayer. Finally, the materials should not have absorption edges in the energy range of interest.

Possible material choices for which high quality multilayers have been fabricated, included W/Si, with a high energy cut-off at 69.5 keV (W K-edge); Pt/C, with a cut-off at 78.4 keV (Pt K-edges). They typically require coating with 50 - 200 layer pairs (depending on graze angle) to operate over the full energy range.

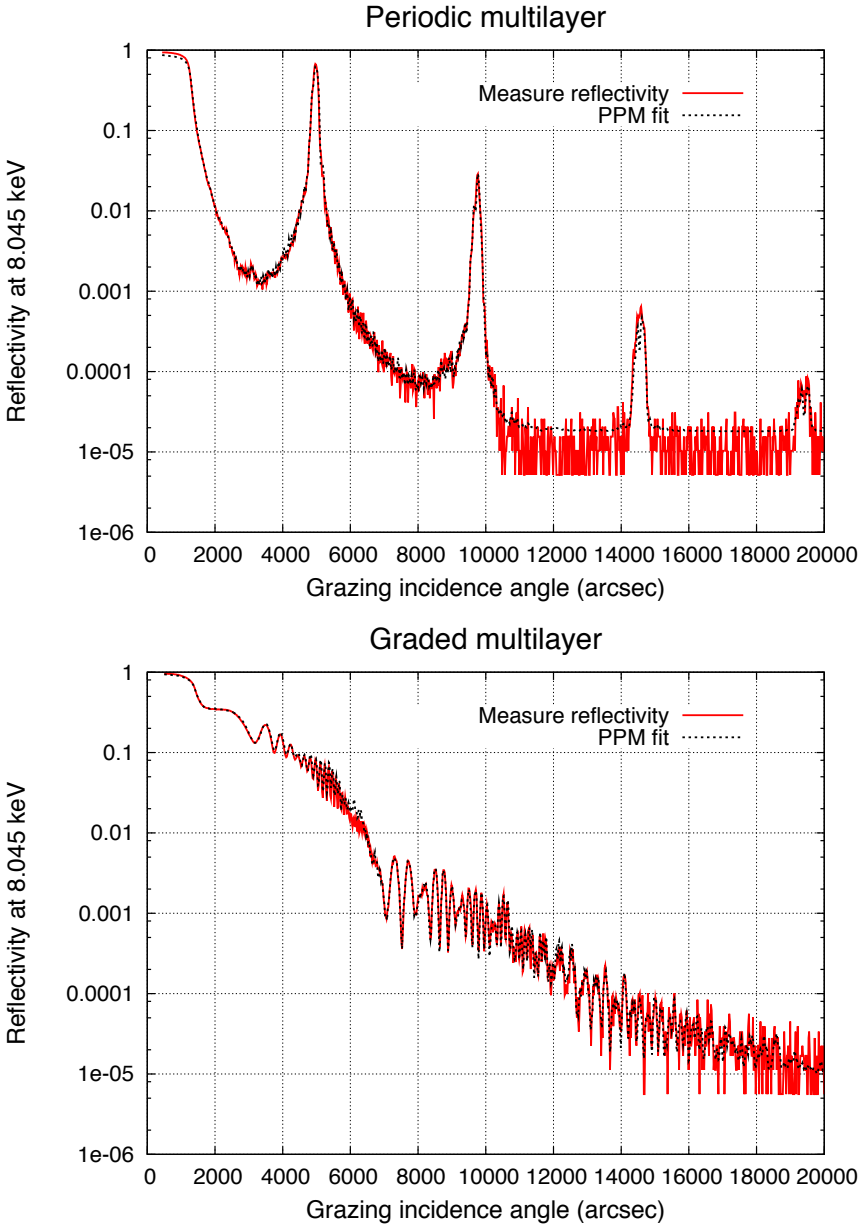

Figure 3.18: Reflectivity curve as a function of grazing incidence angle. Top: a silicon wafer coated with a periodic multilayer with 60 bi-layers. Bottom: a silicon wafer coated with a graded multilayer with 100 bi-layers. Also shown is the accurate fit obtainsd with the PPM program (sect. 4.3.1).

3.4.2 The reflectivity of a multilayer

A rigorous theory (Rouard, 1937) that allows to model the reflectivity of any multilayer (with any d-spacing distribution) as a function of the photon energy and of the incidence angle, starts from the single layer reflectivity:

$$R = \frac{r_{01} + r_{12}e^{-i\Delta\phi}}{1 + r_{01}r_{12}e^{-i\Delta\phi}}, \qquad \Delta\phi = \frac{2\pi}{\lambda}2nd\sin\theta_1 \tag{3.42}$$

where r_{01} and r_{12} are the reflectivity between the different interfaces, provided by the Fresnel's equations. $\Delta\phi$ is the phase shift at each reflection on the substrate. The equation 3.42 accounts for multiple reflection inside the layers. We number the layers from the bottom to the top of the stack j = 0,1,...,N, (j = 0 is the substrate), and the reflectivity of the multilayer composed by the first j interfaces will be indicated by R_j. Obviously the substrate/1^{st} layer interface is

$$R_1 = r_{10} \tag{3.43}$$

and adding the 2^{st} layer will change the reflectivity to:

$$R_2 = \frac{r_{12} + R_1e^{-i\Delta\phi_1}}{1 + r_{21}R_1e^{-i\Delta\phi_1}} \quad \Delta\phi_1 = \frac{2\pi}{\lambda}2d_1n_1\sin\theta_1 \tag{3.44}$$

where θ_1 is the incidence angle in the first layer. At the following steps the same formulas may be repeated by recursion, increasing the index j:

$$R_{j+1} = \frac{r_{j+1j} + R_je^{-i\Delta\phi_j}}{1 + r_{j+1j}R_je^{-i\Delta\phi_j}} \quad \Delta\phi_j = \frac{2\pi}{\lambda}2d_jn_j\sin\theta_j \tag{3.45}$$

After N steps the multilayer ends and its reflectivity is $\mid R_N \mid^2$.

Some general features of *periodic* multilayers can be listed:

- *the position of peaks* depends on Γ ($\Gamma = d_h/(d_h + d_l)$ where d_l and d_h are the spacer and absorber thickness respectively), on the incidence angle θ_i, on the layer material density (the real part of refraction index δ_h and δ_l), on the spacing of bi-layers d and on the energy of incidence wave; the refraction changes the peak position with respect to the Bragg law prediction:

$$2d\sin\theta_i\sqrt{1 - 2\frac{\Gamma\delta_h + (1-\Gamma)\delta_l}{\sin^2\theta_i}} = k\lambda \tag{3.46}$$

  and it is independent of the number of bilayers and of the interface roughness.

- *The reflectivity depends on the* Γ *ratio*: it is maximum for kΓ semi-integer and zero for kΓ integer. The Γ ratio affects the relative height of peaks.

- *The reflectivity increases with the number of bilayers*: this increase is almost linear for small N, but as it approaches the value 1 the increase is slower and slower, tending to 1 asymptotically. This saturation corresponds to the extinction of the incident beam which is mostly (57%) reflected in the first N_{min} stack bilayers:

$$N_{min} \approx \frac{1}{2r \sin(\pi k \Gamma)} \tag{3.47}$$

  The achievable reflectivity with $2N_{min}$ bilayers is 92%, and 99% with $3N_{min}$ bilayers.

- a large number of effective bilayers reduces *the peak width* both in energy and angular scan. This in turn increases its resolving power.

$$\frac{\lambda}{\Delta\lambda} = \frac{1}{2} N_{max} k \tag{3.48}$$

  where N_{max} is the number of bilayer after that the beam typically decays. The maximum depth reached by the incident X-rays is $N_{max}d$. Multilayers with a high resolving power must so have a single boundary reflectivity r very poor in order to keep a large number of effective bilayers (e.g. C/C multilayers (Baranov et al. 2002)). For astrophysics applications, the mirrors must instead have a good reflectivity rather than a good resolution: in their design it is important to choose a couple of materials that guarantees a high single-boundary reflectivity.

- *the height of the peaks* decreases with the roughness. In real multilayer coatings, both roughness and interdiffusion occur. We assume σ for diffuse/rough interfaces that may be defined as the rms of the variation of the refractive index $n(x, y, z)$ in the multilayer volume. The reflectivity reduction at every bilayer of a multilayer coating with roughness/diffusion σ, absorber/spacer refractive indexes n_h, n_l and incidence angles in absorber and spacer (Spiller 1996) θ_h and θ_l obey the usual exponential decay:

$$R_\sigma = R_0 exp\left[-\left(\frac{8\pi^2}{\lambda^2}\sigma^2 n_h n_l \sin\theta_h \sin\theta_l\right)\right] \tag{3.49}$$

  called *Névot-Croce formula*.

3.5 PSF of an X-ray telescope

The angular resolution of an imaging X-ray telescope is chiefly determined by the optical quality of its focusing optics. These in general consist of a variable number

of nested grazing-incidence, double-reflection X-ray mirrors. A widespread mirror profile is the Wolter-I (parabola+hyperbola (van Speybroeck & Chase 1972)), even though polynomial (de Korte et al. 1981) or Kirkpatrick-Baez (Kirkpatrick & Baez 1948) geometries are also suitable. The real optical performances of X-ray mirrors, indeed, are always worse than predicted by the mentioned designs, due to mirror imperfections. The mirror profile can be deformed at any production stage: manufacturing, integration, and handling. Similarly, the mirror surface is not ideally smooth but characterized by a rough topography, as it can be observed along with optical interferometers or Atomic Force Microscopes. Both kind of imperfections concur to determine an optical imaging degradation.

3.5.1 PSF degradation

A common way in X-rays astronomy to describe the performance of an optical system is the *Point Spread Function* (PSF), the annular integral of the focused X-ray intensity around the center of the focal spot. It is a usual practice to express the PSF width along with the *Half Energy Width* (HEW), which is twice the median value of the PSF. A basic issue in X-ray optics is to establish a relation between the mirror imperfections and its PSF – or the HEW – as a function of the X-ray energy, in order to i) predict the angular resolution of the optics from measured profiles and roughness, and ii) establish the tolerable level of mirror imperfections from the desired angular resolution. The PSF gives the spatial distribution profile of detected events in the focal plane of the detector(s) in response to a point-like source. Likewise the encircled energy (EE) is typically defined as the fraction of the energy of a point source collected within a given radius. The Half Energy Width is the diameter that contains half of the total integral of the PSF. The HEW is a parameter that gives a quantification of the angular resolution of an optical system.

If the angular resolution is not a strict requirement, the Wolter I optic may be substituted by a double-cone approximation, a configuration that simplifies the production process. The angular resolution for an ideal double-cone optic is:

$$HEW \propto \frac{LR_0}{f^2} \tag{3.50}$$

is worse than for a Wolter I optic that ideally should be zero.

Apart from definitions related to the measurement technique, or empirically referred to the mirror length (de Korte et al. 1981), the separation of profile geometry and roughness reflect in general the different kind of treatment performed to predict their effect on the angular resolution. Profile errors are believed to fall in the *geometrical optics* regime, therefore they are analyzed along with ray-tracing routines since the path of each X-ray, and in particular the reflection point on the mirror surface, is assumed to be uniquely reconstructed. In contrast, the surface roughness is assumed

to entirely fall in a spectral region of Fourier surface wavelengths where the concept of "ray" is no longer applicable, because the optical path differences involved start to be comparable with λ, the X-ray wavelength. The imaging degradation is due, in this spectral range, to the X-ray scattering (XRS), i.e., the off-surface diffraction of the reflected X-ray wavefront. A well-established first order theory is available (Church 1988) to compute the scattering diagram from the power spectrum of the roughness, or its *Power Spectral Density* (Stover 1995) (PSD).

3.5.2 Impact on the angular resolution of surface microroughness

The normalized scattered intensity per radian at the scattering angle θ_s (either $\theta_s > \theta_i$ or $\theta_s < \theta_i$) is related to the PSD along with the well-known formula at first-order approximation (Church 1979; Church & Takacs 1986), valid for smooth, isotropic surfaces and for scattering directions close to the specular ray (i. e. $\mid \theta_s - \theta_i \mid \ll \theta_i$),

$$\frac{1}{I_0}\frac{dI_s}{d\theta_s} = \frac{16\pi^2}{\lambda^3}\sin^3\theta_i R_F P(f) \tag{3.51}$$

where $P(f)$ is the Power Spectral Density of the surface (see sect 4.3), R_F is the reflectivity at the grazing incidence angle θ_i and I_0 is the flux intensity of the incident X-rays. If the scattered intensity is evaluated at the scattering angle θ_s, the PSD can be immediately evaluated as a function of the spatial frequency f:

$$f = \frac{\cos\theta_i - \cos\theta_s}{\lambda} \approx \frac{\sin\theta_i(\theta_s - \theta_i)}{\lambda} \tag{3.52}$$

The approximation was justified by the assumption $\mid \theta_s - \theta_i \mid \ll \theta_i$ and the negative frequencies are conventionally assumed to scatter at $\theta_s < \theta_i$: the assumed approximations make the XRS diagram symmetric, because the PSD is an even function. For a single-reflection mirror shell, the extension of the formulae above-mentioned is straightforward by regarding $\mid \theta_s - \theta_i \mid$ as the angular distance at which the PSF is evaluated. The focal image is the superposition of many identical XRS diagrams on the image plane, generated by every meridional section of the mirror shell: since a π angle rotation of every meridional plane of the shell sweeps the whole image plane, the scattered intensity is spread over a π angle. The integration on circular coronae used to compute the mirror PSF (at positive angles) compensates this factor multiplying the XRS diagram by 2π (de Korte et al. 1981). The remaining 2-fold factor accounts for the negative frequencies in the surface PSD. The scattered power at angles larger than a definite angle α are measured from the focus. Due to the steep fall of scattering intensity for increasing angles, the integral (of Eq. 3.51) of the scattered

power beyond an angle "α"

$$I[\mid \theta_s - \theta_i \mid > \alpha] = I_0 R_F \frac{16\pi^2 \sin^2 \theta_i}{\lambda^2} \int_{f_0}^{\frac{2}{\lambda}} P(f) df \tag{3.53}$$

where $f_0 = \alpha \sin \theta_i / \lambda$ is the spatial frequency corresponding to the scattering at the angle α. But the integral term is the squared roughness rms

$$\sigma^2 = \int_{f_0}^{\frac{2}{\lambda}} P(f) df \tag{3.54}$$

Finally, the scattering term of the HEW is obtained from the collection of all the reflected/scattered photons: this allows us to avoid problems related to the finite size of the detector, and to extend the surface roughness PSD up to very large spatial frequencies. By definition, $H(\lambda)$ is twice the angular distance from focus at which the integrated scattered power halves the total reflected intensity. Once known the PSD from topography measurements over a wide range of spatial frequencies, the PSD numerical integration allows to recover f_0. In turn, f_0 is related to $H(\lambda)$, which we write in the following form (Spiga 2007)

$$H(\lambda) = \frac{2\lambda f_0}{\sin \theta_i} \tag{3.55}$$

where H is measured in radians. This is the HEW scattering term of a mirror in the spatial wavelength range where the smooth surface limit is fullfilled. In this range, this is the contribution to the PSF degradation due to the scattering term given by the microroughness.

3.5.3 PSF modelling

The modelization of PSF can follow two ways: analytical and numerical. In X-ray telescope applications, generally, is used the second approach because the first one implies a huge bulk of data that has to characterize numerically the PSF. In only one case it was used this approach because the very small dimension of the PSF: the Chandra satellite. For calibration analysis, the unit mirror PSF can often be modelled with a Gaussian core representing the bulk of geometric reflection and Lorentzian tails representing the scattering of X-rays by surface roughness. The Lorentzian tail has a maximum value only about 1% of that of the Gaussian core.
The PSF profile is then a convolution of a Lorentzian (also called King profile) and a Gaussian profile expressed by the equation:

$$PSF(r) = We^{-\frac{r^2}{2\sigma^2}} + (1-W)(1 + (\frac{r}{r_c})^2)^{-\beta} \tag{3.56}$$

For each choice of monochromatic energy and position the PSF profile can be well fitted by a model composed of a Gaussian function that takes into account the central part of the profile and a King function which describes the external faint wings.

There are four free parameters which are functions of the energy E and position θ, two for the Gaussian function and two for the King function respectively: W(E,θ), σ(E,θ), r$_c$(E,θ), β(E,θ). The Encircled Energy Fraction (EEF), corresponding to the total flux of a source, is given by the analytic integral of the PSF function in rdr:

$$EEF(r) = \int PSF(r) 2\pi r dr = \frac{\pi r_C^2 (1-W)}{1-\beta}((1+(\frac{r}{r_c})^2)^{1-\beta}-1)+2\pi W\sigma^2(1-e^{-\frac{r^2}{2\sigma^2}}) \tag{3.57}$$

$$EEF(\infty) = 2\pi W\sigma^2 + \pi r_c^2(1-W)/(\beta-1) \tag{3.58}$$

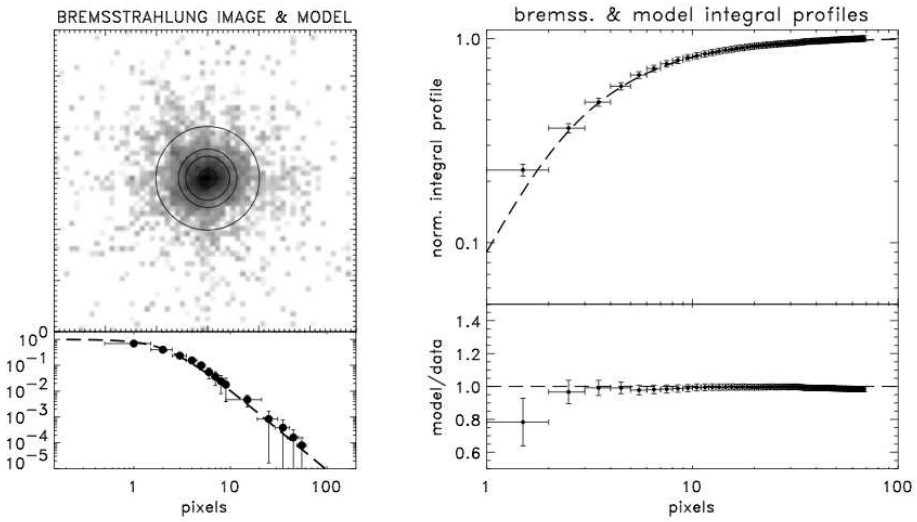

Figure 3.19: An example of PSF modelization (Swift XRT telescope Moretti et al. 2004), In the left panel the isophotes of the model are overplotted to the laboratory image. In the right panel the integral profile of the test image is compared with the model. As we can see from the residual plot if we take a circle larger than 3 pixels the model describes the data with a precision better than 2%.

The main goal of building this model is the calculation of the PSF correction, which gives for a generic observed source the fraction of the flux contained in a given box. This is a fundamental ingredient in the photometric measurements and also in

the construction of the Ancillary Response File (ARF) necessary for the spectroscopy analysis.

The final aim of an analitycal model is to be able to give an accurate description of the PSF profile of a source with a generic spectrum in a generic position of the detector (see Fig. 3.19).

3.6 Future X-ray missions

A number of future hard X-ray telescopes are at present time being conceived: most of them will implement multilayer coatings in order to extend the X-ray focusing technique to the hard X-ray band: in the following we will describe some missions of the next future that include in their trade-off the implementation of multilayer coatings.

3.6.1 NHXM mission project

Simbol-X was a project mission with a new-technology hard X-ray (0.5 - 80 keV) focussing telescope that could provide order of magnitude improvement in angular resolution and sensitivity (Ferrando et al. 2006). Unfortunately, due to budget restrictions, in March 2009, CNES unexpectedly decided to stop the project after the end of Phase A. The Simbol-X mission was therefore cancelled. The NHXM satellite was the attempt to ASI into using the technology already developed in the Simbol-X project, improving the optical system to multilayer technology (Tagliaferri et al. 2011). Unfortunately, in June 2011, the project was cancelled because ESA did not approve the mission as medium size mission. NHXM was made of the service module platform, accommodating the four mirrors modules, and the Instrument Platform accommodating the focal plane assembly. The Instrument Platform will be put at the 10 m focal length distance by a deployable truss, after the satellite has been placed in orbit. Therefore, NHXM can be launched in a very compact configuration allowing for the use of a smaller fairing launcher. The requirement of a very low and stable background count rate dictates the need for a Low Equatorial Orbit (LEO). As shown by the experience of two very successful hard-X-ray missions, BeppoSAX and Swift, a circular nearly equatorial (inclination $< 5°$) orbit, at 600 km mean altitude with an orbital period of 95 min, guarantees a very stable and low background environment.

The four identical NHXM Mirror Modules (MMs) would have been based on nested confocal electroformed Nickel-Cobalt alloy (NiCo) shells with Wolter I profile. The electroforming technology has already been successfully used for the Ni gold-coated X-ray mirrors of BeppoSAX, Jet- X/Swift and XMM-Newton satellites and it is now used for the mirrors of the e-Rosita mission. For the NHXM mirrors, a few technological modifications would have been introduced that have already been

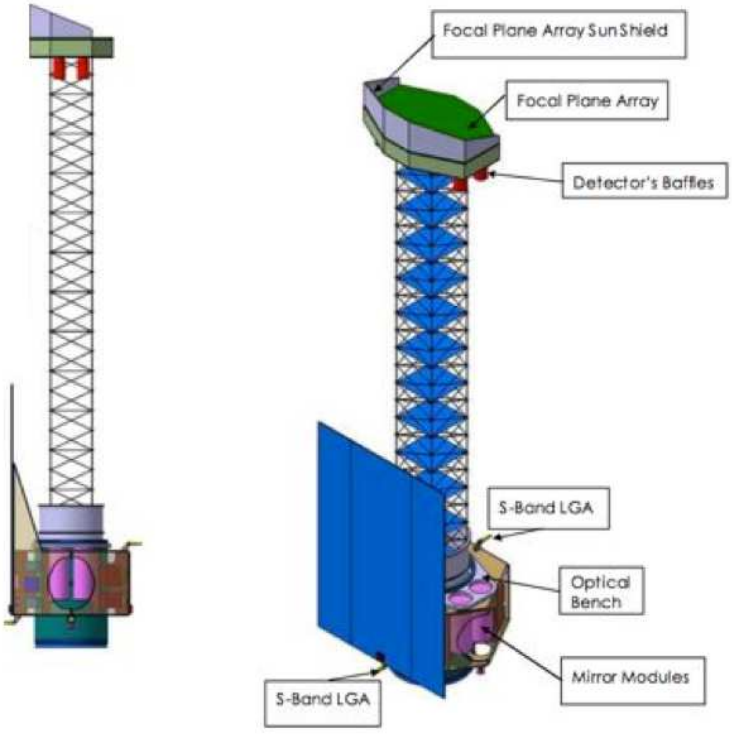

Figure 3.20: Artistic picture of NHXM observatory.

developed in the past several years. We would have used NiCo alloy instead of pure Ni. NiCo is characterized by better stiffness and superior yield properties. We apply nanostructured multilayer X-ray reflecting coatings, permitting a larger FOV and an operating range from 0.3 keV up to 80 keV and beyond. These would be sputtered onto the internal surface of the gold-coated NiCo mirror thin shells after replication from the mandrels. Each MM is equipped with 70 (in the baseline configuration, 90 in the goal configuration) Wolter-I Mirror Shells with a focal length of 10 m and interface diameters in the range 390 to 150 mm (in Tab. 3.6 the telescope main characteristics). The general layout of a MM has been extensively studied via a Final Element Method analysis. Various auxiliary devices would be installed on each MM: a magnetic diverter to prevent background electrons reaching the detector, a thermal baffle and a thermal blanket to maintain the mirror temperature. The effective area for three mirror modules is shown in Fig. 3.21 for the baseline and the goal configuration. The latter is achieved by filling the internal hole of each MM with an additional 20 mirror shells (to a minimum shell diameter of 110 mm). These shells would be fabricated via direct replication of multilayers (e.g. Pt/C/Ni) from TiN-coated su-

Geometry	**Wolter-I**
Energy band	**0.5 - 120 keV**
Focal length	**10m**
Field of view (at 30 keV)	**$\geq$12' diameter**
Coating	**multilayer Pt C**
Effective area	**$\geq$ 100 cm^2 at 0.5 keV; $\geq$ 1000 cm^2 at 2-5 keV**
	$\geq$ 600 cm^2 at 8 keV; $\geq$ 350 cm^2 at 30 keV
	$\geq$ 100 cm^2 at 70 keV; $\geq$ 50 cm^2 at 80 keV
Angular resolution	**$\leq$ 20" (HPD), E $\leq$ 30 keV; $\leq$ 40" (HPD), E = 60 keV**

Table 3.6: some of the NHXM top-level scientific requirements.

perpolished mandrels, adding 5 kg to each MM. Several engineering models (EM) with Ni and NiCo integrated shells coated with W/Si and Pt/C multilayer films (200 bilayers) have been developed and tested at the Panter-MPE X-ray calibration facility demonstrating the feasibility with a microroughness <4 Å. The PANTER test results are reported in sect. 9.

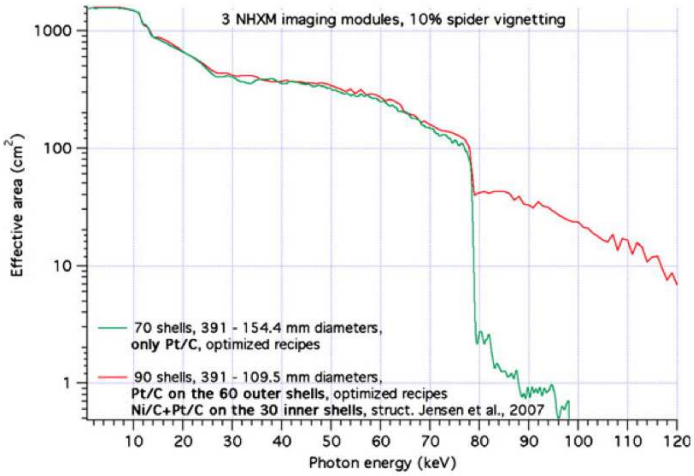

Figure 3.21: Three-MM effective area (baseline and goal)

The mirror technology has been developed and consolidated in the past two decades in Italy by the INAF Brera Astronomical Observatory in collaboration with the Media Lario Technology Company. For the NHXM mirrors, a few important modifications are foreseen: 1) the use of multilayer reflecting coatings, allowing us to obtain a larger

FOV and an operative range up to 80 keV and beyond; 2) the NiCo walls would be a factor of two thinner than the XMM Ni-mirror shells, to maintain the weight as low as possible. In this work of thesis, I have been involved in the characterization of multilayer samples developed by MLT devoted to the NHXM technological project (sect. 5). With respect to the first point, once the gold-coated NiCo mirror shell has been replicated from the mandrel, the multilayer film would be sputtered on the internal surface of the shell by using a two-targets linear DC magnetron sputtering system. This process has been developed and tested for monolithic pseudo cylindrical shells at Media Lario, where a multilayer coating facility has been developed and installed as part of the Phase A activities.

3.6.2 IXO/ATHENA mission project

ATHENA (formerly IXO) will be characterized by a large aperture, and large focal lengths ($\geq$ 10 m) in order to preserve the grazing incident angles needed to reflect X-rays. In the case of ATHENA two mirror modules are foreseen with 0.9 m max. radius and a 12 m focal length (the main technological parameters are shown in Tab. 3.7). With such large diameters it is not realistic to manufacture monolithical mirrors, e.g, obtained by Nickel electroforming of mandrel replicae like the ones made for XMM. Therefore the optical modules of ATHENA are composed by several modular blocks of mirror sectors, each of them with high focusing performances (Fig. 3.22, left), to be carefully aligned in order to fulfill the high angular resolution requirements (better than 10 arcsec HEW). Moreover, to fulfill also the low mass/geometrical area ratio requested, the mirrors cannot be made of Nickel but of a lightweight material, like Silicon or glass. In the development of the ATHENA optics, both approaches are being pursued:

- The baseline technology, under development at ESA/ESTEC since 2004, is based on the Silicon Pore optics. The module elements are obtained by dicing, ribbing and stacking smooth Silicon wafers commercially available, over a shaped mandrel having the shape of the parabolic or hyperbolic segment. X-rays propagate throughout the resulting pores (Fig. 3.22, center) and are reflected by the Iridium+B4C reflective coating applied on its surface.

- The backup technology, also financed by ESA and being studied at INAF/OAB, is based on the hot slumping of thin glass foils, i.e., softening thin glass foils at high temperature and bending them over a formed mould owing to a pressure exerted. The glass foils are subsequently stacked onto a rigid glass backplate via stiffening glass ribs. A prototype made at INAF/OAB is shown in Fig. 3.22, right. We note that the hot slumping of glass foils (without pressure) is the technique adopted to manufacture the NuSTAR optics.

Figure 3.22: Left: the modular structure of a large X-ray observatory optical module like ATHENA (credits: ESA). Center: a Silicon Pore optic stack in Wolter-I configuration manufactured at ESA/ESTEC (credits: ESA). Right: an uncoated prototype of 2 slumped mirror stack optic in Wolter-I configuration manufactured at INAF/OAB.

Geometry	**Wolter-I**
Focal length	**20m**
Field of view	**18 arcmin diameter**
Coating	**C + Ir overcoating**
Total mass	**1800 Kg**
Effective area	**3 m^2 at 1.25 keV**
	0.65 m^2 at 6 keV
	150 cm^2 at 30 keV
Angular resolution	**5 arcsec HPD, 0.1-7 keV**
	30 arcsec HPD, 7-40 keV

Table 3.7: Technological characteristic requirements for IXO optical module.

Regardless of the adopted technique for such large optics, a mass production is required, and, accounting for unavoidable alignment errors, all the blocks with a HEW worse than 5 arcsec have to be rejected (as of today, 20% - 30% of the production). Possible sources of imaging degradation are the geometrical deformations of the reflective surfaces at the bending and/or integration stage, and the surface microroughness that gives rise to X-ray scattering. Accurate metrological characterizations (including both profile and roughness) are routinely performed to predict the optical quality degradation of the mirror assembly. Nevertheless, the optical surfaces are not always easily accessed by metrology, especially after the integration. Moreover, accurate metrology is usually time-consuming and only small portions of the surface can be sampled (e.g., the roughness is in general measured at discrete locations, assumed to be representative of the entire surface).

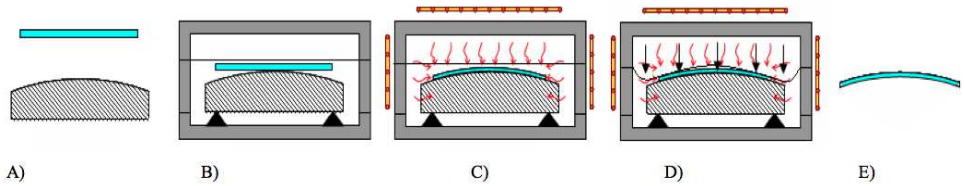

Figure 3.23: Main steps of the direct slumping technology with pressure developed by INAF-OAB. A) The slumping mould is figured with the required shape and microroughness and coated with an anti-sticking layer (if needed); B) The glass foil is placed above the mould in a stainless steel muffle where Ar atmosphere is established. C) The thermal cycle is started. D) Once reached and maintained the maximum T of the cycle, a uniform pressure is applied on the plate, in order to constrain it against the mould. E) After the cooling of the oven, the slumped glass segment is released and it is ready to be characterized and integrated in the X-ray module (Proserpio et al., 2011).

The backup technology being studied at INAF/OAB based on glass slumping process is based on a principle of hierarchical integration. The mirror production begins with the realization of couples of thin glass plate pairs in Wolter I configuration that have a very high surface quality (see Fig. 3.23). Several plate pairs are stacked on top of each other to form a single monolithic unit. To reach the desired performances inside each mirror module the consecutive plates are joined with reinforcing glass ribs that are glued on the plates (See in Fig. 3.24 a sketch of the optical module structure). The integration of the plate pairs is performed with high precision alignment in order to get the desired HEW performances. Such mirror modules once qualified and calibrated are then integrated on ground into the mirror optical bench.

Due to the ATHENA mirror maximum aperture dimensions, the shells need to be azimuthally divided into segments, so that the plate size dimensions will be compati-

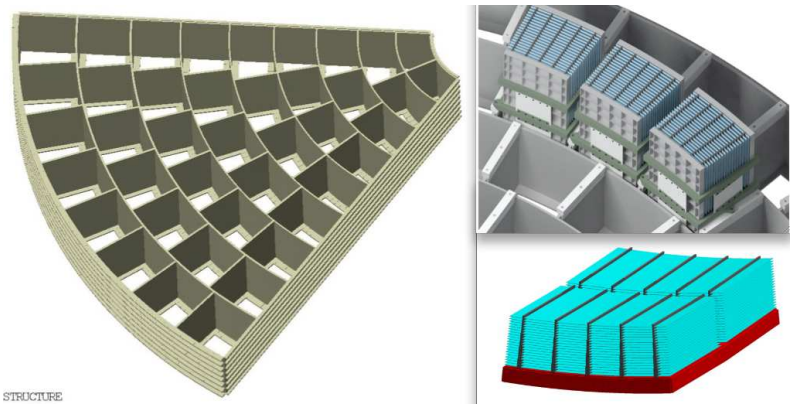

Figure 3.24: IXO optical module structure, in the left panel. Top right panel the X-ray optical Unit (XOU). Bottom right panel a stack of glass plate pairs connected each other by glued ribs. Credits: ESA.

ble with the slumping technique. A symmetric structure of radial arms to sustain the mirrors will be the base for the partition of the telescope mirror into petals. The number of petals and the need for a further division into X-ray Optical Units (XOU) will result from a mechanical analysis of the mirror structure. The designed mirror will be the sum of several XOUs that are segments of circular coronas with dimensions optimized for reducing the obscuration area. At Brera Astronomical Observatory (OAB) we are developing the direct slumping technology that is one of the two baseline methods used to produce the glass foil. This makes the parabola or hyperbola surface according to the Wolter I optical scheme assembled to form the X-Ray Optical Unit. In chapter 8 is described my work about the characterization of several samples of these prototype glasses, some of that are produced by the method of direct slumping (at OAB) and some of that are produced by the method of indirect slumping (at Max Planck Institute). We also compare the two different methods.

3.6.3 ASTRO-H

ASTRO-H is an astrophysics satellite dedicated for X-ray spectroscopic study non-dispersively and to carry out survey complementally, which will be borne out of US-Japanese collaborative effort. Among the on-board instruments there are four conically approximated Wolter-I X-ray mirrors, among which two of them are soft X-ray mirrors, of which the energy range is from a few hundred eV to 15 keV, currently being fabricated in the X-ray Optics Lab at Goddard Space Flight Center. The focal point instruments will be a calorimeter (SXS) and a CCD camera (SXI), respectively. The other two telescopes are hard X-ray mirrors with depth-graded, multilayer reflectors. The JAXA laboratory has advanced the technology for multilayer reflec-

tors through development of a balloon-borne experiment, InFOCuS. While its base model for the multilayer design (with the minimum incident angle of 0.11 degrees and 8 m focal length) is adequate for the ASTRO-H mission, they opt to improve it further so that better performance can be derived with the minimum incident angle of 0.07 degrees and 12 m focal length. The improved design has resulted in the reduction of layers from 28 to 10-21 layers per reflector while gaining higher reflectivity by 3-5% at 40-70 keV.

The main characteristics of ASTRO-H are shown in Tab. 3.8. The reflectors of

Figure 3.25: ASTRO-H EM fully-populated primary housing of 203 shells. There are 13 alignment bars, on each phase, each with 203 grooves that hold the 203 shells by the edges. Credits: JAXA.

the mirror are made of heat-formed aluminum substrate of the thickness gauged of 152 μm, 229 μm, and 305 μm of the alloy 5052 H-19, followed by epoxy replication on gold-sputtered smooth Pyrex cylindrical mandrels to acquire the X-ray reflective surface. The epoxy layer is 10 μm nominal and surface gold layer of 0.2 μm. Improvements on angular response over the Astro-E1/Suzaku mirrors come from error reduction on the figure, the roundness, and the grazing angle/radius mismatching of the reflecting surface, and tighter specs and mechanical strength on supporting structure to reduce the reflector positioning and the assembly errors (see Fig. 3.25).

Geometry	**Segmented conical approx.**
Energy band	**0.5 - 80 keV**
Focal length	**12 m**
Field of view	**$\geq$17' diameter**
Substrate	**Heat-formed aluminum**
Coating	**Pt/C graded multilayer**
Effective area	**each module $\geq$ 500 cm^2 at 1-6 keV**
Angular resolution	**$\leq$ 1.1' (HPD)**
Launch	**ASTRO-H lunch is foreseen 2014**

Table 3.8: Technological characteristic requirements for ASTRO-H satellite (Miyazawa et al. 2011).

3.6.4 NuSTAR

The NuSTAR mission will deploy the first focusing telescopes to image the sky in the high energy X-ray (6 - 79 keV) region of the electromagnetic spectrum. Our view of the Universe in this spectral window has been limited because previous orbiting telescopes have not employed true focusing optics, but rather have used coded apertures that have intrinsically high backgrounds and limited sensitivity.

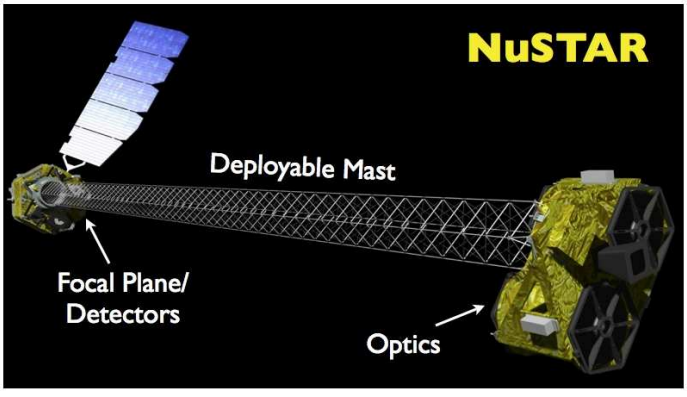

Figure 3.26: Artistic picture of NuSTAR after extension of its 10 meter focal length (credit NASA).

The NuSTAR instrument consists of two co-aligned grazing incidence telescopes with specially coated optics and newly developed detectors that extend sensitivity to higher energies as compared to previous missions such as Chandra and XMM (see Fig. 3.28). After launching into orbit on a small rocket, the NuSTAR telescope

extends to achieve a 10-meter focal length (see Fig. 3.26). The observatory will provide a combination of sensitivity, spatial, and spectral resolution factors of 10 to 100 improved over previous missions that have operated at these X-ray energies.

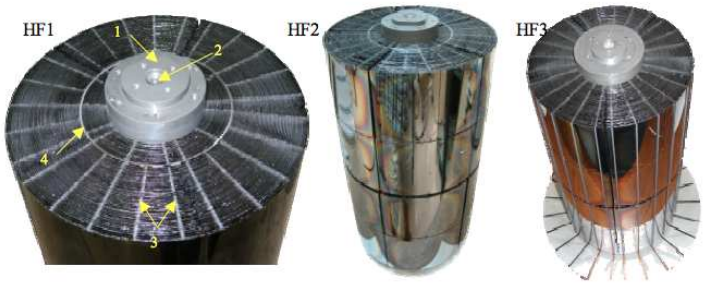

Figure 3.27: Three NuSTAR optic modules: HF1, HF2 and HF3. The following details are noted for HF1: 1 - the central titanium mandrel; 2 - precision alignment cone that defines the optical axis; 3 - stacks of graphite spacers; 4 - intermediate mandrel used for structural support when switching between 3 and 5 spacers per quint section. (credit NASA).

NuSTAR implements a conical approximation to the Wolter-I design and consists of 130 concentric mirror shells coated with Pt/SiC amd W/Si multilayers. The NuSTAR optics have an overall length of 450 mm, a maximum radius of 191 mm and a focal length of 10 m. The NuSTAR team has developed a novel approach to building these optics, focusing on a light-weight design. The mirror substrates are thin sheets of glass forming by hot slumping. At NASA's Goddard Space Flight Center in Greenbelt, Maryland, the glass is heated in an oven and slumped over precision polished cylindrical quartz mandrels to achieve the right curvature (see Fig. 3.27).

The slumped mirror segments are then deposited with a multilayer coating at the DTU-Space at the Danish Technical University in Copenhagen. The optics are built from the inside out, shell upon shell, spaced apart by graphite spacers and held together by nothing but epoxy. This precision assembly is done at Columbia University's Nevis Laboratory outside New York City and provides very light and flexible optics. The main technological characteristics are listed in Tab. 3.9.

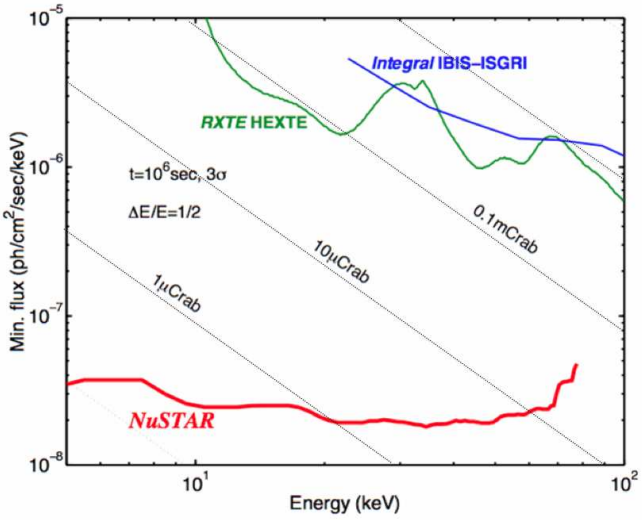

Figure 3.28: NuSTAR improves sensitivity by $\sim$ 100x over non-imaging missions (credit NASA).

Geometry	**Segmented conical approx.**
Energy band	**5 - 80 keV**
Focal length	**10m**
Field of view (at 30 keV)	**$\geq$13' diameter**
Substrate	**Thermally formed glass**
Coating	**W/SiC (outer shells) Pt/C (inner shells)**
Effective area	**$\geq$ 1000 cm^2 at 5-10 keV**
	$\geq$ 200 cm^2 at 45 keV
	$\geq$ 100 cm^2 at 70 keV
Angular resolution	**$\leq$ 90" (HPD), E $\leq$ 40 keV**
Launch	**NuSTAR lunch is foreseen in next March**

Table 3.9: Technological characteristic requirements for NuSTAR satellite.

4 X-ray mirror profile and surface characterization

Improvement of focusing accuracy has been a major consideration in the use of grazing incidence optics in x-ray telescope applications, and in synchrotron beam line instrumentation. This task of paramount importance is achieved via accurate metrology. Profilometers measuring the global shape while roughness measurements "sample" the optical surface. The treatment of complete topography of the optical surface is traditional divided in two principal branch: the study of profile at the long spatial wavelengths (in a range comparable with the mirror length) and the study of the microroughness at shorter spatial wavelength, by means of the Power Spectral Density (PSD). Owing to the finite scan size and resolution, each instrument has a finite window of spectral sensitivity. Therefore, we have to use different instruments, each one is sensitive only to a particular window of spatial frequencies. The Power Spectral Density provides a global description of the statistical properties of the roughness over a vast spectral extent.

In the following we describe the instrumentation used at OAB for characterizations performed on mirror samples.

4.1 Shape measurement techniques

The determination as the optics substrate shape during the manufacturing phase and after is essential in order to evaluate the focusing performances. The presence of errors in the spatial low frequencies range (figure errors or slope errors) causes the rise of unwanted aberration that, in the worst cases, can degrade the focused spot in such a way that the obtained images are unusable for scientific purposes. An accurate evaluation of the effect due to these errors over the optics surface is obtained by using ray-tracing codes that simulate the spot at focus, as well as along the whole optical system provide that the geometrical optics laws can be applied.

4.1.1 Long Trace Profilometer

The Long Trace Profilometer (LTP) is a non-contact optical profiling instrument designed specifically for measuring the slope and figure errors of large optics mirrors (with planar, spherical and aspherical shapes) with an high resolution and repeatability. It is based on the original concept of the pencil-beam interferometer von Bieren (1982), and developed by P. Tackacs et al. (1986), which employs two Ne-He laser beam pencils scanning the surface of the mirror under test. The reflected beam direction changes according to the local surface slope at that position, and a Fourier transform lens converts the angle variation of the reflected beam in a variation of position in its focal plane. Another part of the beam is focused on reference surface, in order to subtract the tilting and rotation of the optical head. The focused laser beam position is recorded by a linear array detector and, after a proper fit, the local slope of the mirror under test is obtained (see figure 4.1).

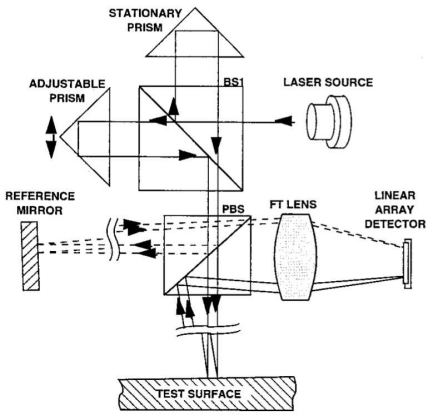

Figure 4.1: Long Trace Profiler layout.

If the instrument is properly calibrated, thermo-isolated and the surrounding environment vibration-free and air-flow controlled, the LTP at INAF/OAB can reach resolutions below 10 arcseconds with a scan length up to meters with a sub-mm lateral resolution. With such a precision, this instrument is widely used during the manufacturing process in order to detect possible shape imperfections of the optics surface (see figure 4.2). This kind of instrument covers a spectral band meters-millimetres and below.

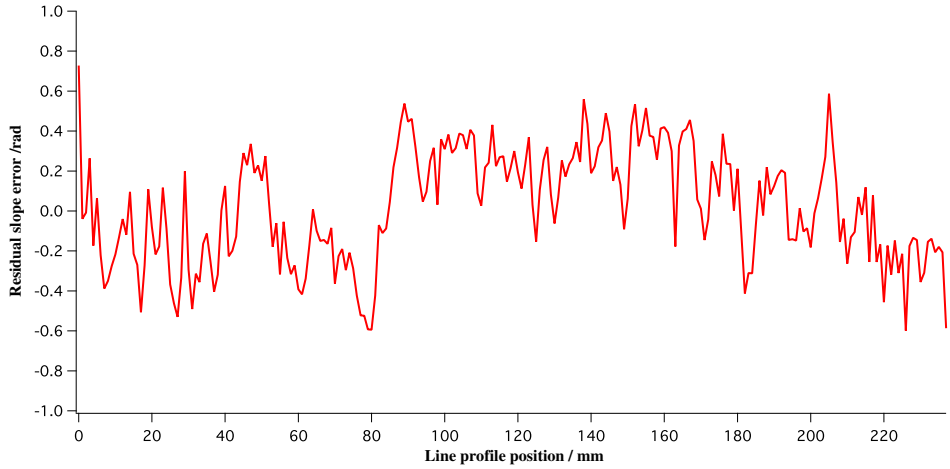

Figure 4.2: Long Trace Profiler measurement result over a flat mirror. The rms residual slope error has been found to be of 0.32 μrad with a radius of curvature of 43 km.

4.1.2 CUP

The *characterization universal profilometer* (CUP) is an 3D-mapping instrument developed at INAF-Astronomical Observatory of Brera (INAF-OAB), aimed at the figure mapping of a general smooth surface both concave and convex.

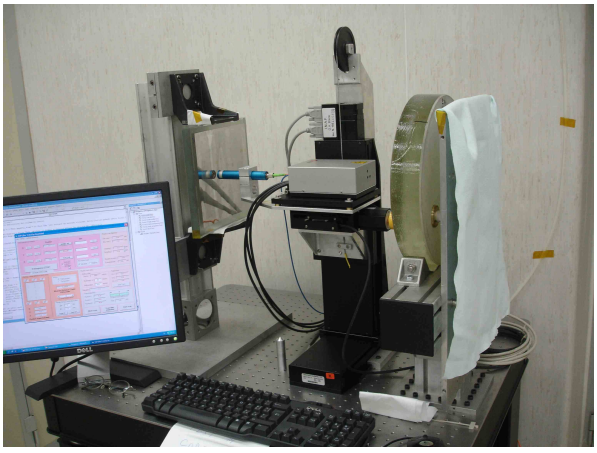

Figure 4.3: Characterization universal profilometer, instrument developed and operated at INAF/OAB.

Unlike the LTP that works with a single sensor, this instrument have two different

sensors. The first one, the high speed sensor CHRocodile X, measures the distance from the surface sample, the second one, a SIOS triple-axis interferometer, returns the absolute distance from the CHRocodile and a reference mirror. Scanning the surface with precision motors returns the 3D profile with a few tenth nanometres accuracy (fig 4.3). The aim of this instrument was to overcome the limitations of many kind of profilometer, e.g. the LTP, the possibility of measuring profiles with a very high curvature radii.

4.2 Microroughness measurement techniques

Since the small dimension of the structures the accurate roughness measurement is a challenge and requires a high control of the environment surrounding the instruments in terms of temperature, pressure and vibration stability. The main instruments devoted to measure such small heigh variations are the Atomic Force Microscope (AFM) and the Phase Shift Interferometer.

4.2.1 Atomic Force Microscope

Atomic Force Microscopy (AFM) is a type of Scanning Probe Microscopy (SPM) that leads to high resolution imaging of conducting as well as non-conducting surfaces. It works scanning with a sharp probing tip very close to the sample surface

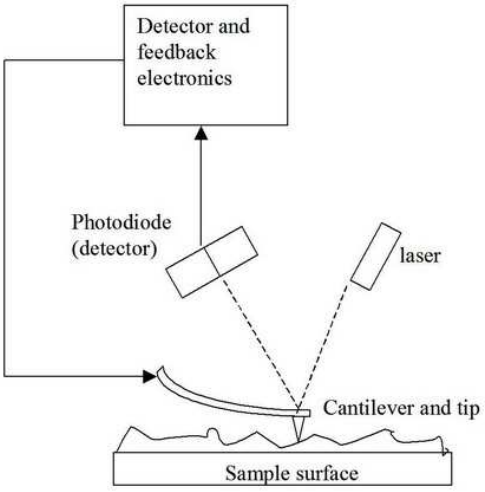

Figure 4.4: General AFM block diagram.

sensing the Van Der Waals attractive/repulsive forces between the tip and the sample in constant height or constant force mode. Piezoelectric elements that ease tiny,

accurate and precise movements enable the very precise scanning (see Fig. 4.4 for a general AFM block diagram).

The reached resolution is much higher than microscope (more than 1000 times better that the optical diffraction limit) 3D scans are. Finally, It does not require any surface preparation and is able to measure at ambient conditions and, in general does not need operating in vacuum.

Basic AFM components

The necessary mechanical AFM parts are the cantilever (ending with the probe tip) and the x/y and z piezo that are separately actuated by x/y drive and z-control with extreme precision, so that distances can be measured to better than 1 Å. The AFM tips

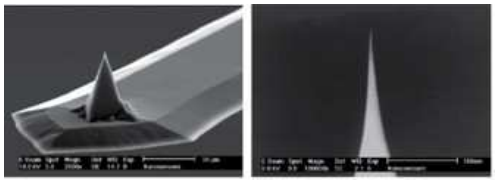

Figure 4.5: Example of silica AFM cantilever and tip.

are usually micro-fabricated silicon cones (sometimes edged) or silicon nitride four-sided pyramids that are commercially available mounted to cantilevers with spring constants $k = 0.05 - 1.5Nm^{-1}$ for contact AFM and $40 - 80\ Nm^{-1}$ for tapping-mode AFM. The cantilevers (see figure 4.5) may be one-leg, triangular, or square. They vary in their spring constants also by the thickness and width of the legs as is required for various application modes. The cantilevers are typically $100 - 400\ \mu m$ long, $40\eta m$ wide, and $1\ \mu m$ thick. A typical height is of $10 - 150\ \mu m$.

AFM working principles

The potential energy V_{ts} between the tip and the sample causes a z component of the tip-sample force $F_{ts} = -\partial V_{ts}/\partial z$ on the order of a few nN. Depending on the mode of operation, the AFM uses F_{ts} , or some derived entity, as the imaging signal (see figure 4.6). F_{ts} has both long-range and short-range contributions. Depending on the situation, forces that are measured in AFM include mechanical contact force, van-der-Waals forces, capillary forces, chemical bonding, electrostatic and magnetic forces.

As an example, in vacuum, there are van-der-Waals, electrostatic and magnetic forces with a long range (up to $100\eta m$) and short-range chemical forces (fractions of nm) for non-contact mode of operation. When the tip is brought into proximity

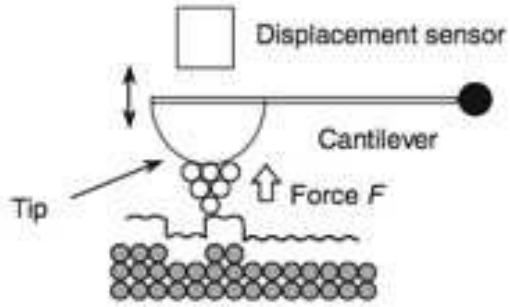

Figure 4.6: Schematic of AFM measurement.

of a sample surface, these forces between the tip and the sample lead to a deflection of the cantilever according to Hooke's law. Typically, the deflection is measured using a laser spot reflected via mirror to a split diode that provides the feedback signal (topologic information) for maintaining the force by z-piezo response. Data sampling is made at discrete steps by means of an analog-to-digital converter. If the tip was scanned at a constant height, a risk would exist that the tip collides with the surface, causing damage. Hence, in most cases a feedback mechanism is employed to adjust the tip-to-sample distance to maintain a constant force between the tip and the sample. For this reason the sample is mounted on a piezoelectric stage, that can move the sample in the z direction for maintaining a constant force, and the x and y directions for scanning the sample. This eliminates some of the distortion effects seen with a tube scanner. In newer designs, the tip is mounted on a vertical piezo scanner while the sample is being scanned in x and y using another piezo block. The resulting map of the area retrieved from the z-piezo displacements $z = z(x, y)$ represents the topography of the sample. A computer reconstructs the three-dimensional image.

Imaging modes

The AFM can be operated in a different modes, depending on the application. In general, possible imaging modes are divided into static (also called contact) modes and a variety of dynamic (tapping and non-contact) modes where the cantilever is vibrated.

In the *static mode*, the probing tip is always in contact with the sample surface, and surface structure is obtained from the deflection of the cantilever. Since in the contact mode, there is a high possibility that the strong repulsive force acting between the sample surface and the probing tip will destroy the sample surface and/or the tip apex. In the *tapping mode*, the probing tip comes periodically close to the sample

surface, and surface structure is obtained from the change of the vibration amplitude or phase of the oscillating cantilever. In the tapping mode, the cantilever is driven at a fixed frequency near resonance with large vibration amplitude. When the probing tip is far from the surface, the vibration amplitude of the oscillating cantilever is held constant. When the probing tip is close to the surface, the probing tip is periodically in contact with the sample surface, and the vibration amplitude of the oscillating cantilever decreases due to cyclic repulsive contact between tip and surface with loss of the energy stored in the oscillating cantilever. The surface structure is obtained by maintaining the vibration amplitude at the constant level using a feedback circuit as shown in figure 4.7.

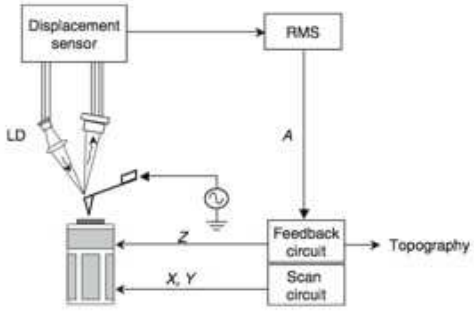

Figure 4.7: Schematic of Dynamic AFM.

In the case of *non-contact mode* the cantilever's tip does not contact the sample surface but, instead, it oscillates at a frequency slightly above the resonant frequency where the amplitude of oscillation is typically a few nanometers ($< 10\ \eta m$). The resonant frequency and the phase can be derived assuming a simple harmonic oscillator model.

The van der Waals forces (as well as the other long-range forces) extends above the surface of the sample and act to decrease the resonant frequency of the cantilever. Practically, when the probing tip approaches the sample surface, effective spring constant of the cantilever changes from k to $k + \partial F/\partial z$ due to the force gradient acting between the probing tip and the sample surface. As a result, the mechanical resonant frequency changes from ν_0, the mechanical resonance frequency of the cantilever, to ν_1. By measuring the frequency shift $\Delta\nu = \nu_0 - \nu_1$, it can be estimated the force gradient.

In terms of optics roughness measurement, the preferred working mode is dynamic, preferring the non-contact, since the cantilever's tip is not in contact with the optical surface minimizing the possibility of surface degradation caused by the measure itself. This fact is even more concrete when multilayer coated optics have to

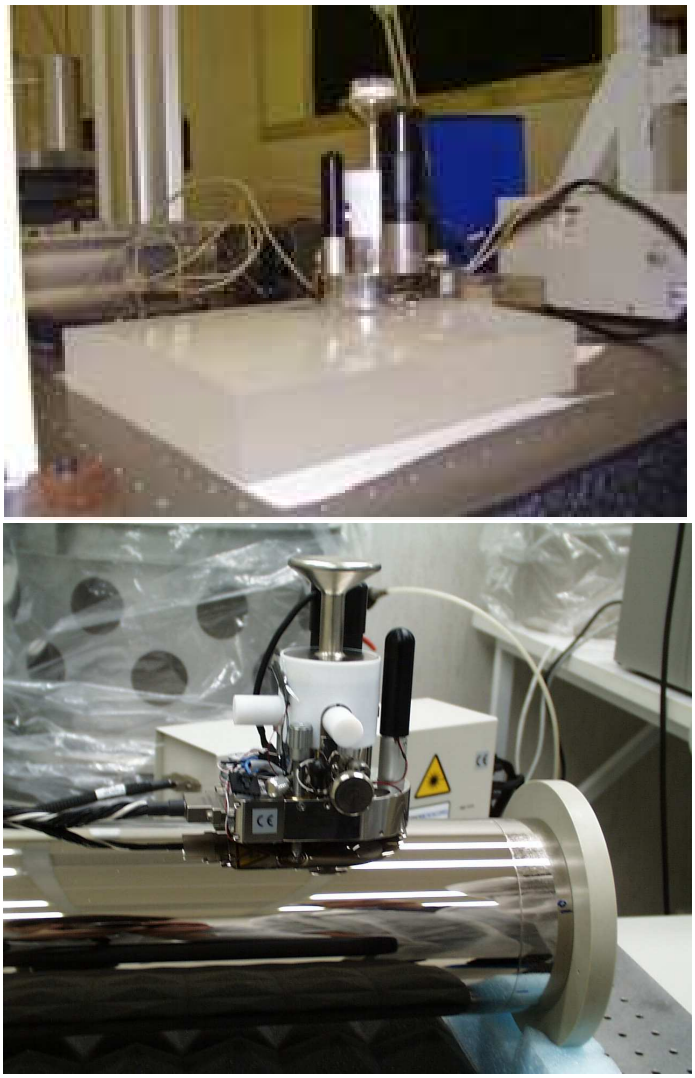

Figure 4.8: The AFM operated at INAF/OAB is a stand-alone model that can operate onto wide samples as a moulds in the top panel or onto mandrels as it shown in the bottom panel.

be measured since the presence of easy-removable soft material in proximity of the scanning tip. Generally the scan areas are form few microns up to $100\mu m$ and the measured vertical structures are resolved with high accuracy.

The AFM operated at INAF/OAB is a Veeco Explorer stand-alone (see Fig. 4.8), i.e. the head can be moved onto wide samples and mandrels.

4.2.2 Phase shift Interferometry

An interferometer is an optical device which utilizes the effect of interference. Typically, it starts with some input beam, splits it into two separate beams with some kind of beam splitter (a partially transmissive mirror), possibly exposes some of these beams to some external influences (e.g. some length changes or refractive index changes in a transparent medium), and recombines the beams. The power or the spatial shape of the resulting beam can then be used for a measuring the optical surfaces quality in terms of roughness and flatness. When a light source with low optical bandwidth is used (even a single-frequency laser), the detector signal varies periodically when the difference in arm lengths is changed. Such a signal makes a possibility

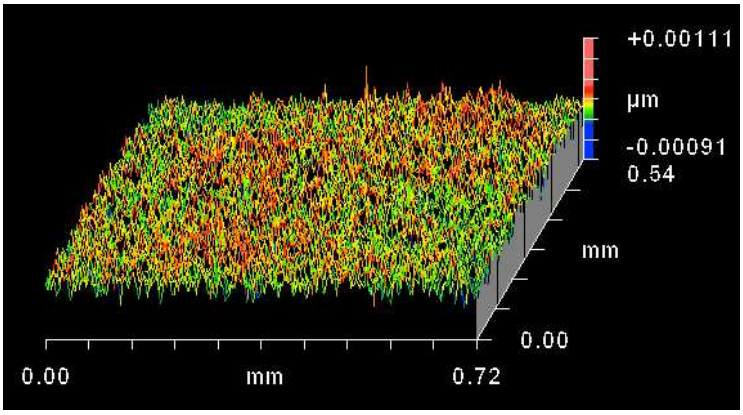

Figure 4.9: Example of Phase Shift Interferometric measurement result during the inspection of a good quality optics. The measured rms roughness has been estimated to be about 2 Å.

to do profile/roughness measurements with a depth resolution well below the wavelength, but there is an ambiguity. For example, the fringe pattern does not reveal if the surface is approaching or moving farther. This problem may be solved by modulating the arm length difference with a vibrating mirror (or with an optical modulator) and by monitoring the resulting modulation on the detector in addition to the average signal power. Simultaneous operation of an interferometer with two wavelengths is another way of removing the ambiguity. If the detector is a kind of camera, like a

Charge Coupled Device (CCD), and the surfaces monitored are fairly smooth, the phase profile (and thus the profile of optical path length) can be reconstructed by recording several images with different overall phase shifts. A phase-unwrapping algorithm can be used to retrieve unambiguously surface maps extending over more than a wavelength. However, such methods may not work for rough surfaces or for surfaces with steep steps. A white light interferometer uses a broadband light source (i.e. with low temporal coherence), so that interference fringes are observed only in a narrow range around the point of zero arm length difference. Likewise, the above-mentioned ambiguity is effectively removed. In figure 4.9 is shown a typical image of a flat and smooth mirror acquired with a white light interferometer.

A wavelength tunable laser can be used to record the detector signal for different optical frequencies. From such signals, the arm length difference can be unambiguously retrieved. If one of the mirrors is intentionally tilted, an interference fringe pattern is obtained. Any change in arm length difference will then move the fringe pattern. This method makes possible to measure phase changes sensitively and also to measure position-dependent phase changes in some optical element.

The spatial wavelength range where this kind of instrument can operate start from microns up to few millimetres with a few angstroms height accuracy.

Mirau interferometer

The interferometer in use at INAF/OAB is a Mirau interferometer WYKO (Fig. 4.10). The WYKO Rough Surface Tester (RST) Light Interferometer is a non-contact optical profiler capable of very sensitive 3D surface profilometry and surface roughness characterization. The RST Light Interferometer operates in the optical phase-shifting mode.

In Fig. 4.11 examples of roughness measurements of a mirror sample with the WYKO at INAF/OAB, with the two possible objectives, 2.5x and 20x.

4.3 Power Spectral Density computation

Characterization of optical surfaces frequently involves the power spectral density (PSD). It can be calculated from surface profiles obtained via optical or a mechanical interference or AFM devices. The PSD is the square of the Fourier transform of the surface profile per spatial frequency unit or equivalently the Fourier transform of the autocovariance function that has been calculated from the surface profile. To improve the representatively of the PSD of a surface that has random roughness, we must take an ensemble average of PSD estimates calculated from profiles made at many different places on a surface.

To obtain an ensemble average PSD from surface profile data, there are two op-

Figure 4.10: Mirau interferometer WYKO in use at INAF/OAB with two objectives: 2.5x and 20x.

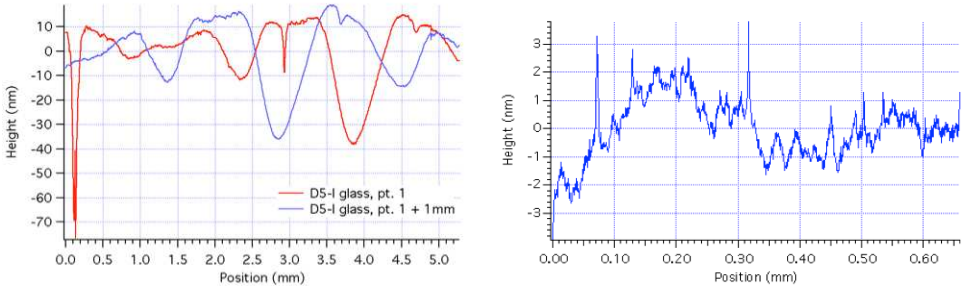

Figure 4.11: Examples of WYKO measurements performed on the D5 glass after integration, at INAF/OAB. Left: 2.5x magnification, 5.2 mm scan length, rms 120 Å. The profile was measured twice after moving the sample laterally by 1 mm, to make sure that the observed undulations are not instrumental effects. Right: 20x magnification, rms 11 Å(see sect. 7).

tions. A large number of profiles can be taken at different places on the surface, the one-dimensional PSD estimate calculated from each profile, and the resulting graphs averaged together to obtain a smooth, noise-free curve. The one-dimensional measured PSD can be modelled with an analytic function, typically a power-law, $P(f) = K_n/F^n$. If z(x) is the surface roughness height as a function of distance x, in the incidence plane of X-rays, a finite length PSD can be written as:

$$P(f) = \frac{1}{L}|\int_0^L dxz(x)e^{(-ikx)}|^2 \tag{4.1}$$

where k is the wave number. Alternatively, the PSD can be computed from 2D data as a 2D-PSD and, under hypothesis of isotropy, integrated over the frequency. Measurements of z(x) yield digitized data, we assume that the surface roughness data set consists of N values for z(x) that are measured at equally spaced intervals Δx over a total length $L = N\Delta x$. If these discrete surface height data are adjusted to have a zero mean value, i.e., there are equal heights above and below a mean surface level, and are denoted by z(n), $n = 0 \rightarrow N-1$, then the PSD becomes:

$$P(f_k) = \frac{L}{N^2} \mid \sum z_j e^{-ikj} \mid^2, \quad with \;\; F_k = 0, \; \frac{1}{L}, \; \frac{2}{L}, ..., F_c \tag{4.2}$$

This value is bandwidth limited, as the magnitude of the highest surface spatial frequency resolved in the measurement process is $f_c = (2\Delta x)^{-1}$, the Nyquist frequency.

In Fig. 4.12 an example of PSD computed with different instruments that work in different spatial wavelength range. Remarkable that the values obtained with the AFM, with the optical interferometer and from scattering measurements are extremely consistent, using three entirely different physical approaches.

4.3.1 X-ray diffractometer Bede D1

The X-ray diffractometer BEDE-D1 installed at INAF-OAB is a multi-purpose instrument aimed at directly testing the X-ray reflectivity, scattering properties of X-ray mirrors. Even if it is not a topographic instrument, it also provides a reliable roughness characterization. It consists of an X-ray shield, which contains an X-ray tube, a Si crystal monochromator, a sample carrier and an X-ray detector, both equipped with precision goniometers (res. 1", see Fig. 4.13). All of these elements are positioned and moved by micrometric motors, driven by an external computer code (see Fig. 4.15).

The X-ray tube (equipped with a copper anode) generates a bremsstrahlung spectrum, superposed to characteristic fluorescence lines of Cu. In particular the Kα1 line (8.05 keV, 1.541 Å) is selected because of its intensity and sharpness (typically

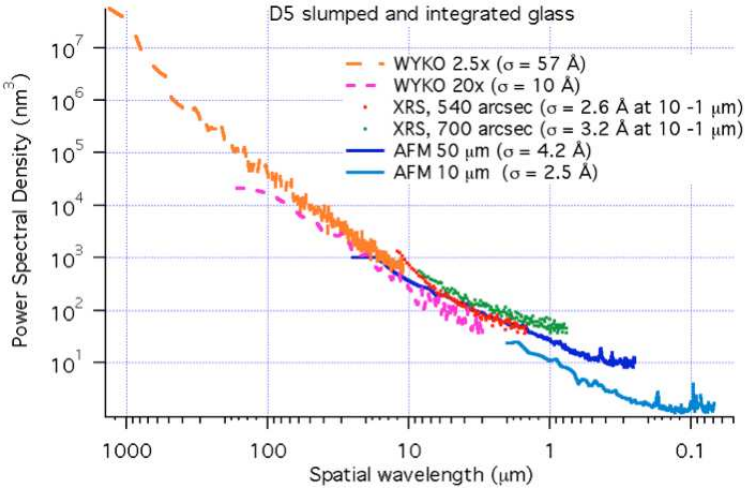

Figure 4.12: The PSD of the D5 slumped and integrated glass (IXO project), as measured with various techniques, with different spatial wavelength range.

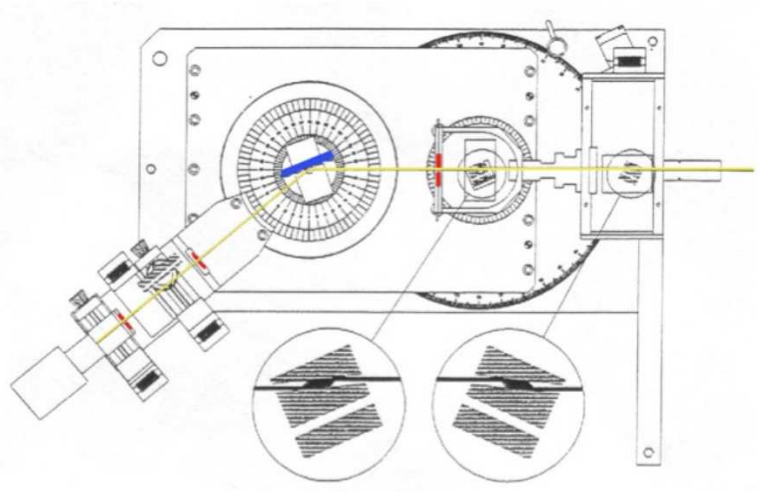

Figure 4.13: sketch of X-ray diffractometer Bede D1. On the right side there is the X-ray source and on the left side there is the detector.

it has a 1eV equivalent width). The line intensity may be changed by external power controls. The X-ray tube is easily removable in order to change the target anode. Different tubes are available: the tube with a target anode in Molybdenum (Kα, 0.709 Å17.4 keV) is implemented to perform measures in harder X-rays. The beam is filtered by a couple of silicon channel-cut-crystals that diffract the fluorescence line according the Bragg law, then after being collimated by a system of slits impinges the sample with a residual divergence of 5". The sample is driven by precision motors in rotation (5") and translation (3 μm). The reflected/scattered beam intensity is then measured by a scintillator with high linearity, moved onto a precision rotating stage. Analysing silicon crystals are also available to increase the angular resolution of the measurement.

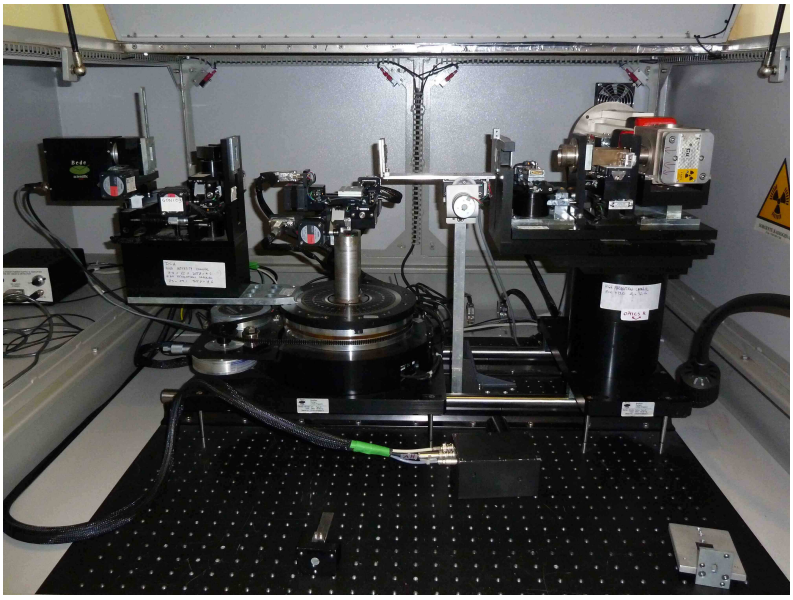

Figure 4.14: X-ray diffractometer Bede D1, available instrument at the Osservatorio Astronomico di Brera.

The BEDE-D1 is a general purpose instrument: it allows X-ray diffraction, reflectance, scattering measurements. For XRR measurements the achievable photon fluxes are N $\approx 10^4 \div 5 \times 10^5$, depending on the desired angular resolution, beam width and the used X-ray tube. Very thin beams have to be used when the samples have a very limited size, while a very high angular resolution is adopted when the reflectance scans have important details to be resolved. In XRR measurements the precision limiting factor is the detector noise, whose counts are around 1 cps (8.05 keV line, rejection photomultiplier parameters correctly set), leading to a reflectivity

determination error of $10^{-4} \pm 10^{-5}$: this error source is important only where the reflectivity falls under this limit. Another error is caused by the Poissonian source fluctuation $N^{-1/2} \approx 1\% \div 0.05\%$. Both errors can be reduced by the increase of the integration time as $t^{-1/2}$, but at the risk of long-term source instability.

The direct measurement of the reflected and scattered radiation by the optics is a powerful tool to measure the roughness PSD and to investigate in-depth the layered structure of a reflectivity coating in a non-destructive way. The available X-ray sources have allowed to extend this kind of measurements to the actual working wavelength range of the mirrors/gratings under test. Commercially available X-ray tubes emit a continuous bremsstrahlung spectrum (with a cut-off maximum energy proportional to the accelerating power) superposed to the X-ray emission lines of an anode material. In such low- power sources, usually an emission line is selected in order to provide a sufficient flux to improve the signal/noise ratio. If more power or a wider energy range is needed, light source facilities (like synchrotrons) all around the world permit to perform such kind of measurement with high accuracy.

X-ray reflectivity and extraction of multilayer parameters

The X-ray Reflectivity (XRR) technique, also known as specular reflectivity, provides useful information about the deposited material's thickness since it is sensitive to the optical constants and density as well as to the interface roughness and diffuseness. The XRR measurements can be divided into two main groups

- angular scans: the energy of the thin incident beam is kept constant and the reflectivity is recorded while the sample under test is rotated under different grazing incidence angles. The reflected beam is followed and measured by a co-rotating detector (usually a scintillator with photomultiplier) known as $\theta - 2\theta$ scans.

- energy scans: the incidence angle is kept constant and the optics surface is illuminated by a broad spectral beam: the reflected beam must be collected by a multi-channel detector which is able to discriminate the energy of the reflected photons. Knowing the source's energy spectrum, it is possible to compute the reflectivity. A variation commonly used consists of using a source implemented with a monochromator, in order to have a very narrow energy band, and to change the incident radiation energy by moving the monochromator

In general, the angular scan does not require a very complex apparatus, because the detector may be sensitive only to the energy to be used (even if usually there are made more angular scans at different representative energies) and the measurement resolution is determined only by the incident beam divergence, controllable by the presence of micro-slits. Being the energy fixed, during an angular scan, the material's

optical constants are fixed and the reflectivity plot is quite easy to model and interpret. In the case of a multilayer coating, energy and angular scans permit to measure the Bragg peaks but, the first reveals in addition the variation of the optical constants as a function of the energy.

The easiest case of XRR measurement is that of a mirror coated with a single layer (4.15 left panel). As shown in 3.2.1 at very small angles the X-rays are completely reflected by the layer, decreasing slowly by effect of the increasing penetration depth of the X-rays. At the layer critical angle $\theta_c \simeq \sqrt{2\delta}$ the reflectivity drops and the interference fringes start to appear. If the substrate is denser than the layer, the interference occurs in total reflection regime for the substrate, and very intense interference fringes appear.

Since the critical angle is proportional to the material density, above the critical angles, the amplitude of the interference fringes is influenced by the $\Delta\delta$ of the layer/vacuum and layer/substrates and by the layer/substrate roughness. From the Snell law and the Bragg law, it is easy to derive the expression for the measured position of two successive maxima or minima

$$\sin\theta \simeq 2\delta + \frac{k\lambda}{2d}, \tag{4.3}$$

i.e., the effect of an increasing density is also a shift of the whole interference pattern to larger incidence angles and not only a shift of the critical angle. The effect is negligible for large interference orders, but this refraction effect may be important at very small angles, where usually the reflectivity is larger and interference fringes are easier to be detected; interference features can be observed up to a maximum angle, where the reflected beam falls down the instrumental noise limit.

In the case of a multilayer coating, the combined effect of these fringes generated by each bilayer interfere constructively following the Bragg law. This effect occurs in several peak observed at angles larger than the critical angle (see section 3.4.1. In Fig. 4.15 right panel an example of reflectivity from a periodic multilayer. The Bragg peaks beyond the critical angle are clearly visible.

It is worth noting that when modelling/fitting XRR reflectivity scans for an optical system, the roughness measurements can be underestimated since the experimental data are assumed to be the specular reflectivity data alone without any contribution from the scattered beam. In fact the detector has always a finite angular acceptance and the acquired data are the sum of the specular reflected beam and part of the scattered beam caused by low-frequency roughness. Of course, the presence of a vignetting slit before the detector reduces this ambiguity but at the cost of photon flux delivered to the detector.

From XRR measurements we can derive a detailed description of a mirror coating structure. This is allowed using the computer tool *PPM* (Spiga et al. 2006). This code specifically conceived for a fast determination of the stack parameters by fitting the

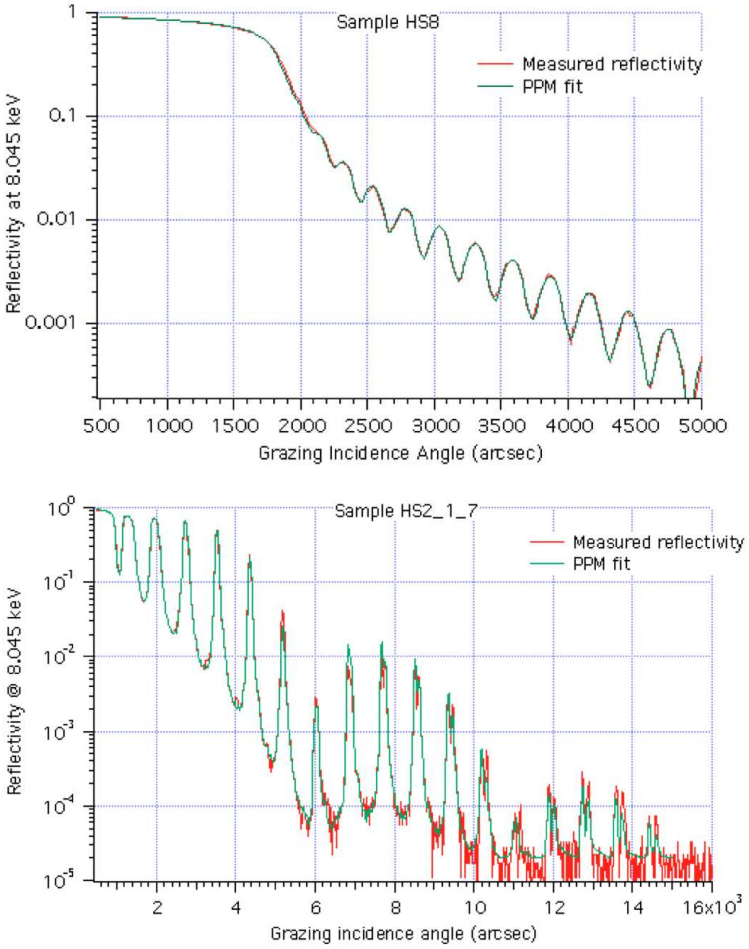

Figure 4.15: X-ray reflectivity measurements. Top: a reflectivity scan in of a single layer of Carbon. Bottom: a reflectivity scan in angle of a periodic multilayer.

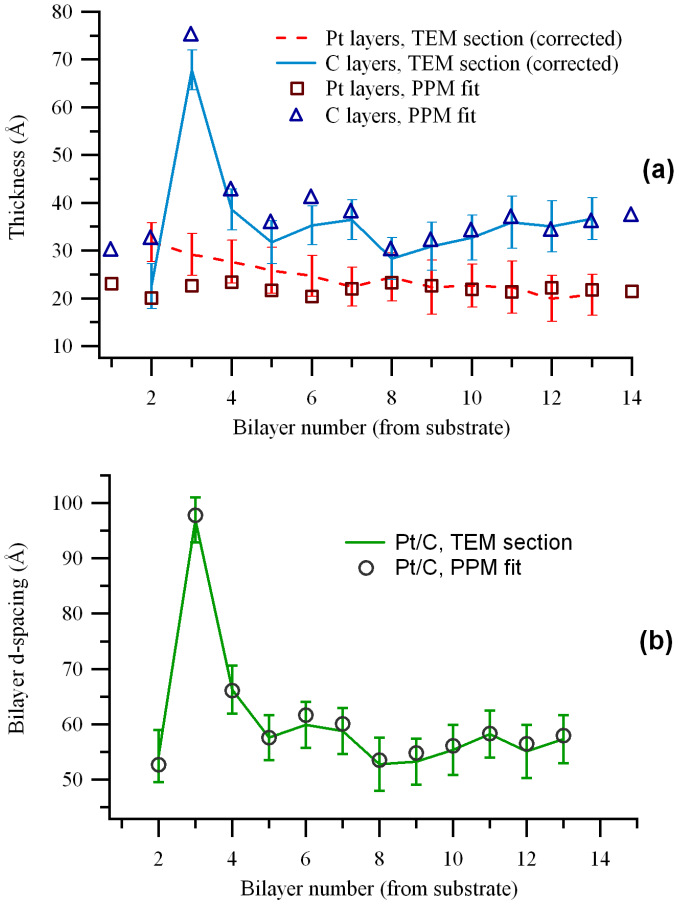

Figure 4.16: Comparison of measurement results between PPM fitting of reflectivity (that we performed at INAF/OAB) and TEM analysis. The sample analysed is a Pt/C 200 bilayer coating on a silicon wafer.

reflectivity scans even in the details: this allows us to take into account the reflectance features caused by the deepest layers. PPM returns the best fit values of: the material layer density, the thickness values of the individual layers (in the graded case, it also returns the power-law parameter a, b and c), the interface roughness trend throughout the stack. The program takes as input the reflectivity curves and a file in XML format that defines the structure scheme. The number of necessary parameters may vary according to the supposed complexity of the stack. For example we can take all the layer thicknesses as free variables, or assume a gradual drift of the layers. Other variables define the layer density and their roughness. Starting from the initial values, PPM computes the reflectivity curve R_c for every available experimental scan R_m and computes the Figure Of Merit (FOM),

$$FOM = \sum_i \mid \ln R_c - \ln R_m \mid \tag{4.4}$$

where i is the index of the angular sampled point. The minimizing algorithm consists in the variation of the stack parameters since the FOM reaches its minimum, a situation corresponding to the best possible fit, that is, the best approximation of the defined structure to the real multilayer structure. The choice of computing the FOM from of the logarithmic reflectivity permits to give more weight in the fit to the reflectance details (which in a linear plot would be likely neglected) that carry important information about the reflection in the deepest layers. The results are in excellent agreement with the transmission electron microscope (TEM) sections of selected samples (which are in contrast, destructive). See the comparison of measurement results between PPM fit of reflectivity and TEM analysis in Fig. 4.16.

The energy dispersive measurements, at the diffractometer Bede D1, are made in a different set-up to respect the mono-chromatic one. In this case, we adopt the X-ray tube with a target anode in Tungsten and we operate without mono-chromator. The output emission is Bremsstrahlung like, cut at low energy at 5 keV (air absorption) and cut at high energy at a value determined by the maximum voltage given from the power supply. The sample is mounted with a fixed incidence angle illuminated by a broad spectral beam (see Fig. 4.18). The reflected beam is collected by a multi-channel detector Amptek, a solid-state energy sensitive detector (see Fig. 4.17). Knowing the source's energy spectrum we can compute the reflectivity. In figure 4.18 we show some example of reflectivity obtained with this set-up at Bede D1 in use at INAF/OAB.

X-ray scattering

The reflectivity in the specular direction is related to the surface/interfacial σ roughness, but it does not allow a complete characterization of the surface. If the surface is not ideally smooth, the X-rays can be diffusely scattered in any direction. The

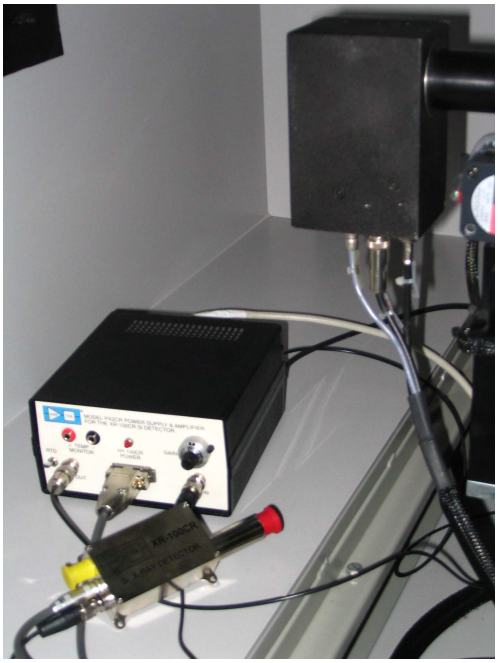

Figure 4.17: The solid-state energy sensitive detector Amptek XR100CR avalaible at Bede D1 diffractometer.

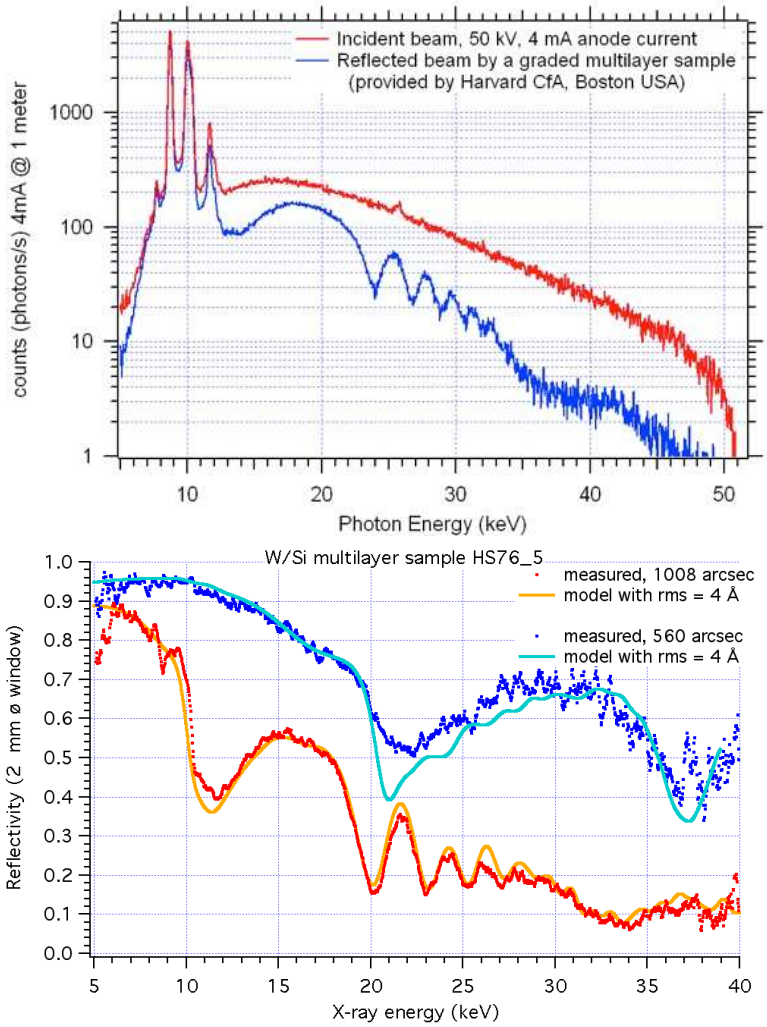

Figure 4.18: Measurement in energy dispersive configuration. Top: the direct and reflected broad spectral beam of Tungsten tube, we can see the L-lines linearound at 8.4 keV. Bottom: the reflectivity from a multilayer sample as a function of the X-ray energy in two different incidence angles.

experimental technique is known as X-ray diffuse scattering (X-ray non-specular reflection).

The X-ray scattering (XRS) technique enables the determination of the surface properties by measuring the intensity distribution of the scattered photons, which leads to a direct information of the surface's PSD. In the case of a single boundary mirror, the PSD can be simply obtained from a single scattering scan while the interpretation of the scattering due to multilayered structures is much more complex (Salmaso et al. 2011). In the typical experimental setup, the incident beam impinges over the optics surface with an angle of incidence θ_i and it is mainly reflected specularly with an angle $\theta_r = \theta_i$ if the smooth surface condition is satisfied. When irregularities are present over the test surface, light is scattered light in other direction than the specular one.

The relation between the observed scattering due to a non-ideally smooth surface, with a given PSD, is provided by a well consolidated 1^{st}-order perturbation theory (see Windt et al. 1994, Stover 1995). In this approach, the surface is assumed to be within the smooth surface limit $2\pi\sigma \sin\theta_i < \lambda$ so that the Fresnel equations (see sect 3.2.1) are still valid and the scattering is treated as a correction. The most remarkable result is that *there is a simple proportional relation between the scattered intensity distribution and the PSD of the surface expressed as a function of spatial wavelengths*. In particular the roughness σ is obtained by direct integration of the scattered power.

The classically predicted results are (see also Church 1979, Church & Takacs 1986):

- the bidimensional X-ray scattering diagram (i.e. the scattered fraction of the incident power per solid angle at the angles (θ_s, ψ_s)) is *proportional to the bi-dimensional surface PSD* $P(f_x, f_y)$

- if the surface is isotropic, the scattering in the incidence plane (θ_s direction) is $100 - 1000$ times more effective than in the normal plane (ϕ_s direction) when in grazing incidence configuration. In this way the scattered power in the ϕ_s direction may be easily integrated to derive the scattered power per angle unit at the angle θ_s:

$$\frac{1}{I_0}\frac{dI_s}{d\theta_s} = \frac{16\pi^2}{\lambda^3} Q_{is} \sin^2\theta_s \sin\theta_i P(f) \tag{4.5}$$

  where $P(f)$ is the mono-dimensional surface PSD and Q_{is} is a polarization factor, that can be approximated to be $Q_{is} = \sqrt{R(\theta_i)R(\theta_s)}$, where $R(\theta_i)$ and $R(\theta_s)$ are the Fresnel reflectivity evaluated at the incidence angle θ_i and scattered angle θ_s

- in case of an isotropic surface, every mono-dimensional PSD value evaluated

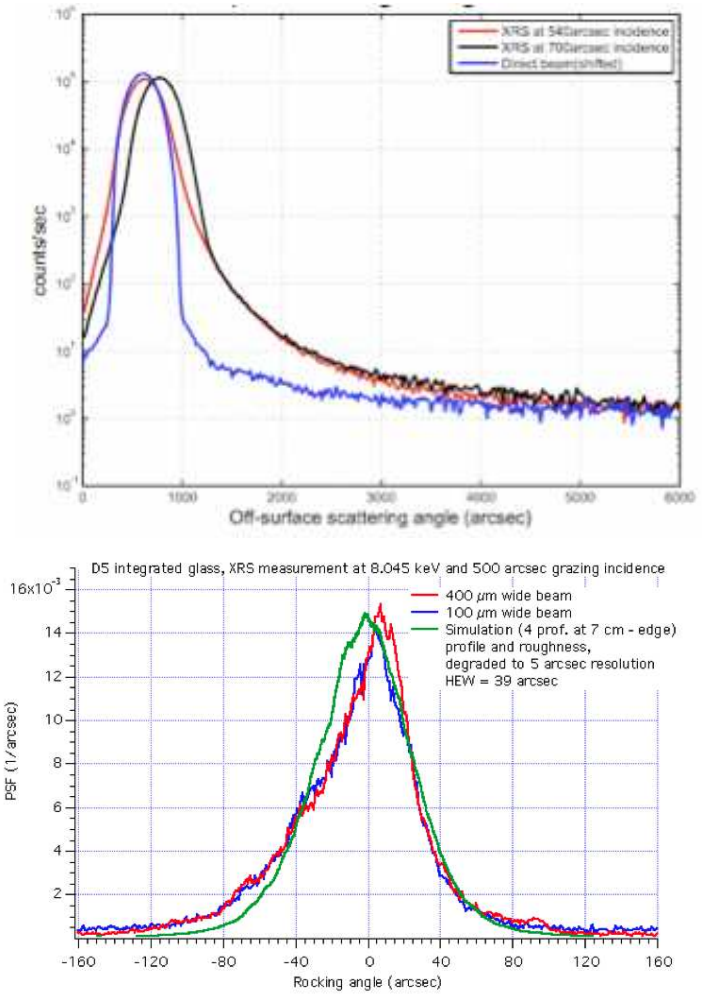

Figure 4.19: Top: a low resolution XRS measure of a sample mirror under developing at OAB. Bottom: an high resolution XRS of a sample mirror under development at OAB.

Figure 4.20: Bede diffractometer in configuration XRS low-resolution measurement.

at the scattering angle θ_s is related to a corresponding *spatial wavelength*. Obtained from the 1^{st}-order grating formula:

$$l = \frac{1}{f} = \frac{\lambda}{|\cos\theta_s - \cos\theta_s|} \tag{4.6}$$

If the smooth surface condition is not met, the equations above cannot be applied: this typically occurs in the low and mid-frequency range (1 cm - 0.1 mm), where neither the geometrical optics nor the 1^{st}-order theory is applied. In this case a different treatment has to be done (see sect 6).

There are two main kind of XRS measurements possible with the diffractometer:

- In *low resolution XRS* (see Fig. 4.20) the sample is set at a fixed incidence angle θ_i and the scattered intensity is measured while varying the scattering angle θ_s around the specular reflected ray at $2\theta_i$: the scattering diagram is in this case easier to interpret (an example of a low resolution XRS measure in Fig. 4.19, left panel). Since the large angular offset makes possible to distinguish the diffuse emission from the reflection this setup in general covers the 10-1 μm

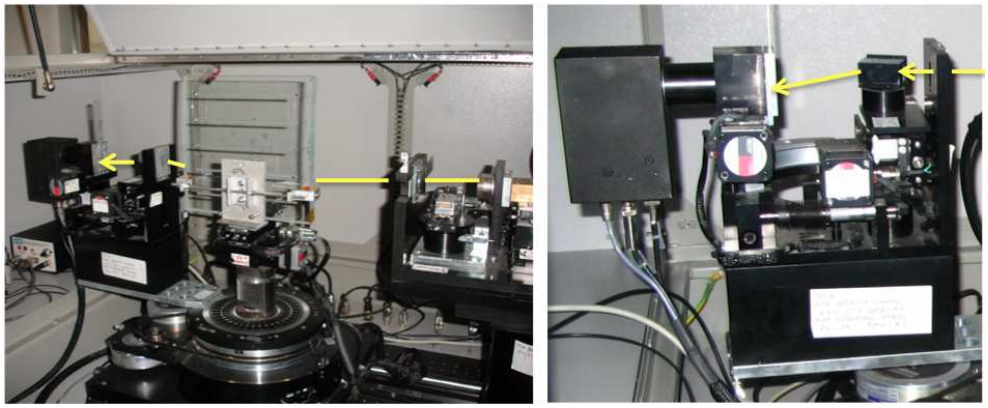

Figure 4.21: Bede diffractometer in configuration XRS low-resolution measurement.

range, where the 1^{st}-order XRS is applicable hence the PSD can be derived from Eq. 4.5, and compared with results obtained from direct methods (e.g. interferometer, AFM), with the advantage of much larger sampled surface. The set-up of the diffractometer provide a single or double mono-chromator in high or low resolution configuration outbound the X-ray tube. This measurement configuration is highly affected by the size of the incident beam that does not allow to get information on the scattering angles smaller than the size of the beam itself. The scattering tails intensity allow us to calculate the PSD. The spatial wavelength range of the PSD given by these measures is limited by the beam size, for long spatial wavelengths, and by the instrument background for short spatial wavelengths. Reducing the size of the beam, we extend the range on the side of long wavelengths, but reduce it on the short ones side because the intensity decreases.

- In *high resolution XRS* (see Fig. 4.21) the sample is still set at a fixed angle θ_i, the set-up of the diffractometer provide two mono-chromator in high or low resolution set-up outbound the X-ray tube, and the detector, with a mono-chromator mounted between the sample, is fixed at the reflection angle $2\theta_i$. In this case the scan is provided by rocking the mono-chromator coupled with the detector. In this configuration, the distribution of scattering directions can be determined with high accuracy but the intensity of the measured beam is much weaker. The FWHM of the direct beam after diffraction and collimation plus the angular response of the analyzer is 5", this allows us to investigate also around small scattering angles, essentially those produced by long spatial wavelengths of the surface defects. The result is the PSF expected from the illuminated portion of the mirror tested accounting for geometry deformations

and scattering caused by the low-frequency roughness.

5 Multilayer characterization for the NHXM hard X-ray telescope

In this section is reported the X-ray characterization and analysis of multilayer samples for the NHXM project, that I performed with the BEDE-D1 X-ray diffractometer, the AFM and the LTP operated at INAF-OAB. The multilayers are deposited using the dedicated facility at MLT. The coating deposition technology of the multilayer onto mirror shells has been developed during the phase A of the SIMBOL-X X-ray telescope. Even if SIMBOL-X mission was cancelled in early 2009, almost all results achieved in the Phase A could be reused for carry on the development of the 4 optical modules of a New Hard X-ray Mission (NHXM) approved by ASI, with diameters and focal length reduced by a factor of 2 with respect to the SIMBOL-X case. Since the energy band and the incidence angles remain essentially unchanged, however, the multilayer recipes retain their validity and the development could be restarted from the endpoint of that phase. In this section, in particular, we show the completion of the development of W/Si multilayers and the first steps taken in the optimization of Pt/C multilayers deposition, a mandatory activity since only Pt/C multilayers can bring the NHXM optics reflectivity close to 80 keV. Unfortunately, the NHXM mission was not down selected by ESA, therefore the mission development has been suspended also by ASI. The achieved work have enabled a deep characterization and optimization of the multilayer deposition in terms of reflectivity performance, process repeatability, and stress.

5.1 Reflectivity and stress characterization of W/Si and Pt/C multilayer samples

The X-Ray Reflectivity (XRR) measurement and PPM analysis were described in sect 4.3.1. They enabled not only the direct measurement of reflectivity performances, but also to extract the characteristic parameters of the stack like thickness,

density values, roughness, by means of a very accurate fit of the reflectivity. The resulting feedback to the multilayer manufacturing allowed the tuning of the facility to deposit wideband multilayer coatings for focusing X-rays up to 50 keV that have been tested at the PANTER facility.

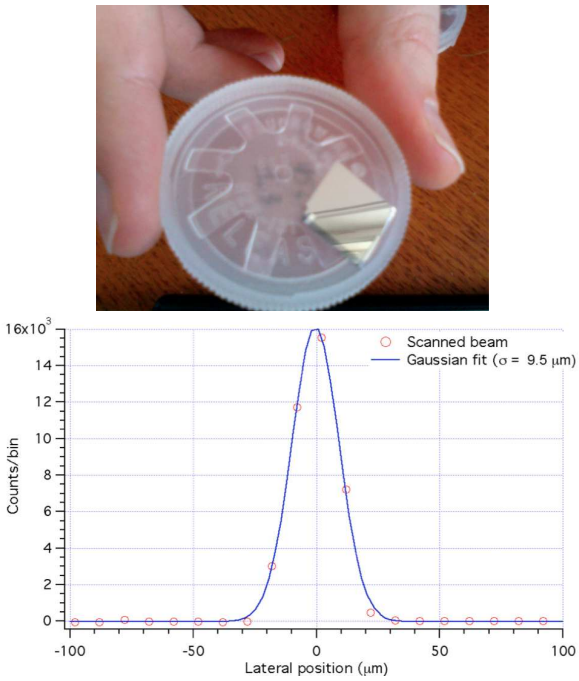

Figure 5.1: Left: a sample produced and measured in the test campaign for XRR measures. Right: the width of the X-ray beam in use to measure the XRR curve of the samples. The beam width is < 40 μm FWHM.

Most of characterization is performed in monochromatic setup at 8.045 keV (the Cu-Kα1 line), with a high angular resolution ($\sim$ 15 arcsec) useful to constrain the fit of the XRR. The beam width is < 40 μm (Fig. 5.1), which allows measurements onto small samples (13 mm) starting from glancing angles $>$ 500 arcsec. Some measurements will also be dealt in polychromatic setup. These are less useful to characterize in depth the multilayer stack, but they return a measurement of the optical performances in X-rays at 5 to 50 keV, so they can be directly compared with the results achieved at PANTER.

Stress measurements. For the profile measurements before and after the coating we have used the LTP operated at INAF/OAB. The instrument returns a 1D profile over long scan lengths with a lateral accuracy of 0.5 mm and a vertical accuracy that, depending on the scan length and the environmental noise, can reach a 30 m

P-V. The instrument records the local slope along the scan with respect to a fixed reference mirror, and derives the profile by integration a technique that makes the measurement almost insensitive to oscillations of the optical head. The substrates we used are Si wafers have a thickness τ = 0.525 mm, a 5 mm width and a length of 30 - 40 mm. The Young modulus of crystalline Si is E_s =170 GPa, and its Poisson ratio is ν = 0.25. The total film thickness, as well as its thickness ratio Γ, is derived from the XRR measurements. The stress is then obtained from the Stoney equation by measuring the radius of curvature.

For the correct measurement of stress, it is important to avoid introducing spurious deformations. Nevertheless, any way to support the sample will affect its shape, due to the extreme deformability of the thicknesses we are dealing with. It is not, indeed, the deformation itself that will change the measured stress value, since we are interested in comparing only the deformation introduced by the coating, but an uncontrolled change of the contact points with the reference plane. Were the samples laid onto a rigid plane, for example, the weight of the uncoated wafer would be distributed among a set of points, in general unknown. Even if we were able to put the coated sample at the same position on the table, the shape of the sample changes after coating, and so do the contact points. Therefore the deformation due to the fixtures of the sample would be different in the two cases in a nearly unpredictable manner.

A possible way to make the deformation repeatable before and after coating could be to make them float over a liquid surface, with a sufficient surface tightness to sustain them. In this case the pressure on the sample would be uniformly distributed, and the sample deformation would be repeatable. A shortcoming of this method is that it is not always recommendable to contaminate samples with liquids, if they are to be coated in high vacuum. A viable alternative would be to lay the samples onto an optical paper sheet, which expectedly exert a uniform pressure over all points of the Silicon wafer. Though less affordable than floating over a liquid, this method is clearly more convenient. In practice, however, the samples are so thin and lightweight that the lower surface does not goes into contact with the optical paper at all its surface. It has been thought to be more convenient to lay the Silicon sample onto a tight plastic sheet, which provides an even and smooth mattress, to which the wafer does not stick. Therefore, there remains a thin layer of air in between, which should provide a uniform and repeatable pressure. This is the method we adopted in these characterizations, and the parabolic shape of the profiles difference witnesses the uniformity of the exerted pressure.

Defined the film thickness t, the total stress σ_f for multilayers. The relation between the radius of curvature of the sample R induced by the stress, the elastic mod-

ule E, the poisson ratio ν, and the suress is given by the Stoney equation

$$\sigma = \frac{Et_s^2}{6(1-\nu)tR} \tag{5.1}$$

In my thesis work I have measured by XRR and analysed more than 500 samples and measured the stress of some of them. Only the most representative are reported here. The feedback provided to the deposition facility has enabled a real improvement of the process.

5.1.1 W/Si single-layer measurements

Some XRR measurements were performed onto single layers samples deposited with the same deposition facility to be used to perform multilayer depositions. This was mainly aimed at determining the density of multilayer materials, that in turn affect the reflectivity and - to a lesser extent - the peak position. In fact, the analyses of XRR curves always returned density values lower (by 10-15%) than the bulk ones. This is not surprising in principle, because several voids can remain in a thin film structure while it is grown. In particular, it is the W density that affects the reflectivity, which is proportional to the difference of the optical constants. In addition, it is known that density variations result in a small Bragg peak shift due to refraction. This is, indeed, also affected by the Γ factor of the stack; therefore a firm estimation of the layer density ought to be confirmed by measurements on single layers, which are reported in this section.

W single layers (HS8, HS14, HS20)

The HS8 sample is a single W layer deposited onto a Silicon Wafer. Fringes in the XRR scan (Fig. 5.2) can be clearly detected at grazing angles larger than the critical one of Tungsten. The spacing and the shape of fringes is thoroughly reproduced by the fitting model, that finds out a thickness value of 487 Å and a density value of ρ = 16.7 g/cm^3), which is much less than the bulk density of Tungsten (19.3 g/cm^3)). It should be noted, indeed, that the fitting model matching to the experiment is improved by accounting for a Si oxide layer on the substrate, 2 nm thick, and a W oxide atop the Tungsten layer of a 3.7 nm thickness, as expected. The layer roughness is close to 6 Å. The presence of Si substrate oxide is in general of negligible impact on multilayer samples, because the reflection in general occurs far from the substrate. The oxidization of the outermost layer, indeed, cannot be ignored also in that case, because it affects the depth of reflectance minima (see e.g. Sect. 5.1.2).

Similar results are achieved with the XRR scan of the HS20 sample, still a W layer but deposited onto a glass piece. Also in this case (Fig. 5.3) the fringes are fitted in detail by the model, and due to the adoption of glass as substrate we do not expect

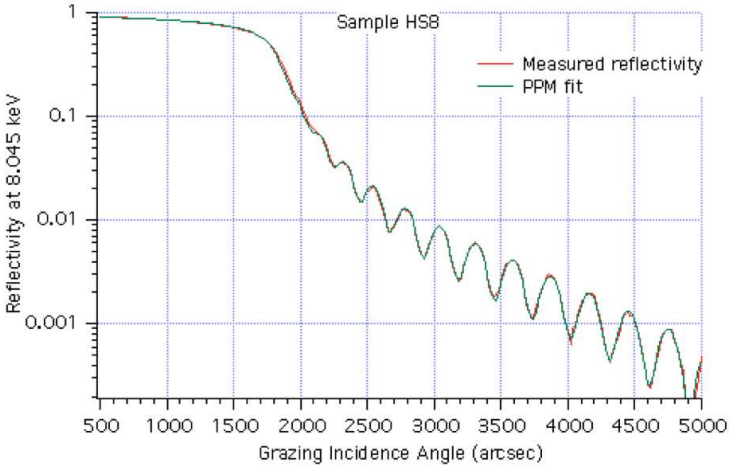

Figure 5.2: Results of the fitting procedure with PPM for the HS8_1_7 sample, a W layer deposited onto a Si wafer.

any substrate oxidization. In this case PPM inferred a thickness value of 450 Å, and a density value ($\rho = 18.2$ g/cm^3) higher than for the sample HS8, but still lower than the bulk density value of the Tungsten. A 1 nm thick, W oxide layer is clearly detected. The surface roughness is 5 - 6 Å, quite close to the one we expect from this kind of glass substrate (7 Å, non optically polished).

Si single layers (HS9, HS18)

Measurements onto Silicon layers are more difficult to perform, because they exhibits a smaller refractive index contrast with the substrate. In fact, the XRR of the HS9 sample (Fig. 5.4) shows very weak interference fringes, even though the PPM analysis returned an accurate XRR modelling.

The fit yielded a Si layer thickness of 554 Å and a Si layer density quite uncertain, but close to 2.5 g/cm^3, which is also close, if not even larger, than that of the crystalline Silicon (2.3 g/cm^3), even though the density contrast should not be computed from the density of Silicon but that of Si oxide (2 nm thick) onto which the Si layer comes into contact. The oxidization of Si layer seems to be almost negligible, at least over short timescales. The surface roughness of the Si layer approaches the value of 5 Å.

The HS18 sample was then obtained by depositing the Si layer onto a glass substrate (as it was done for the HS20 Tungsten sample) in order to enhance the fringes amplitude. In fact, the XRR curve exhibits much higher interference fringes (Fig.

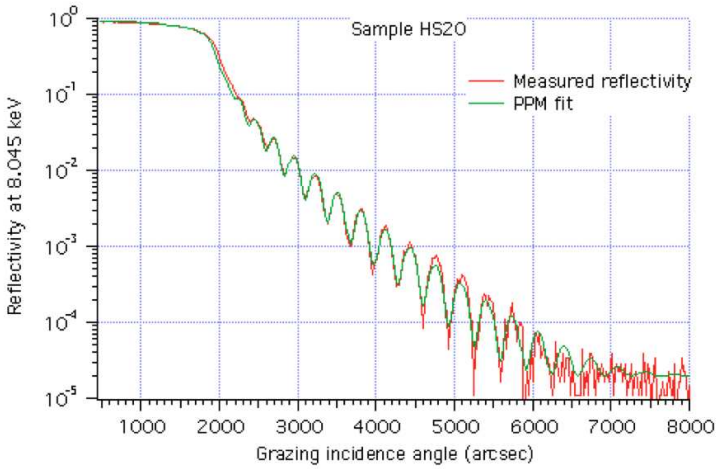

Figure 5.3: Results of the fitting procedure with PPM for the HS20_1_7 sample, a W layer deposited onto a glass substrate.

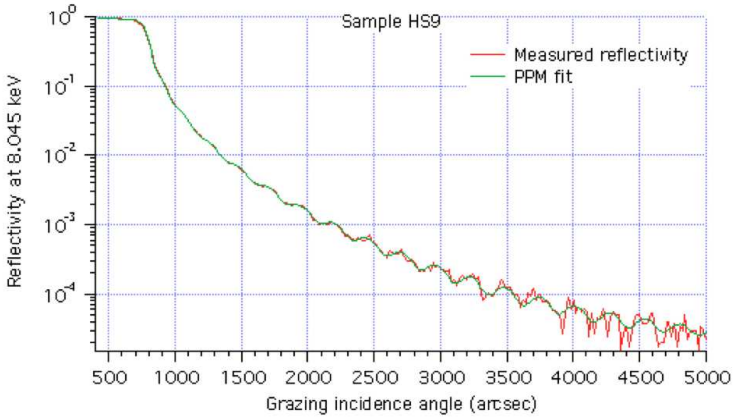

Figure 5.4: Results of the fitting procedure with PPM for the HS9_1_7 sample, a Si layer deposited onto a Si wafer.

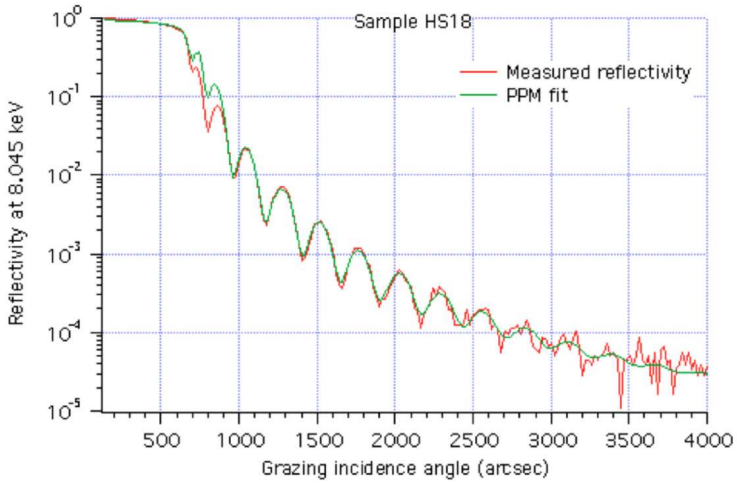

Figure 5.5: Results of the fitting procedure with PPM for the HS18_1_7 sample, a Si layer deposited onto a glass piece.

5.5) that could be fitted much more easily than for the HS9 sample, but at angles close to the critical one, where the PPM model overestimates the fringes height. The model returns a layer thickness of 546 Å and a Si layer density that can be more firmly estimated than for the sample deposited onto Si wafer: 1.7 g/cm^3, with a surface roughness of 7 Å rms. Still no evidence of a Si oxide atop the layer comes from the fit.

5.1.2 W/Si multilayer sample measurements

Several samples were deposited for every coating run, aimed at determining the coating uniformity along the optical axis. Samples are labelled as n. 1_1 to 1_13 going from the maximum to the minimum diameter of the shell. The central sample is the n. 1_7. Samples numbered 2_1 to 2_13, if present, are located at 180 deg azimuthal positions. In most of cases, indeed, we were not interested in the lateral uniformity but only in the improvement of process repeatability; therefore only the central sample was measured. In the following, all samples have to be intended to be the *_1_7 unless stated otherwise.

For all the periodic samples considered, the fitting strategy of XRR curves consisted of:

(I) a first run aimed at the determination of the average layer thickness. In this phase we assumed that both W and Si layer thickness is rigorously constant.

The density values are close to the ones we derived in Sect. 5.1.1. Nevertheless, in some cases the fit could not be reached unless the densities were not left free to vary. They then returned values sometimes different from those obtained in Sect. 5.1.1, but still lower than the bulk ones. Roughness values have been left free to drift within narrow limits;

(II) if necessary, a second run aimed at refining the fitting, leaving each single layer thickness value to vary around the values found in the previous structure, within a small interval (2 to 4 Å wide) that can be increased, if necessary, in a subsequent run. Linear drifts of thickness have never been detected to a significant extent, but in the case of HS2 and HS7 samples.

For a-periodic samples the first run adopts as free variables the a,b,c, power law parameters of each stack, for W and Si separately. The second phase is run only if the number of free variables is < 250, due to the software limits of the program.

HS1 sample (periodic, 30 bilayers)

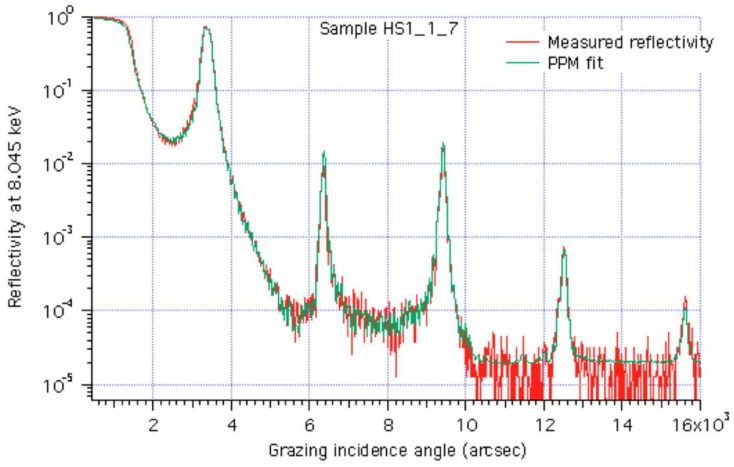

Figure 5.6: Results of the fitting procedure with PPM for the HS1_1_7 sample. Logarithmic scale. The model accurately fits the XRR scan. The steep decrease after the 1^{st} peak indicates - at first glance - that $\Gamma > 0.5$, i.e., the Tungsten layers are thicker than those of Silicon.

The XRR curve of the sample HS1 (see Fig. 5.6) shows the first 5 XRR peaks of the sample at the photon energy of 8.045 keV, superposed to the accurate fit achieved with the PPM program. The peak positions and heights fit the experimental curve with a d-spacing d = 51.1 Å and a ratio $\Gamma = 0.55$. The interfacial roughness/diffuseness

rms inferred from the fit is $\sigma \approx 3.5$Å, and the density of W matches the value 16.6 g/cm^3, while that of Si is less than 2.0 g/cm^3. The peaks are well defined and narrow, meaning a good regularity of the stack. Only a little broadening at higher orders can be observed, from which we derive a spread of thickness values less than 1 Å (3%) for W in the first 10 deposited layers. The irregularity of Si layers is almost undetectable. Finally, a Si oxide layer on the outermost Si layer (that serves as capping layer), of density close to 1 g/cm^3 and 1 nm thick can be detected as it improves the fit in minima. We can state that the W/Si deposition is an advanced state. This is partly due to the previous development achieved for the Simbol-X study.

HS2 sample (periodic, 30 bilayers)

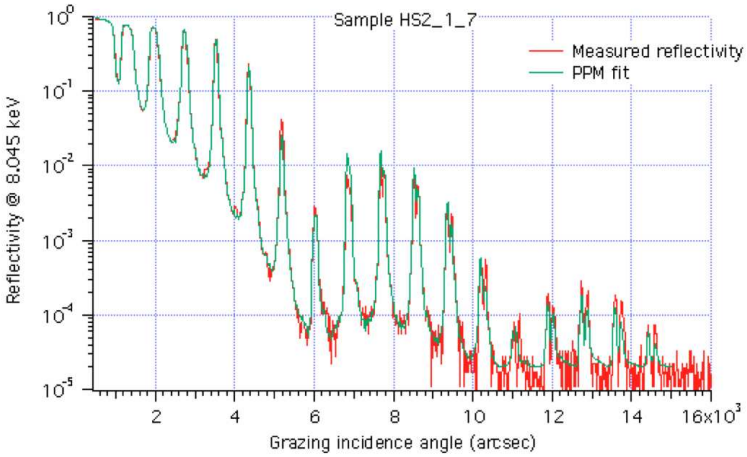

Figure 5.7: Results of the fitting procedure with PPM for the HS2_1_7 sample. Logarithmic scale. Notice the peak duplication at high orders.

Fig. 5.7 displays the XRR curve at 8.045 keV of the HS2_1_7 sample, superposed to the best fit reached with PPM. Up to 18 Bragg peaks could be detected, narrowly spaced. The high order peaks exhibit a clear trend to split into two, denoting a continuous drift of the layer thickness (Fig. 5.8): in fact, this is the one of the few samples (with the HS7, Sect. 5.1.2, to a lesser extent) for which a fitting stage with a linear drift was needed. The d-spacing of this multilayer is in general much larger than for the HS1 sample (Sect. 5.1.2): in fact, the fit returned an average thickness of W almost unchanged (28.7 Å), but a much thicker Si (153.7 Å, for layers close to the substrate), yielding d = 182.4 Å and a $\Gamma = 0.157$, always for deepest layers. The layer thickness drift is mainly due to the Si layers (a 7 Å increase throughout the stack, from substrate to surface). Also a small layer thickness fluctuation (up to $\pm$2Å) for

both W and Si can be inferred from the fit, superimposed to the systematic d-spacing variation. These short-period fluctuations can also be seen in Fig. 5.8. Other results out of the fit are: a) W density is still lower than the bulk value (18 g/cm^3), though not very much; b) the equivalent roughness rms derived from the fit is 3.8 Å, still very close to that of the Si wafer substrate; c) the fit show evidence of an outer Si oxide layer, 1 nm thick. So far, the deposition process yielded a very good interfaceroughness. Only some long-term drift of the deposition rate is observed.

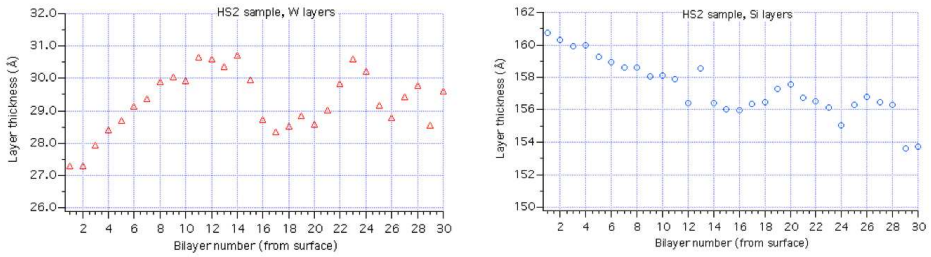

Figure 5.8: Stack structure of the HS2_ 1_ 7 sample, as resulting from the fit with PPM of the XRR scan.

HS3 sample (periodic, 30 bilayers)

The experimental XRR curve of this sample is reported in Fig. 5.9. With respect to the sample HS2 (Sect. 5.1.2) the peaks returned narrow and well defined, with a few irregularities. The fit obtained with PPM matches the measurement with a W thickness of 28.6 Å and a Si thickness of 40 Å. A layer thickness fluctuation at random with maximum amplitude of 1 Å is responsible for the smearing of secondary minima - as well as for the "step" just before the 3^{rd} Bragg peak (Fig. 5.9, arrow). Like for the previously analyzed samples, there is a little or no evidence for roughness growth, since the PPM model matches the experiment assuming a 3.4 Å roughness equivalent rms, very close to the 3 Å of the Si wafer substrate. A 1 nm thick Si oxide layer is, still, detected atop the stack. Moreover, evidence of a lightweight (ρ = 15.3 g/cm^3) W in this sample is inferred from fit. Variation of the Silicon layers density is more uncertain, as it could be due to a small misalignment of the sample with respect to the impinging X-ray beam. The lightweight W is a drawback, since it reduces the single interface reflectivity. After the calibration of the deposition rate via the periodic multilayers, the collected information was judged sufficient to start the deposition of graded ones.

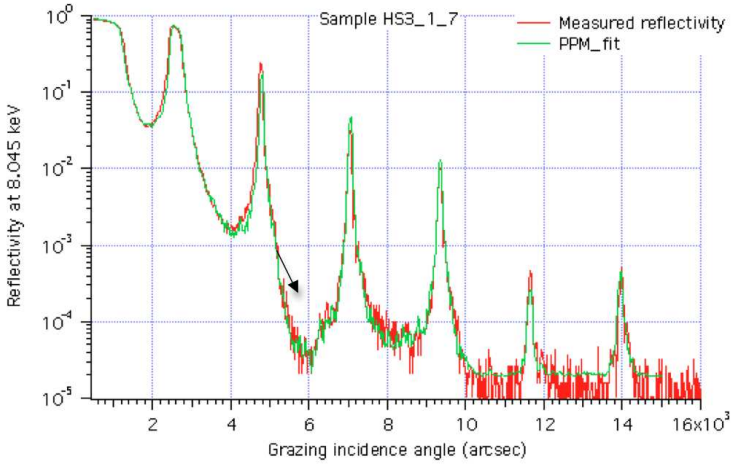

Figure 5.9: the XRR curve at 8.045 keV of the HS3_1_7 W/Si sample (log scale), superposed to the best fit obtained with PPM. Some layer irregularity is witnessed by the step at minima (arrow). The experimental curve is thoroughly fitted.

HS4 sample (periodic, 30 bilayers)

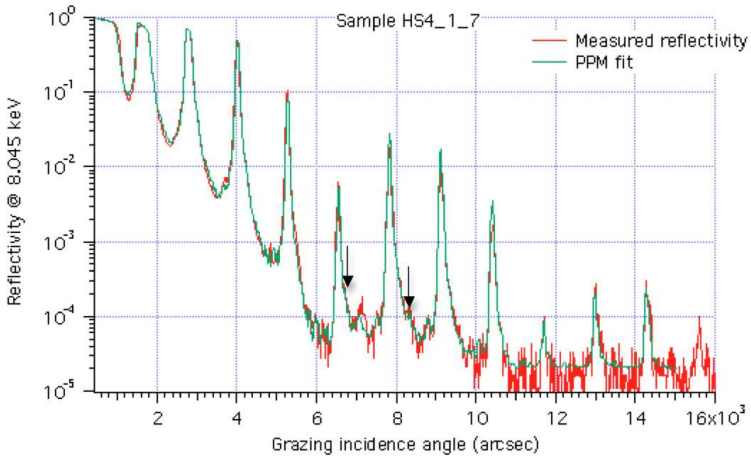

Figure 5.10: the XRR curve at 8.045 keV of the HS4_1_7 W/Si sample (log scale), superposed to a very accurate fit obtained with PPM. Arrows mark some irregularity in the XRR minima. Notice the clear modulation of peak heights.

The XRR scan of the HS4_ 1_ 7 (see Fig. 5.10) sample resembles the HS2_ 1_ 7 (Sect. 5.1.2), excepting for the double peaks, which are not observed; therefore we expect a little or no thickness drift throughout the stack. Rather, some aperiodicity in the minima of the XRR scan - also fitted by PPM quite thoroughly - and a slight asymmetry of high order peaks denote a layer thickness fluctuation for both W and Si, not larger than $\pm$2Å. The average thickness of W layers is 27.0 Å; the one of Si layers is 95.7 Å. The stack structure, as derived by PPM, is sketched in Fig. 5.11. Like in previous samples, we detect a small growth of interfacial roughness: the PPM model infers an equivalent ρ = 3.5 Å, due mostly to the Si wafer substrate. A 1 nm oxide layer is still present and clearly detected atop the stack. Regarding inferred density values (16.9 g/cm^3 for W, 1.9 g/cm^3 for Si), they are still lower than the respective bulk values. It should be noted that the apparent variation of Si density - unlike that of Tungsten - might be due to sample misalignments.

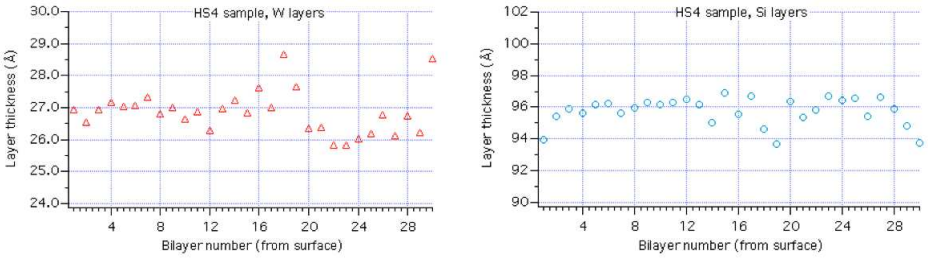

Figure 5.11: Stack structure of the HS4_ 1_ 7 sample, as resulting from the fit with PPM of the XRR scan. For sake of comparison with the HS2_ 7_ 7 sample (Fig. 5.8), the same ranges of y-axes have been adopted. No thickness drift is observed in Silicon layers.

HS6 sample (graded, 200 bilayers)

This wideband multilayer sample is a 200 bilayers one, structured according the well-known supermirror (power-law) model, d(j) = a/(b+j)c, with j =1,2,...200 going towards the substrate, and a, b, c, parameters with opportune values. The XRR scan is shown in Fig. 5.12, together with the best fit reached by PPM making use of the sole power-law modelization. The fit is satisfactory, but not perfect. An improvement of the fit performance would have required a further stage to allow the individual thickness to oscillate around the power law trends.

The supermirror parameters out of fit of the XRR scan in Fig. 5.12 are (between bracket the nominal recipe):

- for Tungsten: a = 57.9 (40.3) Å, b = 2.1 (0.9), c = 0.31 (0.27);

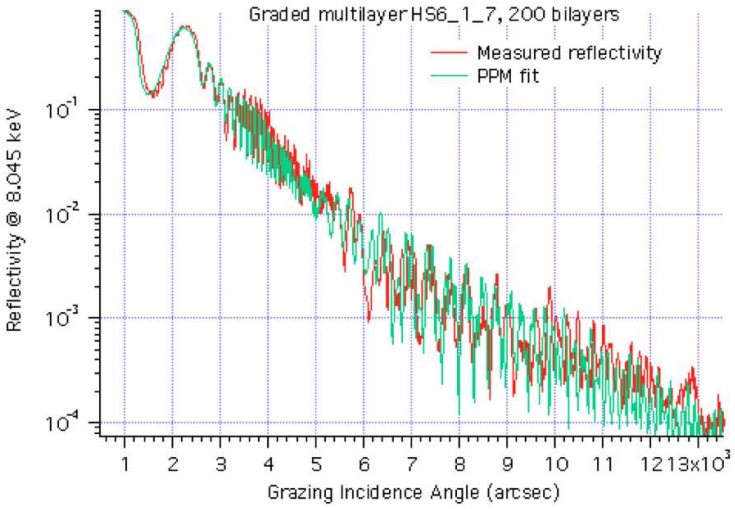

Figure 5.12: the XRR curve at 8.045 keV of the HS6_ 1_ 7 W/Si sample, superposed to the best fit obtained with PPM, adopting the a,b,c parameters of a power law as fit variables. The fit is imperfect because the individual layer thickness could not be left free to oscillate around the power law trends.

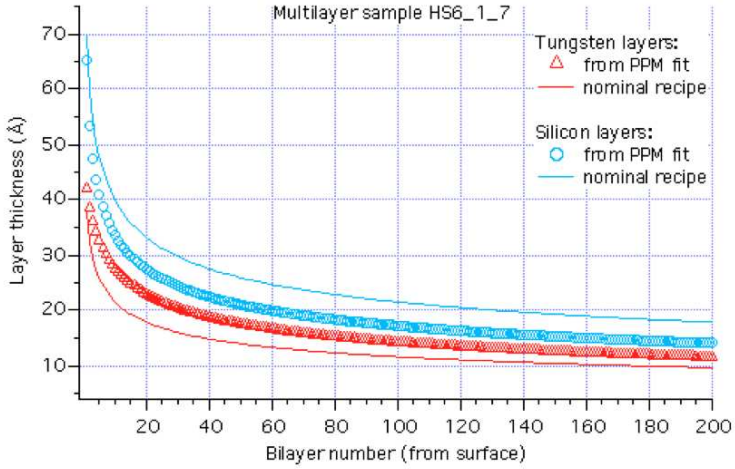

Figure 5.13: the multilayer structure of the HS6 sample out of the PPM fit (symbols) compared with the nominal recipe (lines).

- for Silicon: a = 65.4 (74.7) Å, b = 0.0 (0.9), c = 0.29 (0.27).

The resulting thickness trends, as computed from these parameter values, are displayed at Fig. 5.13. It can be seen that the actual thickness of W exceeds the nominal prescription, while the thickness distribution of Silicon remains underneath the nominal recipe. The d-spacing, as computed layer by layer, better approximates the nominal trend, even though it still underestimates the intended d-spacing trend. Other fit results are in line with those obtained from the previous samples: the density of W inferred from the fit is 16.2 g/cm^3 and that of Si is 1.6 g/cm^3 (although with a relevant uncertainty). The roughness rms that makes the model match the experiment is 3.5 Å, mostly inherited from the Si wafer substrate, as usual.

HS7 sample (periodic, 30 bilayers)

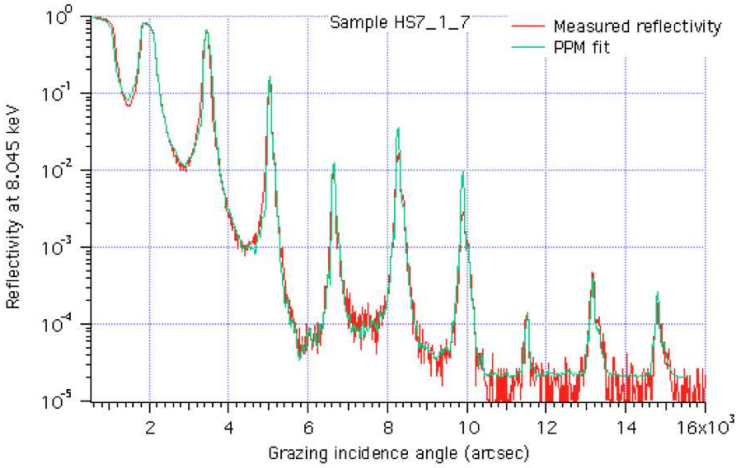

Figure 5.14: the XRR curve at 8.045 keV of the HS7_ 1_ 7 W/Si sample (log scale), superposed to the best fit obtained with PPM. The fit is accurate but atop the 5^{th} and 6^{th} peaks.

The HS7_ 1_ 7 multilayer sample is another periodic W/Si multilayer aimed at re-calibrating the deposition rate after the imperfect result of the HS6 (like the HS1, Sect. 5.1.2 and the HS3, Sect. 5.1.2). The experimental XRR curve at 8.045 keV is posted at Fig. 5.14. Also shown is the best fit found with PPM, which accurately fits every reflectance features (excepting the exact heights of the 5^{th} and 6^{th} peak). The fit returned an average W layer thickness of 27.3 Å and an average Si layer thickness of 69 Å. Like for the sample HS2 (Sect. 5.1.2), a continuous drift of the Si layer thickness can be detected, with a very slow (2 Å) decrease from the substrate outwards (Fig. 5.15). Such a drift is not detected in the W layers, that are affected

instead by a short-period oscillation of thickness with a maximum amplitude of 1 Å. Similar fluctuations also appear in the Si layers trend, superimposed to the linear drift. Like in previous samples, the density of W layers (17.3 g/cm^3) is smaller than its nominal value, and the interfacial roughness (σ = 3.5 Å) is very close to that of the substrate.

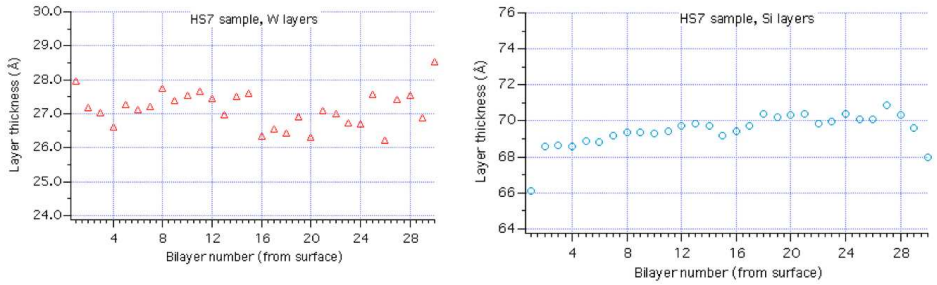

Figure 5.15: Stack structure of the HS7_ 1_ 7 sample, as resulting from the fit with PPM of the XRR scan.

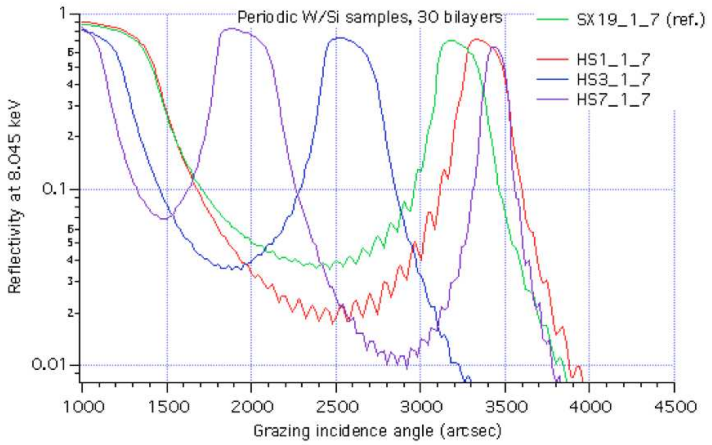

Figure 5.16: a comparison of the first Bragg peaks of the HS1, HS3, HS7 samples (for the HS7 also the 2^{nd} peak is visible).

Finally, in Fig. 5.16 we plot the comparison among a detail of the XRR curves of some calibration samples analyzed so far, together with the XRR expected from multilayer structure to be repeated in the runs mentioned in Fig. 5.15. It can be

seen that both HS3 and HS7 are quite distant from the intended recipe in terms of d-spacing (HS7 has a d-spacing that is almost twice as large). The HS1 sample (as anticipated in Sect. 5.1.2), instead, approximates much better the recipe (d = 51.1 Å Vs. 52.5 Å intended, and Γ = 0.55 Vs. 0.54 Å intended). However, it should be noticed that the HS7 has a deeper minimum before the 1^{st} Bragg peak. Since the density and roughness values inferred are similar for the two samples, the only possibility is that the HS series has a thicker oxide layer atop the stack. With respect to the reference multilayer (SX19).

HS10 sample (periodic, 60 bilayers)

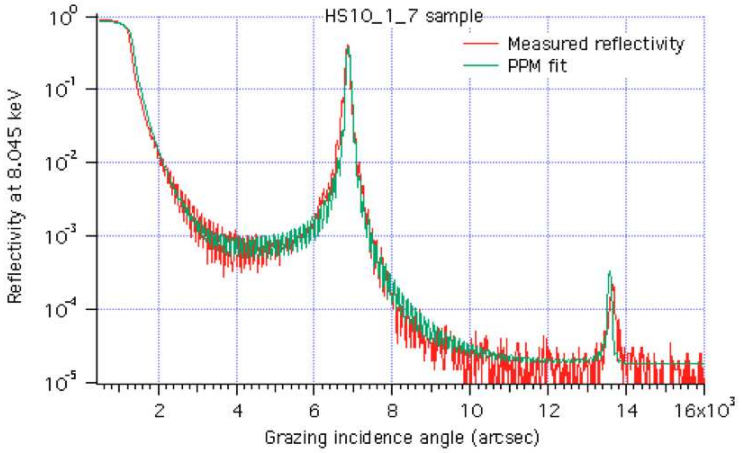

Figure 5.17: the XRR curve at 8.045 keV of the HS10_1_7 W/Si sample (log scale), superposed to the best fit obtained with PPM, using a simple model of periodic multilayer. Notice the presence of dense and regularly spaced Kiessig fringes in the minimum before the 1^{st} Bragg peak, a clue of a good stack periodicity.

This multilayer sample is the first of a set of 60 bilayers calibration samples, i.e. the removal of part of the last deposited layer when atoms of the subsequent layer impact onto it, aimed at checking the re-sputtering of the deposited film. With respect to the HS series presented in the previous pages, this kind of samples have a much thinner d-spacing. The experimental XRR curve of the HS10 sample and the respective PPM fit is displayed in Fig. 5.17 because only 2 Bragg peaks were detected, and since the measurement was essentially aimed at the absolute determination of the layer thickness, the adopted model is simply a periodic multilayer with 60 couples of layers, without allowing for thickness fluctuations throughout the stack. It can be seen from the figure that even such a simple model reproduces the measurement

quite accurately. The fit returned the following thickness values: 10.5 Å for W, and 13 Å for Si. The outermost Si layer is completely oxidized. The multilayer interfacial roughness is close to 4 Å. Also for this sample we found that the density of deposited Tungsten (17.3 g/cm^3) is sensitively lower than its natural value, in line with the results obtained with previous samples. This deposition run allowed us to stabilize the layer rate, obtaining multilayer close to the desire recipe.

HS23 samples (graded, 200 bilayers)

This set of samples is obtained by depositing a 200 bilayer W/Si multilayer stack. The different samples HS23_ 1, HS23_ 7, HS23_ 13 are located at the parabolic end, the intersection plane, and the hyperbolic end respectively. The XRR scan of the HS23_ 7 sample at 8.045 keV is reported in Fig. 5.23. Also plotted is the best fit reached with PPM, adopting a single power-law model superposed to oscillations grouped in blocks of 10 layers: in spite of the simplicity of the model adopted, it can be seen that the fit performed very well, even if not all details are reproduced. The power law parameters are: a = 54.55 Å, b = -0.612, c = 0.213 for the Si; a = 32.9 Å, b = 2.19, c = 0.248 for the W. Fluctuations do not exceed 2-3 Å.

Other findings from the fit are: the density of Tungsten is 18.5 g/cm^3 and that of Silicon 2.2 g/cm^3, while the interfacial roughness that is inferred from fit is 3.5 Å, very close to that of the substrate. The HS23_ 7 sample has been also used for a cleaning test: it has been cleaned with a acetone- soaked optical paper to check the endurance of the coating to possible cleaning steps (i.e. absence of corrosion or roughness degradation). The sample has been subsequently measured (see Fig. 5.19) at 8.045 keV. No apparent change in reflectivity is visible, meaning that the multilayer stack has remained unchanged after the cleaning. The small angular shift visible in the comparison of the two curves before and after the cleaning is of a few tenths arcsec and it can be related to a difference in the sample alignment.

Finally, in Fig. 5.20 we can see the comparison of the three measured XRR curves for the three samples. We note that the 3 curves apparently resemble each other, even if the primary peaks of the samples 1 and 13 are located at smaller angles than the sample 7. In other words, the samples located at the two sides have thicker layers than that of the sample 7, but the difference is of 4% for the HS23_ 13 sample and 8% for the HS23_ 1 sample. An excellent lateral uniformity.

Finally, in Fig. 5.21 we plot the XRR curve measured in energy-dispersive setup of the sample HS23_ 7, after being cleaned, at the incidence angle of 0.21 deg (i.e. the nominal reflection angle of the shell on which the multilayer will be deposited). Also plotted is the reflectivity expected from the multilayer parameters (without accounting for layer fluctuations) derived from the PPM fit. We note that the reflectivity matches a 4 Å roughness rms up to 50 keV, very close to the value found by PPM at 8.045 keV.

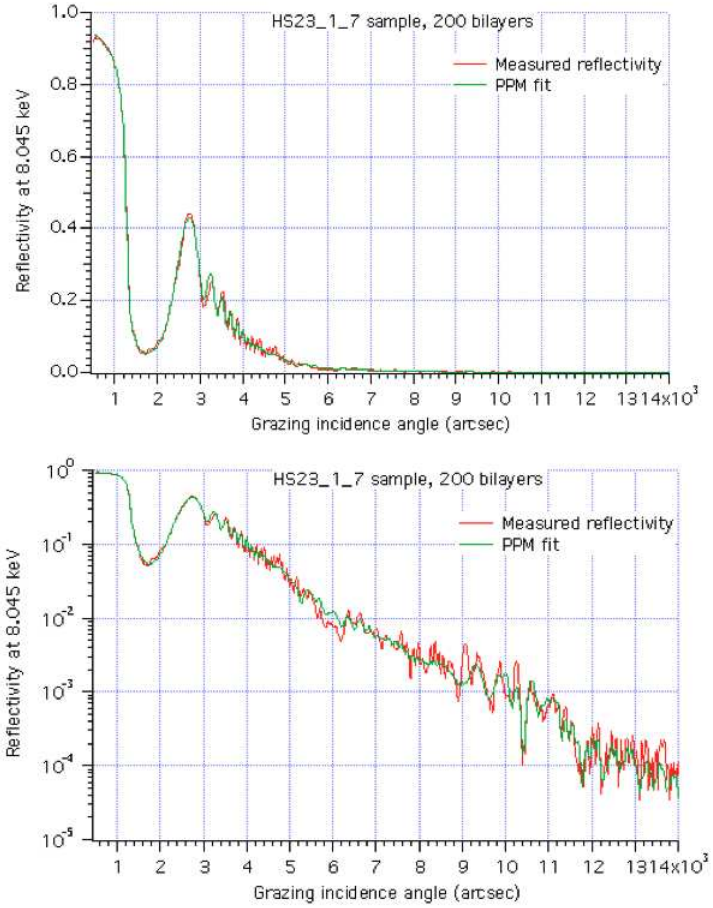

Figure 5.18: the XRR curve at 8.045 keV of the HS23_ 1_ 7 W/Si sample, superposed to the best fit obtained with PPM. (top) linear scale, (bottom) logarithmic scale.

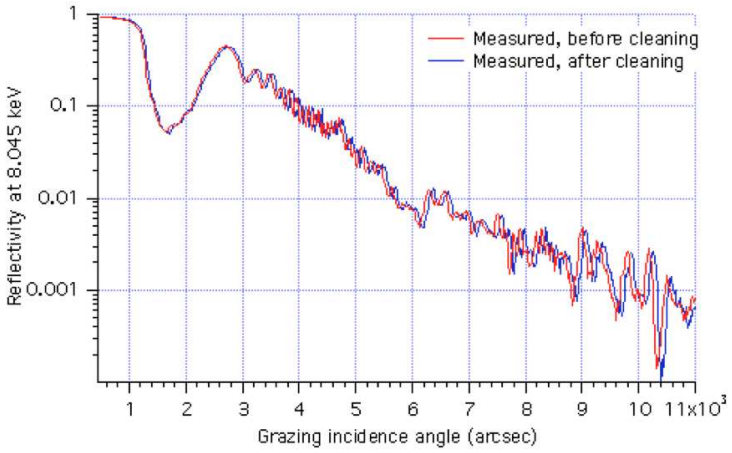

Figure 5.19: cleaning test of the HS23_1_7 sample. No significant variation the reflectivity curve is visible, meaning that the film has entirely withstood the cleaning process.

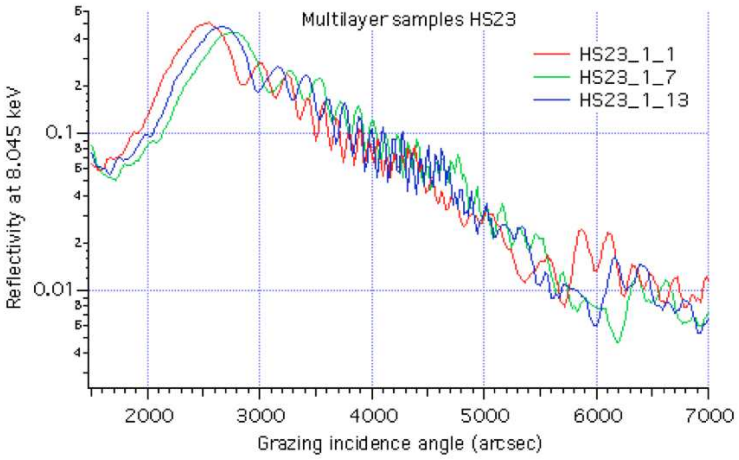

Figure 5.20: comparison of the XRR curves of the HS23_1_7, HS23_1_1, and HS23_1_13 samples.

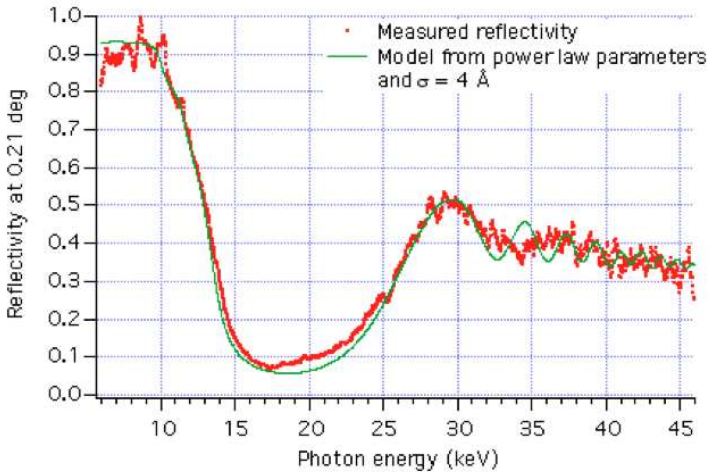

Figure 5.21: XRR measurement of the HS23_1_7 sample in energy-dispersive setup, after sample cleaning.

The stress measurement performed onto the graded multilayer deposited in the HS23 run is shown in Fig. 5.22. The profile of the Silicon wafer (named S1) before coating has been reported in green. The profile after coating, always taken with the LTP, is also plotted in red. The difference of the two profiles (blue) is the net curvature induced by the multilayer stress. The net curvature is concave downwards, because the stress is compressive, i.e., it tends to expand the substrate. In other words, when this multilayer is applied to a Wolter-I mirror shell, it will cause a slight enlargement of the diameter of the mirror, which will result, multiplied by the f-number of the mirror, in a focal length increase. This is what we actually observed in absolute focal length measurements at PANTER (see sect. 9).

The difference of the two profiles is almost perfectly parabolic, which means, as expected, that the stress is uniform. Only in correspondence of the minimum there is a deviation, probably due to a difficult data acquisition because the sample was heavily deformed in transverse direction. The total deformation is 4 μm over a scan length of almost 40 mm, while the measurement error (estimated along with a stability scan) is less than 20 nm, peak to valley. The parabolic fit of the profiles difference returns a curvature radius of 45.179 m. The total thickness of Silicon is 0.445 μm, the total thickness of Tungsten is 0.177 μm, and therefore the Stoney formula yields a stress measurement of -370 MPa (see sect. 5.1).

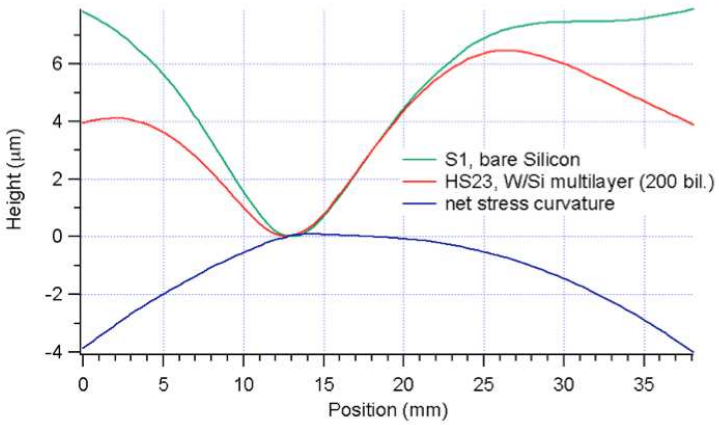

Figure 5.22: stress measurement on the S1- HS23 sample. The difference of the two profiles is almost parabolic, excepting the minimum point, where the profile is affected by a relevant transverse component.

HS26 sample (graded, 95 bilayers)

This W/Si multilayer consists of a double power law stacks of the kind $d(j) = (a + j)^{-c}$, j =1,2... the outer stack has 20 thicker bilayers, the deepest stack 75. The reflectivity curve of the witness sample (HS26) of the MS286/4 is displayed in Fig. 5.23, and the parameter values, a, b, c, obtained from the XRR curve fit are reported in Tab. 5.1. This sample is also the witness sample for the deposition of the multilayer onto the TDM1.

	Supermirror parameters for Si	Supermirror parameters for W
1^{st} PL (20 bilayers):	a = 54.6 Å, b = -0.89, c = 0.37	a = 52.4 Å, b = -0.32, c = 0.298
2^{nd} PL (75 bilayers)	a = 56.5 Å, b = 46.5, c = 0.28	a = 20.9 Å, b = 0.19, c = 0.24

Table 5.1: Power law multilayer structure, as derived from the XRR fit of the HS26 sample (Fig. 5.23).

We note that the fit reached with PPM is able to accurately reproduce all reflectance features, even though the model exhibits a superimposed modulation at 4000 - 6000 arcsec incidence angle, that is not observed in the experimental XRR curve. This cannot be explained by a random fluctuation of thickness throughout the stack, since this was already included in the fitting model and returned a maximum deviation from the power laws trend of only $\pm$ 2 Å. Also a degradation of the beam collimation seems unlikely. Rather, this mismatch can be explained by supposing that the d-spacing

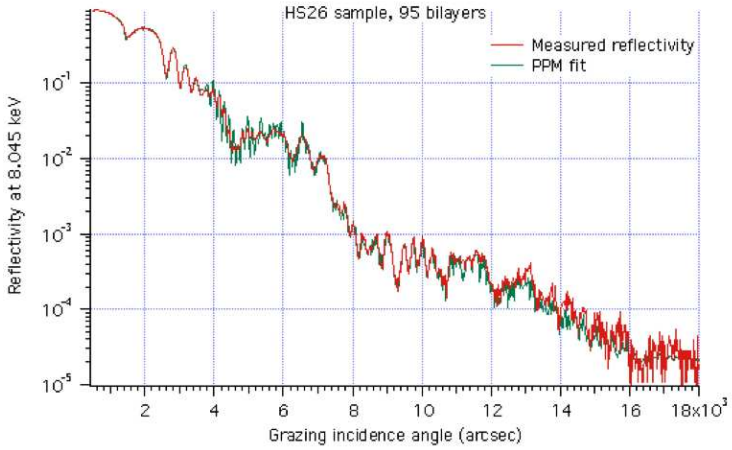

Figure 5.23: the XRR curve at 8.045 keV of the HS26_1_7 W/Si sample (log scale), superposed to the best fit obtained with PPM. Notice how the model exhibits oscillations that are not observed in the measurement, probably due to a pronounced lateral gradient of thickness that smoothes out such fine reflectance features.

varies from point to point of the sample because it was located at the edge of the W and Si targets, where the deposition rate expectedly drops off, to leave room for the shell MS286 coated in the same run. A simple computation shows that a lateral thickness variation of 1% over the sampled area with the X-ray beam (a few mm^2) is sufficient to explain such a smoothing of reflectance peaks. This hypothesis is supported by the inspection of XRR experimental curve of a similar multilayer previously deposited, placed in front of the target and not at its edge, that does exhibit similar short-period fringes. Comparison of the thickness trend obtained from parameters in Tab. 5.1 with the nominal recipe shows that the W layers match very well the nominal recipe, whereas the Si layers are thinner by a 30% wrt. the nominal prescription (Fig. 5.24). The model matches well an equivalent roughness/interdiffusion of 3.5 Å, very similar to the one of the Silicon wafer substrate (3 Å), and density values lower than the nominal ones (17.7 g/cm^3 Vs. 19.3 for W, 1.8 g/cm^3 Vs. 2.3 for Si). The measurement outcome, and in particular the density values and the roughness rms, is confirmed by an independent measurement at 5 to 50 keV at the incidence angle of 0.222 deg (Fig. 5.25).

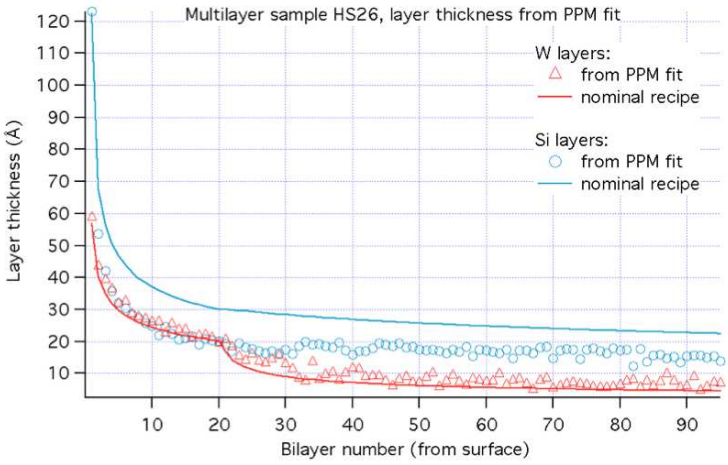

Figure 5.24: multilayer structure on the witness sample HS26. The W layers are in excellent accord with the nominal recipe, whilst the Si layers underestimate the intended trend.

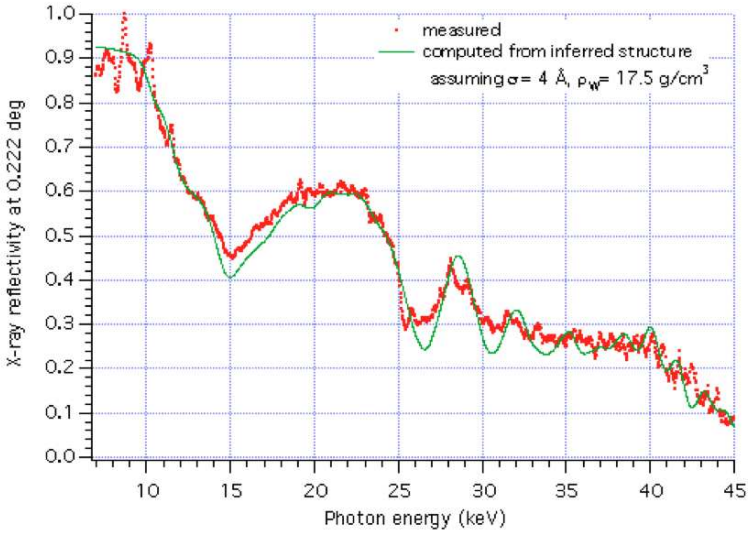

Figure 5.25: XRR measurement of the HS26 sample in energy-dispersive setup at 0.22 deg grazing incidence.

HS76 sample (graded, 95 bilayers)

These samples have been deposited to calibrate the multilayer deposition of the MS297/9 of the TDM2, after a long time dedicated to the deposition of Pt/C multilayers using the same deposition facility (see next sections). A sample XRR scan with the best fit is displayed in Fig. 5.23, top. The fit results are summarized in Tab. 5.2. We also performed some reflectivity measurement in energy- dispersive setup (5-40 keV, Fig. 5.23, bottom), at the incidence angles of the parabola and the hyperbola of the MS297 at PANTER. We note that the multilayer roughness inferred from the fit is very close to that of the Silicon wafer substrate, for both measures at 8.045 and 5-40 keV. The inferred W density is 17.3 g/cm^3, the Si density is 1.6 g/cm^3, in line with previous coating runs. However, the Si layers are much thinner than the nominal recipe: the recipe replicates almost exactly the HS26 run. The deposition is uniform within 6%, as it can be seen from the dispersion of Bragg peaks (Fig. 5.23).

	W outer stack a (Å), b, c	**W inner stack a (Å), b, c**	**Si outer stack a (Å), b, c**	**Si inner stack a (Å), b, c**	**R. (Å)**
w1	40.1, 0.12, 0.59	11.7, 0.48, 0.11	45.1, 0.76, 0.36	48.9, 35.8, 0.40	4.0
1	56.5, -0.34, 0.36	18.6, 0.13, 0.31	57.8, -0.85, 0.36	60.2, 44.5, 0.23	3.2
2	52.2, -0.48, 0.31	20.8, 0.23, 0.22	57.3, -0.88, 0.38	56.6, 47.4, 0.27	3.5
3	53.6, -0.28, 0.29	22.3, 0.22, 0.25	55.3, -0.92, 0.34	62.6, 46.5, 0.27	3.4
4	53.5, -0.37, 0.28	22.0, 0.49, 0.22	58.8, -0.89, 0.35	59.7, 35.3, 0.28	3.3
5	50.2, -0.45. 0.29	17.9, 0.46, 0.27	53.1, -0.91, 0.36	59.9, 43.8, 0.27	3.5
6	52.3, -0.47, 0.3	20.3, 0.46, 0.26	54.6, -0.87, 0.36	58.1, 39.7, 0.25	3.4
w2	40.5, 0.14, 0.57	13.0, 0.47, 0.12	45.1, 0.98, 0.35	45.1, 37.0, 0.42	3.9

Table 5.2: Stack parameters of the W/Si samples of the HS76 series. W1 and W2 are the sample so called *witness*, they are posed outside the shell in order to allow us charactering the deposition whenever we cannot measuring directly the shell.

A higher roughness and a larger amount of thickness fluctuation had to be admitted for the witness samples (Fig. 5.27) in order to explain the absence of reflectivity oscillations, which are probably averaged out by a lateral thickness gradient. This was already observed with previous samples, but in this case the effect is so relevant, i.e., the deposition rate drops so quickly just outside he targets/shell length that the two witness samples are not reliable to represent the stack structure. This is confirmed by the low values of the 'a' parameter (Tab. 5.2) of both W and Si for the two samples.

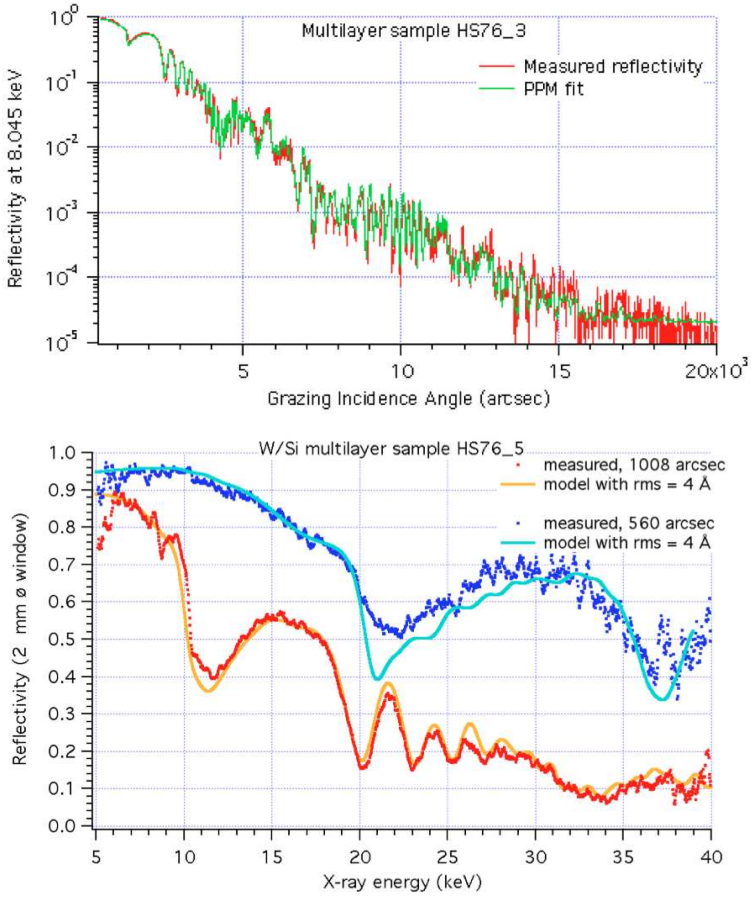

Figure 5.26: Top: the XRR curve at 8.045 keV of the HS76_3 W/Si sample, superposed to the best fit obtained with PPM. Bottom: the measured reflectivity at 5 -50 keV of the HS76_5 sample at the incidence angles of the shell at PANTER, superposed to the reflectivity expected from the modelization at 8.045 keV.

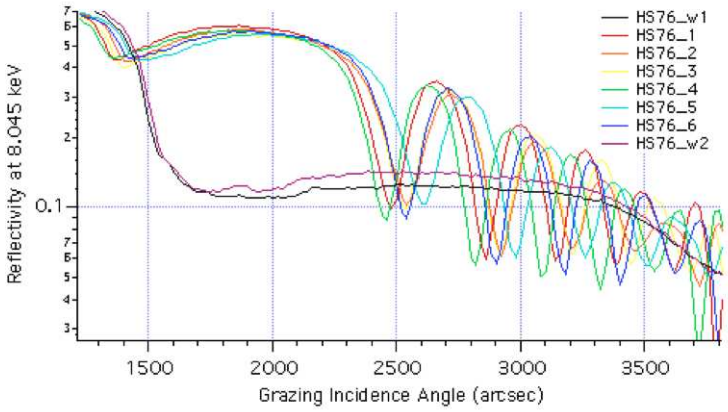

Figure 5.27: the XRR scans of the HS76 series (detail). The lateral uniformity can be derived from the peak dispersion over the angular scale.

5.1.3 Pt and C single layer measurements

In this section we describe the outcome of the tests performed onto Pt and C single layers. This allows a preliminary characterization of the film properties, like its density, and a calibration of film thickness as a function of the deposition parameters. The results obtained provide useful findings to start the deposition of Pt/C multilayers. Not shown hereby is the presence of a few nm thick oxide with uncertain composition. This does not affect, indeed, the thickness measurement, but only the roughness to a small extent. The dispersion in layer density could be ascribed to some uncertainty in the initial sample alignment due to some loose screws in the sample holder - a problem discovered and fixed from the next section on. A picture of a Carbon and a Platinum layer sample is shown in Fig. 5.28. The Carbon sample is brownish, whilst Platinum exhibits a bright, silvery colour.

C single layers

The measured density is consistent with the known value, and that the roughness, though uncertain, is sometimes larger than that of the Si substrate, due to the thickness of these layers, much larger than the one used for multilayers. The nominal density value we hereafter refer to is the one of amorphous carbon (2.1 g/cm^3). It should be pointed out that the density of Carbon could be also much lower, down to 1.8 g/cm^3 or even less (see Fig. 5.29 left panel).

Figure 5.28: a picture of a Carbon (left) and Platinum (right) single layer samples, deposited onto pieces of Silicon wafer.

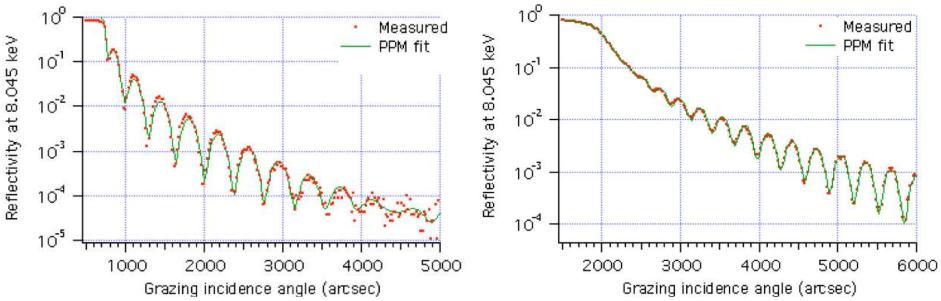

Figure 5.29: Left: reflectivity of HS32 sample with Carbon single layer. Right: reflectivity of HS37 sample with Platinum single layer. Both fitted with PPM.

Pt single layers

The PPM fits returned the thickness, density, and roughness of these coatings. We note that the density of Platinum is always close to its nominal value (21.1 g/cm^3) within a few percent (see Fig. 5.29 right panel), although with some uncertainty due to some alignment errors (but for the HS59), still due to loose screws in the goniometer, which have been tightened later. We recall that this was not the case with Tungsten (see previous sections). Like for Carbon, the high surface roughness is probably related to the unusual large thickness of these layers, even though the presence of a surface oxide layer makes the roughness estimation quite uncertain. The thickness measurement, indeed, is not affected by such uncertainty.

5.1.4 Pt/C multilayer characterizations

In this section we show the results obtained with Pt/C multilayers. The first deposited stacks are periodic in order to test the source calibration, the deposition repeatability, and the rate stability. The final point of the deposition runs in this development phase is the production in a reliable and stable way of graded Pt/C multilayers. In particular, the nominal recipe (not optimized yet, but with good reflectivity properties) to be obtained in this phase is a power law

$$d_k = \frac{a}{(b+k)^c} \tag{5.2}$$

where k =1,2,... 200, from *the outer surface toward the substrate*. The outermost layer is *Carbon*. The power-law parameters a, b, and c, take on the values:

- Platinum layers: a = 32.5 Å, b = -0.9432, c = 0.223: max thick. 61.6 Å, min thick. 10.0 Å

- Carbon layers: a = 44.9 Å, b = -0.9432, c = 0.223: max thick. 85.0 Å, min thick. 13.8 Å.

As can be seen, the stack has a constant factor $\Gamma = 0.42$. Before this series of measurements, some motors of the BEDE-D1 goniometer stage have been recognized as malfunctioning and replaced. Also, some screws were loose and have been tightened. This may have affected some measurements in the previous section (i.e. single Pt and C layers) by introducing some spread in the measured density values, which should have been compensated by the angular offset correction in the PPM fit. The thickness estimates are unaffected. The calibration measurements listed hereafter are characterized by a better repeatability of the measure.

HS46 samples (periodic, 60 bilayers)

This series of samples, the first one delivered for XRR analysis to INAF/OAB, exhibits very good optical properties. Four samples were measured at the same coordinate along the axis but different distance from the targets. All XRR peaks (Fig. 5.30) are narrow and well defined.

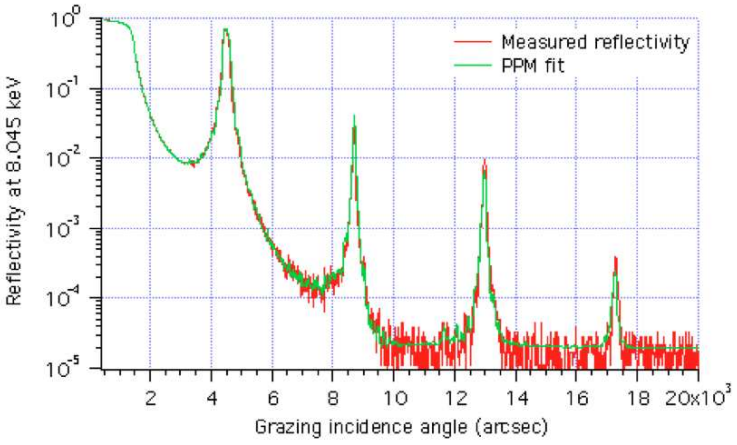

Figure 5.30: XRR scan of the sample Pt/C HS46_1_1, superposed to the best fit reached with PPM.

Secondary maxima are not detected very clearly, but this is probably due to their close spacing (a 50 arcsec interfringe), that becomes comparable to the angular resolution of the measurement. Some little irregularity in minima allows, indeed, putting an upper limit to the layer thickness instability, which is < 1 Å. For all samples, the layer density inferred - (21.2 ± 0.2) g/cm^3 for Pt and (2.2 ± 0.1) g/cm^3 for C - is very close to the respective nominal values: 21.1 g/cm^3 and 2.1 g/cm^3 (amorphous Carbon) respectively. This is an important aspect because the interfacial reflectivity, and consequently the multilayer performance, gets increased when the density contrast is large. Also, the inferred roughness rms (3.1 Å) is still very close to that of the substrate (3.0 Å). This seems to indicate that the multilayer deposition process does not seem to cause a significant surface roughening. Finally, the thickness of surfacial oxide is only of a few angstroms. The XRR comparison of all the samples (Fig. 5.31) exhibits a relevant d-spacing variation, linearly varying with the different target-substrate distance. The layer thickness values, as inferred from the fit, are listed in Tab. 5.3.

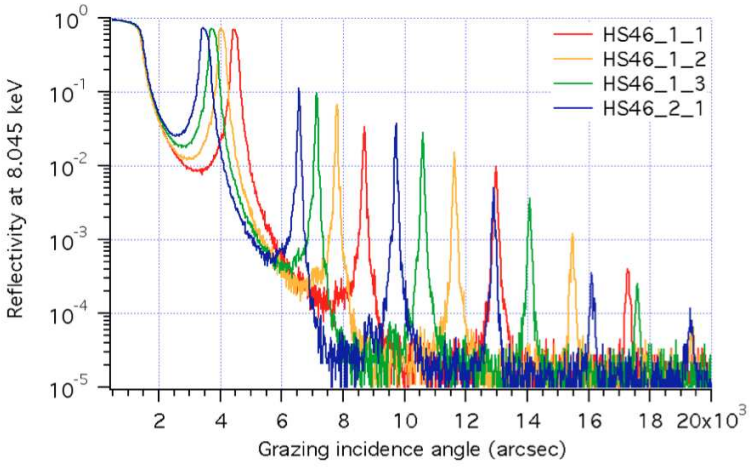

Figure 5.31: XRR scan of the sample Pt/C HS46_ 1_ 1, superposed to the best fit reached with PPM.

Sample	Pt thickness (Å)	C thickness (Å)
HS46_ 1-1	16.0	21.0
HS46_ 1-2	18.2	23.4
HS46_ 1-3	19.4	26.1
HS46_ 2-1	21.8	27.9

Table 5.3: thickness parameters of the Pt/C samples of the HS46 series.

HS60 samples (graded, 15 bilayers)

This deposition is aimed at simulating the capability to deposit the thicker layers of the graded Pt/C recipe, Fig. 5.32 shows the XRR scan of the HS60_ 1_ 1, superposed to the best fit found. Note that the peaks are sharp, but a slight broadening is visible from the 3^{rd} peak on: the layer thickness was therefore refined by allowing the layers to fluctuate around the average thickness values, with resulting deviations not larger than 2 Å. Fig. 5.33 recapitulates the XRR scans of the sample set. The average thickness values of the samples of this series are listed in Tab. 5.4, while the multilayer roughness inferred from the fit is 4.2 Å, not far from the substrate's but sensitively larger. The density values are 20.4 g/cm^3 for Platinum, 2.0 g/cm^3 for Carbon.

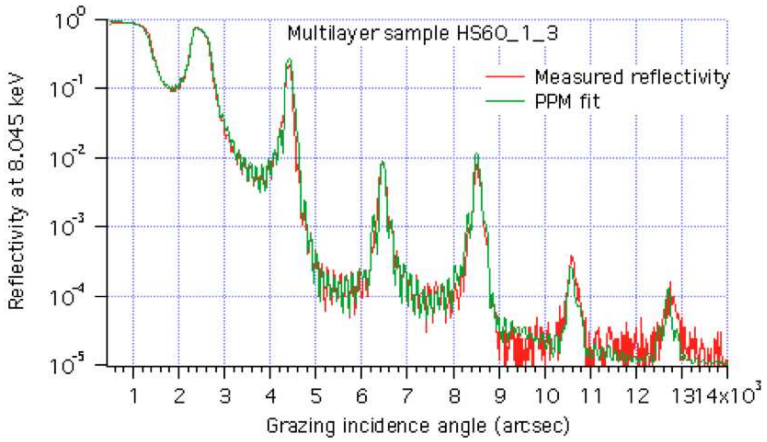

Figure 5.32: the XRR scan of the HS60_ 1_ 3 sample, superposed to the best fit found with PPM.

Sample	Pt thickness (Å)	C thickness (Å)
HS60_ w1	26.8	36.9
HS60_ 1-1	29.7	41.0
HS60_ 1-2	30.5	41.3
HS60_ 1-3	29.1	46.4
HS60_ w2	28.6	39.8

Table 5.4: average thickness parameters of the Pt/C samples of the HS60 series.

Additionally, we have also performed some direct roughness measurements with the AFM at INAF/OAB on the HS60_ 2_ 3 sample (Fig. 5.34). The 10 x 10 μm scan

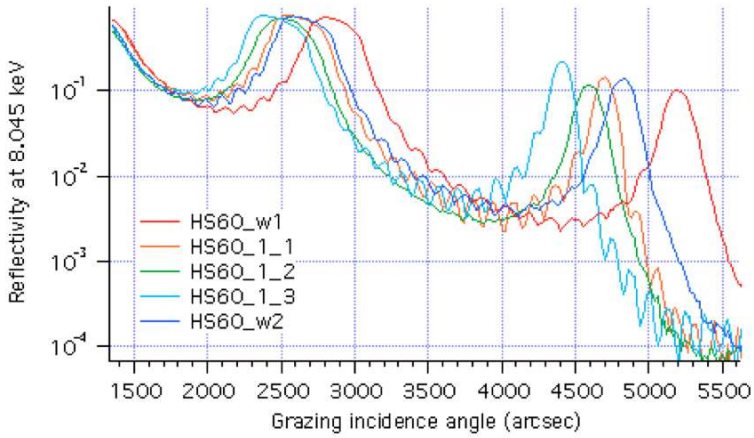

Figure 5.33: the XRR scan of the HS60_1_3 sample, superposed to the best fit found with PPM.

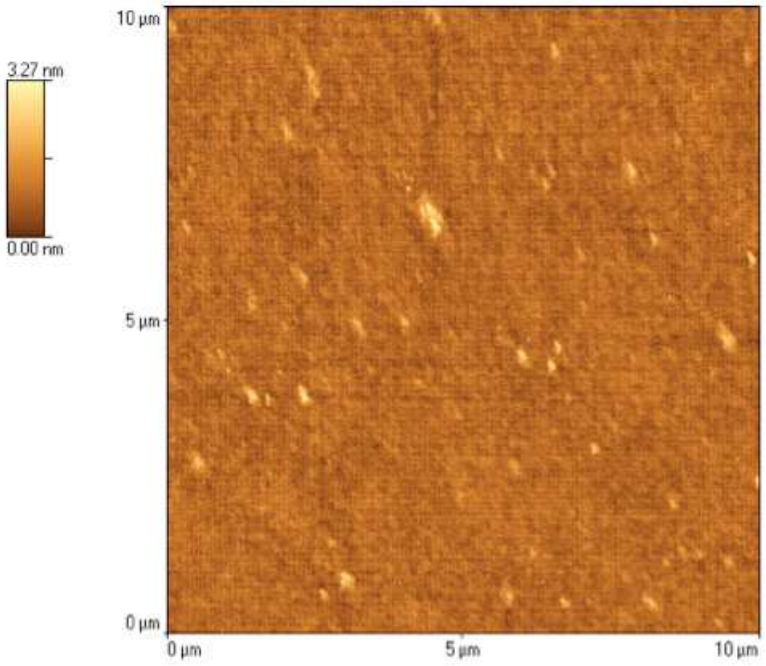

Figure 5.34: two 10 x 10 μm AFM scan of the HS60_2_3. The rms is 3 Å, in substantial agreement with the surfacial value inferred from the XRR.

shows a quite smooth topography, with a minority of point-like defects, probably contaminations. The underlying surface relief exhibits a 3 Å rms, essentially the same as the Si wafer substrate and in substantial agreement with the roughness inferred from the XRR scans.

HS61 samples (graded, 200 bilayers)

After the calibration achieved with the previous periodic multilayers, this is a rehearsal of the 200 bilayers recipe. The reflectivity at 8.045 keV, as measured from 500 to 8000 keV, is plotted in Fig. 5.35. The best fit is obtained by varying with PPM the a, b, and c, parameters of the power-law, independently for the Pt and C layers. After finding the best fit parameters, we improved the fit by allowing the single layer to fluctuate, which allowed to reproduce the reflectivity at angles larger than 5000 arcsec, but they did not exceed 0.5 Å, but for a few layers.

Sample	Pt parameter (a, b, c)	C parameter (a, b, c)
HS61_w1	NA	NA
HS61_1-1	36.7, -0.857, 0.263	49.1, -0.476, 0.274
HS61_1-2	36.8, -0.888, 0.234	45.7, -0.786, 0.284
HS61_1-3	39.7, -0.804, 0.272	48.2, -0.686, 0.271
HS61_w2	NA	NA

Table 5.5: average thickness parameters of the Pt/C samples of the HS60 series.

The fit is satisfactory, but the reflectivity is much lower than it should be, and the discrepancy rapidly increases with the incidence angle. A comparison of the obtained thickness trend (Fig. 5.36) with the nominal recipe shows that the thickness trend of Platinum is well reproduced. The thickness of Carbon is, in contrast, slightly underestimated. The a, b, and c parameters are also listed in Tab. 5.5.

The low measured reflectivity is apparently due to a high roughness of the multilayer coating. Moreover, the PPM fit of the reflectivity curve matches a very large roughness increase, from 5 Å (at the substrate) to 20 Å (at the outermost layer), whereas the density values of Platinum and Carbon did not differ from the nominal ones (20.6 g/cm^3 Vs. 21.4 g/cm^3 for Pt, 2.2 g/cm^3 Vs. 2.1 g/cm^3 for C).

To have an independent proof of the roughness growth, and also in order to rule out a major contribution of the layer interdiffusion, we performed some 10 x 10 μm scans of the multilayer coating surface (Fig. 5.37). As expected, the external source is very rough when compared to the roughness of the initial substrate and also when compared to the AFM mapping of the surface of a more performing multilayer (Fig. 5.34). The surface appears crowded with point-like defects in ejection, that bring the overall rms to 11.5 Å, a value close to the one inferred from the fit of the XRR scans.

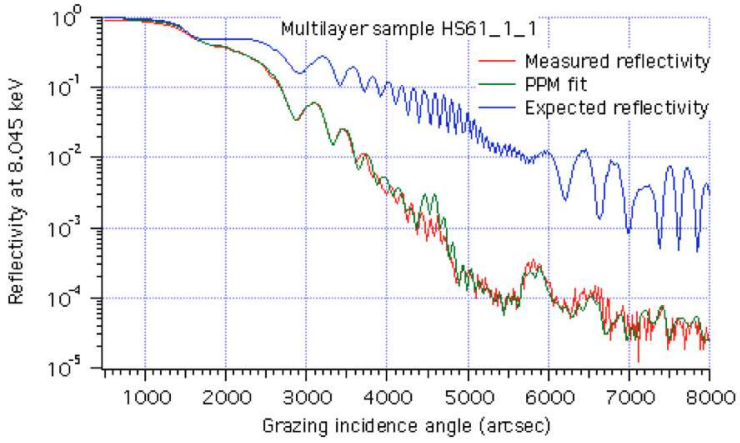

Figure 5.35: the XRR scan of the HS61_1_1 sample, superposed to the best fit found with PPM. Also shown is the expected reflectivity. Note the quite good matching of peak angular positions, but the reflectivity is much lower than required.

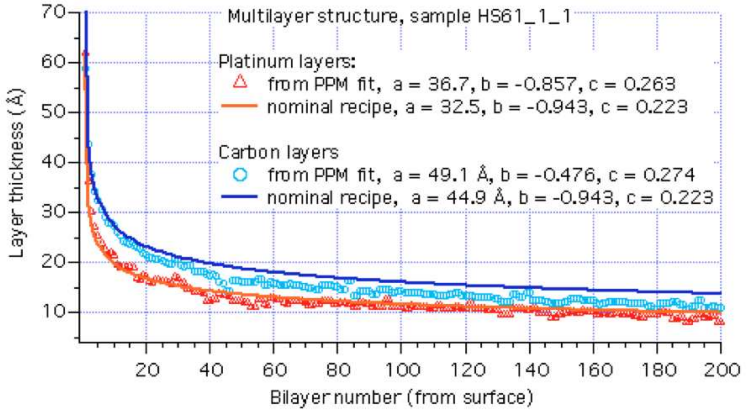

Figure 5.36: stack structure of the HS61_1_1 sample. The best-fit parameters of the power-law trend are reported.

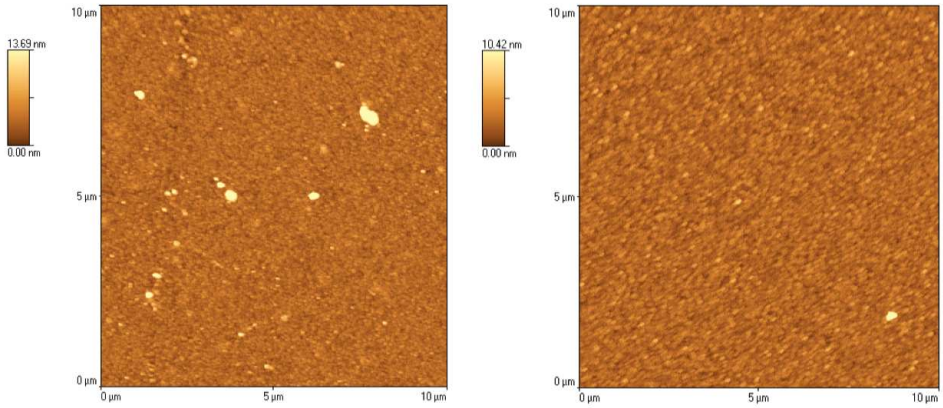

Figure 5.37: two 10 x 10 μm AFM scan of the HS61_1_3 (left) and the HS61_2_3 (right). The rms is 11.5 Å, in substantial agreement with the surfacial value inferred from the XRR.

Stress measurements were performed. The same HS61 multilayer was deposited onto two substrates having a different initial profile, in order to check the absence of relevant spurious deformations in the measurement.

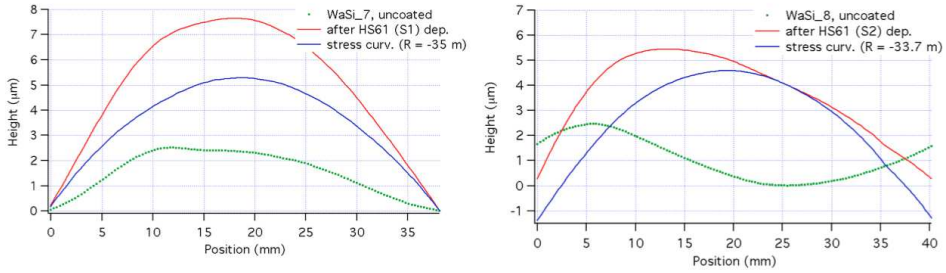

Figure 5.38: stress measurement on the HS61 samples. S1 sample (left), and S2 sample (right): the two net deformations nearly have the same curvature radius.

The measured profiles are shown in Fig. 5.38. The differences of profiles after/before the coating are almost perfectly parabolic, and they have the same negative radius of curvature within a 3% error due to the LTP stability (50 nm). The net deformation is quite large (5-6 μm of P-V) due to the coating thickness. The estimated stress value from the Stoney equation is -534 MPa, compressive and significantly higher than the W/Si (HS23).

Trying at improving the roughness of the multilayer, we have reduced the number

of bilayer to 100.

HS74 samples (graded, 100 bilayers)

These samples are made of 100 outermost bilayers of the nominal recipe. This deposition run was performed aiming at improving the reflectivity performances reducing the thickness that triggers the roughness growth 100 bilayers process, before proceeding to the coating deposition on a mirror shell to be tested at PANTER.

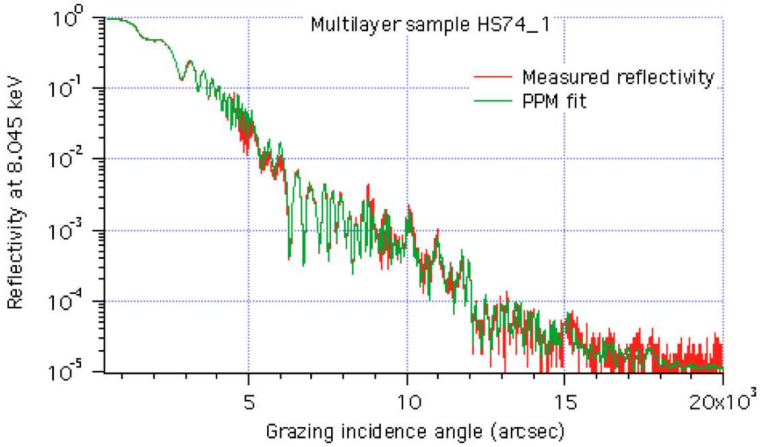

Figure 5.39: the XRR scan of the HS74_ 1 sample at 8.045 keV, superposed to the best fit found with PPM.

XRR scan is shown in Fig. 5.39, along with the best fit found by PPM. The model accurately reproduces all reflectance features: the reflectivity curve has a structure with clear and defined oscillations and matches a power-law model with parameters listed in Tab. 5.6. A layer thickness fluctuation is present, although always small and not exceeding 1 Å with a few exceptions. The layer density values are 21.4 g/cm^3 and 2.0 g/cm^3, close to the nominal ones. The roughness rms inferred from the fit is 3.5 - 4.5 Å, *close to that of the substrate*. The same roughness value is obtained from measurements in energy-dispersive setup at 5 to 40 keV (Fig. 5.42), at the incidence angles close to the mirror shell's at PANTER. Finally, the lateral uniformity along the length of the shell/targets is good (6%) as can be recovered from Fig. 5.40, and the multilayer structure is in good accord with the nominal recipe (Fig. 5.41).

These samples can be considered as the true witness samples of the deposition onto the MS185 shell to be tested at PANTER (TDM2), because no affordable information can be extracted from the w1 and w2 samples, locate out of the shell length. The witness samples seem to have multilayer with a smaller thickness, especially of Pt, as

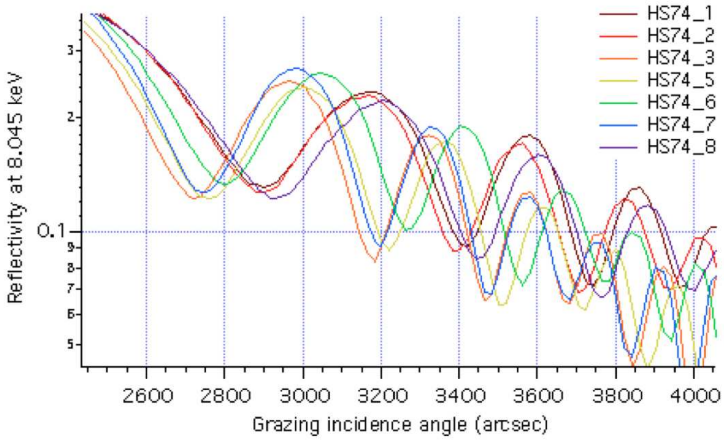

Figure 5.40: the XRR scans of the HS74 series (detail). The samples 3 to 7 are up to 6% thicker than the others.

Sample	Pt parameter (a, b, c)	C parameter (a, b, c)	Roughness (Å)
HS74_ w1	24.3, -0.95, 0.25	47.0, -0.94, 0.18	6.0
HS74_ 1	31.8, -0.94, 0.23	44.4, -0.94, 0.22	3.5
HS74_ 2	31.2, -0.96, 0.23	45.1, -0.96, 0.21	4.1
HS74_ 3	30.3, -0.97, 0.21	44.5, -0.95, 0.21	5.0
HS74_ 5	31.2, -0.96, 0.22	45.3, -0.94, 0.22	4.5
HS74_ 6	32.2, -0.95, 0.24	46.8, -0.97, 0.21	4.3
HS74_ 7	30.3, -0.96, 0.2	46.8, -0.93, 0.21	4.8
HS74_ 8	30.3, -0.96, 0.22	45.8, -0.95, 0.23	3.3
HS74_ w2	24.9, -0.97, 0.2	46.3, -0.77, 0.2	6.5

Table 5.6: parameters of the Pt/C samples of the HS74 series.

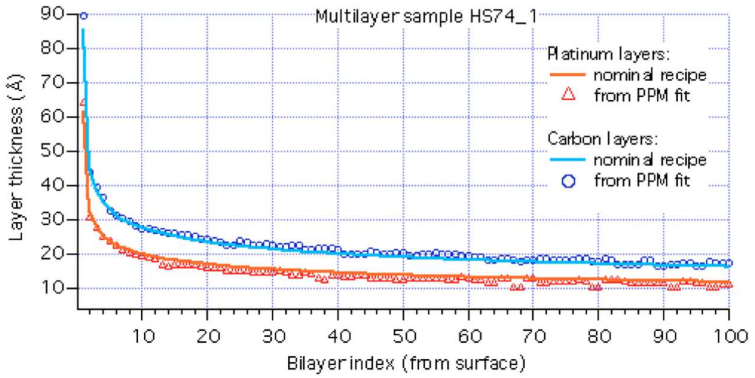

Figure 5.41: the multilayer stack structure of the HS74_1 sample, as inferred from PPM, superposed to the nominal recipe trend.

already observed with previous samples. As usual, this suggests that the layer thickness decays outside the targets/shell length, resulting in a lateral thickness gradient that causes the reflectance curve of these samples to appear smoothed out.

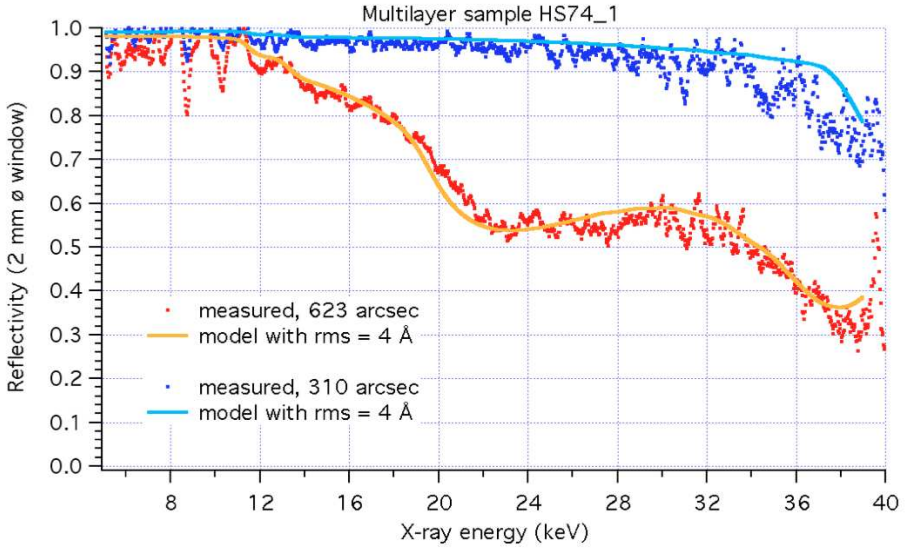

Figure 5.42: the XRR scan of the HS74_1 sample at 5 to 40 keV, at the incidence angles of the MS185 at PANTER. The lines represent the expected reflectivity from the stack model inferred at 8.045 keV.

HS79 samples (graded, 100 bilayers)

This is another graded Pt/C multilayer deposition, for the coating of the MS350 shell to be tested at PANTER (see results in sect. 9). The nominal recipe differs from the baseline by a multiplicative factor of 0.84. The resulting recipe is a 200 Pt/C bilayer stack, with Carbon on top, and thickness as follows:

- Platinum layers: a = 27.6 Å, b = -0.9432, c = 0.223: max thick. 53 Å, min thick. 9 Å
- Carbon layers: a = 38.1 Å, b = -0.9432, c = 0.223: max thick. 71 Å, min thick. 12 Å.

The stack has still a constant factor $\Gamma = 0.42$.

The XRR curve of a sample is plotted in Fig. 5.43 with the best fit found with PPM. The experimental curve is accurately fitted, but for some points around 7000 arcsec. The fit results (power- law parameters and roughness) are listed in Tab. 5.7 we can see that in general the nominal recipe is well reproduced, with a good lateral uniformity (6%, in line with previous depositions), excepting the sample w1, whose XRR is much less structured and could be fitted poorly, always because of a probable lateral gradient of thickness over the sample's surface. This is also seen from the direct comparison of the actual thickness with the nominal recipe (Fig. 5.44). The roughness values inferred from the fit (3.5 - 4 Å rms) are in general good because they are close to that of the substrate (3 Å rms), meaning a low roughness introduced by the process itself, excepting the sample n. 2, which undoubtedly exhibits a higher roughness (6.5 - 7.0 Å rms). The density values are $\sim$ 20 g/cm^3 for Platinum and 2.0 g/cm^3 for Carbon (the density of Pt is somehow lower than the bulk value, but in this case this is doubtful). The reflection performance in hard X-rays has also been checked at 5 to 40 keV, finding a confirmation of the low roughness and the multilayer structure found with PPM (Fig. 5.45).

Sample	Pt parameter (a, b, c)	C parameter (a, b, c)	Roughness (Å)
HS74_ w1	27.6, -0.89, 0.23	39.7, -0.58, 0.24	7.0
HS74_ 1	26.3, -0.94, 0.22	37.8, -0.97, 0.22	4.0
HS74_ 2	27.6, -0.85, 0.29	37.8, -0.75, 0.19	6.5
HS74_ 3	27.2, -0.95, 0.21	39.6, -0.98, 0.21	5.0
HS74_ 4	27.5, -0.95, 0.21	38.1, -0.97, 0.22	3.5
HS74_ 5	26.6, -0.94, 0.22	38.8, -0.97, 0.22	4.6
HS74_ 6	28.2, -0.93, 0.23	39.4, -0.97, 0.22	3.5

Table 5.7: parameters of the Pt/C samples of the HS79 series.

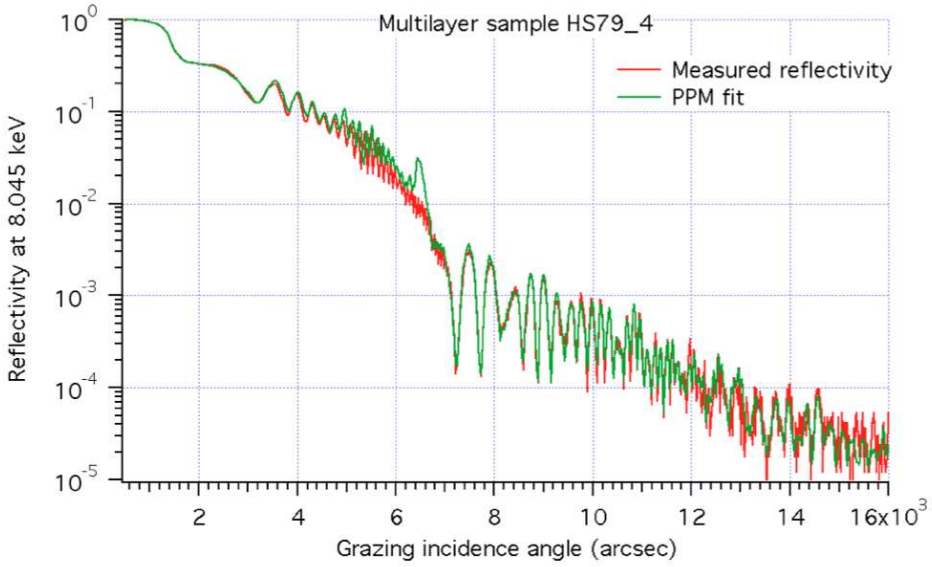

Figure 5.43: the XRR scan of the HS79_4 at 8.045 keV, superposed to the best fit found with PPM.

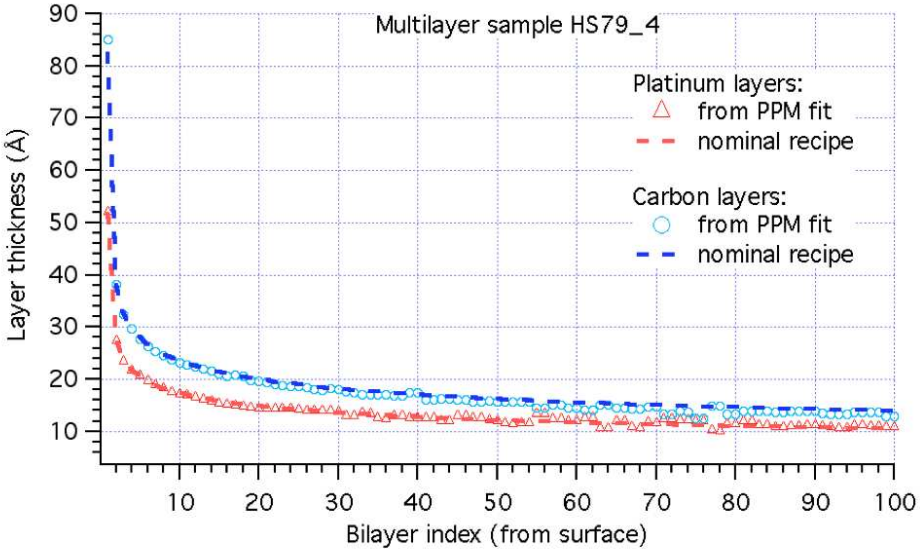

Figure 5.44: the structure of the HS79_4 sample (symbols), superposed to the nominal recipe (line). The superposition is perfect excepting for some thickness fluctuation.

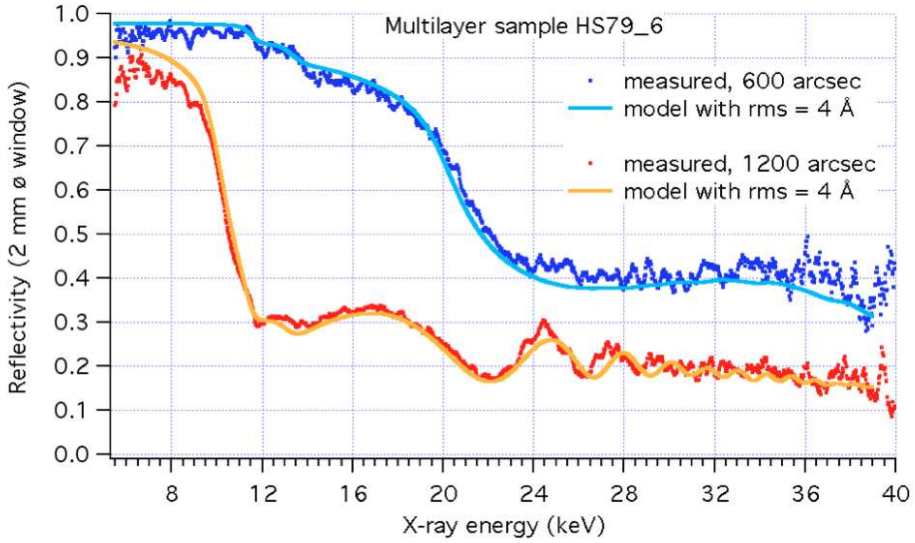

Figure 5.45: the XRR curves of the HS79_6 at 5 to 40 keV, at incidence angles close to those of the hyperbolic and parabolic segments of the MS350 at the PANTER.

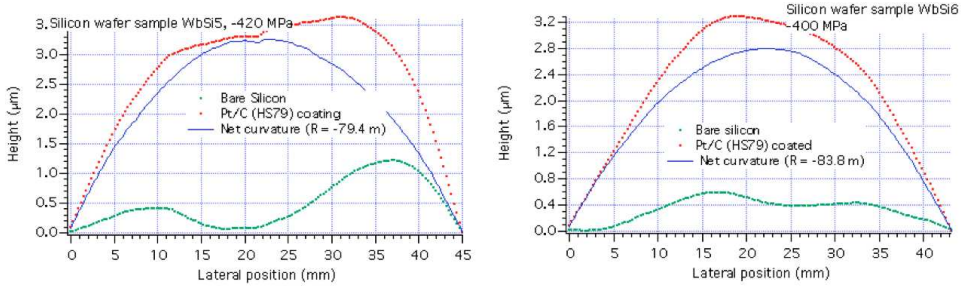

Figure 5.46: stress measurements on two HS79 samples.

Also some stress measurements were performed for the HS79 deposition run. The profiles of Si wafers recorded with the LTP, before and after coating, are plotted in Fig. 5.46. The difference of the profiles is almost perfectly parabolic. From the curvature radius, the total film thickness, the wafer thickness, we derive, using the Stoney equation, a compressive stress of $\sim$ -400 MPa, a smaller value than those of the HS61 samples. This can be related to the smaller thickness (d-spacing 100 Vs. 200 bilayers) of these samples.

5.1.5 Conclusions of the XRR characterizations

W/Si multilayers

The W/Si multilayer development has reached a very good level, also because it took the benefits of the previous Simbol-X phase A development. The results of tests performed onto W/Si multilayers can be summarized as follows:

(I) The thickness control and the compliance to the nominal recipe has attained good levels, with random deviations of $\pm$ 2 Å at most in the thickness.

(II) The repeatability of the stack deposition is very good, with a 1% of variation of the stack structure on average.

(III) The lateral uniformity, when measured, is within 6% over the shell length, Vs. a 5% tolerance.

(IV) The layer density of Tungsten (17.0 g/cm^3) is lower than its nominal value (19.3 g/cm^3). This is a negative point, because it conveys a sensitive reflectivity reduction. The density of Silicon is also slightly lower but this does not relevantly affect the reflectivity.

(V) The multilayer stress is compressive, and close to -370 MPa for a thickness ratio of 0.36 (only the HS23 sample has been measured).

(VI) The growth of the roughness and the layer interdiffusion are very low, because the final roughness replicates almost exactly the one of the Si wafer substrate. This is clearly a very positive aspect.

Pt/C multilayer

The deposition of Pt/C multilayers exhibited more complex problems than the one of the W/Si, as expected, because this kind of multilayer was never deposited with the PVD deposition machine of MLT, before this phase.

(I) The thickness control and the compliance to the nominal recipe were optimal at the beginning of the development (HS46 samples). The subsequent tests yielded alternate results at this regard, but the thickness stability was reduced soon to acceptable values (< 2Å). The nominal recipe is reproduced to within a few percent.

(II) The repeatability of the stack deposition has probably reached good levels (a $\sim$5% variation), even if it should be further investigated.

(III) The lateral uniformity is close to 6% over the shell length, Vs. a 5% tolerance.

(IV) The layer density of Platinum (20.6 g/cm^3) is - on average - very close to its nominal value (21.4 g/cm^3), an important aspect because a density reduction would have affected the reflectivity performance. The density of Carbon is also similar to the nominal value, even if this has a lesser impact.

(V) The multilayer stress is compressive, i.e. negative. Initial measurements yielded a very high stress value of -1000 MPa (0.44 thickness ratio): subsequent measurements returned a compressive stress of -400 MPa (0.42 thickness ratio), more similar to the one of W/Si multilayers.

(VI) Roughness growth and layer interdiffusion: XRR data highlighted soon a problem with the surface roughness. The first graded sample, though thinner than the nominal recipe, is much rougher than its substrate. The subsequent periodic samples, moreover, systematically show a surface roughness that increases with the total thickness. The behaviour is repeatable. The roughness inferred from the XRR data is correlated to the measurement performed with the AFM. The agreement is good with the AFM 10 μm scan, when available (HS60 and HS61). The XRR-AFM data matching allows ruling out a significant contribution of the interdiffusion of layers, which could not be distinguished from the sole XRR dataset. In addition, it was also possible, in some cases (e.g., the HS61 series), to detect from the XRR the increase of the interface rms throughout the stack, a typical behaviour of the roughness growth. This would be unexplainable if the interdiffusion were responsible for the reflectivity loss observed. From the HS72 sample on, the interfacial roughness has been improved, partly because the number of graded bilayers has been reduced to 100, but the real reason of the improvement is to be clarified yet. The number of samples in every series with little or no roughness growth was gradually increased, and in the last series of samples almost all did not show a roughness growth with respect to the substrate. In spite of the undoubted improvement, there always remain one or two samples per deposition run showing evidence for growth of roughness, usually the No. 2 or 3. Because the different samples are located at different positions in the coating chamber, the multilayer

deposition might have an inhomogeneous roughness, i.e., scattering properties variable from point to point, which is clearly a negative point. Future developments of the Pt/C multilayer in the context of this project should be aimed at understanding the reason of the roughening of the multilayer interface and correcting it, improving thereby the reflectance/focusing performances of the coating.

5.2 Improvement of mirror shell substrate roughness by reduction of the Gold thickness

In X-ray mirror shell electroforming process (Engelhaupt et al. 1994), a Gold layer acts both as a release agent and as reflective layer for soft X-rays, provided that it is sufficiently thick (<100 nm) to allow the total reflection of X-rays. Extending the concentration properties of such mirrors beyond 10 keV and up to 80 keV with incidence angles above 0.1 deg will, indeed, require the adoption of interferential coatings, such as graded multi-layers (Joensen et al. 1995). In this case, the Nickel mirror is replicated from the mandrel with the Gold layer and the multilayer is deposited on the optical surface using dedicated facilities (Romaine et al. 2005) (Garoli et al. 2009), over all the mirror length. Therefore, the Gold layer has the only function of making the release possible, and its thickness can be reduced until the thin layer becomes porous and no longer able to chemically isolate the mandrel from the mirror. On the other hand, the surface of thin films is known to become rougher and rougher while they are grown. The resulting process leads in general to a surface finishing degradation of increasing relevance as the film thickness is increased. Essentially the Gold layer thickness affects the roughness of X-ray mirrors manufactured by electroforming process (Sironi et al. 2009). The effect depends on the interaction between the Gold layer bulk structure, the starting master surface quality and the electroformed material structure. To determine which Gold thickness values are suitable for X- ray mirror production, the study has been continued by replicating a Nickel mandrel, which roughness is in general higher than that of Zerodur optically polished glass.

The finally aim was to evaluate how the Gold layer thickness affects the mirror angular resolutions. At high energies, the angular resolution degradation is completely driven by the scattering term. Hence, in the context of hard X- ray missions' development, it is crucial to evaluate the scattering impact. Hereafter we show the evaluation of dimension of gold crystallites in several samples with different coating thickness, through X-ray diffraction (XRD) measurements to determine the dimensions of the nucleation crystals by means of the broadening of the Bragg's peak.

5.2.1 Surface metrology

The mandrel characterization has been repeated at several steps (Sironi et al., 2011):

- A preliminary characterization has been performed to qualify the optical surface of the new mandrel. The mandrel surface has been investigated for the first time before undergoing thermal cycles. In this preliminary phase only images at 2 μm have been acquired with the intent of evaluating the initial material characteristics. The mandrel surface exhibits several pores. The pores have a dimension of < 0.1 μm and a depth of < 5 - 6 μm
- After thermal cycles the mandrel has been completely characterized before undergoing the first replica. The corresponding PSD and the calculated roughness values are reported in Fig. 5.48 right panel and in Tab. 5.8.
- After the mentioned replicas the mandrel has been re-characterized. This characterization shall allow evaluating the degradation of the mandrel after five replicas. The corresponding PSD and the calculated roughness values are reported in Tab. 5.8.

The four mirror shell replicas have been characterized by means of the AFM. The mirror shells have to be cut in small pieces to be measured with the AFM. To avoid possible scratches and deformation of the mirror shells optical surface the shells have been electro-eroded in circular samples with diameter of about 5 cm. The corresponding PSD's and data are reported in Fig. 5.48 right panel and Tab. 5.8. The case that shows the lowest roughness is the one with 50 nm Au thickness (see AFM images in Fig. 5.47).

5.2.2 XRD

The 1 μm scale AFM images comparison reveals a variation in the Gold morphology for different thickness layers. The Gold structure arrangement, composed of nucleation crystals (Arnault et. Al 1995) of increasing size with the layer thickness is apparent at first glance. An independent proof of the observed trend is given by the XRD data. The XRD Bragg peaks', reported in Fig. 5.48 left panel, exhibit an increasing trend with the Gold layer thickness, and correlate with the measured roughness. This is exactly what we would expect if the size of the Gold nano-crystals were growing with the layer thickness. This effect drives to a surface roughening as expected. The calculated nucleation crystals diameters (d) are reported in Tab. 5.8, computed with the Scherrer formula

$$d \simeq \frac{K\lambda}{\beta \cos\theta} \tag{5.3}$$

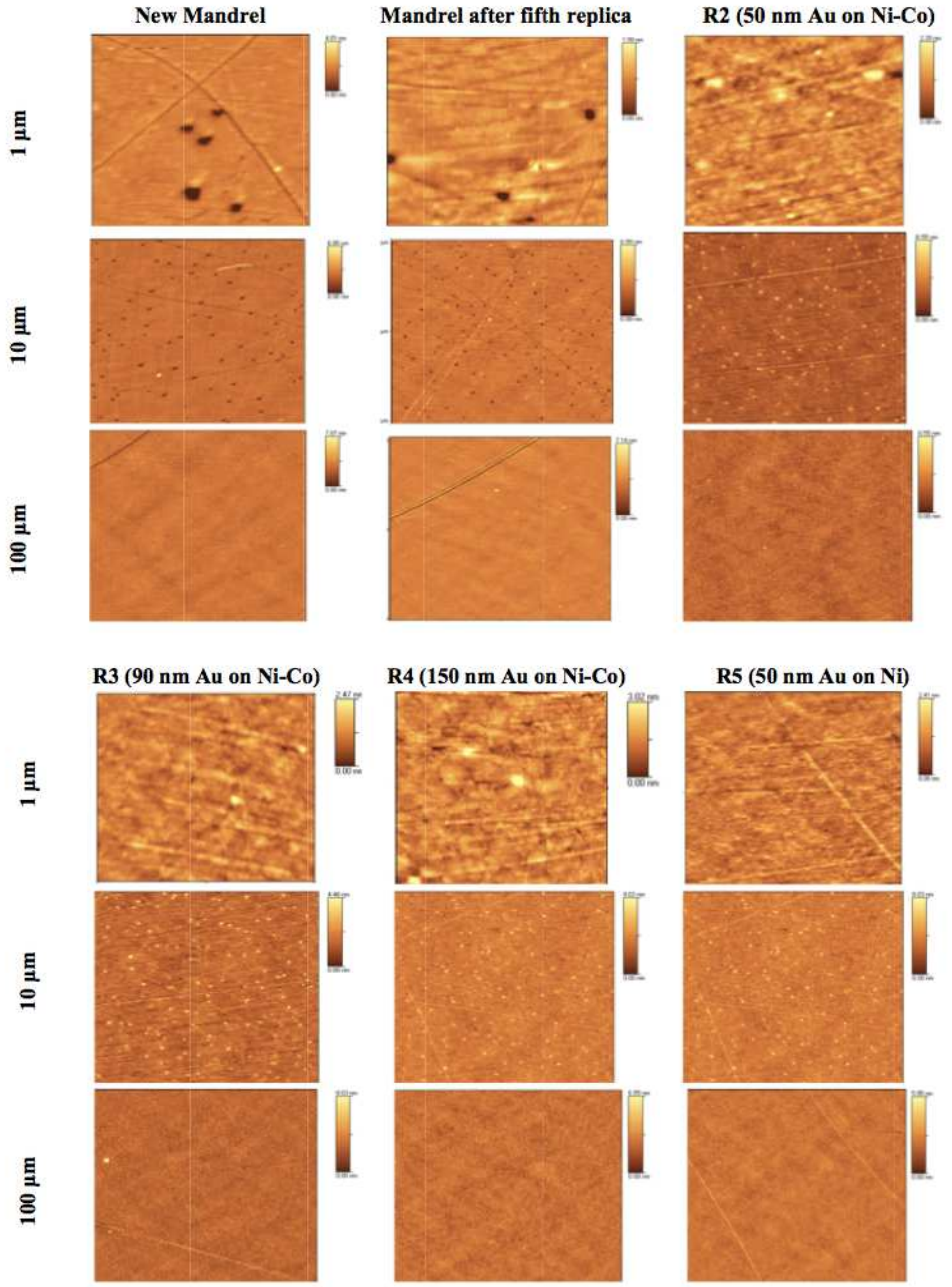

Figure 5.47: AFM images of the mandrel and mirror shell surfaces. The pores on the mandrel surface are replicated in negative in all mirror shell samples (10 μm scans). Note the variation of the grain size with the layer thickness in the 1 μm scan (e.g. R2/R4). Credits: Sironi et al. (2011)

where λ is the incident X-ray wavelength (1.54 Å for Cu source), θ is the Bragg angle, β is the broadening FWHM of the Bragg peak at half maximum intensity and K is a shape factor (0.9). The smaller are the crystal, the broader is the Bragg peak.

The mandrel and its four replicas can be compared by means of their mono-dimensional PSDs (Fig. 5.48 right panel), obtained by superimposing the PSD of the various measurements. Starting from this comparison, it is possible to make the following points:

- At high spatial frequencies ($> 1\ \mu m^{-1}$) all the replicas introduce a micro-roughness term with respect of the original mandrel roughness (black continuous line). The thick replica (red/dark stars) introduces the maximum roughness growth
- n the region around $1\ \mu m^{-1}$ all the replicas micro-roughness are almost comparable
- At lower spatial frequencies ($< 50 \mu m^{-1}$) a major contribution to roughness is given by the pure Nickel substrate (cyan/light stars)
- The mandrel surface roughness degrades, probably during the first replica process, in the spatial frequencies $> 1 \mu m^{-1}$

From these remarks we can infer that the Gold layer thickness is correlated with the micro-roughness increase. This effect is, however, affecting the only high spatial frequencies range. At lower spatial frequencies the dominant contribution to the mirror surface errors is due to the print-through effect of the substrate. An even more complete similar study shall be performed after multilayer deposition. This will allow taking into account the total roughening effect due to the substrate and the layers deposition.

5.2.3 Thin gold vs. PSF degradation

At the end of this study, we can predict the effect of XRS on the angular resolution at high energy. This prediction is possible following the analytical formalism given in Spiga (2007). To simulate the effect of the analyzed micro-roughness on a NHXM-like mirror shell, we consider an incidence angle of 0.21° and a detector size of 720 arcsec. With the actual PSD this choice does not affect the HEW $<$ 30 keV. We set 15 arcsec as constant HEW term, due to shape error.

The obtained angular resolution trend for the different characterized mirror is reported in Figure 5.49. For energies below $<$ 20 keV the dominant term of angular resolution degradation is due to figuring error (energy independent) and is hence constant. Above this limit the scattering effect due to micro-roughness becomes the major contribution to HEW. We can observe the strong effect on the image quality

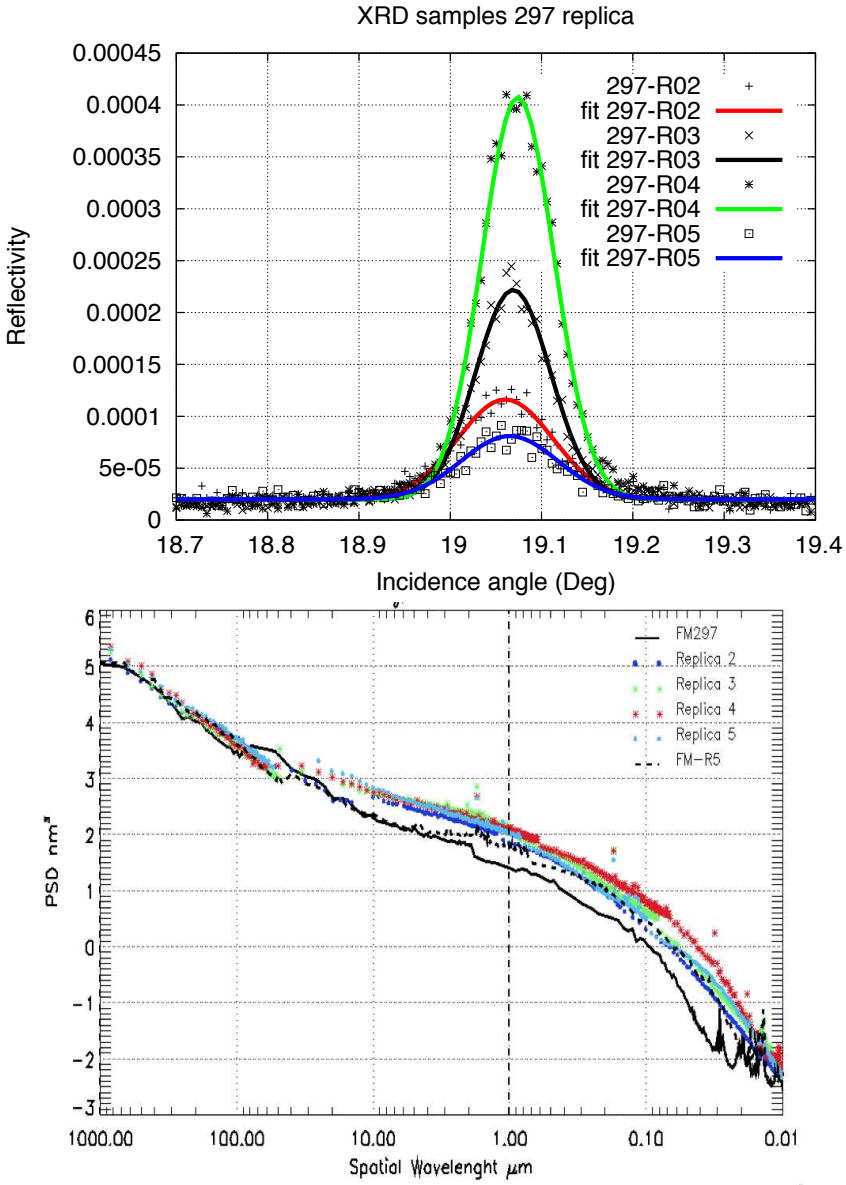

Figure 5.48: Left: Bragg's peak obtained by means of XRD measurements for the characterized mirror shells. Right: PSD obtained from the AFM and PROMAP 2.5x. As shown in the legend, coloured curves refer to different shells and mandrel steps. Credits: Sironi et al. (2011)

			AFM			XRD
	100 μm	10 μm	1 μm	MSF	HSF	
	σ[Å]	σ[Å]	σ[Å]	σ[Å]	σ[Å]	D[Å]
Mandrel	3.9	3.4	2.3	5.8	2.4	-
R2	5.5	4.8	3.8	6.4	3.8	378±8
R3	6.1	5.6	3.1	7.3	4.6	482±7
R4	6.1	5.9	3.8	7.5	5.4	500±4
R5	6.3	5.1	2.7	7.6	4.2	366±12
Mandrel after R5	4.0	4.3	3.0	6.4	3.7	-

Table 5.8: Mean roughness values of the measured shells. The HSFR interval is 1-100 μm^{-1}. The MSFR interval is 1 mm^{-1} - 1μm^{-1} and is partially covered by PROMAP 2.5x data. Last column: nucleation crystal sizes obtained by XRD measurements.

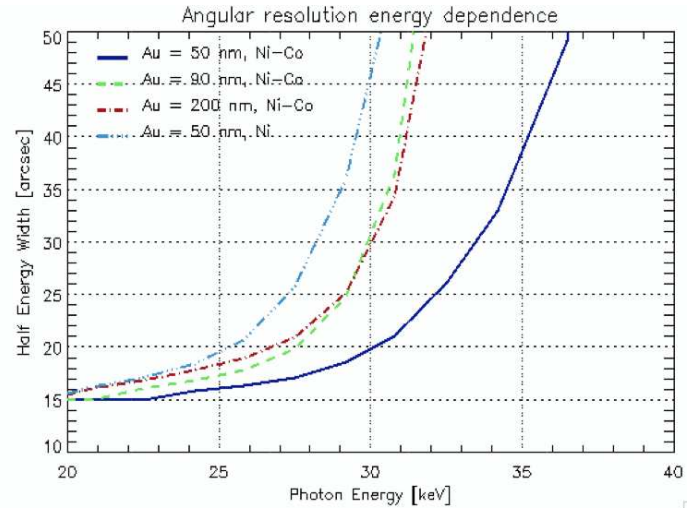

Figure 5.49: HEW prediction for the four analyzed mirror shells. For energies below $<$ 20 keV the dominant term of angular resolution degradation is due to figuring error (energy independent). Above this limit, the scattering effect due to micro- roughness becomes the major contribution to HEW. Credits: Sironi et al. (2011)

degradation due to the different manufacturing used for the four considered shells. In particular we can observe that:

- The angular resolution has different trends for mirror shells replicated by Nickel or in Nickel-Cobalt. The double points dashed line, referring to the Nickel substrate shell, exhibits a steeper raise in the $<$ 20 - 35 KeV energy interval, than the other curves.
- The thin Gold layer results in a mitigation of the image quality degradation at high energies. The thinner layers (continuous line) have better performances than the standard thick Gold layer (single point dashed line) at high energies.
- The double points dashed line becomes parallel to the continuous line at energies $>$ 40 keV. We remind that the two curves correspond to mirrors shells with identical Gold layer thickness and different substrate.

We will see in the sect. 6 that a more general treatment, based on Fresnel diffraction, can be used to derive the mirror PSF from the mirror profile. Nevertheless, for smooth surfaces exempt from mid-frequencies the applied formalism returns the correct increase of the HEW with the X-ray energy caused by the roughness.

6 A general method for PSF computation of real X-ray mirrors

In the previous sections we have shown the methods to measure and characterize the profile, roughness, the reflectivity of an X-ray mirror. We have also seen how the structure of a multilayer coating can be analyzed in detail. However, we still do not know how treat those data in a consistent framework: is the measured surface quality acceptable? which angular resolution would they return as a function of the X-ray energy? In other words, *which Point Spread Function would we expect from a mirror with such characteristics*? So far, this question was not answered with certainty.

As we mentioned, two sources of imaging degradation are classically identified:

- *figure errors* - large spatial wavelengths, comparable with the mirror length
- *roughness* - short spatial wavelengths (generally assumed to be shorter that 1 mm)

but the problem is how to exactly separate there two asymptotical regimes. In this section we show how the problem can be solved. Experimental proof is given in sect. 8 and 9.

Even though several contributions (Christensen et al. 1988) (Harvey et al. 1988) (Willingale 1988) (O'dell et al. 1993) were given in the past years in order to establish a relationship between the mirror PSF and the surface finishing level, all these approaches require treating separately the geometrical profile and the roughness effects. This in turn requires that one sets a spatial frequency that serves as a boundary between the two regimes, presumably depending on the incidence angle and λ. However, this limiting frequency is neither abrupt, nor clearly established, therefore the adoption of the geometric or scattering treatment has so far been, within large limits, "a matter of taste" (Aschenbach 2005). To make things worse, even if such a limit were clearly set, the mentioned X-ray scattering theory would be valid only within

the *smooth surface limit*, i.e., on condition that

$$4\pi\sigma \sin\theta_i < \lambda, \tag{6.1}$$

where θ_i is the grazing incidence angle of X-rays and σ is its surface rms in a given spectral band. As a consequence, the first order theory cannot be always extended to the low-frequency limit, where the surface defects are expectedly higher.

Some light in identifying the separation between the spectral ranges of figure errors and roughness was shed by Aschenbach (Aschenbach 2005), who concluded that a *single* Fourier component whose rms fulfills the smooth-surface condition (Eq. 6.1) should be mostly treated as roughness, and as figure error otherwise. However, the criterion operates a selection on the rms values of a spectrum of *discrete* frequencies, therefore it appears difficult to apply to a continuous roughness spectrum since the "single component" rms would depend on the spectral resolution adopted, which in principle can be made as small as one wants.

A different approach to the problem of translating the HEW scattering term of a mirror, as a function of the X-ray energy, into a surface finishing requirement, was elaborated by Spiga (2007) (see sect. 3.5.2). This method, based on the first order scattering theory, returned analytical formulae that can be used to convert the surface PSD of a mirror – with an arbitrary number of identical reflections – into the X-ray scattering term of the HEW, as a function of λ, and vice versa. Although the method is fast and reliable, it still suffers from the assumption that a separation between figure errors and roughness treatment can be uniquely set. Moreover, it requires the surface PSD in use to entirely fall in the smooth surface limit. Finally, the computed XRS term of the HEW is *assumed* to be small and added quadratically to the figure error HEW, an assumption difficult to verify immediately. These example show another problem: once we have treated the profile and the roughness and we have the respective PSFs, how to combine them? Moreover, the spectral range in the mid-frequency that fall between the two cannot be treated with the mentioned methodology (Fig. 6.1). An alternative approaching to this problem was suggested in 2003 by Zhao and van Speybroeck (Zhao & Van Speybroeck 2003), who treated the XRS as surface diffraction in Fraunhofer approximation to overcome the smooth surface and small scattering angle limits. Nevertheless, they seem to have restricted this method to the sole XRS computation. In this chapter we generalize their method, by showing that we can predict the PSF – and consequently the HEW – of a single, grazing incidence parabolic X-ray mirror from measured or simulated longitudinal profiles, simply making use of the Fresnel diffraction theory. This is a widespread technique to compute the PSF in the UV or visible light to account for the diffraction aperture and optical aberrations, but apparently it seems not to have been applied to rough mirror profiles, i.e., accounting for both profile errors and roughness in a *very wide spectral range of frequencies*. We show that if this is done, the mirror PSF can

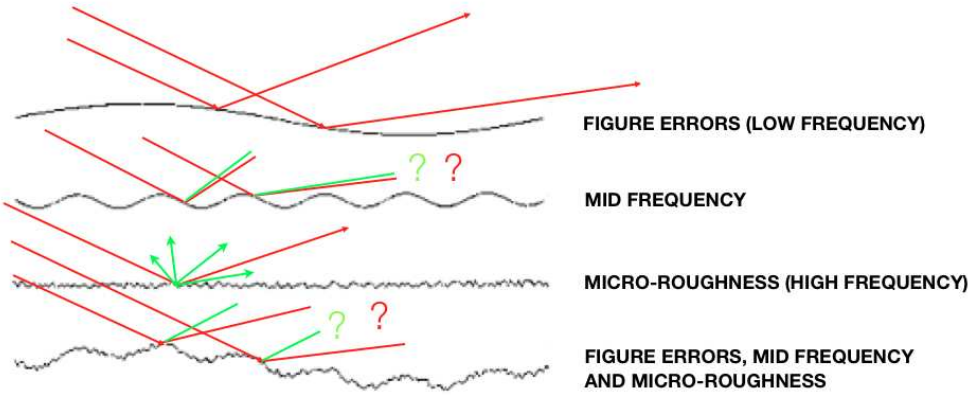

Figure 6.1: Different spatial wavelengths in a mirror profile. Long wavelengths are treated with geometrical optics, and high frequency roughness with the first order scattering theory. The treatment of mid-frequencies ir more uncertain.

be computed *from UV to hard X-rays* without relevant approximations but that we neglect mirror roundness errors, since in grazing incidence they have a lesser impact on the PSF.

Another advantage of this method is that it is self-consistent: one does not need to adopt different treatments in different spectral ranges. The geometrical optics results are automatically obtained at X-ray energies at which aperture diffraction and X-ray scattering turn out to be negligible *a posteriori*. Whenever such energy ranges can be identified, we are allowed to define a "figure error" HEW term, and therefore we can compare of the computed HEW(λ) from Fresnel diffraction with the results obtained from the analytical treatment (Spiga 2007) of the XRS term of the HEW. A very good agreement is found between the two methods, provided that the two terms of the HEW are summed linearly, rather than in quadrature as initially supposed.

6.1 Huygens-Fresnel principle applied to the reflection

The Huygens-Fresnel principle (named after Dutch physicist Christiaan Huygens and French physicist Augustin-Jean Fresnel) is a method of analysis applied to problems of wave propagation both in the far-field limit and in near-field diffraction. In this construction, every point of a wave-front may be considered as a centre of a secondary disturbance which gives rise to spherical wavelets, and the wave-front at any later instant may be regarded as the envelope of these wavelets. The postulate is that the secondary wavelets mutually interfere according to the linear superposition principle

(Fig. 6.2).

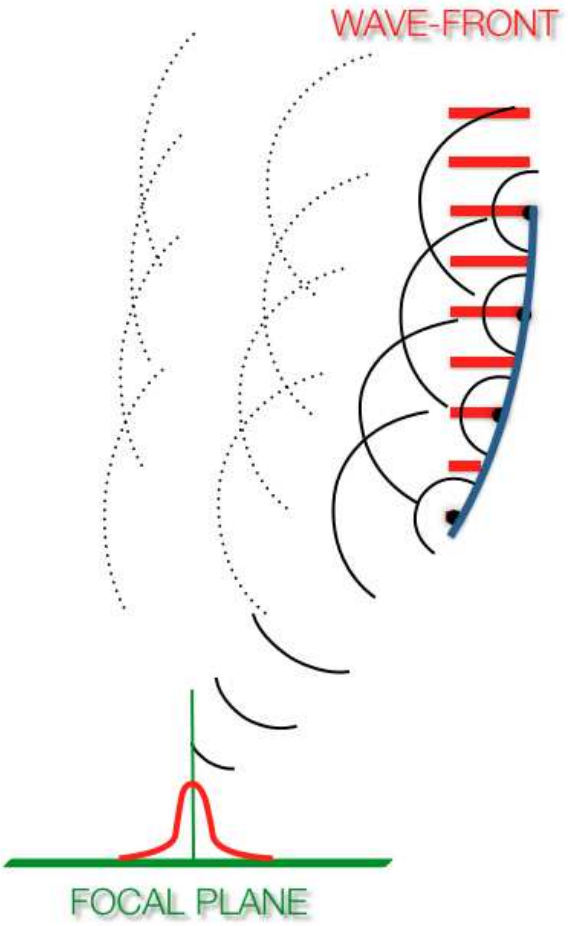

Figure 6.2: Secondary waves generated at each point of the mirror (application of Huygens Fresnel principle). The electric field on the focal plane is given by the wave interference.

Let S be the instantaneous position of a spherical monochromatic wave-front of radius r_0 which proceeds from a point source P_0, and let P be a point at which the light disturbance is to be determined. The time periodic factor $e^{-\omega t}$ can be omitted, the disturbance at a point Q on the wave-front may be represented by Ae^{ikr_0}/r_0, where A is the amplitude at unit distance from the source. In accordance with the Huygens-Fresnel principle we regard each element of the wave-front as the centre of a secondary disturbance which is propagated in the form of spherical wavelets, and

obtain for the contribution d$U(P)$ due to the element dS at Q the expression:

$$dU(P) = K(\chi)\frac{Ae^{ikr_0}}{r_0}\frac{e^{iks}}{s}dS, \qquad K(\chi) = \frac{1+\cos\chi}{2} \tag{6.2}$$

where $s = QP$ and $K(\chi)$ is an *obliquity factor* which describes the variation with direction of the amplitude of the secondary waves, χ being the angle (often called the *angle of diffraction*) between the normal at Q and the direction QP. Following Fresnel we assume that K is maximum in the original direction of propagation, i.e., for $\chi = 0$, and that it rapidly decreases with increasing χ, being zero when QP is tangential to the wave-front, i.e., when $\chi = \pi/2$; and finally, that onlythat part S' of the primary wave contributes to the effect at P, which is not obstructed by obstacles which may be situated between P_0 and P. Hence the total disturbance at P is given by:

$$U(P) = \frac{Ae^{ikr_0}}{r_0}\int\int_S \frac{e^{iks'}}{s'}K(\chi)dS' \tag{6.3}$$

In a small-angle deviation approximation, one can assume $K(\chi) = 1$ When a wave-front impinges an obstacle, for example a mirror, all the points generate a spherical waves that interfere together. In order to compute the electric field in an arbitrary point of the space, e.g. the focal plane of the mirror, we can apply the Huygens-Fresnel principle starting from the equation 6.3.

6.2 Point Spread Function construction methodology

In this approach, we construct the PSF of the mirror using the Huygens-Fresnel principle. The shallow angles in use for X-ray mirrors allows us to adopt some very reasonable approximations: the first one is that we can work in scalar approximation: secondly, we can deal the computation using the meridional *profiles* rather than the complete mirror map, ignoring thereby the roundness defects. The last approximation, which allows dramatically reducing the computational complexity and time, is justified by the following considerations:

(I) The *X-ray scattering* pattern in grazing incidence is 100 to 1000 times more extended in the incidence plane than in the perpendicular direction, i.e., it essentially lies in the incidence plane (Church 1979). Moreover, it is determined by the roughness PSD as computed in incidence plane direction; therefore it is unaffected by the roughness in the azimuthal direction.

(II) If the geometrical optics is applicable, the slope errors of the longitudinal sections of the mirror result in an angular dispersion twice as large, while the same slope errors along the azimuth result in an angular spread of rays smaller by a

factor of $\tan 2\theta_i$, where θ_i is the incidence angle. Therefore, the deviation of reflected rays is dominated by the slope variation of the longitudinal sections.

(III) Finally, if θ_i is small enough, the mirror aperture is a thin circular corona, whose width is much smaller than the mirror radius. In these conditions also the *aperture diffraction* – visible when testing the mirror PSF in UV light – resembles the diffraction pattern of a long, straight slit, which can be computed monodimensionally. This can be seen in Fig. 6.3, where we compare the aperture diffraction PSF of a thin circular corona aperture and the one of a straight slit of the same width.

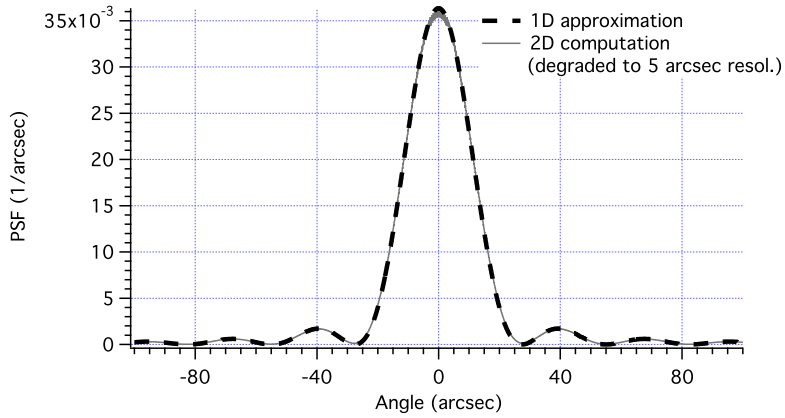

Figure 6.3: The aperture diffraction PSF at λ = 3000 Å of a grazing incidence parabolic mirror with f = 10 m, a minimum radius R_0 = 150 mm, and a length L = 300 mm, resulting in a circular corona aperture of 2.25 mm width. The dashed line is the usual diffraction pattern of a straight slit 2.25 mm wide, while the accurate computation (solid line) is obtained computing the exact diffraction pattern integrated over circular coronae. The first pattern would exhibit a superimposed high-frequency modulation, but it is smoothed out by the finite resolution of the detector (5 arcsec).

In this work, we limit ourselves to the PSF computation for a single-reflection mirror with a parabolic nominal profile. We define (see Fig. 6.4) f to be the focal length of the mirror, R_0 and $R_{\rm M}$ its minimum and maximum radii, L its length along the z-axis. We define the radial aperture $\Delta R = R_{\rm M} - R_0 \approx L \tan\theta_i$. The focal plane section along which the PSF is evaluated is the x-axis. We initially consider the case of a perfectly parabolic profile, which is expected to return a delta-like PSF. We treat later the case of real mirrors with deformations and with a rough surface, whose PSF is expectedly broader, by applying the same computation to the actual profile. In any case, the generic mirror profile, $z_p(x_p)$, act as a diffractor of a electromagnetic plane wave of wavelength λ and electric field amplitude E_0, initially directed towards the

negative direction of the z-axis. The superposition of the secondary waves generated at each point of the mirror returns the total electric field on the focal plane, neglecting the obliquity factor,

$$E(x,y) = \int_S \frac{E_0}{d_2 \lambda} \exp\left[-2i\pi \frac{d_1 + d_2}{\lambda}\right] \mathrm{d}^2 s, \tag{6.4}$$

where d_1 and d_2 are the distance of the generic mirror point from the initial wavefront, and from the focal plane point at x, respectively. The integral is meant to be extended to a "slice", S, of the mirror with the actual longitudinal profile and a small width Δy along the azimuth. Because $f \gg L$, we are allowed to approximate $d_2 \approx f$ in the denominator of Eq. 6.4.

The two distances can be written, to a very good approximation, as

$$d_1 = L + f - z_p, \tag{6.5}$$

and

$$d_2 = \sqrt{(x - x_p)^2 + y_p^2 + z_p^2} \approx \sqrt{(x - x_p)^2 + z_p^2} + \frac{y_p^2}{2f}. \tag{6.6}$$

By noting that the mirror curvature along the azimuth focuses the rays in the y direction, the last term has to be written as $y_p y/f$ in Fraunhofer approximation, and the Eq. 6.4 becomes

$$E(x,y) = \frac{E_0}{f\lambda} \int_L e^{-i\frac{2\pi}{\lambda}(L+f-z_p+\sqrt{(x-x_p)^2+z_p^2})} \mathrm{d}l \int_{-\Delta y/2}^{+\Delta y/2} e^{-i\frac{2\pi y}{\lambda f} y_p} \mathrm{d}y_p. \tag{6.7}$$

The second factor in the Eq. 7.1 can be integrated easily, and we remain with

$$E(x) = \frac{E_0}{f\lambda} \Delta y \frac{\sin\delta}{\delta} \int_L e^{-i\frac{2\pi}{\lambda}(L+f-z_p+\sqrt{(x-x_p)^2+z_p^2})} \mathrm{d}x, \tag{6.8}$$

where $\delta = \frac{\pi y \Delta y}{\lambda f}$. The intensity distribution then becomes

$$I(x,y) = \frac{E_0^2}{f^2\lambda^2} (\Delta y)^2 \frac{\sin^2\delta}{\delta^2} \left| \int_L e^{-i\frac{2\pi}{\lambda}(\sqrt{(x-x_p)^2+z_p^2}-z_p)} \mathrm{d}x \right|^2. \tag{6.9}$$

To obtain the distribution along the x-axis, we integrate the intensity distribution along y. However, since $\lambda \ll \Delta y$, the last factor becomes a Dirac delta; therefore the integral on y is immediate and we obtain

$$I(x) = \frac{E_0^2 \, \Delta y}{f\lambda} \left| \int_L e^{-i\frac{2\pi}{\lambda}(\sqrt{(x-x_p)^2+z_p^2}-z_p)} \mathrm{d}x \right|^2 : \tag{6.10}$$

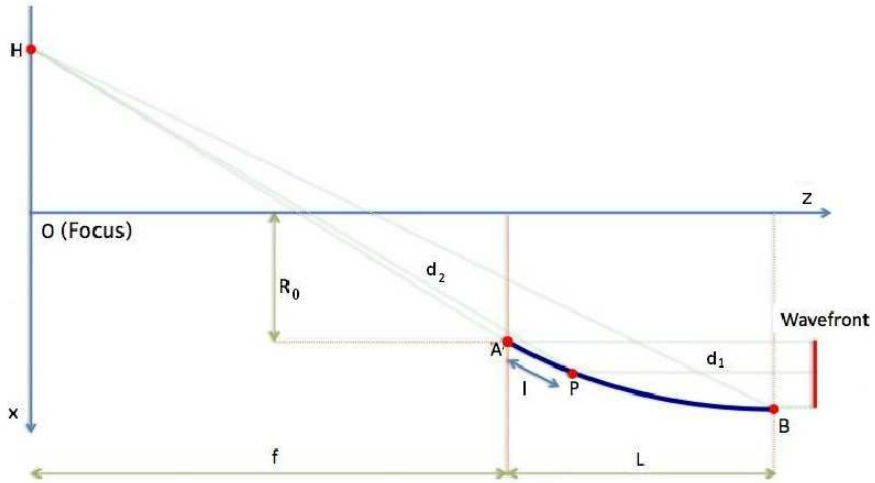

Figure 6.4: The adopted geometry for the computation of the PSF of a parabolic mirror. A plane wavefront impinges the mirror from right side, and the scattered amplitude at the generic point H of the focal plane is obtained by superposing the secondary waves generated at each point of the mirror profile, P, located along the curvilinear abscissa l.

this is the intensity profile along the x-axis, but it is the PSF of the mirror as well, because the entire intensity distribution on the focal plane is obtained by superposing the linear diffraction from every "slice" in its meridional plane. The mirror curvature in the azimuth causes the diffracted intensity (Eq. 6.10) to be spread over an increasing surface with the angular distance from the focus, but this spread is compensated by the integration over the circular coronae needed to compute the PSF. Finally, we normalize the PSF to the total power impinging the mirror, $\Delta R \Delta y E_0^2$, and we obtain the final formula

$$PSF(x) = \frac{\Delta R}{f\lambda L^2} \left| \int_L e^{-i\frac{2\pi}{\lambda}(\sqrt{(x-x_\mathrm{p})^2+z_\mathrm{p}^2}-z_\mathrm{p})}\, \mathrm{d}l \right|^2 . \tag{6.11}$$

Equation 6.11 is correctly normalized to 1. If all coordinates are measured in mm, the PSF is in mm^{-1}. If one wants the x-axis graded in arcsec, it is sufficient to multiply the x-axis times the plate-scale factor $2.06\times10^5/f(\mathrm{mm})$ and to divide the PSF by the same factor.

We check the correctness of Eq. 6.11 in the case of a perfect parabolic mirror with focus in the origin of the reference frame, $z_\mathrm{p} = ax_\mathrm{p}^2 - \frac{1}{4a}$, where a is a parameter describing the aperture of the parabolic profile. After substitution and some manipulation, this yields

$$PSF(x) = \frac{\Delta R}{f\lambda L^2} \left| \int_L e^{-i\frac{2\pi}{\lambda}(\sqrt{x^2-2x_\mathrm{p}x+\left(ax_\mathrm{p}^2+\frac{1}{4a}\right)^2}-ax_\mathrm{p}^2)}\, \mathrm{d}l \right|^2 ; \tag{6.12}$$

an exact solution of this integral is possible only if $x = 0$. If $x \neq 0$, we notice that the image is much smaller than the mirror's size, i.e., $x \ll x_\mathrm{p}$, therefore we can neglect x^2 with respect to $2x_\mathrm{p}x$ in the exponent of the integrand of Eq. 6.12, and the square root can be developed at the first order. In this way, we remain with

$$PSF(x) \approx \frac{\Delta R}{f\lambda L^2} \left| \int_L e^{-i\frac{2\pi}{\lambda}\frac{x_\mathrm{p}x}{z_\mathrm{p}}} \,\mathrm{d}l \right|^2. \tag{6.13}$$

Setting now $\mathrm{d}l \approx \mathrm{d}z_\mathrm{p} \approx (L/\Delta R)\,\mathrm{d}x_\mathrm{p}$ and $z_\mathrm{p} \approx f$ in the exponent denominator, the integral is easily computed:

$$PSF(x) \approx \frac{1}{f\lambda\Delta R} \left| \int_{R_0}^{R_0+\Delta R} e^{-i\frac{2\pi x}{\lambda f}x_\mathrm{p}} \,\mathrm{d}x_\mathrm{p} \right|^2 = \frac{\beta}{\pi}\frac{\sin^2\beta x}{(\beta x)^2}, \tag{6.14}$$

where we set $\beta = \frac{\pi\Delta R}{f\lambda}$. This is the usual diffraction pattern from a slit of aperture ΔR, correctly normalized to 1: when $\Delta R \gg \lambda$ the PSF tends to a Dirac delta, as expected.

Excepting a few cases, the integral in Eq. 6.11 has to be computed numerically. This entails the issue of approximating the integral with a sum of sufficiently large number of terms. We estimated (Raimondi & Spiga 2010) the maximum frequency to be sampled to avoid the appearance of aliases. We only have to determine the minimum profile sampling at which the integral has to be computed to avoid the appearance of aliases: we can do it by noting that, if the focal plane has a half-width r, the maximum scattering angle is r/f, therefore for an X-ray wavelength λ the minimum spatial wavelength scattering at the focal plane's edge is, using the grating formula,

$$l_\mathrm{min} \approx \frac{\lambda f}{r\sin\theta_i}. \tag{6.15}$$

Even if the adopted profile sampling, Δl, already oversampled this maximum frequency by a factor of 2π, the sampling should be halved as per the Nyquist criterion:

$$\Delta l \approx \frac{\lambda f^2}{2\pi R_0 r}, \tag{6.16}$$

where r is the detector half-size and where we made use of the relation $R_0 \simeq f\tan(2\theta_i)$, for a single-refection mirror. This sampling was derived assuming that the scattering at the detector edge can be described by the 1^{st} order theory, i.e., that the detector is sufficiently large to fit all the PSF associated to higher scattering orders, which blend to form the "figure error" PSF (also owing to the imperfect monochromaticity of the incident radiation). Actually, this condition is automatically fulfilled, because any scattering of the k^{th} ($k > 1$) order at the detector's edge would be generated by a spatial wavelength k times *larger*, which would be even more oversampled by the sampling of Eq. 6.16.

However, we did not specify yet the minimum required sampling on the focal plane in order to avoid undersampling of the PSF: this is obtained from the smallest spatial frequency visible on the mirror profile, $1/L$, resulting in a scattering at a distance Δx:

$$\Delta x \approx \frac{\lambda f^2}{\pi R_0 L}, \tag{6.17}$$

where we increased the sampling by a factor of 2π for consistency with Δl. We note that

$$\frac{L}{\Delta l} = \frac{2r}{\Delta x} := N, \tag{6.18}$$

i.e., N, the number of points on the mirror profile and on the detector line is the same. N increases linearly with the X-ray energy, but even assuming *very* hard X-rays of wavelength $\lambda = 0.1$ Å, $r = 2$ cm, $f = 10$ m, $R_0 = 150$ mm, and $L = 300$ mm we obtain $N \approx 10^6$, a number of terms that can be managed quite easily. The total computation time increases as N^2, i.e., with the square of the X-ray energy, E,

$$\tau \propto \frac{E^2 R_0^2 r^2 L^2}{f^4}. \tag{6.19}$$

6.3 Examples of computation of Point Spread Functions

In this section we show some applications of Eq. 6.11 to derive the PSF of a parabolic X-ray mirror with different profile errors. We firstly consider the theoretical case of a perfect parabolic mirror, whose PSF is solely affected by the aperture diffraction. In the following section we check the behaviour of a single frequency perturbation superimposed to the mirror profile. Finally, we simulate a realistic case of a mirror with a geometrical deformation and a microroughness relief.

6.3.1 The PSF of ideally smooth mirrors

Adopting a parabolic profile $z_p = z_p(x_p)$ and solving Eq. 6.11, we have computed the PSF from 3000 Å to 30 Å. We expect that the effect of diffraction aperture is dominant in the UV, while the PSF approaches a Dirac delta as the energy is increased. The computation behaves as expected. In Fig. 6.5 we display the PSF at 3000 Å and 1000 Å, completely enlarged by the aperture diffraction. As the X-ray energy is increased, the aperture diffraction decreases and the PSF tends to resemble a Dirac delta (Fig. 6.6).

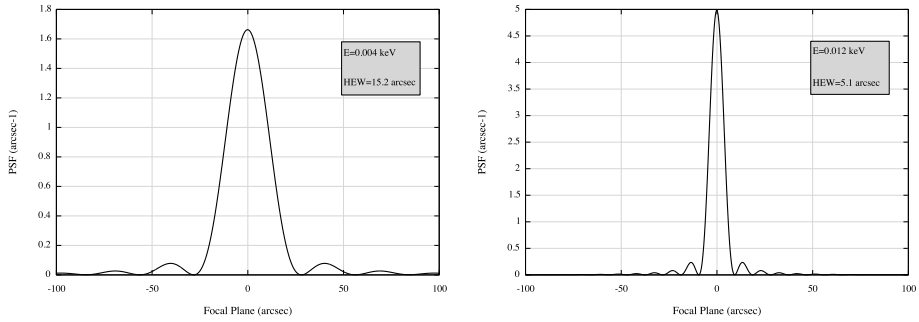

Figure 6.5: The PSF of an ideal parabolic mirror at 3000 Å (left) and 1000 Å (right).

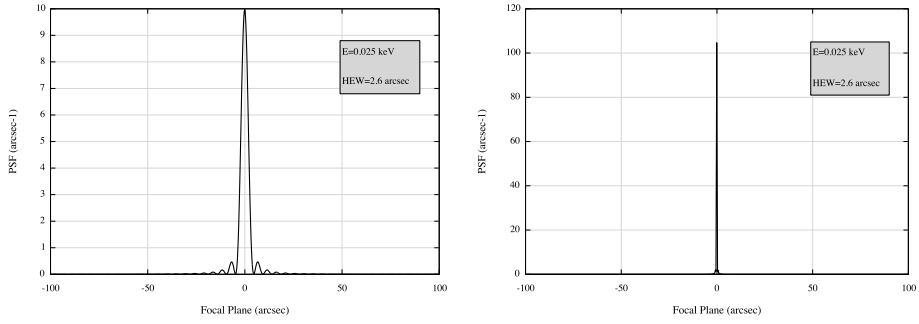

Figure 6.6: The PSF of an ideal parabolic mirror at 500 Å (left) and 30 Å (right).

6.3.2 Behavior of a sinusoidal perturbation

As a further example, we consider the case of a *single frequency* perturbation superimposed to the parabolic profile. In particular, we choose the spatial wavelength – ϕ =1 cm – and the amplitude – A = 0.1 μm – in a range that cannot be immediately classified as "figure error" or "microroughness", and therefore is usually labelled as "mid-frequency". We hereafter see that such a frequency can behave as roughness, figure error, or a mixture of the two, depending on λ. More precisely, as already derived by Aschenbach (Aschenbach 2005), its behavior depends on whether λ exceeds or not the characteristic wavelength $4\pi\sigma \sin\theta_i$, where θ_i is the incidence angle and σ the rms of the sinusoid.

As long as $\lambda \gg 4\pi\sigma \sin\theta_i$, only the central spot of the PSF is visible. However, as λ is decreased, two peaks appear aside, while the central peak decreases (Fig. 6.7, left). This situation is found when still $\lambda > 4\pi\sigma \sin\theta_i$, but starts to be comparable. This is exactly, if fulfilled, the smooth-surface condition (Stover 1995), which allows us to apply the X-ray scattering theory at first order (Church 1979). The two scattering peaks exactly correspond to the PSD peaks at the 1 cm frequency, for an X-ray energy of 0.12 keV and an incidence angle of 0.42 deg. However, if λ is decreased further, the situation changes because the scattering theory at the first order becomes no longer applicable: in Fig. 6.7 (right) we show the PSF computed at 30 Å, a wavelength *almost exactly at the boundary of the smooth-surface condition* (33 Å) for the considered example. We see that the higher scattering orders appear gradually, making the PSF more complex than predicted by the first order theory.

The mentioned example also allows us to check the correctness of our approach, because the peak positions and intensity are predicted by the sinusoidal grating theory (Stover 1995): more exactly, the scattering angles θ_s fulfill the equation

$$\phi = \frac{N\lambda}{\cos\theta_i - \cos\theta_\mathrm{s}} \tag{6.20}$$

with N integer, and the N^{th} peak intensity is

$$I_N = J_N^2 \left[\frac{2\pi A}{\lambda}(\sin\theta_i + \sin\theta_\mathrm{s})\right], \tag{6.21}$$

where J_N is the N^{th} Bessel function of the first kind. By means of Eqs. 6.20 and 6.21 we verified that the peak positions and heights of Fig. 6.7 match the theoretical predictions. This can be done at *any* X-ray energy: for instance, we can decrease λ below the limit $4\pi\sigma \sin\theta_i$ and notice the evolution of the PSF: higher and higher diffraction orders appear then, until the peaks are superposed and cannot be easily discerned from each other. Despite that, we note that the PSF *does not expand*: rather, it tends to keep within definite angular limits ($\pm$ 26 arcsec in the present ex-

ample, see Fig. 6.8, left), and when $\lambda \ll 4\pi\sigma \sin\theta_i$, the PSF *tends to converge to a shape almost independent of* λ.

The explanation of this behavior is the following: for very small λ values, the PSF is built up by high diffraction orders, and the intensity of diffraction peaks is given by Eq. 6.21. But for large N, $J_N(x)$ is nearly zero for $|x| < N$. Therefore, the PSF is non-zero if

$$\frac{2\pi A}{\lambda}(\sin\theta_i + \sin\theta_s) > N. \tag{6.22}$$

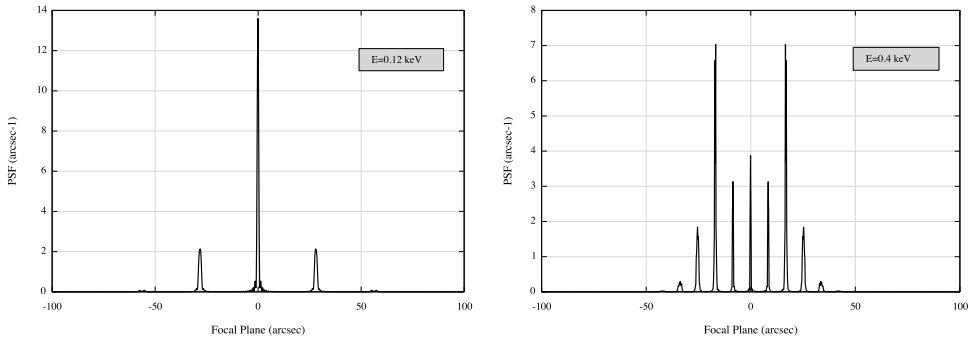

Figure 6.7: Computed PSF of a parabolic mirror plus a sinusoidal perturbation of 0.1 μm amplitude and a 1 cm period, for an X-ray wavelength of 100 Å (left) and 30 Å (right). The higher diffraction orders appear when the smooth-surface limit is no longer met.

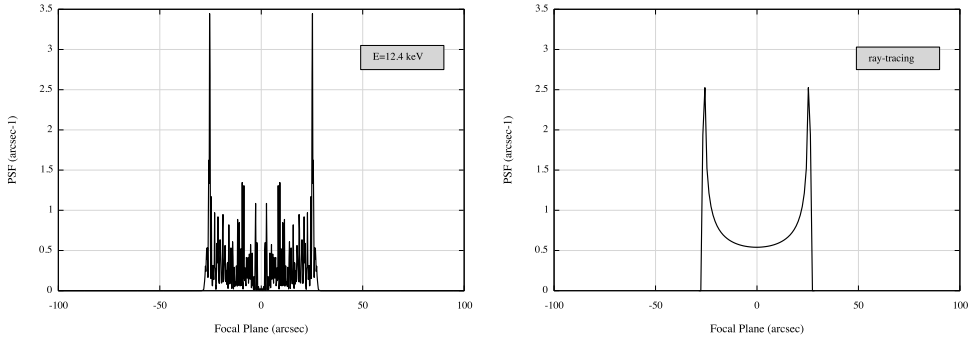

Figure 6.8: PSF computation of parabolic mirror plus a sinusoidal perturbation with A = 0.1 μm and ϕ = 1 cm at λ = 1 Å (left). Ray-tracing simulation on the same sinusoidal profile (right), with the typical $1/\cos$ shape. The two PSFs differ only for the rapid modulation in the first case.

By comparison with the Eq. 6.20, one obtains

$$\frac{2\pi A}{\phi}(\sin\theta_i + \sin\theta_\mathrm{s}) > \cos\theta_i - \cos\theta_\mathrm{s}, \tag{6.23}$$

which no longer depends on N and λ. For small angles, we can approximate $\sin\theta_i \simeq \theta_i$ and $\cos\theta_i \simeq 1 - \theta_i^2/2$, hence

$$\theta_\mathrm{s}^2 - \theta_i^2 < \frac{4\pi A}{\phi}(\theta_i + \theta_\mathrm{s}), \tag{6.24}$$

which is equivalent to

$$|\theta_\mathrm{s} - \theta_i| < \frac{4\pi A}{\phi} = 25.9\,\mathrm{arcsec}. \tag{6.25}$$

The limit on right hand of Eq. 6.25 is exactly *twice the maximum slope of the sinusoidal perturbation*, corresponding to the maximum deviation of rays in geometrical optics approximation. We therefore find, as expected, that the application of the Fresnel diffraction for small λ returns the results of geometrical optics. This becomes even more apparent if we compare the PSF at 1 Å computed by Fresnel diffraction (Fig. 6.8, left) with the PSF computed by ray tracing on the same profile (Fig. 6.8, right). The two PSF essentially coincide, but for a rapid modulation of the PSF in the first case, which in practice is not observed due to the imperfect monochromaticity of real X-ray beams, which would cause the oscillations to be smoothed out. To summarize, the method is able to reproduce in a self-consistent fashion the PSF of a“ mid-frequency” deformation at any λ, regardless of whether it is considered “roughness” or “figure error”. Obviously, in the limit of large λ, the PSF would be dominated by the aperture diffraction also in this case.

6.3.3 The PSF of rough mirrors: continuous power spectrum

The finished optical surface microrelief of X-ray mirrors cannot be obtained, in general, by superposing a discrete spectrum of frequencies (an exception is represented by mandrels at intermediate polishing stages, after the diamond turning process). Rather, their roughness is characterized by a *continuous* power spectral density, often modeled along with the power-law model (Church 1988),

$$P(f) = \frac{K_n}{f^n}, \tag{6.26}$$

where $1 < n < 3$ and K_n is a factor representing numerically the PSD at 1 μm. After selecting reasonable values for the two parameters, we can construct infinite possible profiles corresponding to that PSD, from which we derive the PSF by means

of Eq. 6.11. This situation would indeed correspond to the case of a rough but undeformed mirror: to account also for deformations that can arise at the manufacturing, integration, or handling stage, we superpose to the rough profile a deformation with a typical period equal to the mirror length. For the present simulation we adopt at all energies a 4^{th} order polynomial, 3 μm sag, long-period deformation (Fig. 6.9, left), superposed to rough profiles derived from Eq. 6.26 with n = 2.2, K_n = 0.5 nm$^3\mu$m$^{-2.2}$ (Fig. 6.9, right). We have thereby computed the mirror PSF from UV to hard X-rays, applying Eq. 6.11. They are displayed, already with the correct normalization, in Fig. 7.7 to 7.11.

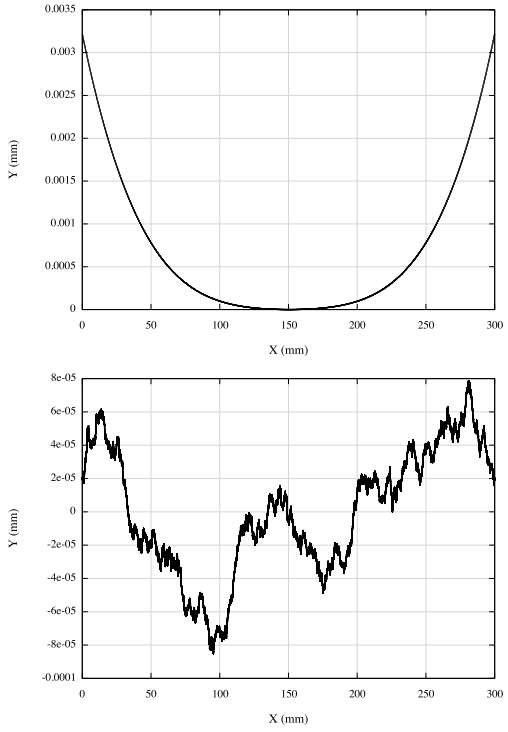

Figure 6.9: Left: the adopted "profile error" for this simulation. Right: a possible microroughness profile from a PSD with parameters n = 2.2 and K_n = 0.5 nm$^3\mu$m$^{-2.2}$.

In UV light (Fig. 7.7) we can clearly see how the aperture diffraction component is dominant. Almost no effect of the deformation can be seen, and the roughness is completely irrelevant at these wavelengths. However, the diffraction peaks become less pronounced and the HEW diminishes as the energy is increased (Fig. 7.8), but it does not tend to be infinitely narrow like in Sect. 6.3.1. At 100 Å, the PSF is already dominated by the polynomial deformation, with a $\sim$10 arcsec HEW, but it is only around 0.4 keV (Fig. 6.12), that geometrical optics is almost completely applicable,

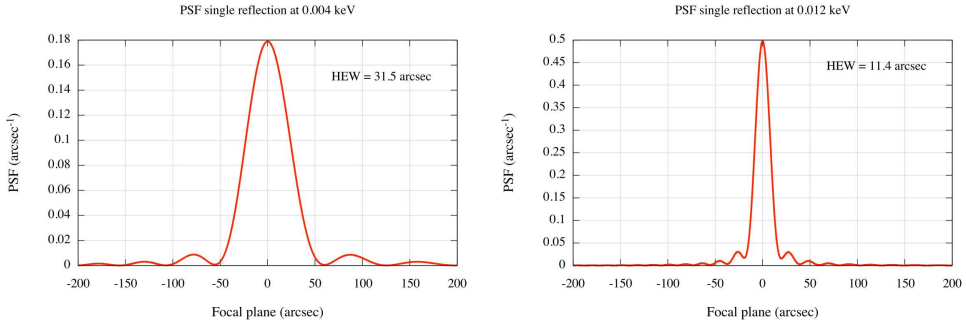

Figure 6.10: The simulated PSF in near UV, at (left) 3000 Å and (right) 1000 Å. The aperture diffraction prevails: the HEW is only slightly larger than for a perfect mirror (Fig. 6.5).

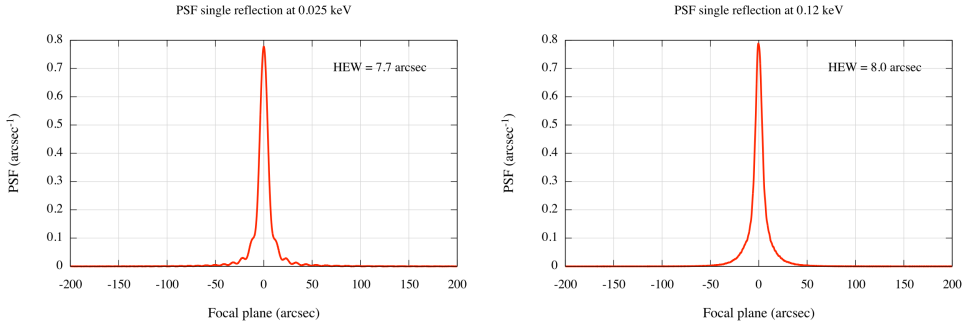

Figure 6.11: The simulated PSF in far UV, at (left) 500 Å and (right) 100 Å. The "figure errors" start to take over.

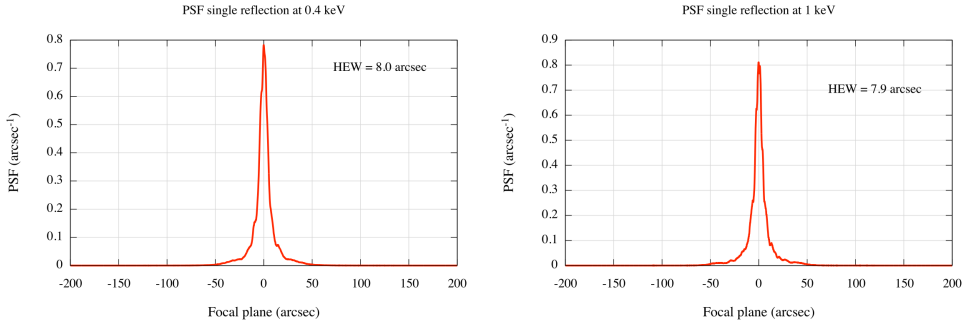

Figure 6.12: The simulated PSF in soft X-rays. At 30 Å (left), the PSF is dominated by mirror figure, since the PSF coincides with the ray-tracing of the mirror with the polynomial deformation. At 10 Å (right), the X-ray scattering starts to appear, and the HEW begins to increase.

as the PSF can be computed by ray-tracing the mirror plus the sole polynomial profile. In X-rays (Fig. 7.10 and 7.11) the effect of roughness starts to be visible: the X-ray scattering causes the PSF to broaden, with a consequent HEW increase. For a more realistic simulation, the last 4 PSF's have been computed by averaging the results for a variable number of computations (max 50) with different roughness profiles from the same PSD. This also allows to average out the PSF fringing, which in real cases is cancelled by the statistical nature of roughness.

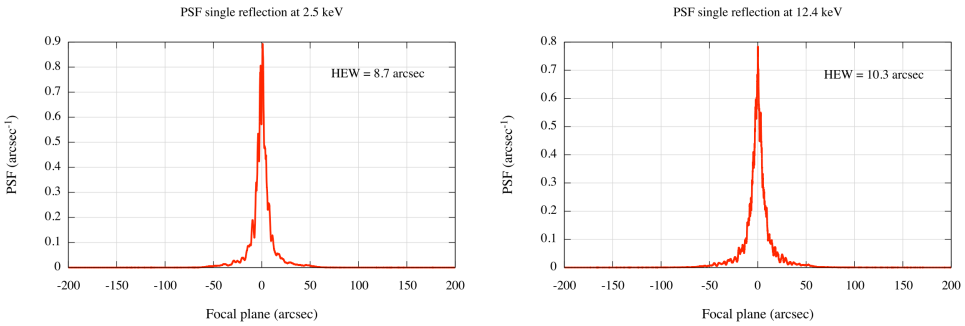

Figure 6.13: The simulated PSF in soft X-rays, at (left) 5 Å and (right) 1 Å. The X-ray scattering contribution is now clearly visible.

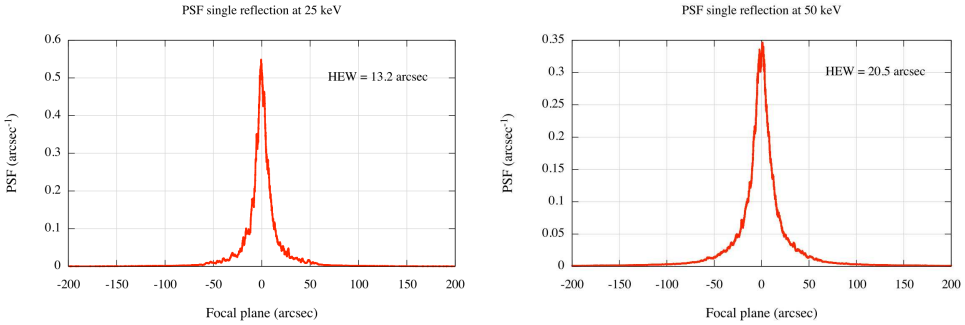

Figure 6.14: The simulated PSF in hard X-rays, at (left) 0.5 Å and (right) 0.25 Å. The X-ray scattering is now overwhelmingly dominating.

6.4 Comparison of the HEW results with the analytical model

We finally compare the results of the PSF computation of Sect. 6.3.3 with the HEW predictions of the analytical model (Spiga 2007). To do that, we consider 2 possible

couples of PSD parameters: either $n = 2.2$, $K_n = 0.5$ nm$^3\mu$m$^{-2.2}$, or $n = 1.8$, $K_n = 2.2$ nm$^3\mu$m$^{-1.8}$. Note that the first choice returns a steeper PSD, which has a larger content in low frequencies. This results in a different dependence of the HEW trend on the X-ray energy.

Firstly, we consider the case of a rough mirror without figure deformations. Form the PSF, computed using Eq. 6.11 at the X-ray energies, we have computed the HEW values as a function of the energy (Fig. 6.15, left) for the considered PSD. Then we compare them with the theoretical (Spiga 2007) scattering HEW prediction for a power-law PSD, in single reflection,

$$H(\lambda) = 2\left[\frac{16\pi^2 K_n}{(n-1)\ln 2}\right]^{\frac{1}{n-1}}\left(\frac{\sin\theta_i}{\lambda}\right)^{\frac{3-n}{n-1}}. \qquad (6.27)$$

Eq. 7.9 is a particular case of a more general formula (Spiga 2007) that allows computing the XRS term of the HEW from any PSD, and it can be applied because the PSD is below the smooth surface limit. The comparison shows a very good accord between the findings of the two techniques, excepting for the aperture diffraction, which cannot be reproduced by Eq. 7.9.

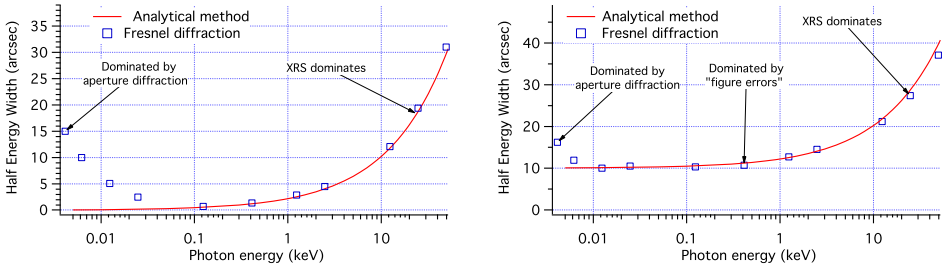

Figure 6.15: HEW simulations from the Fresnel diffraction and the analytical method. Left: roughness PSD only, with $K_n = 0.5$ nm$^3\mu$m$^{-2.2}$, n=2.2. Right: the same PSD, plus polynomial deformation.

As a second exercise we compare the HEW values with the analytical model, assuming not only the mentioned PSD for roughness, but also the polynomial deformation. This is the case already treated in the previous section (Fig. 7.7 to 7.11). The results, in Fig. 6.15, right, are similar to the left panel, but the HEW in the region 0.01 – 1 keV is nearly constant and close to 10 arcsec. In this region we can therefore say that the PSF is dominated by "figure errors" because the HEW – which *a posteriori* we can denote as *figure HEW*– is almost independent of the X-ray energy, and computable along with the geometrical optics. Interstingly, the Fresnel diffraction results can be reproduced by summing the figure HEW (10 arcsec) and Eq. 7.9 *linearly* instead of quadratically, as usually assumed. In Fig.6.16 we repeated the same

exercise with the smoother power-law PSD: also in this case the agreement of the two methods is very good, even if the HEW trend diverges more steeply.

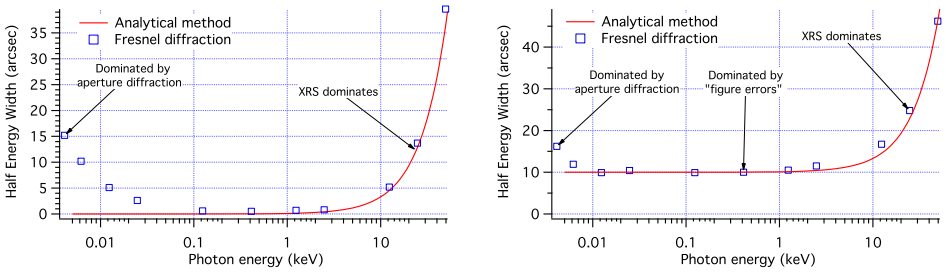

Figure 6.16: HEW simulations from the Fresnel diffraction and the analytical method: (left) roughness PSD only, with $K_n = 2.2$ nm$^3\mu$m$^{-1.8}$, n=1.8. (right) the same PSD, plus polynomial deformation.

6.5 Conclusions

In this section we have demonstrated how the Point Spread Function of a focusing X-ray mirror with imperfections can be computed at *any* monochromatic energy along with the Huygens-Fresnel principle, applied to meridional profiles of the mirrors. This can be done regardless of any distinction between figure errors and microroughness, also accounting for the aperture diffraction effects.
From this viewpoint, the classical distinction between figure errors and microroughness is unessential to the aim of computing the PSF: this treatment does not require setting any boundary. Moreover, the results of the geometrical optics and the first order scattering theory are automatically retrieved, wherever they can be applied, even if both represent "asymptotical" regimes not always well defined *a priori*. As an example, we have treated in a self-consistent way the behavior of a "mid-frequency" perturbation, in general difficult to manage because it cannot be uniquely attributed to one of two mentioned regimes. In particular, we have seen that the geometrical optics approximation results from the superposition of high order diffraction peaks, when their spacing becomes smaller than the detector spatial resolution.

7 The double reflection: Wolter-I system

In this section is presented the extension of the Fresnel diffracion method, seen in the previous section for a single reflection mirror, to an optical system with two grazing incidence reflections, and in particular applied to the Wolter-I geometry. It is shown some applications to a Wolter-I mirror including profile errors and roughness, from UV to hard X-rays, comparing the results to the corresponding PSFs for the parabolic (singly-reflecting) segment. We compare the HEW trends obtained from the Fresnel diffraction with the results of the analytical computation (Spiga 2007) if a "figure error" spectral regime can be easily recognized: in the considered case, characterized by a very low level of roughness in the millimeter range, the HEW trend from Fresnel diffraction matches very well the analytical approach results, provided that the figure HEW and the scattering HEW terms are *added linearly*, in accord with our previous findings for single-reflection mirrors (Raimondi & Spiga 2010) seen in the previous section.

In the general case, this method enables the computation of the PSF for any double reflection mirror.

7.1 Extension of the method to double reflection mirrors

7.1.1 Method generalization

Consider a grazing incidence mirror, with the axis oriented as the z-axis, and have the image formed at $z = 0$, at a distance f from the mirror exit. Let the mirror be completely described by its axial profile of length L in the xz-plane, specified by the function $x_{\mathrm{p}}(z_{\mathrm{p}})$. A planar wavefront of electric field amplitude E_0 impinges the profile along the z-axis from an infinite distance, at a nearly-constant incidence angle off-surface α. The mirror linear aperture, i.e., the difference of the maximum radius

$R_{\rm M}$ and the minimum radius R_0, has therefore the expression $\Delta R = L \sin\alpha$.

In principle, the electric field computation (Eq. 6.4) can be generalized to any mirror surface even if the incident wavefront is not planar,

$$E(x,y) = \int_S \frac{E_0(\underline{x}')e^{-i\xi(\underline{x}')}}{d_2\lambda} \exp\left(-2i\pi\frac{d_2}{\lambda}\right) \mathrm{d}^2 s_\perp, \tag{7.1}$$

where E_0 is the electric field amplitude at the coordinates $\underline{x}'$ on the mirror and ξ its phase at the same position. The method to extend the PSF computation to a double reflection consists of computing the electric field amplitude and phase as diffracted by the first mirror, at the surface of the second one, using Eq. 6.4. The subsequent computation of the diffracted field at the focal plane is obtained via Eq. 7.1. Nevertheless, the reduction to a single integral (like in Eq. 6.11) is an important step, otherwise the complexity of the computation will be overwhelmingly increased. Now, Eq. 6.11 is derived assuming that *the distance to the diffracting mirror is much larger than its linear dimensions* ("far field"). The reason is that some approximations are needed (Raimondi & Spiga 2010) to enable the fast integration over the $y_{\rm p}$ variable. If the mirrors are not separated by a large distance, like in the Wolter-I case (Sect. 7.1.2), the reduction to a single integration over the axial profile is more complicated, but still viable.

7.1.2 Application to a Wolter-I configuration

In a Wolter-I mirror shell, we cannot apply the far field approximation in the computation of the electric field on the hyperbolic profile, because the two segments intersect each other. For this reason, we cannot approximate $d_2 \approx f$ in the denominator of Eq. 6.4. Moreover, the funneling of rays toward the hyperbola owing to the azimuthal curvature is negligible at such a short distance, therefore the integration over the azimuthal coordinate is more complicated than in Fraunhofer approximation. Nevertheless, the integration is still feasible. We assume the two segments to have the same lengths, L, as measured *along the z-axis*, and f to be the distance of the intersection plane from the focal plane xy. We denote with R_0 the mirror radius at the focal plane, and with $R_{\rm M}$ the mirror radius at the shell entrance ($z_{\rm p} = f + L$).

The computation of the field at the hyperbolic profile (Fig. 7.1) at $y_{\rm h} = 0$, ($x_{\rm h}$, $z_{\rm h}$) is performed along with Eq. 6.4, using the expressions of d_1 and d_2, mapping the parabola in cylindrical coordinates $(r_{\rm p}, \phi_{\rm p}, z_{\rm p})$,

$$d_1 = f + L - z_{\rm p} \tag{7.2}$$

$$d_2 = \sqrt{r_{\rm p}^2 + x_{\rm h}^2 + (z_{\rm p} - z_{\rm h})^2 - 2x_{\rm h} r_{\rm p}\cos\phi_{\rm p}}, \tag{7.3}$$

where $r_{\rm p} = x_{\rm p}$ in the xz plane because of the supposed axial symmetry. Assuming that $\lambda L \ll R_0^2$, an hypothesis in general fulfilled, we are allowed to simplify the

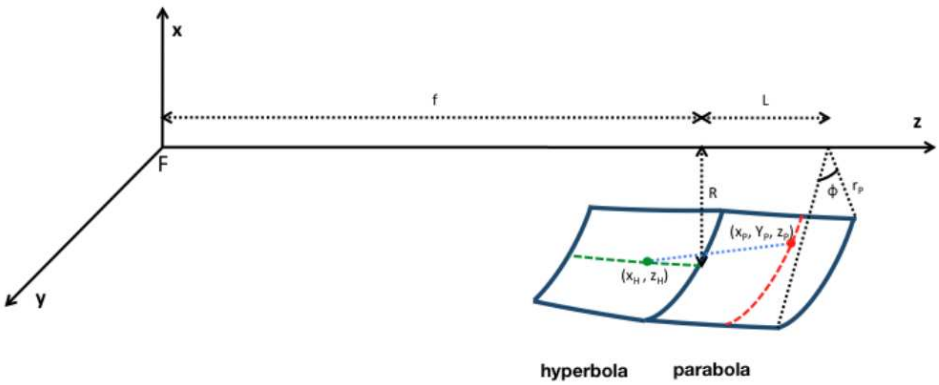

Figure 7.1: Scheme of a Wolter-I mirror. In this case we cannot apply the *far field* approximation in the computation of the electric field at the hyperbolic profile, therefore the integration over the azimuth has to be performed carefully.

exponent. Then, making use of Fresnel integrals, we can perform the integration over ϕ_p. The computation is too long to reproduce here, but this reduces the expression for the (complex) field at the hyperbolic surface to a simple integral in z_p:

$$E_\mathrm{h}(x_\mathrm{h}, z_\mathrm{h}) = \frac{E_0 \Delta R}{L\sqrt{\lambda x_\mathrm{h}}} \int_f^{f+L} \sqrt{\frac{x_\mathrm{p}}{\bar{d}_2}}\, e^{-\frac{2\pi i}{\lambda}(\bar{d}_2 - z_\mathrm{p})}\, \mathrm{d}z_\mathrm{p}, \tag{7.4}$$

where $\Delta R = R_\mathrm{M} - R_0$ (Sect. 6.2), we omitted an unessential phase factor and defined

$$\bar{d}_2 = \sqrt{(x_\mathrm{p} - x_\mathrm{h})^2 + (z_\mathrm{p} - z_\mathrm{h})^2}. \tag{7.5}$$

In Eqs. 7.4 and. 7.5 we have restored the x_p variable, replacing r_p.

The intensity of the electric field intensity on the hyperbolic profile exhibits the typical oscillations of the Fresnel diffraction pattern from a straight edge (Fig. 7.2). Moreover, note that the field is diffracted *beyond the hyperbola edge*, where the intensity is always nonzero: both oscillations and edge transition become more abrupt as λ decreases. All curves intersect at the edge of the region geometrically illuminated by the parabolic segment, where the intensity is – as expected from diffraction theory – 1/4 of the incident one. This is slightly shorter than the hyperbola length, owing to the curvature of the axial profile: were it a double cone, the illumination edge would have exactly matched the edge of the hyperbola.

The complex electric field E_h (Eq. 7.4) is then used to compute the field intensity on the focal line, this time in far field approximation and accounting for the power concentration owing to the azimuthal curvature (Raimondi & Spiga 2010). Then we

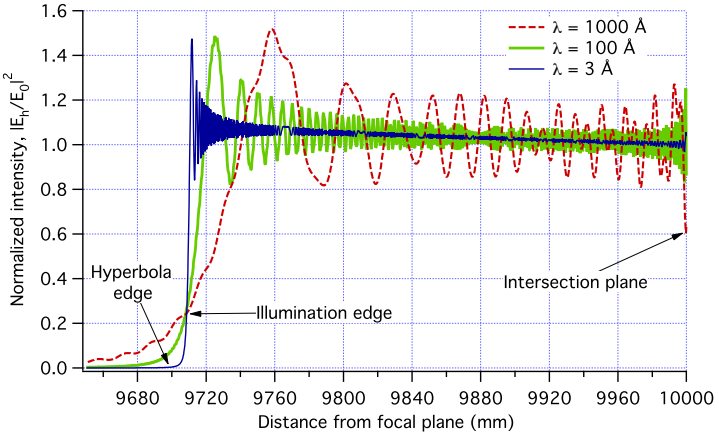

Figure 7.2: The field intensity along the hyperbolic profile in a perfect Wolter-I mirror, at λ = 3000 Å, 100 Å, and 3 Å, as computed with Eq. 7.4. We assumed that L = 300 mm, R_0 = 150 mm, and f = 10 m.

obtain the normalized PSF by dividing the focused intensity by the incident flux,

$$PSF(x) = \frac{\Delta R}{E_0^2 f \lambda L^2} \left| \int_{f-L}^{f} E_\mathrm{h}(x_\mathrm{h}, z_\mathrm{h})\, e^{-i\frac{2\pi}{\lambda}\left(\sqrt{(x-x_\mathrm{h})^2+z_\mathrm{h}^2}\right)}\, \mathrm{d}z_\mathrm{h} \right|^2 . \qquad (7.6)$$

The PSF is independent of the incident radiation intensity and normalized to 1 when integrated over x.

In the remainder of this thesis we make use of Eqs. 7.4 and 7.6 to simulate the PSFs of Wolter-I mirrors characterized by various profile errors and roughness. The numerical computation requires appropriate sampling of the parabolic profile, of the hyperbolic profile, and of the focal line: the optimal samplings can be established along with arguments analogous to those reported in Sect. 6.2, e.g., for the sampling on the parabola the angular acceptance of the detector shall be replaced with the one of the hyperbola, α. All the computed PSFs will behave according to the expectations.

7.2 Examples of PSF computation for Wolter-I mirrors

7.2.1 Perfect Wolter-I mirrors

He hereafter consider as a test case a Wolter-I mirror shell with f = 10 m, R_0 = 150 mm, L = 300 mm, θ_i = 0.21 deg. The analytical expressions $x_\mathrm{p} = x(z_\mathrm{p})$ and $x_\mathrm{h} = x(z_\mathrm{h})$ of Wolter-I nominal profiles (van Speybroeck & Chase 1972), when substituted into Eqs. 7.4 and 7.6 return a sinc-shaped PSF (Fig. 7.3, left) that becomes

more peaked and narrow as λ is decreased, as expected. In UV, the broadening caused by the aperture diffraction is clearly seen. It is worth pointing out that, even for a perfect Wolter-I mirror, the HEW in UV light is sensitively larger than the one resulting from a sole perfect parabolic segment, because the aperture diffraction occurs *twice*. Traditionally, the aperture diffraction of an optical system such as the double reflection Wolter-I is always considered that it was due to the effect of the edge shading of the sole parabola. Usually, the problem is treated like the incident wave is solely obstructed by an annular diaphragm of width $d = R_{max} - R_{min}$, where R_{max} and R_{min} are the minimum and maximum radius of the paraboloid mirror. If we compute the exact diffraction pattern integrated over circular coronae with diameter d in a single dimension applying the grating diffraction theory, this perfectly match with a predicted result of the single reflection simulation from a ideally parabola mirror (see Fig. 6.3). In contrast, in the Wolter-I configuration, the hyperboloid can not be considered only a *wave transducer*, it also has a diffrating effect, even if less produced than the first reflection. This is evident from Fig. 7.3 left, where we compare the PSF in UV light diffracted by a single paraboloid mirror and by a Wolter-I system. If we once again suppose that their surfaces are ideally smooth, we should expect the same focal spot as the single reflection. The comparison of the simulations that we presented in the previous chapter of the single reflection from a perfect parabola in the ultraviolet, with those made for Wolter-I always ultraviolet (assuming the identical parabola parameters), seems to contradict this hypothesis. This speculation is still under study.We are planning to measure this effect with a dedicated experiment, with characteristics of the mirrors that make the difference between single and double reflection is very pronounced (i.e. small figure errors, high obstruction).

Since many optical tests on Wolter-I X-ray mirrors are performed in UV light, the accurate subtraction of the diffraction aperture term should account also for the small difference introduced by the double reflection. In X-rays, the PSF resembles a Dirac delta function for both single and double reflection cases, as expected (Fig. 7.3, right).

7.2.2 Sinusoidal grating on parabola, perfect hyperbola

As a first example of imperfect Wolter-I mirror (sized as in Sect. 7.2.1), we have considered a sinusoidal grating with 0.1 μm of amplitude and 10 cm of period, *on the sole parabolic profile* (Fig. 7.4, left). This case was already treated extensively for the case of a single reflection mirror (Raimondi & Spiga 2010), finding that the same grating may behave according the 1^{st} order XRS theory, exhibit higher interference orders, or even comply the geometrical optics, depending on the X-ray wavelength in use. In particular at 0.4 keV, an energy that slightly exceeds the smooth surface limit (Eq. 6.1), we find that higher orders appear, but the grating is far from behaving according to geometrical optics.

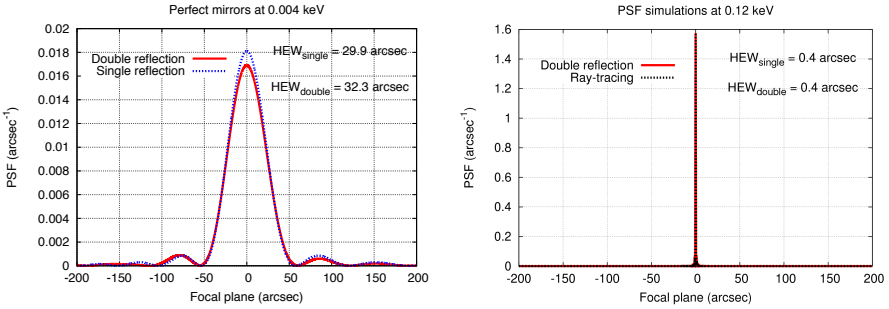

Figure 7.3: The PSFs of an ideal Wolter-I mirror. Left: in UV light at 3000 Å. Right: at 100 Å.

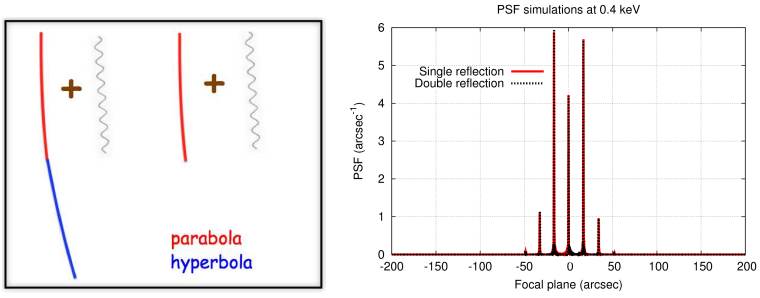

Figure 7.4: Left: Scheme of a Wolter-I profile with a sinusoidal grating (period 1 cm, amplitude 1 μm) on the sole parabola, Vs. a single reflection parabolic mirror with the same defect and the same size as the one of the Wolter's. Right: At 30 Å, the PSF simulation for the Wolter-I mirror with the perturbed parabolic profile returns exactly the same result as the single reflection case. The first orders are still dominant, but the second order peaks are already visible.

Now, since the hyperbola profile is not perturbed and aperture diffraction effects are negligible at 0.4 keV, we expect that the beam diffracted by the grating is simply reflected to the focal plane preserving the intensity distribution plus a very small aperture diffraction term. In fact, the simulated PSF is very well superposed to the one of the parabolic profile with the same incidence angle and grating (Fig. 7.4, right). This example puts Eq. 7.4 to the test: if the calculation were inaccurate, the subsequent diffraction would not have reproduced the exact positions and heights of the single reflection peaks, which – as a further confirmation – correspond exactly to those predicted by the sinusoidal grating theory. The same result is obtained imparting the sinusoidal profile to the sole hyperbola.

7.2.3 Long-period deformations of parabola and hyperbola

As a second example, we take into account a deformation on both mirror segments. Aiming at checking the validity and the accuracy of Eqs. 7.4 and 7.6, we have considered a profile whose effects are easily predictable in an independent fashion, e.g., along with a ray-tracing code. From the previous discussion (Sect. 6.2) we can expect that a single deformation with a long period, i.e., comparable to a 300 mm mirror length, should be treated with geometrical optics at, e.g., 0.1 keV. We have superposed the following perturbation to the segments of the Wolter-I mirror:

$$x_{\rm p}(z_{\rm p}) = \pm\frac{Lw}{4\beta}\log\cos\left(\frac{\beta z_{\rm p}}{L}\right),\ \text{with}\ \beta \lesssim \pi, \tag{7.7}$$

where w is the Half Energy Width for a single reflection, measured in radians, and β must be slightly less than π to avert a profile divergence. This figure error is tailored to return a Lorentzian-shaped PSF (a particular case of the well-known King function), as long as the aperture diffraction is negligible:

$$PSF(\theta) = \frac{2w}{\pi\left(w^2 + 4\theta^2\right)}, \tag{7.8}$$

where $\theta = x/f$, in radians. This PSF is a realistic model, e.g., SWIFT-XRT's matches very well a King shape: Moretti et al. (2004) on the other hand, Eq. 7.7 is the simplest profile, though not the only one, to be consistent with such a PSF. Since the $x_{\rm p}(z_{\rm p})$ profile can be taken with either sign, we have added the profile in Eq. 7.7 to the two segments with either the same sign or opposite signs. We have then computed the PSFs applying Eqs. 7.4 and 7.6.

If the two deformations have the same sign, the PSF spread is amplified (Fig. 7.5) with respect to the single reflection case. More exactly, the HEW of the Wolter-I deformed mirror equals 16 arcsec, exactly twice the HEW in single reflection. In contrast, if the two errors have opposite signs (Fig. 7.6), the angular deviations are

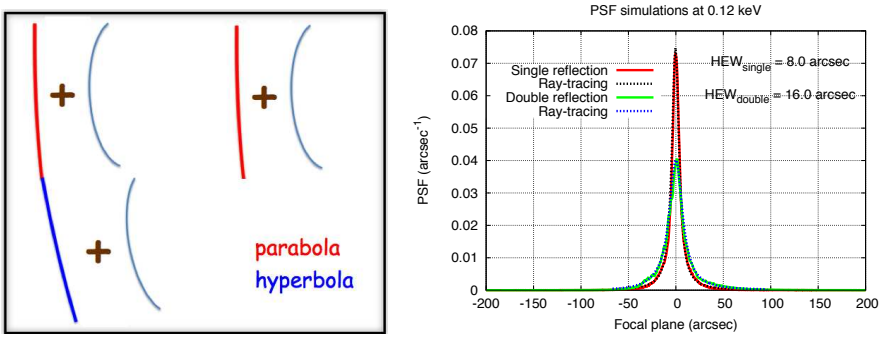

Figure 7.5: The PSF of a Wolter-I mirror with the same figure error (Eq. 7.7) at 100 Å, assuming $L = 300$ mm and $w = 8$ arcsec. Also plotted for comparison is the PSF simulated from the single reflection. The results match the ray-tracing prediction accurately (dots).

expected to compensate each other: in fact, the PSF computation correctly returns a nearly perfect delta function, with a HEW close to zero. All results are in perfect agreement with the results of the ray-tracing routine (definitely applicable in these cases). It is worth noting that these results contradict the common belief that the PSF of the Wolter-I mirror is the convolution of the PSFs of the two segments, because the convolution would return a broader PSF, not a narrower one.

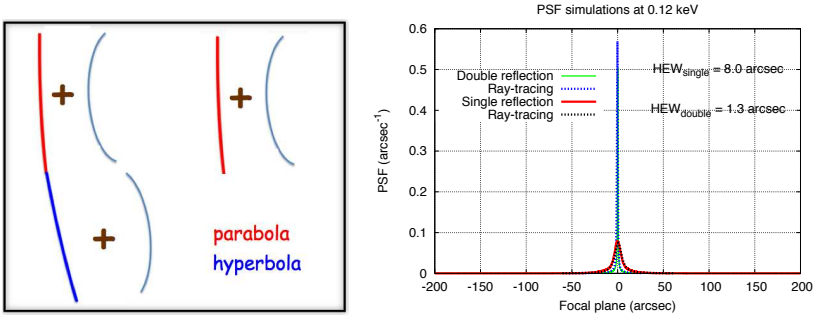

Figure 7.6: The PSF of a Wolter-I mirror with opposite figure error (Eq. 7.7) at 100 Å, assuming $L = 300$ mm and $w = 8$ arcsec. Also plotted for comparison is the PSF simulated from the single reflection. The results match exactly the ray-tracing prediction (dots)

7.2.4 Parabola and hyperbola with long-period deformations and roughness

As a last example, we consider a more realistic case accounting for both figure errors and roughness, as we already did for the single reflection (Raimondi & Spiga 2010).

We have adopted the mirror dimensions as in Sect. 7.2.1 and as figure error the same profile of Eq. 7.7 for both mirror segments (Fig. 7.5). The roughness is described by a Power Spectral Density (PSD) expressed by a power-law function (Church 1988), $P(f) = K_n/f^n$, where the spectral index n and the coefficient K_n depend on the surface finishing level. We have assumed as realistic parameter values n = 1.8 and K_n = 2.2 nm^3 μm$^{-1.8}$, and we have generated two of the infinitely possible profiles from this power spectrum. After superposing the rough profiles to the modeled figure errors and selecting a value for λ, we have computed the expected PSF using Eqs. 7.4 and 7.6. To reduce the noise in the PSF resulting from the pseudorandom nature of roughness, we have repeated the computation a few times and averaged the results. The average is needed only in hard X-rays, where the roughness effect starts to become apparent. Finally, the PSF has been degraded to a realistic spatial resolution of the detector (20 μm). The computation has been performed at several wavelengths from ultraviolet light to hard X-rays, always applying the same equations. The resulting PSFs are reported in Figs. 7.7 through 7.11, for increasing energies. We note that the aperture diffraction gradually disappears and the mirror deformation effects become visible. For $\lambda < 10$ Å, the effect of roughness causes the PSF to broaden and the HEW to consequently increase (see also Sect. 7.3).

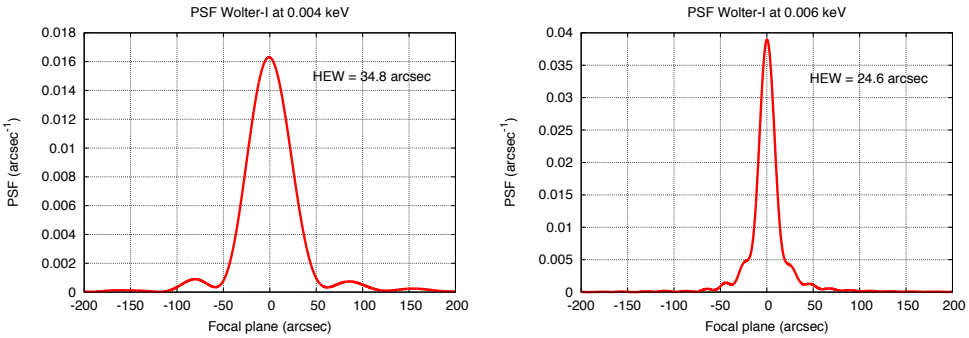

Figure 7.7: The simulated PSF in near- and mid-UV. Left: λ = 3000 Å: the aperture diffraction conceals most of mirror defects, the HEW is not much larger than that of a perfect mirror of the same size (32.4 arcsec, see Fig. 7.3). Right: λ = 1000 Å: the diffraction off the aperture (ΔR = 1.1 mm) is reduced and the PSF due to mirror shape becomes visible.

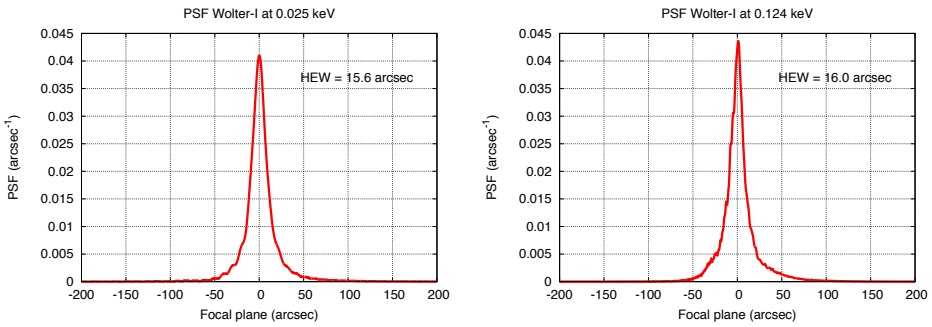

Figure 7.8: The simulated PSF in far UV. Left: λ = 500 Å: the PSF is solely determined by mirror shape deviations, and the HEW has decreased to a minimum value. Right: λ =100 Å: aperture diffraction fringes have completely disappeared, and the PSF is almost equal to the ray-tracing result from the the sole figure (compare with Fig. 7.5).

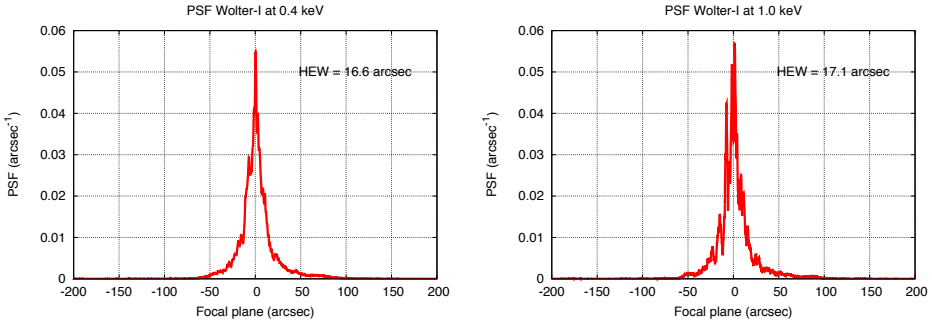

Figure 7.9: The simulated PSF in soft X-rays. Left: λ = 30 Å. Right: λ =12 Å: the first roughness effects start to appear.

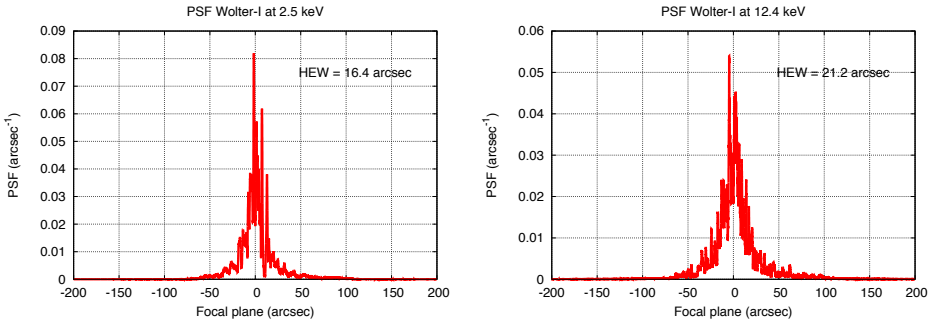

Figure 7.10: The simulated PSF in soft X-rays. Left: λ = 5 Å. Right: λ = 1 Å: the effects of roughness are now clearly seen. The PSF is much broader and the HEW is rapidly increasing.

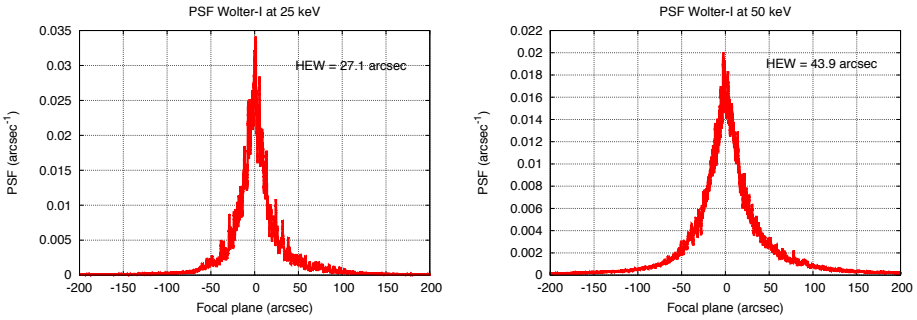

Figure 7.11: The simulated PSF in hard X-rays. Left: $\lambda = 0.5$ Å. Right: $\lambda = 0.25$ Å: the X-ray scattering is now overwhelmingly dominating.

7.3 Theoretical and experimental validation of results

We finally deal with a comparison of results of Sect. 7.2.4 with the HEW trend directly obtained from the roughness PSD, along with the analytical formalism (Spiga 2007) mentioned in Sect. 6. This method, applicable provided that a separation between figure roughness and scattering can be clearly set, allows us deriving the X-ray scattering term of the HEW as a function of λ, $H(\lambda)$, from the roughness PSD. This is the case of the mirror imperfections treated in Sect. 7.2.4, which are obtained by superimposing a long-period deformation to a microroughness profile: even though the PSD partially overlaps the spectral range of the assumed figure error, the amplitude of rough profile is much smaller (a few angströms Vs. a few microns), hence the mid-frequency component is very low. Moreover, the PSD fulfills the smooth surface limit (Eq. 6.1) for almost all the energies considered in the computation (< 55 keV), therefore the XRS theory at the first order can be applied to a good approximation. In the particular case of a power-law PSD (Church 1988) like the one adopted in Sect. 7.2.4, $H(\lambda)$ can be written in an explicit and useful form (Spiga 2007):

$$H(\lambda) = 2\left[\frac{16\pi^2 K_n}{(n-1)\ln\gamma}\right]^{\frac{1}{n-1}}\left(\frac{\sin\theta_i}{\lambda}\right)^{\frac{3-n}{n-1}}, \tag{7.9}$$

is a generalization of the 7.9 to an arbitrary number of identical reflections, where $\gamma = 2$ for a single reflection and $\gamma = 4/3$ for the double reflection (Wolter-I) case. The HEW trends for the parameter values used in Sect. 7.2.4 are reported as lines in Fig. 7.12 (left), for both single and double reflection cases. The respective HEW values, computed from the PSFs using the Fresnel diffraction applied to the sole roughness profiles, are plotted with symbols in the same graph.
At low energies, the two trends differ because the Fresnel diffraction method also accounts for aperture diffraction, while Eq. 7.9 does not. At high energies, the HEW

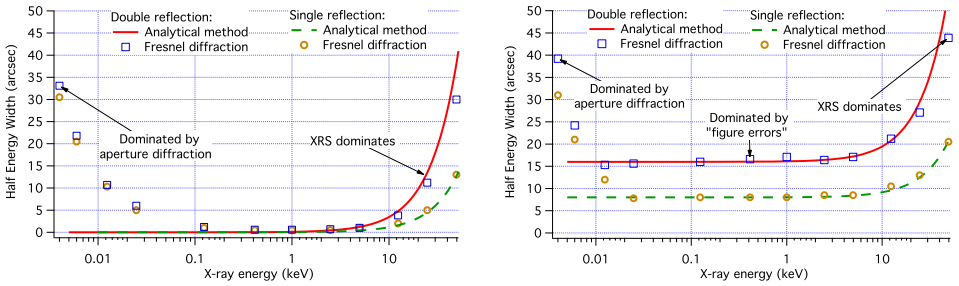

Figure 7.12: HEW results as computed by means of the analytical method (lines) and using the Fresnel diffraction (symbols). Left: only roughness PSD, Right: roughness and figure errors, same parameters as in Sect. 7.2.4.

computed with the two methods increase in mutual accord: the slight HEW overestimation with the analytical formula at higher energies can be due to the small scattering angles approximation, required by the 1^{st} order XRS theory, which is not exactly fulfilled (the Fresnel diffraction method does not require this condition). The low- and high-energy regimes are separated by a wide plateau where neither the aperture diffraction nor the scattering are relevant. Since no figure errors are by now assumed, the HEW plateau is close to zero.

If the figure error term is added to the rough profile, we obtain the PSF simulated in Figs. 7.7 through 7.11. The HEW trend (Fig. 7.12, right, symbols) appears similar to the one in the left graph, but the mid-energy plateau is at a 8 arcsec HEW for the single reflection and at a 16 arcsec HEW for the Wolter-I case. These figure error HEW values are the same obtained from the computation in Sect. 7.2.3 using the sole figure errors, taken with the same sign. The analytical simulations match the Fresnel diffraction results, for both single and double reflection, only if the respective figure error HEW values are added *linearly* to the $H(\lambda)$ functions computed from the sole PSD. In other words, *the XRS and the figure error terms of the HEW, when they can be computed separately, are apparently to be combined linearly* (Raimondi & Spiga 2010) and not quadratically as initially supposed. (Spiga 2007) This does not disprove the validity of the analytical approach, but it seemingly suggests the correct way to mix the two contributions. Tab. 7.1 compares the advantages of either method to compute the PSF.

7.4 Conclusions

We have implemented the self-consistent method based on the Huygens-Fresnel principle to compute the PSF to the double-reflection X-ray mirror. The method does not require distinguishing between figure errors and roughness, between ray-tracing and

	Fresnel diffraction	**Analytical method**
Computation result	Point Spread Function	Half Energy Width (XRS)
Smooth-surface condition	*Not required*	Required
Separation figure/roughness	*Not required*	Required
Mid-frequency treatment	*Fully consistent*	Uncertain
Computation time	Variable	*Very fast*
Formalism inversion	Very difficult	*Very easy*
Aperture diffraction	*Included*	Not included
Roundness errors	Not included	Not included

Table 7.1: Performances and drawbacks of the PSF computation based on Fresnel diffraction (Raimondi & Spiga 2010), and of the analytical method to translate the PSD into an HEW (and vice versa) (Spiga 2007).

scattering, and works at all energies, accounting also for aperture diffraction. It also provides a consistent treatment of mid-frequencies. The only approximations needed are that the incidence angle is shallow (i.e., $<$ a few degrees), and that the roundness errors have a negligible impact on the PSF. We have drawn our attention to a widespread category of double-reflection mirrors in X-ray astronomy, the Wolter-I, verifying that the resulting PSF behaves as per the expectations, taking the parameters of a NHXM mirror shell as a test case. The PSF computation reproduces the ray-tracing results wherever the geometrical optics may be applied. In hard X-rays, the single- and double-reflection results are consistent with the prediction of the analytical model, when it is applicable, provided that the separate contributions to the HEW from the geometrical profile and from the microroughness are summed linearly. The applications of this method to the development of X-ray optics for astronomy or terrestrial sources are potentially numerous.

8 Glass characterization for the IXO/ATHENA X-ray telescope

Within the project's mission IXO / ATHENA the Brera Astronomical Observatory is involved in the technological development of mirrors. The technology being studied is that of the *thin glass hot slumping*. The basic concept (as for other missions like ASTRO-H) is to segment the shell into radial sectors, manufacturing the two parabola hyperbola segments separately. This is achieved by hot slumping of the basic segments which are then integrated to obtain the form of nested shells. Mirror prototypes are made of a single cylindrical glass foil 200 x 200 mm with R=1 m and fixed to a backplane via 5 glass ribs. They were produced in the context of the phase A of the "IXO backup optics" with slumped glasses financed by ESA (Pareschi et al. 2011). Some glass foils were slumped at INAF/OAB using the direct slumping, others were produced by indirect slumping at the MPE (Max-Planck Institute), then integrated onto cylindrical backplanes via glass ribs (see Fig. 8.4). The figure and roughness of these glass mirrors was measured at INAF/OAB, but a coherent description of the expected angular resolution accounting for both roughness and profile was still lacking. The directly slumped glasses appeared to be superior in terms of figure accuracy, therefore the direct technique was selected for the 2^{nd} phase of the project.

In the context of my PhD project, I contributed to the study of metrology and analysis of these mirrors expected performance in terms of angular resolution using the new method presented in the previous sections based on the Fresnel diffraction. These results were then confirmed by tests carried out using the X-ray diffractometer.

8.1 Metrology characterization

The mirrors under examination have been characterized in profile and roughness. The final mirror shapes have been mapped with the *Characterization Universal Profilometer* (CUP, Civitani et al. 2010), with a lateral resolution of 5 mm. The microroughness has been measured with several instruments as an Atomic Force Micro-

scope (AFM, $50 \div 0.1$ μm), an X-ray diffractometer (20 μm $\div$ 50 nm) and a WYKO profilometer (2 mm $\div$ 10 μm), yielding a consistent roughness characterization in terms of Power Spectral Density (PSD) over more than 4 decades in spatial frequencies range.

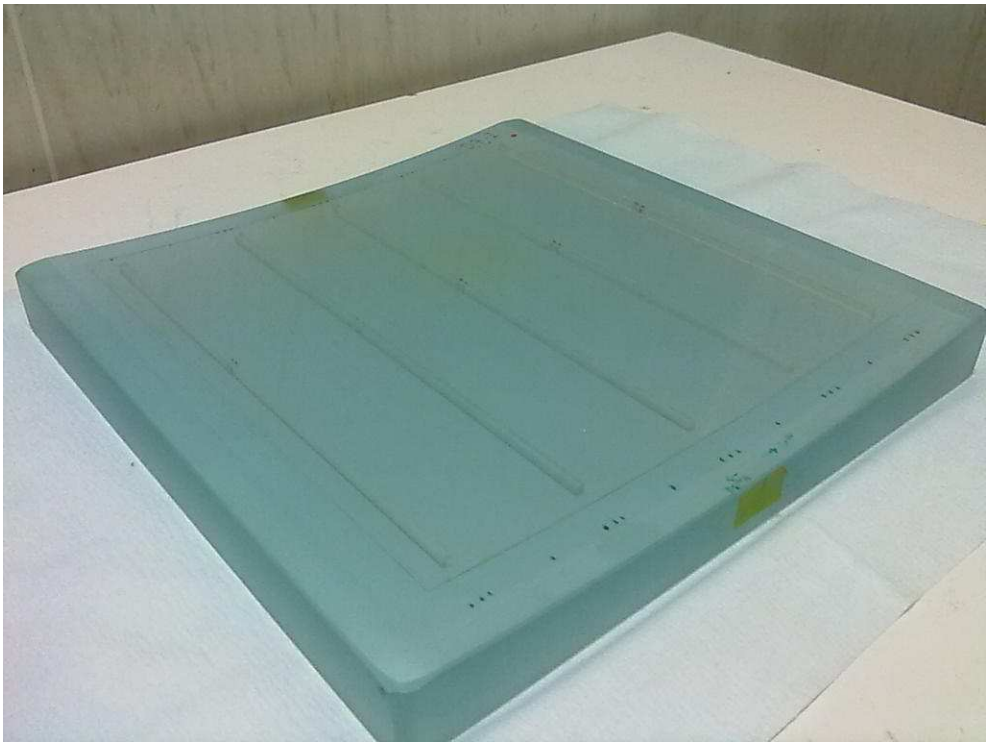

Figure 8.1: D7 integrated glass, fixed to a backplane via 5 glass ribs. Credits: INAF/OAB

We note that there is a spectral gap between the highest (the Nyquist's) frequency sampled by the CUP (1 cm) and the lowest frequency at which the PSF was measured. This spectral range will turn out to be very important for the imaging degradation of the mirrors at 1 keV at the actual incidence angle (0.72 deg), therefore the estimations would probably be *optimistic* with respect to the true mirror performances. For this reason, the part of the spectrum in the 10-1 mm range has been derived by interpolation of CUP and WYKO data.The four glass X-ray mirrors under test are two, D5, D7, directly slumped glass plate and two, T20, T112, indirectly slumped. The surface mapping of the four glasses being considered are shown in Fig. 8.2 and Fig. 8.3 in 3D view, after subtraction of the best cylindrical fit. The residuals, which exhibit clear undulations in the direction orthogonal to the cylinder axis because of the spring-back of the foil where it is not held by the ribs, are used to derive the linear profiles in

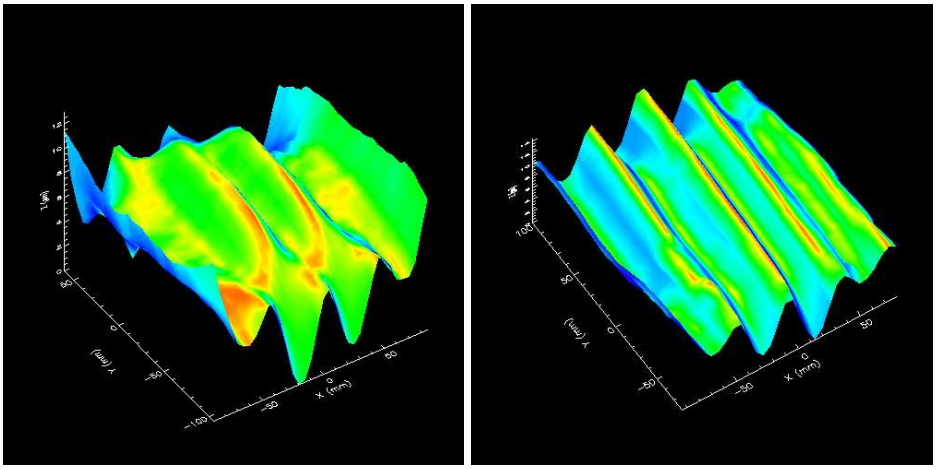

Figure 8.2: Direct slumping. Residuals of surface mapping of the glasses being analyzed, obtained with the CUP (measurement by M. Ghigo and M. Civitani INAF/OAB). The best fitting cylinder for the D5 (*left*) glass has a 1001 mm radius and a -2.57 deg tilt, the D7 (*right*) glass has a 1000.6 mm radius and a -0.19 deg tilt. The longitudinal grooves are in correspondence of the ribs used for fixing the glass to the backplane.

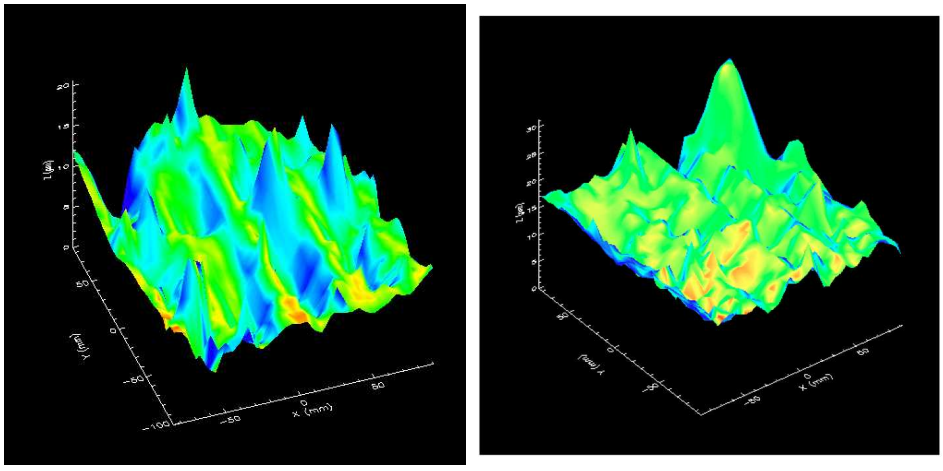

Figure 8.3: Indirect slumping. Residuals of surface mapping of the glasses being analyzed, obtained with the CUP (measurement by M. Ghigo and M. Civitani INAF/OAB). The best fitting cylinder for the T20 (*left*) glass has a 1001 mm radius and a -2.57 deg tilt, the T112 (*right*) glass has a 1000.6 mm radius and a -0.19 deg tilt. The longitudinal grooves in correspondence of the ribs used for fixing the glass to the backplane are less evident than in the direct slumping case.

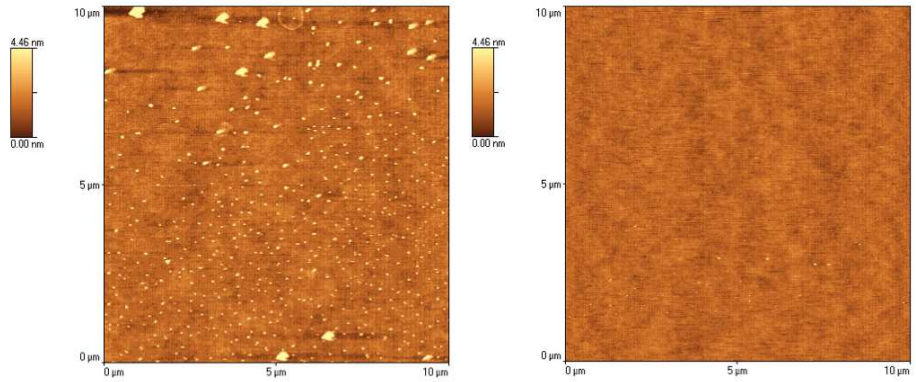

Figure 8.4: AFM maps, 10 μm range, of the T20 glass. A contaminated point (left) and a clean point (right). The PSD from AFM shown in Fig. 8.6 left panel, which refers to a clean point, matches the PSD derived from the LR XRS. This means that the contaminations are likely unseen by 8 keV X-rays. Credits: INAF/OAB

the axial direction that are responsible for a large part of the HEW. The undulations are oriented perpendicular to the incidence direction therefore they have only a minor impact on the HEW degradation (a few arcsec) (see sect, 6). The roughness of the four glasses is represented in Fig. 8.5 and Fig. 8.6 in terms of PSD for the four glass plates. We note that the two glasses have similar roughness, with a steeper slope at spatial wavelengths larger than 500 μm, but at low frequencies ($\sim$1 mm) the D5 is worse.

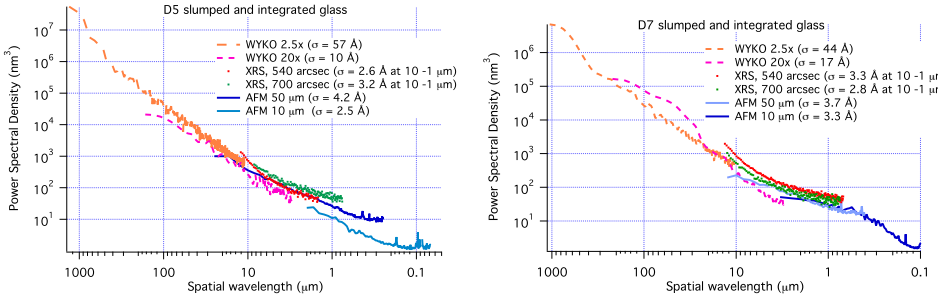

Figure 8.5: PSD's obtained from AFM, WYKO and X-ray scattering at 8.05 keV measurements. D5 glass (*left*) and D7 glass (*right*).

However, the WYKO measurements have shown that the directly slumped glasses are often characterized by defects over the millimetre scale (Fig. 8.7). The reason of this different behaviour is not understood yet: indeed, this spectral region is known

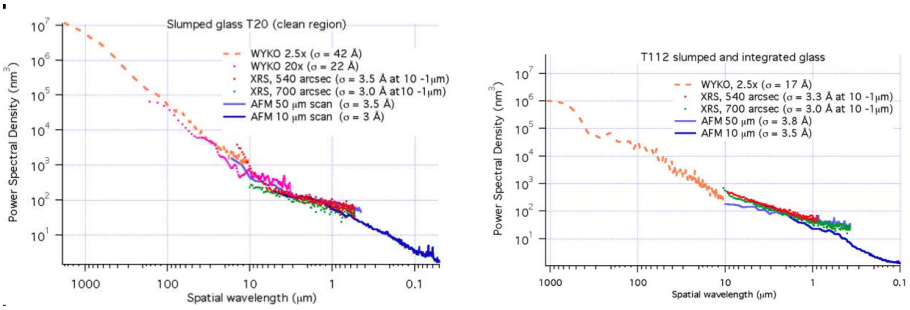

Figure 8.6: PSD's obtained from AFM, WYKO and X-ray scattering at 8.05 keV measurements. T20 glass (*left*) and T112 glass (*right*).

to degrade heavily the PSF already at low energies (1.5 keV), as it can be verified by computing the PSF expected from the CUP topography and the glass PSD. It is thereby important to ascertain the real presence of such a low-frequency roughness: we note that at higher frequencies the roughness takes on similar values for both kind of slumping techniques (Fig. 8.5 and Fig. 8.6) excepting a much higher level of surfacial contamination of indirectly slumped glasses. Finally, the spectral region 1 cm - 2 mm was not measured because it falls in a gap between CUP and WYKO: the vertical sensitivity of the CUP sensor (20 nm) used in phase 1 would not allow us seeing such defects, even with a smaller step than the 5 mm adopted.

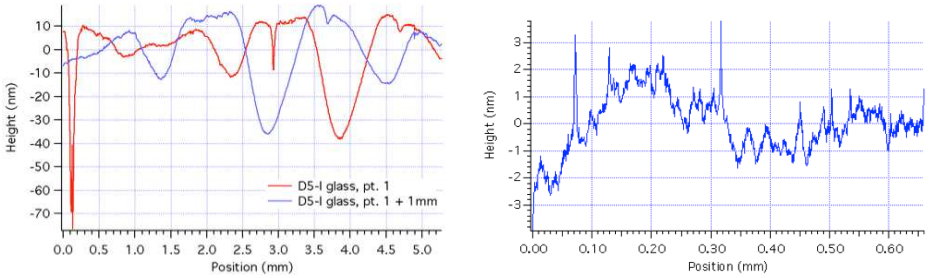

Figure 8.7: WYKO measurements performed on the D5 glass after integration. Left: 2.5x magnification, 5.2 mm scan length, rms 120 Å. The profile was measured twice after moving the sample laterally by 1 mm, to make sure that the observed undulations are not instrumental effects. Right: 20x magnification, rms 11 Å.

8.2 Low resolution XRS measures

To the end of checking the real presence of low-frequency roughness on the optical side of directly slumped glasses and their effect on the PSF at low energies, we executed XRS measurements using the BEDE-D1 diffractometer (Fig. 4.15) at the standard energy of 8.045 keV (Cu-Kα line). Such measurements are addressed at measuring the PSD in the micron range (Fig. 8.5 and 8.6), hence they explore the faint scattering signal at large angles off the specular reflection direction (Fig. 8.8). In this condition, the priority was to get an intense X-ray beam (i.e. a photon flux of 105 count/sec or more) without paying a particular attention to the spatial resolution of the measurement, which in turn determines the spectral resolution of the measured PSD. We have then shapes a collimated beam along with the double monochromator at low resolution emerging from a 400 μm wide slit (20 arcsec FWHM divergence in the horizontal plane). The beam impinges the glass at a graze angle and is analysed by an angular scan of the scintillation detector (Fig. 4.20). The measurement angular resolution was - in LR configuration - determined by the width of the slit in front of the detector (400 μm, yielding a 320 arcsec angular acceptance), unsuitable to measure an expected 20 arcsec HEW. However, the scattered intensity at high frequency has returned a roughness characterization to be compared with the direct topography results, using the equation 4.5. The accord of the two measurement methods is excellent (see Fig. 8.5 and 8.6). We note that all glass foils have a similar scattering level in this configuration.

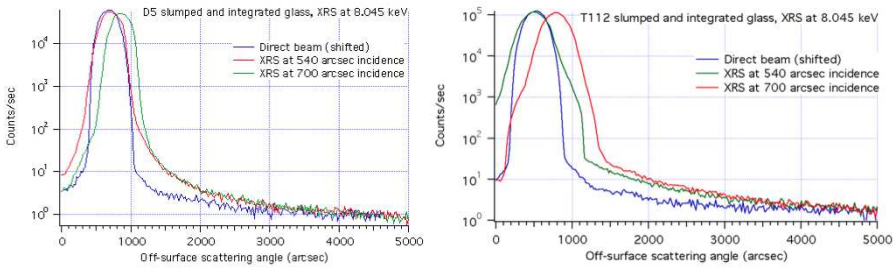

Figure 8.8: Left: Low-resolution XRS measurement of the D5 glass. Right: of the T112. In this setup the CCC analyser in not used: the beam spread is measured by rotating the detector. The higher low- frequency roughness in the former and the worse shape in the latter are barely visible at a glance, even though the poor angular resolution does not enable seeing them clearly.

8.3 High resolution XRS measures

In this section is reported the high resolution XRS measurement performed onto some slumped and integrated glasses in phase 1 of the "IXO backup optics" project, aimed at checking the impact of the mid-frequency microroughness on the low-energy PSF. The measurement achieved with CUP on the integrated glasses D5 and D7, with a lateral resolution of 5 mm, and - correctly - treated using geometrical optics, returned HEW values close to 20 arcsec. The same measurement achieved on the glasses T20, and T112 obtained by indirect slumping, returned much higher values ($>$ 80 arcsec). This has been ascribed to glass thickness variations, which in the indirect slumping process affect the optical surface of the glass foil (Fig. 8.3). To detect the

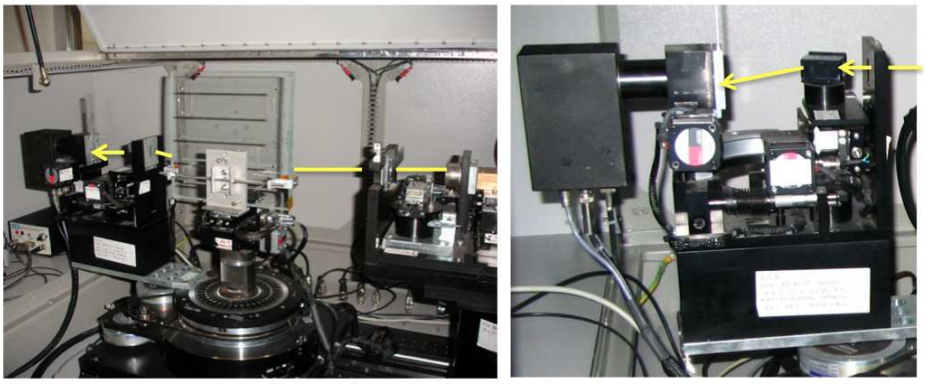

Figure 8.9: Experimental setup for high resolution XRS measurements (left) and close view of the detector stage (right). In the HR-XRS measurement, the angular distribution of X-ray photons is analysed by a high-resolution Si CCC before being counted by the scintillator.

PSF of the glass region covered by the beam, therefore, we have left the detector at the fixed position of specular reflection and we analysed the angular distribution of scattered X-rays using the analysing CCC, whose nominal angular resolution is a few arcseconds if the HR channel is adopted. The achievable angular resolution is thereby dominated by the incident beam divergence, which has been minimized by filtering the beam out of the X-ray tube with the double Si CCC, using the high-resolution channels. The price we have to pay, of course, is a dramatic reduction of the beam intensity (5000 - 7000 count/sec). This is partly compensated by the higher intensity of the scattering power in the vicinities of the specular reflection. A long integration time ($>$ 10 sec) per point is suitable to obtain affordable statistics in the photon count.

Using the dual channel analyser crystal in high-resolution configuration, we checked that the incident beam is highly collimated in the horizontal plane (within 5 arcsec of FWHM, Fig. 8.10). To reach such performances it is crucial to adjust the analyser tilt

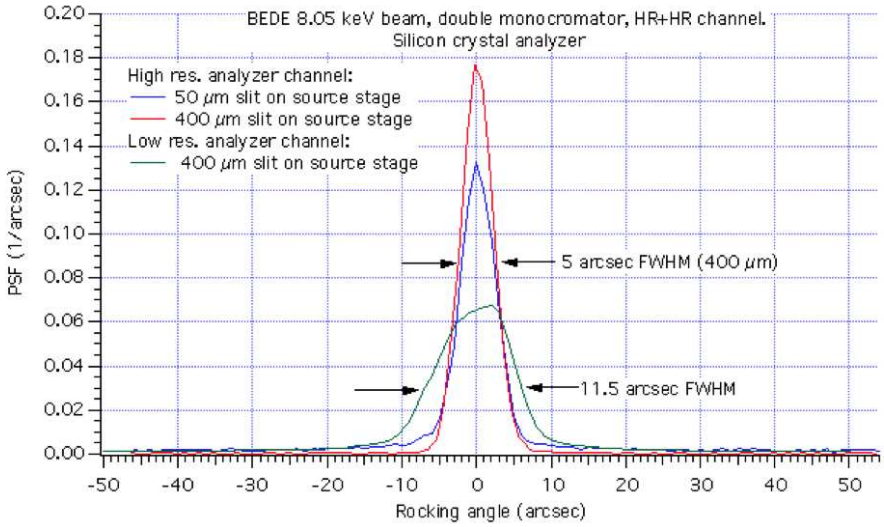

Figure 8.10: direct beam characterization collimated by the HR monochromators, using the HR (red and blue lines) and the LR (green line) channel of the dual channel analyser. The angular width of the beam distribution (always normalized to unity) is a bit larger in the 50 μm case, probably because of some scattering on the collimating slit walls.

in such a way the beam lies in the crystal surface. If this is not done, some part of the vertical angular dispersion (uncollimated) is read with the horizontal one. Once the tilt is optimized, the beam collimation becomes nearly independent of its width, as one can check by placing slits of variable width after the monochromators (Fig. 8.8). The LR channel returns an angular distribution more dispersed by a twofold factor. It is worth noting that in all the XRR measurements we had hitherto performed the angular resolution was much worse (20 arcsec) because we always preferred a high intensity beam, therefore we always used the LR channels of monochromators. Even when using thin slits to obtain a few tenths micron wide beam, we always used a single monochromator because we were not interested in achieving an angular resolution better than 20 arcsec. The monochromatic energy in use is 8.045 keV, much higher than the 1.5 keV at which we are meaning to measure the PSF. Nevertheless, adopting an incidence angle smaller than the nominal one (0.72 deg) by the same factor, the $\lambda/\text{sen}\alpha$ ration which the scattering - at any order - depends on remains unchanged. Therefore, we approximately reproduce the XRS effects at 1.5 keV by impinging the glass surface at 500 arcsec with the 8.045 keV beam. This angle remains - opportunely - in the total external reflection range of the glass at 8.045 keV. The reflected beam angular distribution is the convolution of the PSF expected from the glass topography and the response function of the instrument (i.e. the direct beam after normalization). The angular dispersion of the X-rays after the reflection has been analysed using a beam 400 μm wide or sometimes using a narrower slit (50 μm or 100 μm wide). In the former case we are covering 165 mm of the glass length, i.e. almost all of its length, whereas in the latter we are illuminating a much smaller length, circa 20/40 mm. Much attention must be paid to the alignment of the beam to the cylinder axis to avoid a spurious curvature term that would disperse the incidence directions up to a maximum angle of

$$\Delta\theta_{refl} \approx \frac{\alpha^2 L}{R} \tag{8.1}$$

with R = 1 m, L = 200 mm. If for example we are misaligned by α = 1 deg, this would be equivalent to include a 12 arcsec curvature term. However, by scanning the pivot axis the alignment error can be reduced to 0.5 deg at most, hence the spurious HEW is 4 arcsec at most, that is much less than we are expected to measure. Moreover, by performing the measurement with a 50 μm wide beam we would cover a 2 cm length on the surface, hence the spurious term is negligible even in case of misalignment. Another very important point concerns the glass surface tilt, which needs to be co-planar to the beam, otherwise the beam will be reflected no longer co-planar to the analyser crystal surface, and the analyser will read the angular dispersion of the beam in the vertical plane. As we could not check that by watching the beam in the camera because of the low beam flux, we have realigned the analyser crystal by minimizing the width of the rocking curve of the CCC.

In the next sections we display the results of the measurements performed on the slumped glasses.

8.3.1 D5 slumped glass (direct slumping)

The rocking curve of the scattered beam off the D5 glass is displayed in Fig. 8.11. This is also a direct measurement of the PSF stemming from the surfacial defects of the mirror in X-rays at 8.045 keV at a 500 arcsec grazing incidence, or, almost equivalently, at 1.5 keV at 0.72 deg. The reflected beam (normalized to the unity) is apparently broadened with respect to the direct beam (Fig. 8.10), and the broadening in nearly the same for both settings with the 400 μm and 50 μm slit, meaning that most of PSF degradation is caused by short-scale defects (< 2 cm).

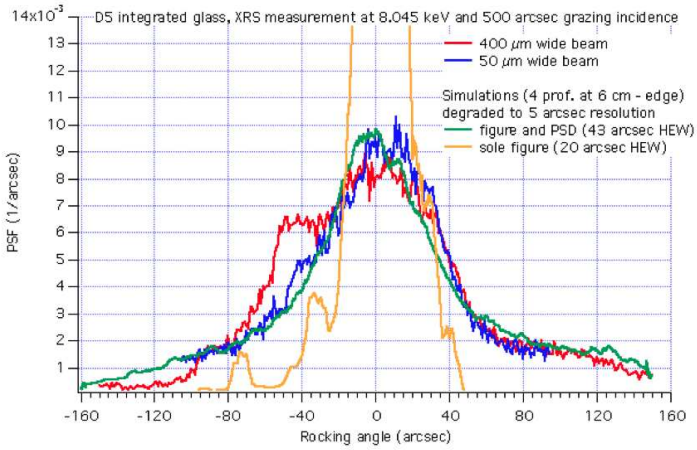

Figure 8.11: HR-XRS measurement of the D5 sample, along the cylinder axis at 6 cm from the edge. The measurement (red and blue) is compared to the simulation (green) obtained from profile and roughness. The agreement is good. The discrepancy might be due to the poor sampling of profiles used over the vertical extension of the beam (2 cm). The measured HEW is larger than 43 arcsec. Note that the simulation using the sole CUP profile (yellow) would not match the data.

The experimental result has been compared to the simulation using the available data from CUP and the measured PSD. The PSF simulation has been performed using the Fresnel diffraction algorithm adopting as glass shape the 4 profiles parallel to the ribs (5 mm spaced) in the strip covered by the X-ray beam (2 cm high), located at 6 cm from the side. Regarding the extension covered by the beam along the axis, using the measurement setup with a 400 μm wide beam, we obtain a 165 mm footprint length, i.e. almost the total glass length, and the exact width of the CUP scan. The adopted

roughness collects the WYKO and the AFM measurements, which cover together the spectral band 2 mm - 0.1 μm. The missing spectral range (1 cm - 2 mm) is bridged by interpolating the PSD from WYKO to the one obtained from CUP residuals. In order to smooth out the noise caused by the pseudo-random nature of roughness, we averaged the PSFs from 36 simulated rough profiles using the PSD and cycling over the 4 CUP profiles in use. Eventually, the simulation has been convolved with the normalized direct beam (5 arcsec FWHM) to account for the measurement system resolution. It is noteworthy that in this case the 1st order scattering application is not accurate for spatial wavelengths of a few millimetres, because the oscillations are too large, so they create relevant higher orders at larger angles: for these spatial frequencies, the geometrical optic begins to be applicable.

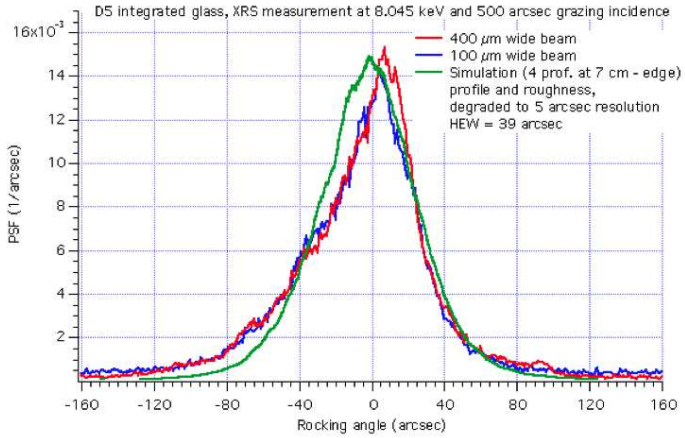

Figure 8.12: experimental PSF of the D5 glass, at a different location than the one used in Fig. 7. Also in this case the PSF shape is well reproduced by the simulation, even if the experimental result is more asymmetric than the simulated one.

The 1st order theory is suitable, indeed, for spatial wavelengths $<$ 1 mm, and it returns a 13 arcsec HEW contribution at 1.5 keV. The remainder of the HEW - that brings the HEW to 43 arcsec - is related to the finite resolution of the measurement ($<$ 5 arcsec) and to the unmeasured band 1 cm - 2 mm. The validity of the Fresnel approach adopted here, in contrast, is unrestricted as it is applicable at any spatial frequency and for any profile and roughness. The comparison theory/experiment is shown in Fig. 8.11. The matching of theory (green) and experiment (red) is quite good, even if the experimental broadening is still wider than the simulated one. The matching is also good with the PSF measured with the smaller slit (50 μm wide), denoting a dominant influence of the scattering in the PSF degradation. To verify that, we also performed a simulation using the sole CUP profiles (yellow line, out of

vertical range). The resulting PSF is much more peaked than the experimental one, with a HEW of 20 arcsec. The discrepancies in the PSF shape are also caused by the inaccurate location of the region covered by the beam on the glass. Since the D5 shape is quite irregular, this may result a sensitive variation of the exact shape of the PSF, even if the low-frequency roughness effect is detected clearly. Another measurement has been obtained in another region of the slumped glass by flipping the integrated glass (a mounting at a different height has been adopted, therefore the profiles illuminated by the X-rays are now at a 7 cm distance from the edge). The shape of the PSF (Fig. 8.12) is more triangular than in Fig. 8.11, but the HEW value is only slightly lower. Also in this case the simulation using the Fresnel diffraction (using both profile and roughness) approximately reproduces the measured results.

8.3.2 D7 slumped glass (direct slumping)

The same high-resolution XRS measurement has been performed on the D7 slumped and integrated glass. The deviation from the ideal cylinder and the roughness PSD of the optical surface are shown in Fig. 8.2 right panel and Fig. 8.5 right panel. With respect to the D5, the shape is more regular, which makes less critical the selection of profiles to be used for the simulation. The roughness is similar but slightly better than D5, and moreover the 20x and 2.5x WYKO magnifications returned mismatching results.

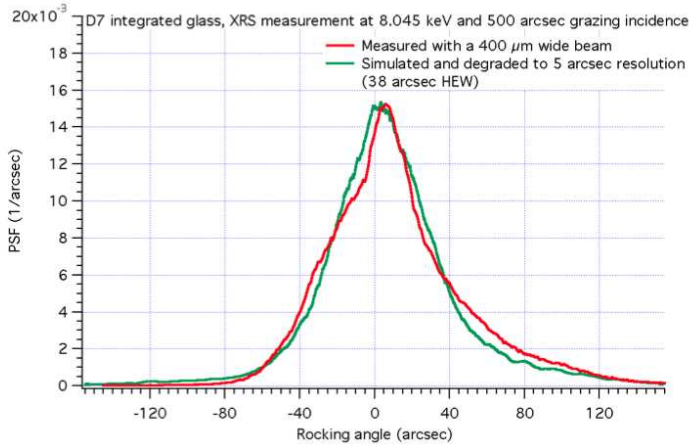

Figure 8.13: high-resolution XRS measurement of the glass D7, along a profile at 7 cm from the edge of the foil. The XRS measurement and the PSF simulated from surface map and roughness match very well.

The XRS measurement at 8.045 keV and 500 arcsec incidence in high-resolution

setup is shown in Fig. 8.13. The PSF exhibits a triangular shape with asymmetric tails. The PSF has also been simulated from 4 profiles of the CUP map and the (extrapolated) roughness PSD. The agreement of the simulation with the experimental PSF is excellent (Fig. 8.13). We note, from comparison with that the spectral region 1 cm - 2 mm obtained from extrapolation is essential to determine the PSF broadening.

8.3.3 T112 slumped glass (indirect slumping)

This glass foil was obtained by indirect slumping. As it appears from the CUP map in Fig. 8.3 right panel, the shape of the glass, after subtraction of the best-fit cylinder, is very irregular, and consequently the HEW, even the one obtained with geometric methods, if much higher (114 arcsec only from the CUP map). The roughness PSD is very similar, in the high frequency range, to the one of directly slumped glasses (Fig. 8.6 right panel). In the millimetre - 0.1 mm realm, indeed, the surface of this indirectly-slumped glass is better.

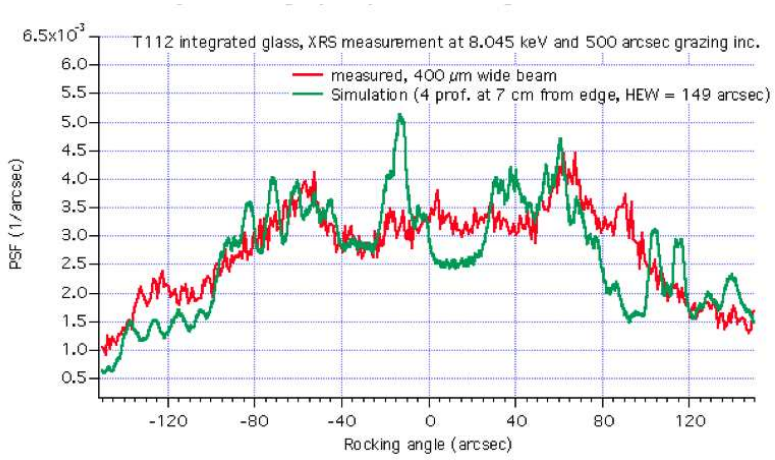

Figure 8.14: high-resolution XRS measurement of the T112 indirectly slumped glass. The reflected beam is heavily broadened by the irregular profile of the glass. The simulation matches well the experimental PSF if we remind that only 4 profiles were included in the computation.

The PSF was measured in high-resolution configuration (Fig. 8.14) and, in spite of all possible optimization of the mirror alignment, we could not obtain a PSF narrower than this. The simulated PSF including topography and roughness also returns a good matching with the experiment, even if the roughness PSD is almost irrelevant. The HEW reaches the huge value of 149 arcsec, not far from the 112 arcsec derived by ray-tracing the CUP map. In fact, executing a ray-tracing (using the sole CUP

profile!) instead of using the physical optics would nearly return, in this case, the same result of the computation.

8.3.4 T20 slumped glass (indirect slumping)

The T20 glass, obtained by indirect slumping, exhibits a less irregular map of residuals (Fig. 8.3 left panel and Fig. 8.6 left panel) then the T112. The HEW due to the sole figure is, in fact, 82 arcsec Vs. 114 arcsec of the T112. However, the roughness PSD is worse. Some undulation in the low-frequency regime is present to a level comparable to the D7 glass obtained by direct slumping. For this reason the simulation is affected by scattering, even if it is dominated - unlike the D7 - by profile errors.

The surface of this glass, when viewed with the AFM, appears somewhere covered by small defects that are interpreted as surface contaminations. The PSD adopted for the computation (Fig. 8.6 left panel) in the AFM spectral band is derived from a contamination-free zone, in accord with the low-resolution XRS measurements. This might indicate that either 1) the sampled region with the X-rays is clean or 2) the defects are contamination from organics or dust, which do not affect the propagation 8 keV X-rays. The situation might be different for 1.5 keV X- rays, that could be more easily scattered: this is a limit of the computation based on the same $\lambda/\sin\alpha$ ratio.

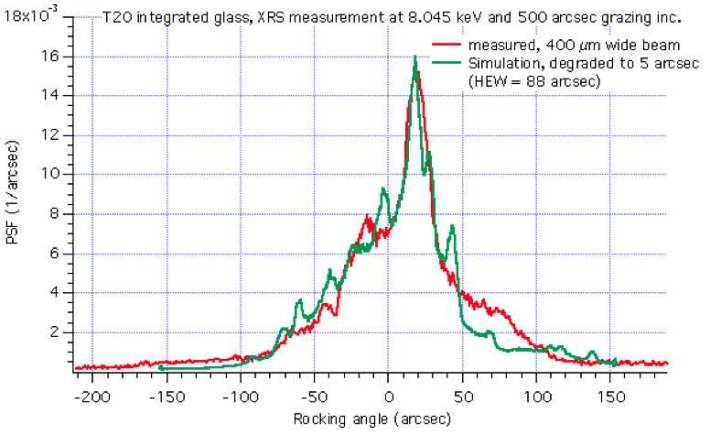

Figure 8.15: high-resolution XRS measurement of the T20 indirectly slumped glass, along a profile at 7 cm from the edge. The PSF simulation is also shown.

The high-resolution XRS measurement of the T20 glass is reported in Fig. 14 (red line). Also in this case, the X-ray beam covered a 2 cm-high region. The 400 μm

wide beam, de-projected at a 500 arcsec incidence angle along the profile, impinged almost all the length of the slumped glass along the axis. The shape of the PSF is peaked with a relevant "skirt" of scattered photons. The simulation of the PSF from the glass profiles and the roughness is also shown: the shape of the peak and the width of the skirt are well reproduced. Also some secondary peaks are drafted, even though their positions do not perfectly match the ones of the experimental PSF. The mismatch is related to the inaccurate knowledge of the relief of the surface portion illuminated by X-rays. Since - like in the case of the T112 - the shape of the glass dominates the PSF, 4 longitudinal profiles in the region probed by X-rays might be insufficient to characterize it.

8.4 Analysis of different spatial wavelength ranges impact on PSF degradation

In the previous section we have computed the expected PSF's of the D5 and D7 slumped glasses, and we have shown that the X-ray scattering for the D5 glass is relevant also at $\sim$1 keV. We did not show yet, however, which part of the PSD spectrum is responsible for such an effect. Even though it is commonly believed that the high-frequency part of the spectrum is responsible for scattering, we hereafter show that it is the PSD at wavelengths in the millimeter range to cause the PSF broadening at 1 keV – for an incidence angle of 0.72 deg. To this end, we report in Fig. 8.16 the computed PSF of the D5 glass at 1 keV, with profile and roughness (like in Fig. 8.16) and with roughness only (i.e., assuming a perfect figure). The second simulation differs completely from the first one, as a delta-like peak appears at the centre instead of a uniform broadening. This is the residual specular reflectivity, though damped by the roughness. At nearby angles, moreover, an intense "skirt" of scattered intensity appeared, as expected. This computation has the advantage that it clearly separates the effects of the two components, and it clearly shows the impact of the X-ray scattering also at these energies.

We then re-computed the PSF of the D5 glass at 1 keV, but after setting to zero all values of PSD at frequencies higher than $(100\ \mu\text{m})^{-1}$. In Fig. 8.17 we show the PSF's obtained from the filtered PSD with and without figure errors. Comparison with the PSF's of Fig. 8.16 clearly shows that the PSF are the same. Also the HEW values are almost unchanged, like the roughness at spatial wavelengths smaller than $(100\ \mu\text{m})^{-1}$ has no relevance. We then conclude that at the X-ray energy of 1 keV, for an incidence angle of 0.72 deg, the X-ray scattering component of the HEW *is mainly affected by spatial wavelengths larger than 100 μm*.

For the D5 case at 1 keV the X-ray scattering contribution is large, and mainly due to the spatial wavelengths above 100 μm. For the D7 glass we can draw the same conclusion at X-ray energies immediately larger, even though the lack of PSD data

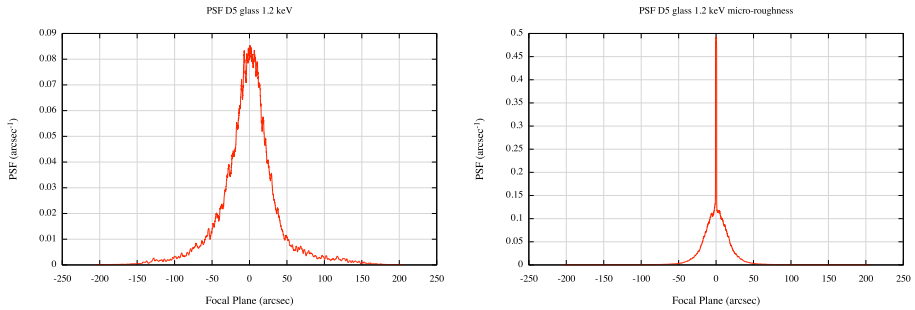

Figure 8.16: D5 glass, PSF's computed at 1 keV; measured figure and complete PSD, yielding a HEW = 36.9 arcsec (*left*); complete roughness PSD only, HEW = 17.9 arcsec (*right*). Note that the difference of the two HEW's returns to a good approximation the figure HEW (23 arcsec).

in the 1 cm ÷ 1 mm spectral range affects the prediction in an ameliorative fashion.

To push even further the analysis of the spatial wavelengths impact on the PSF degradation, we have analysed the D7 case, by filtering the spatial wavelengths of the profile and computing in each case the PSF. We start from a perfect mirror, then we added surface defect components from the high frequencies to the lower frequencies, until the complete profile. We divided the study in two parts, one at low energy (UV-soft X-ray, Fig. 8.18 left) and one at high energy (soft X-ray hard X-ray, Fig. 8.18 right). In the case of low energies, Fig. 8.18 left panel, we start from a perfect mirror that returns HEW completely dominated by the diffraction aperture, which varies depending on the incident wavelength. We started adding spatial wavelengths, from shorter (than those measured with the AFM), up to longer ones (up to that one with period equals to length of the mirror) that will complete the profile. For each new implemented profile we have achieved the relative PSF and the HEW. The HEW begins to increase in correspondence of a particular value of the spatial wavelength that depends on the incident wave length. The more the energy is high, the more this spatial wavelength is short. This effect is visible also in the case of high energies (Fig. 8.18 right panel), where the sole difference is that in the case of perfect mirror there is not aperture diffraction contribution and the HEW value is close to zero. For example, If we consider the case of 1.5 keV, the contribution up to 1 mm in terms of spatial wavelengths is negligible to the enlargement of the PSF. Viceversa, in the UV light (often used to asses the HEW at integration time), not only the PSF is flooded by an aperture diffraction term unseen in X-rays, but also the spatial wavelengths below a few cm are irrelevant. They turn out to be very important in X-rays. This is the reason why mirror shells tested in UV light sometimes reveal to have a better HEW when tested in X-rays, even at low energies where the contribution of the roughness

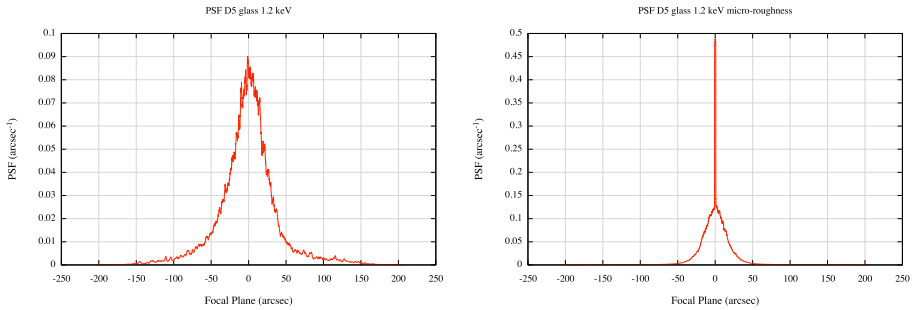

Figure 8.17: D5 glass, PSF's computed at 1 keV, roughness PSD with low-pass frequency filter, cutoff at 100 μm; (*left*) measured figure and filtered PSD, HEW = 36.3 arcsec. (*right)* filtered PSD only, HEW = 17.5 arcsec.

is generally negligible.

8.5 Conclusions

Concluding, the low-frequency roughness seems to affect to a larger extent the directly slumped glasses (D5 and D7) than the indirectly slumped ones (T112). The T20 glass, indirectly slumped, represents a borderline case, because it exhibits a quite high low-frequency roughness, but the glass shape dominates its PSF anyway. XRS measurements in high-resolution setup allow, after a proper alignment of the sample and the analyzer, a direct measurement of the PSF of the slumped and integrated glass, at an X-ray energy and incidence angle that approximately reproduces the operational condition of the grazing incidence mirror at 1.5 keV. The PSF measurement is larger than predicted by the shape measured with CUP for directly slumped glasses. The simulation of the PSF using the profiles from CUP and the measured roughness PSD, along with the self-consistent computation *à la Fresnel*, **correctly reproduces the measured PSFs in X-rays**. This also required the gap 1 cm - 2 mm in the spectral characterizations to be bridged by a proper interpolation. The correctness of the computation method is thereby confirmed. The discrepancies are likely due to the insufficient knowledge of the glass shape in the surface portion illuminated by X-rays, since only 4 profiles are involved in the computation. The profile and roughness characterizations are consistent with the XRS measurements in the regions probed with X-rays.

We can also conclude that our Fresnel diffraction method allows to evaluate quantitatively the interaction between the incidence wavelength and the different spatial wavelengths. Given the complete surface metrology of a mirror and all its bound-

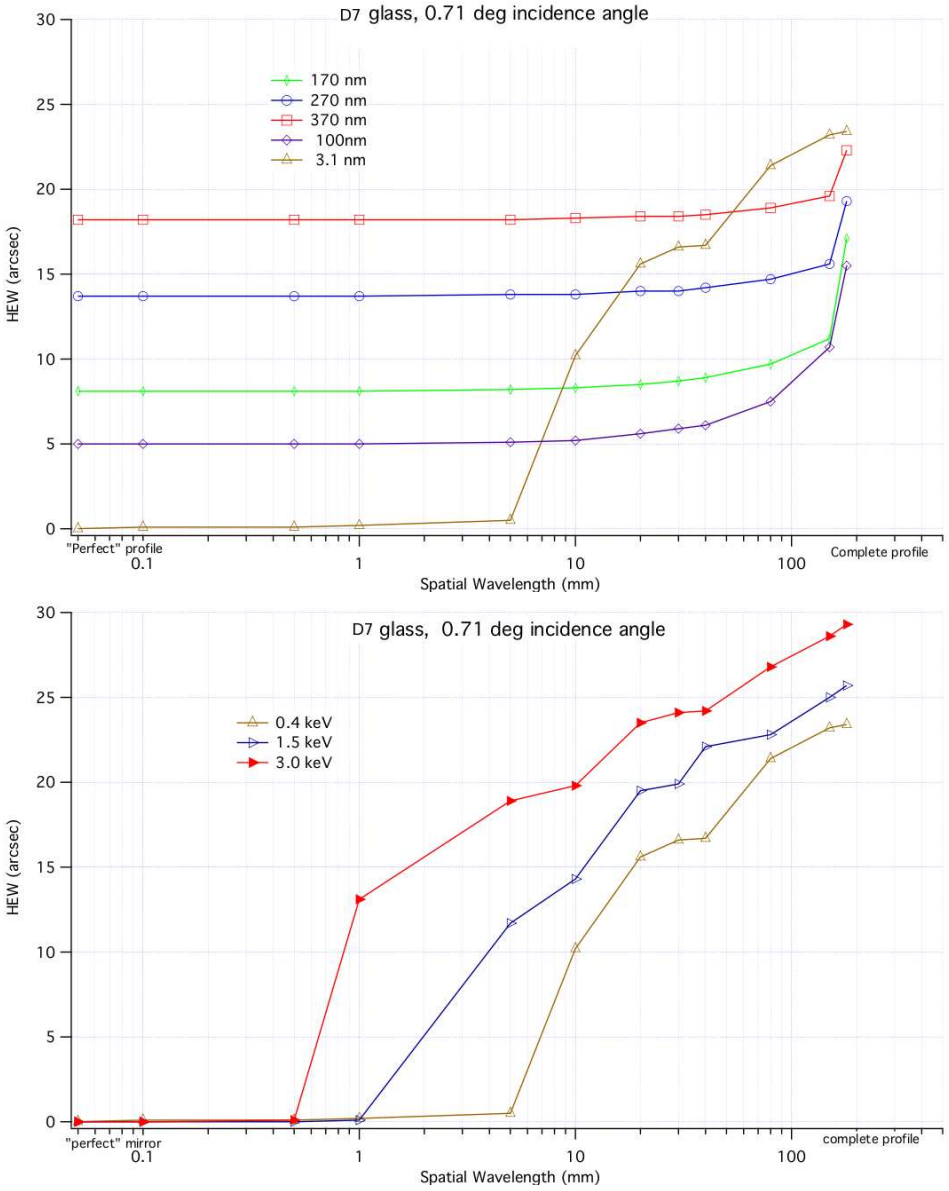

Figure 8.18: On the left we can see the behavior of HEW at low energy where the aperture diffraction is dominant. On the right we have the higher energies, where we can evaluate the contribution to the HEW of a single range of spatial wavelengths. At around 1 keV the contribution of spatial wavelengths up to 1 mm is negligible. The range of a few mm is very important, however.

ary conditions as the incidence angle and the incidence wave energy, it is possible to know the impact of the spatial wavelengths on the PSF broadening and the spectral range where a particular care to the surface smoothness should be taken. Finally, the better overall accuracy of directly-slumped glasses with respect to indirectly-slumped ones was directly measured in X-rays, confirming the choice of the direct slumping based initially on the sole CUP mapping. The major impact of low-frequency roughness, however, requires to concentrate on that spectral range in order to improve the technique.

9 Optical module calibration and test at Panter and Spring-8

During my PhD, I performed several calibrations of mirror shells in different configurations as demonstrators for the NHXM hard X-ray imaging telescope (0.3 - 80 keV), with a requested HEW (Half Energy Width) below 20 arcsec at E$<$30 keV. Prototypes of NHXM mirror modules with a few mirror shells were manufactured (Basso et al. 2011), aiming at demonstrating the feasibility of mirrors with such angular resolutions, e.g., adopting an electroformed Nickel-Cobalt alloy, stiffer than pure Nickel (Orlandi et al. 2011), and reducing the thickness of the gold layer used for the mirror release to improve the roughness (Sironi et al. 2010) (see sect. 5.2). In this chapter is shown, in particular, different tests and simulations of the Technical Demonstrator Model No. 2 (TDM2) for the NXHM project. Even though the module included 3 mirror shells with diameters 185, 297, and 350 mm, representative for the smallest, the average, and the largest mirrors of the NHXM module.

The direct performance verification was done by measuring the X-ray PSF (Point Spread Function) up to 50 keV in full-illumination setup at PANTER (MPE, Germany) (Freyberg et al. 2005) of the three shells (here we report only the case of the shell with 297 mm diameter, heretofore MS297) and in pencil-beam set up at monochromatic X-ray energies of 15 to 63 keV at the BL20B2 beamline of the SPring-8 synchrotron radiation facility (Japan, JASRI) of only on the mirror shell MS297. This is the mirror shell on which we concentrated the investigation.

Finally, we have simulated the PSF from the metrology profile of the mirror shell MS297 using the Fresnel diffraction method presented in chapter 6, finding an excellent agreement with the measured PSFs.

9.1 Full illumination Vs. Pencil beam set up

Full-illumination tests of X-ray mirrors with focal lengths $\geq$10 m are usually performed with on-ground X-ray facilities, aimed at measuring their effective area and

the angular resolution; however, they in general suffer from effects of the finite distance of the X-ray source, e.g. a loss of effective area for double reflection. These effects increase with the focal length of the mirror under test; hence a "partial" full-illumination measurement might not be fully representative of the in-flight performances. Indeed, a pencil beam test can be adopted to overcome this shortcoming, because a sector at a time is exposed to the X-ray flux, and the beam divergence can be compensated by tilting the optic. Testing double reflection mirrors with long fo-

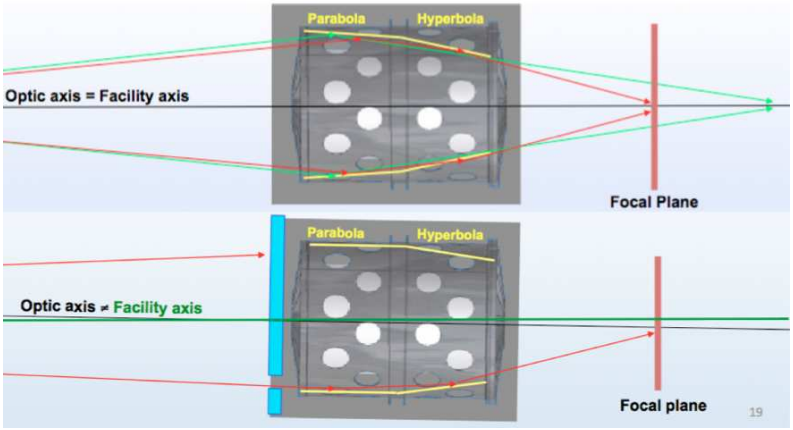

Figure 9.1: Top: Full illumination setup: rays hitting the primary front-end miss the second reflection; hence only a part (Eq. 1) of the mirror surface is seen in double reflection. Bottom: Pencil beam setup: a sector at a time is illuminated and tested. The lateral tilt corrects the effect of the source at finite distance.

cal lengths, in full illumination setup, requires extremely collimated and wide X-ray beams. At PANTER, this is obtained by locating the X-ray source at a 120 m distance from the module under test. Even so, the finite distance effects are clearly felt. The effective area loss represents a major problem: rays reflected at points close to the parabola front-end miss the second reflection and are not focused at the correct distance (Fig. 9.1, top). For mirrors with large f-numbers, the ratio of double-reflected rays (Basso et al. 2007) only depends on the focal length, f, and the distance of the source, D:

$$V = \frac{D - 4f}{D + 4f} \tag{9.1}$$

For a NHXM mirror tested at PANTER this ratio descends to 50%.

Even if an adoption of the pencil beam at PANTER (Basso et al. 2007) is foreseen to calibrate the NHXM optics after completion of an appropriate manipulator (Basso et al. 2011), we envisaged conducting parallel measurements with synchrotron light at the beamline BL20B2 of the SPring-8 radiation facility (JASRI, Hyogo prefecture,

Japan). The reason is that SPring-8 is a powerful source with a copious emission flux extended to more than 110 keV, thereby minimizing the exposure time per tested sector. Although BL20B2 was mainly designed for medical imaging, it has been equipped with a manipulating drum and specific imaging detectors to perform the calibration in pencil beam of the X-ray telescope ASTRO-H (Miyazawa et al. 2008, Ogasaka et al. 2008, Miyazawa et al. 2010).

9.2 Mirror calibration tests at Panter facility

The Max-Planck-Institut für extraterrestrische Physik (MPE) in Garching, Germany, uses its 130 m X-ray beam line facility PANTER (Fig. 9.2) for testing X-ray astronomical instrumentation up to 50 keV in energy. At one end of the vacuum system an X-ray source is installed, the other end is given by the test chamber. The test chamber has a diameter of 3.5 m and a length of 12 m to assimilate X-ray telescopes and small satellites. A number of telescopes, gratings, filters, and detectors, e.g. for astronom-

Figure 9.2: Aerial view of the x-ray test facility (PANTER) of the Max-Planck-Institut fur Extraterrestrische Physik. The 130 m long, 1 m diameter vacuum pipe extends from the upper left to the lower right in the photograph.

ical satellite missions like Exosat, ROSAT, Chandra (LETG), BeppoSAX, SOHO

(CDS), XMM- Newton, ABRIXAS, Swift (XRT), have been successfully calibrated in the soft X-ray energy range (<15keV). Moreover, measurements with mirror test samples for new missions like ROSITA and NHXM are being carried out at PANTER. The two main detectors available at PANTER are the low energy detector PSPC (0.1 - 10 keV) and the high energy detector TRoPIC (0.1-50 keV). The PSPCs are multiwire proportional counters each consisting of essentially two separate counters: the first anode (with two cathodes) as the position sensing, X-ray sensitive counter, and the second anode as the anticoincidence counter for background rejection. The TRoPIC camera is a CCD using a DUO-CCD lab-module with a CCD format of 256 x 256 pixels.

The results of measurements performed at the X-ray facility MPE- PANTER (Freyberg et al. 2005) on the 2nd Technical Demonstrator Model (TDM2) optic prototype for the NHXM hard X-ray telescope development project are here reported. The optic prototype comprises 3 mirror shells in $Ni_{0.8}Co_{0.2}$ alloy with 10 m focal lengths, and 185, 297 and 350 mm diameters at their principal plane, in the diameters range of the NHXM optical modules (400 - 150 mm). The mirror wall thickness is 0.2 mm, in the thickness range foreseen for NHXM (0.3 - 0.15 mm). The Au coating used as a mirror release agent from mandrels, which the multilayer coating is deposited onto, is reduced to 50 nm with the aim of minimizing the substrate roughness of the mirror. Finally, the mirrors are 600 mm long, exactly like those of NHXM.

Figure 9.3: Internal chamber at Panter facility. Mounting of a technical demonstrator TDM2.

We have been using the monochromatic sources with the PSPC, and the polychromatic source with the 20, 35, 50 kV setup with TRoPIC. Images of the focal spot of the MS297, are shown in Fig. 9.4, Fig. 9.5 and Fig. 9.6. The out of focus images reveal an "hexagonal" shape of the focal spot, related to roundness errors of the mirror shell. The out of focus image is, indeed, a clearly defined ring, and this means that the scattering contribution is quite small. The 3 arcmin off-axis image (Fig. 9.6) does

not significantly differ, in focus, from the on- axis ones, while off-axis, out-of-focus exposures reveal that the sector in the direction opposite of rotation are enhanced, at the expense of the other side. The HEW of the focal spot at 1 keV, in focus, on-axis, is 18.5 keV, in good agreement with the UV measurement at 2180 Å (21 arcsec), preliminary obtained by the vertical UV bench used for integration.

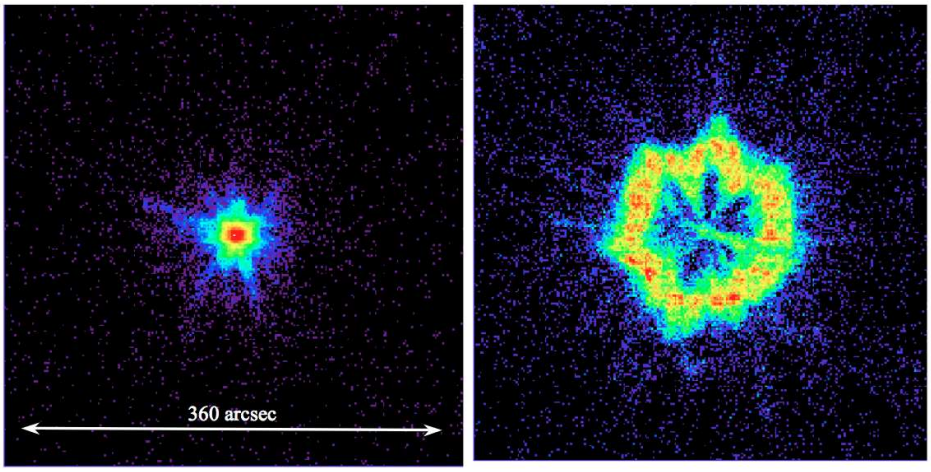

Figure 9.4: the on-axis focal spot of the MS297 at 0.93 keV (the Cu-Lα line), as seen by the PSPC. In focus (left), 25 cm intra-focal (right). Logarithmic colour scale, magnified view to a 2 cm side image.

The HEW values were extracted from all in-focus exposures, as a function of the energy. The on-axis HEW curve is shown in Fig. 9.8, whereas the 3 arcmin off-axis curve is plotted in Fig. 9.9. In the two cases the HEW trends have been corrected for the lost effective area on-axis and off-axis, respectively, to account for X-rays scattered beyond the detector edge. After the correction, the HEW at low energies, on-axis, remains unchanged (19 arcsec at 1 keV). The correction starts to increase the HEW values beyond 15 keV, and at 30 keV it reaches $\sim$ 35 arcsec, much more than the specification for NHXM (HEW $<$ 20 arcsec for E $<$ 30 keV).

In the 35 kV exposure of the MS297 in focus, for example, 1/3 of the effective area is not detected in the TRoPIC field. To estimate the amount of photons scattered out of the detector area, 2 additional exposures have been obtained by shifting the detector aside the focal spot, in focus, increasing the source current up to 25 mA to improve the statistics in $\sim$1 h exposure time. The mosaic is shown in Fig. 9.7 (left). We can see, in the lateral insets, that a non-negligible amount of scattered photons can be detected. More exactly, the 2% of the normalized photon count of the central image is detected in the side inset, and 1% in the corner one. Therefore, a 12% of

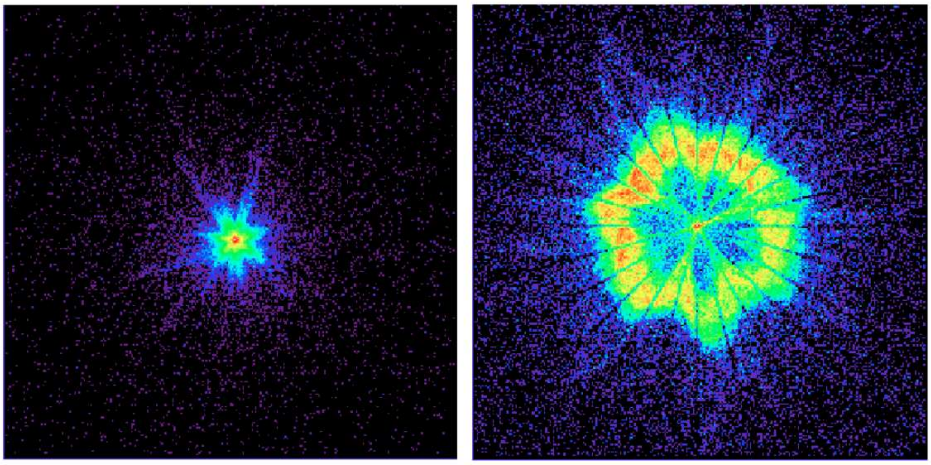

Figure 9.5: on-axis focal spot of the MS297 at seen by TRoPIC, with the X-ray source at 35 kV setup (20-35 keV). In focus (left), 25 cm intra-focal (right). Note the hexagonal shape of the focal spot and ring.

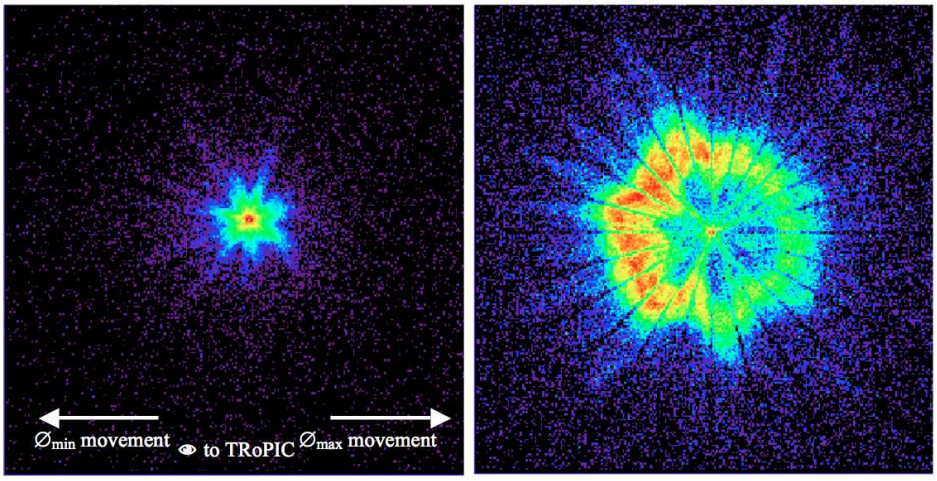

Figure 9.6: the +3 arcmin off-axis focal spot of the MS297 as seen by TRoPIC with the source at 35 kV (20 - 35 keV). In focus (left), 25 cm intra-focus (right).

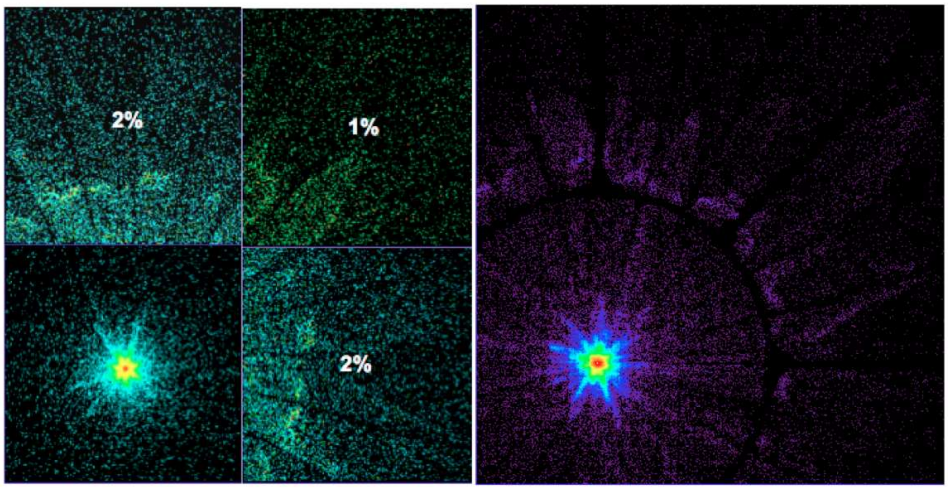

Figure 9.7: Left: a small mosaic of TRoPIC images around the focal spot of the MS297 in the 35 kV setup. The lateral insets were taken with a source intensity 12 times as large as that of the focal spot image - actually the image on right is a flipped copy of the image on top, and it as been added just to complete the square. Right: the same field, as seen by the PSPC at 0.93 keV.

the effective area (at 20 - 35 keV) in the central inset is found already in the nearby 2 cm wide frame (2% in the 20 kV setup, and 14% in the 50 kV setup). Moving outwards, the scattered intensity will expectedly decrease, but the number of insets per frame increases, hence one can expect another non-negligible photon fraction to be found there. The sum of contributions from all frames might then be large, and a 33% area loss is not so unlikely. Note that the next outer frame has not been acquired, because it would have included the single-reflection corona at its margin. In the same figure we show the same field seen by the PSPC at 1 keV. It is easy to see that also in this case there is a relevant fraction of scattered photons: however, they are much less numerous than in the hard X-ray band measured with TRoPIC (4% of the expected area in the first frame Vs. 12% at 20 - 35 keV). It is interesting to note that the circular halo around the spot is concentrated in a faint "corona", whose radius ($\sim$1.5 cm) does not apparently change with the energy. This means that the corona is caused by geometric errors; if it were due to scattering, the radius would have decreased in inverse proportion with the energy. For example, it might be due to a typical 'trumpet' deformation at the mirror's end.

The corrected HEW trend for the mirror off-axis also merges with the uncorrected trend at energies up to 23 keV (with a 20 arcsec HEW at 1 keV), because all the effective area is collected in the TRoPIC field. At higher energies, it increases linearly

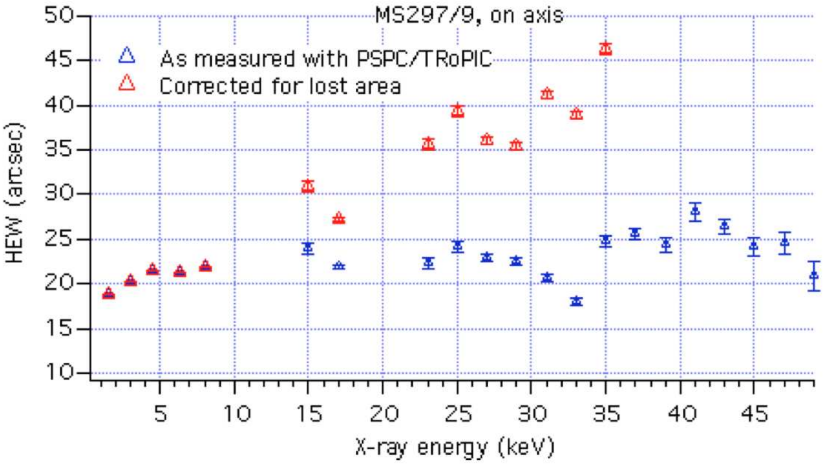

Figure 9.8: on-axis HEW values for the MS297, as measured with the PSPC in monochromatic setup and in energy-dispersive setup with TRoPIC. The red triangles represent the trend corrected for effective area loss.

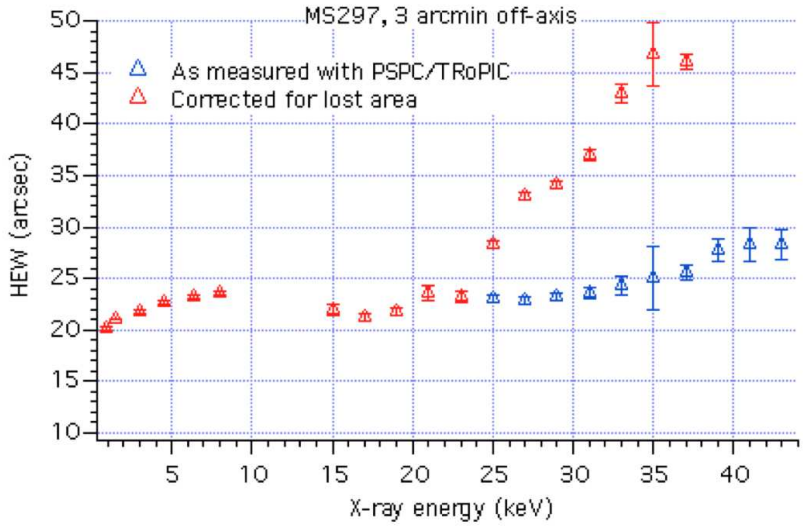

Figure 9.9: the 3 arcmin off-axis HEW values for the MS297, as measured with the PSPC in monochromatic setup and in energy-dispersive setup with TRoPIC. The corrected trend for area loss is also shown.

and reaches 35 arcsec at 30 keV, like the on-axis case. However, the increase is slower. This is consistent with the effective area measurements, which yield a better average roughness off-axis, i.e., in the first part of the parabolic segment, at least in the high-frequency regime (wavelengths < 12 μm).

9.3 Mirror calibration tests at Spring-8

SPring-8 is the world's largest 3^{rd} generation synchrotron light source. The beamline BL20B2 (Fig. 9.11) is 215 m long from the bending magnet to the end of the experimental hutch, leaving 201.203 m from the X-ray source (150 μm hor. size $\times$ 10 μm vert. size) to the principal plane of the optic. The remaining 14.8 m are sufficient to accommodate the 10.523 m distance to the detector (the distance is larger than the 10 m focal length because of the finite distance of the source). A Silicon double crystal

Figure 9.10: Aerial view of the SPring-8, the world's largest 3^{rd} generation synchrotron light source. Credits: JASRI.

is used to monochromate the radiation at 5 to 113 keV. For our scopes we have used the (311) reflection, enabling the selection of a X-ray energy in the 8.4 - 72.5 keV band, with a ΔE/E resolution of 10^{-4}. The beam enters the experimental hutch No. 2 through a Kapton window and impinges the mirror under test. The beam is very intense (1.5×10^7 count/sec/mA/mm^{-2} at 30 keV, at the hutch No. 3) and collimated: less than 1 arcsec per mm of entrance slit width, in the horizontal direction.

The vertical divergence is negligible for our scopes. The maximum available beam size is 300 mm in horizontal and 22 mm in vertical.

The TDM2 optic was mounted at BL20B2 in front of the Kapton window (Fig. 9.12). The manipulating drum was suited to perform an accurate alignment of each mirror sector with respect to the X-ray beam, and to spin the optic about its axis for exposing different sectors to the X-ray flux. The annular width of the mirror's parabolic segment (1 mm) determined the beam divergence, which resulted in a collimation within 1 arcsec within the cross section of the sector. The vertical size of the slit used was 20 mm, which entirely fitted the height of a sector (35 mm) between two consecutive spokes of the spider without obstructions. The exact horizontal size (5 mm) was not relevant, provided that it was sufficient to include the annular width of the primary segment (1 mm).

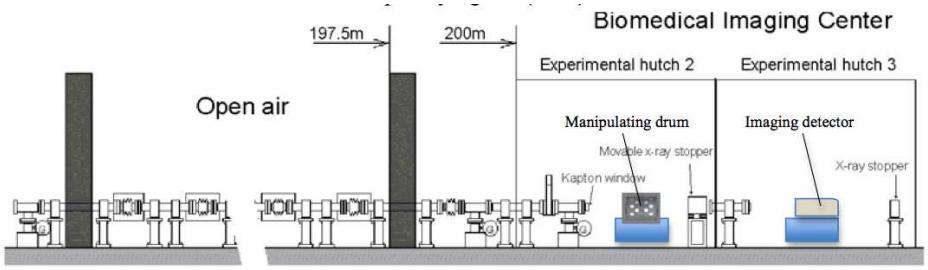

Figure 9.11: the setup of the beamline at the beam exit (after http://www.spring8.or.jp/). The mirror module under test was located in front of the Kapton window in the hutch No. 2. The detector was set in the experimental hutch No.3, 10.52 m away from the optic's principal plane.

After selection of a monochromatic X-ray energy in the 15 to 63 keV energy range, a single sector was located in front of the beam (Fig. 9.13). The uniformity of the beam intensity is 3% in the horizontal direction, therefore an exact positioning of the mirror sector was not crucial. The reflected beam was then recorded using a CCD+Scintillator imaging detector with 11.3 μm-sized pixels and a 45 mm x 30 mm lateral size. To the end of seeding the readout up every second pixel was read, resulting in an effective pixel size of 22.6 μm, which at a 10.5 m distance is equivalent to an angular resolution of 0.5 arcsec. The alignment of every sector was achieved by varying the tilt and rocking angles of the optic, until the stray light from the parabolic segment just disappeared completely. Actually, because the spin axis of the manipulator does not coincide with the optic axis, the optic spinning did not maintain the correct orientation of rays on the sector, hence we had to check and refined the alignment of each sector, before recording the focus image. After the alignment, the focal spot of a single sector looks like in Fig. 9.14. The first measurement at 30 keV was

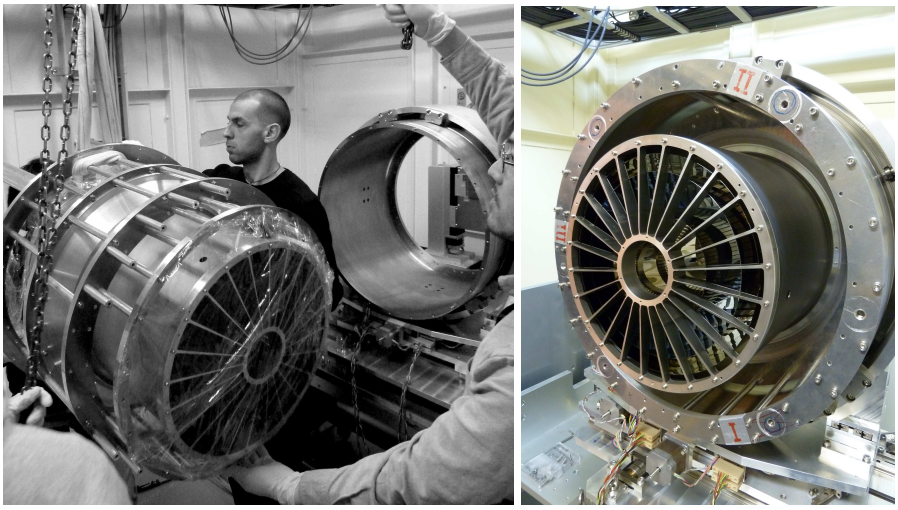

Figure 9.12: Mounting phase of NHXM demonstrator TDM2 in the beamline BL20B2 chambre test.

also addressed to the search for the best focus, i.e., the detector distance from the mirror at which the intensity distribution for the single exposure exhibits the most symmetric distribution on the left and the right side (the method suited in full illumination, i.e., the HEW minimization, would not have worked because it is mostly sensitive to the simultaneous convergence of the focused beam from all the sectors). After removing the effect of the distance of the X-ray source at BL20B2, the measured focal length of the mirror is 10.05 m, in accord with measurements in UV light and X-rays in full illumination. The copious photon flux allowed us integrating for a very short time with excellent statistics, therefore the all sectors have been aligned and exposed at several X-ray energies: 15, 20, 30, 35, 40, 45, 50, 55, 60, 63 keV. The exposure time varied from 70 msec (20 keV) to 3 sec (60 keV) to avoid pixel saturation. The detector noise was measured in separate "dark" exposures.

From the exposures of the individual sectors at the best focus we have reconstructed the PSF at each of the X-ray energies. To do this, we preliminarily subtracted from every image the dark exposure at the same energy. However, because the noise level might be fluctuating in time, we have selected a 200 pixel-high box in the central region of every image, approximately as wide as the detector. We have then subtracted another noise map, obtained as the average of two horizontal slices of the same size taken from the top and bottom of the image, which should represent the noise of the CCD at the measurement time. Finally, we selected a 100 pixel-high region, centered on the focal spot without changing the width, and we performed a final subtraction of the noise using the 50 pixel-high trimmed regions, joined together.

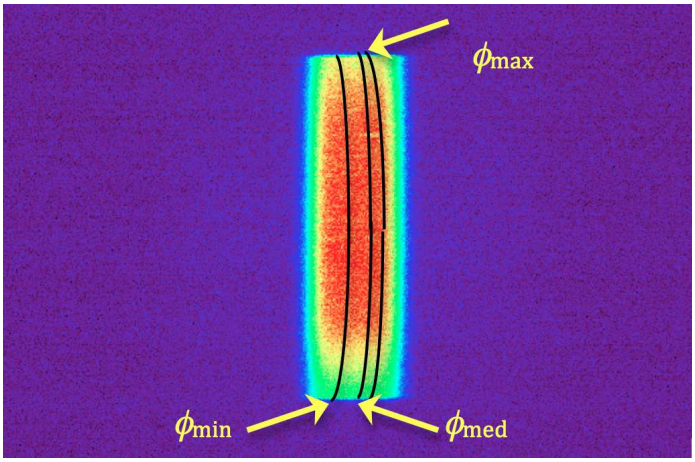

Figure 9.13: the direct beam emerging from the 2 cm-high slit. We have superposed to the image the position of the maximum, the median and the minimum diameter of the Wolter-I mirror, once aligned. The collecting area is between the maximum and the median diameter.

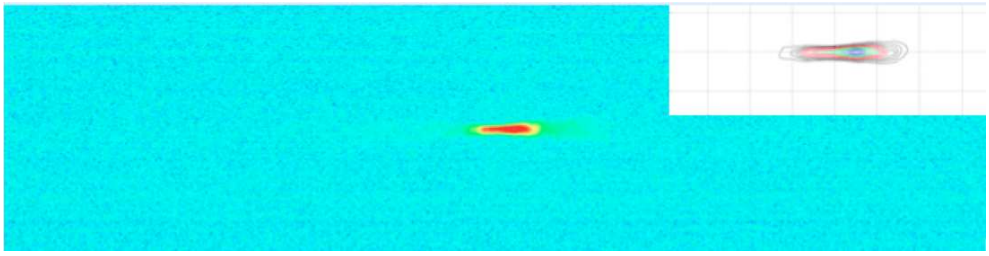

Figure 9.14: the focused image of a single exposure after sector alignment. The image width is 4 cm. We also show a contour plot of the image. The intensity distribution exhibits a sharp peak.

Doing that, we have removed any noise fluctuation over different spatial scales of the detector. After noise removal, we have rotated the resulting slices and superposed the rotated images. Since the axes mismatch may have introduced a lateral displacement of the sectors, which we could not measure, the center of rotation was not kept at fixed coordinates, but fluctuated by a few pixels. Therefore, we set the rotation center at the maximum count position in every exposure. This choice suppresses the impact of roundness errors on the PSF, but preserves the angular spread due to longitudinal profiles and scattering, which are expected to be the dominating terms. The resulting PSF does not sample the entire mirror surface, because the slit height is smaller than that of the sector, but the measurement is representative of a large fraction (63%) of the mirror's effective area. The missing regions correspond to gaps in the azimuthal angle but are representative of the entire mirror length, whereas at PANTER the azimuthal angle is mapped completely at the expense of the primary mirror length, which is not focused by 50%. In short, the two characterizations are complementary. The reconstructed focal spots at some selected energies are displayed in Fig. 9.15.

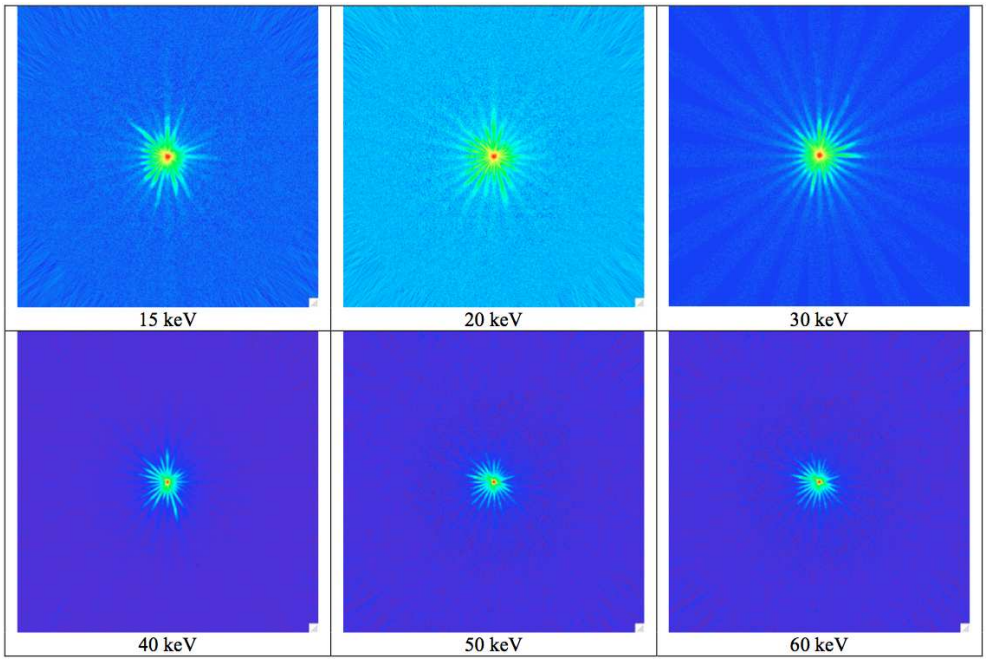

Figure 9.15: the reconstructed focal spot images. All images appear to be consistent with each other. The focal spot appears to shrink because of the decreasing reflectivity that causes the focused beam to be less prominent in the background (even though the background is nearly reduced to zero on average).

The mirror PSFs have been derived from reconstructed images at SPring-8 by annular integration, and the HEW values have been derived. The HEW trend, clearly increasing with the X-ray energy especially beyond 40 keV, is shown in Fig. 9.16. A comparison with the corresponding HEW values measured at PANTER shows that the results of PANTER and SPring-8 are consistent since the trends are quite well superposed in the 15-40 keV common energy range (Basso et al. 2011). At 30 keV, however, the HEW measured at SPring-8 is sensitively larger (28 arcsec Vs. 24 arcsec measured at PANTER). The difference can be ascribed to the different region of mirror tested, in particular the better value found at PANTER might denote a better roughness of the parabolic segment near the intersection plane. In the next section we reproduce the measured HEW trend using the metrology results performed on the shell post SPring-8 campaign. We also show that the measured PSFs at any X-ray energy are perfectly superposed to the simulated ones from measured profiles and roughness.

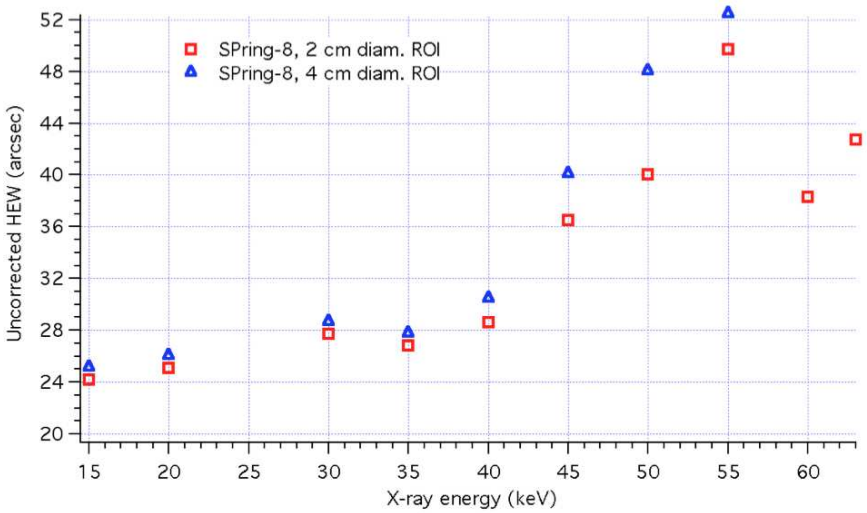

Figure 9.16: the HEW values of the MS297, measured at SPring-8 BL20B2. The slightly higher values for a wider region of interest (ROI) denote some scattering of X-rays also at the detector's edge. The results comply the measured HEW measured at PANTER (Basso et al. 2011) at 15 to 40 keV.

9.4 X-ray mirror optic module surface characterizations

The MS297 has been characterized in profile and roughness in order to explain the focusing performances observed in X-rays, especially at high energies. Usually, figure errors determine the PSF at low energies (∼1 keV) and can be treated with geometrical optics methods (i.e., ray-tracing). On the other side, roughness covers the high frequency range of mirror imperfections, and need to be treated with the X-ray scattering theory, which contributes to degrade the PSF to an extent increasing with the X-ray energy (Stover 1995). This simplified view supposes an abrupt boundary be-

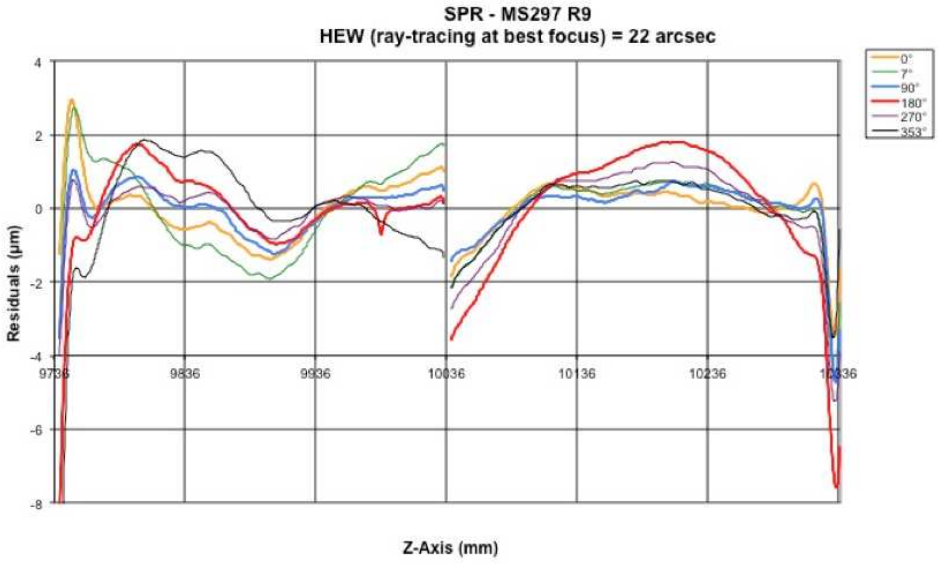

Figure 9.17: some longitudinal profiles of the MS297, as measured with the Shell Profilometer/Rotondimeter (SPR, Sironi et al. 2011) operated at MLT (0.4 mm lateral resolution). The graph shows the residuals of the 6 measured profiles with respect to the nominal Wolter-I. The hyperbola is on the left side, the parabola at right.

tween the two regimes, which is neither abrupt nor easy to locate as we have seen in sect. 6 the Fresnel diffraction method overrides this problem. Nevertheless, we will later see that this approach is correct in the case of this mirror: longitudinal profiles can then be used to derive a figure error term of the HEW, whilst roughness measurements, once processed in terms of Power Spectral Density (PSD), can be used to derive the HEW scattering term, as a function of the X-ray energy (Miyazawa et al. 2010)

Six longitudinal profiles of the MS297 (Fig. 9.17) have been measured using the instrument SPR (Shell Profilometer/Rotondimeter) specifically developed and operated at MLT for the NHXM project (Sironi et al. 2011). The SPR enables high-accuracy profile measurements of mirror shells without the need of removing them from the integration case. Actually, for this specific case the innermost shell (MS185) had to be removed, therefore the profile measurement of the MS297 was taken without the upper spider. This might potentially have slightly changed the shape of the mirror, even if the integration process is conceived and proven to not change the mirror profile, hence the spider removal could have changed the HEW only by a few arcsec. In fact, the HEW resulting from ray-tracing the profiles is 22 arcsec, Vs. 18 arcsec measured at PANTER at 1 keV (Basso et al. 2011). The overestimate may also be caused by the incorrect application of geometrical optics to the highest spatial frequencies present in the measurement (i.e., close to $(0.4\ \mathrm{mm})^{-1}$). After

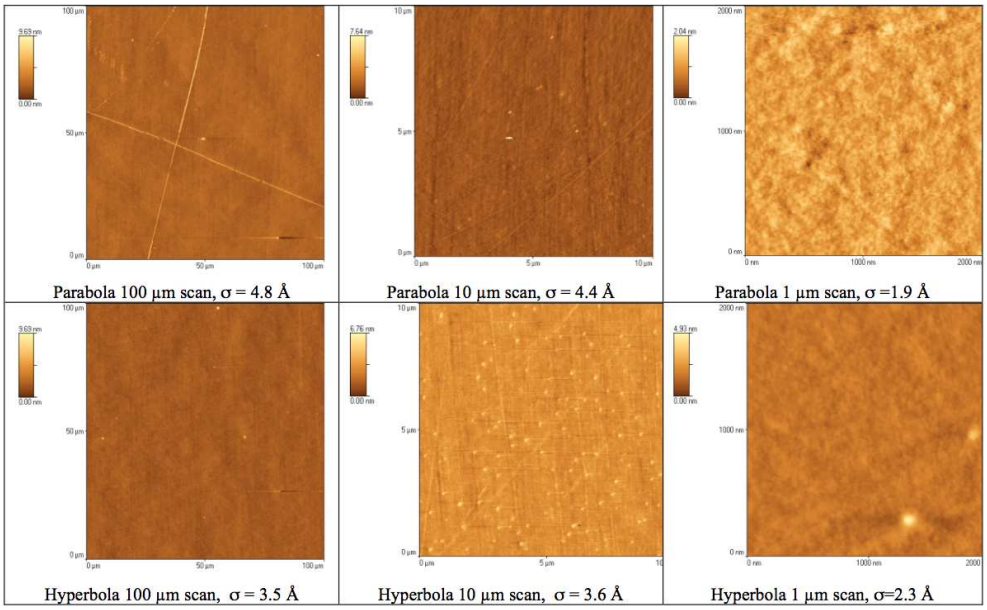

Figure 9.18: AFM images of the MS297 surface. The dots visible on the surface are more evident on the hyperbolic segment, but they are also present on the parabola, even though they are less visible, because they are confused among other defects.

the profile characterization, the MS297 was removed and cut into pieces to perform roughness measurements at INAF/OAB. High-frequency roughness measurements were performed using a stand-alone Atomic Force Microscope (AFM) Veeco Explorer at 3 different magnifications (Fig. 9.18) down to a maximum lateral resolution of 2 nm. The most noticeable feature, especially in the 10 μm scan, is the presence

of small dots spread over the surface. These defects were already detected on the mandrel as small pores, which were filled by the gold layer and replicated by the mirror shell (Sironi et al. 2010). AFM measurements cover the spectral band 50 nm - 4 nm of spatial wavelengths. Measurements with PSI (Phase Shift Interferometry) to characterize the roughness at larger spatial wavelengths (1 mm - 50 μm) could not be performed due to the sample curvature. Based on previous experiences, we have assumed in this region the same roughness of the mandrel, which was characterized completely prior to mirror replication.

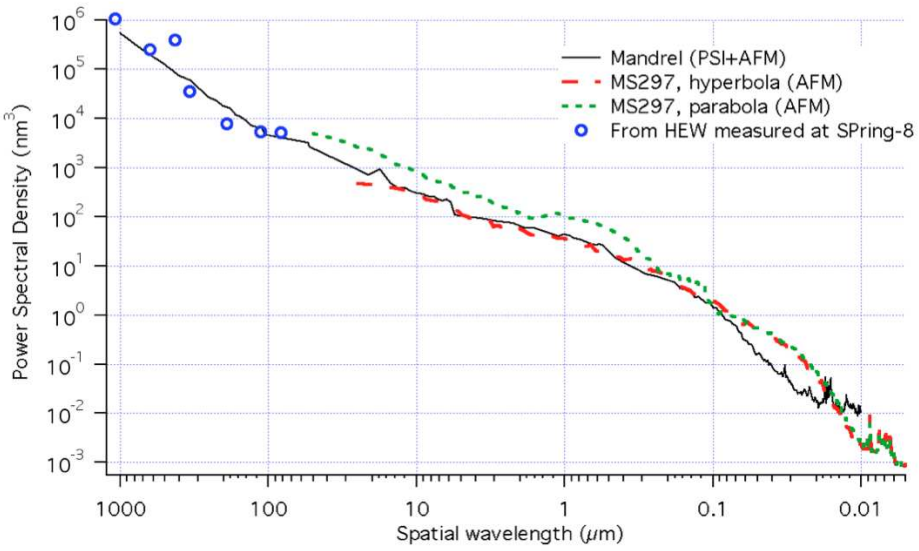

Figure 9.19: Power Spectral Density characterization of the MS297. The parabolic segment has nearly the same finishing level as the mandrel after the 5th replica. The hyperbolic segment is rougher. The PSD in the PSI spectral range is obtained from the HEW trend measured at SPring-8, assuming a 18 arcsec HEW to be subtracted linearly from the measured trend.

The complete roughness characterization of the MS297 is reported in Fig. 9.19. We have computed the average PSD from the AFM maps, and compared them to that of the mandrel. The PSD of the hyperbola is very well superposed to that of the mandrel excepting for wavelengths below 0.1 μm, where the shell is slightly rougher. This suggests that the multilayer deposition did not increase the surface roughness significantly. The parabola surface, in contrast, is sensitively rougher in all the AFM range. As we mentioned, the roughness of the mirror could not be measured with PSI techniques: however, we can reasonably assume that the PSD of the shell in the sub-millimeter range is the same as that of the mandrel. In fact, the PSD can be indirectly derived from the HEW values measured at SPring-8, using the inverse

analytical formalism (Spiga 2007) relating the XRS term of the HEW as a function of the X-ray energy to the PSD of the mirror. The PSD computed in this way is in the range 1 mm - 70 μm of spatial wavelengths and matches well the PSD of the mandrel, on condition that 18 arcsec of figure error HEW (i.e., the measured HEW value at 1 keV) are linearly (and not in quadrature) subtracted from the measure HEW trend. We thereby obtain that the HEW increase measured at SPring-8 are justified assuming that the mirror surface PSD has replicated the topography of the mandrel in the 1 mm - 70 μm spatial wavelength range.

9.5 Simulations with the Fresnel diffraction method

Using the measured profiles (covering the perturbation spectrum down to 0.8 mm) and the measured roughness PSD (at 1 mm to 4 nm spatial wavelengths), we can now simulate the Point Spread Function (PSF) at any X-ray energy. To this end, we make use of the method described in section 7. In Fig. 9.20 we compare the PSF at 1.5 keV measured at PANTER and the simulation. The simulation is made taking into account of finite distance of the X-ray source and matches well the measured points. The discrepancies are caused by the low number of profiles measured, intro ducting some fictitious oscillations in the simulation. This provides a first confirmation of the correctness of the metrology and the computation method, at least at low energies.

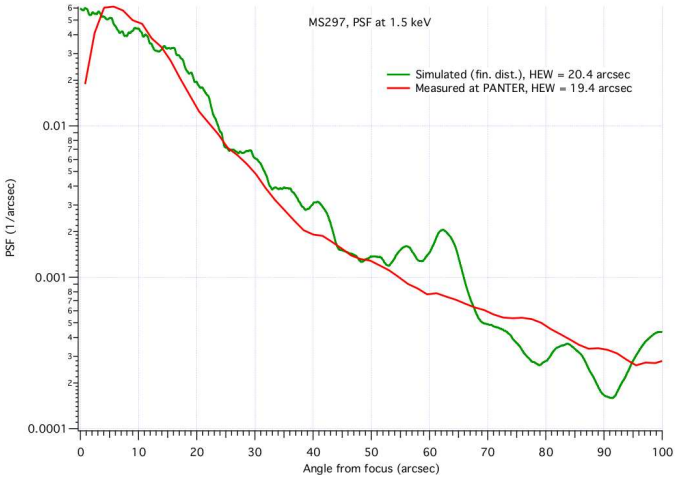

Figure 9.20: The encircle energy of the MS297 mirror shell given by the measure of the PSF at 1.5 keV at PANTER (red line) compare with the simulation with Fresnel method (green line).

In Fig. 9.21 we compare the HEW values as computed from the simulated PSFs

using the Fresnel diffraction theory with the measured at SPring-8. We also show the HEW trend computed analytically from the PSD (Spiga 2007), after adding linearly 18 arcsec of figure error, as we assumed in the inverse computation of Fig. 9.19. Data match to within a few arcseconds.

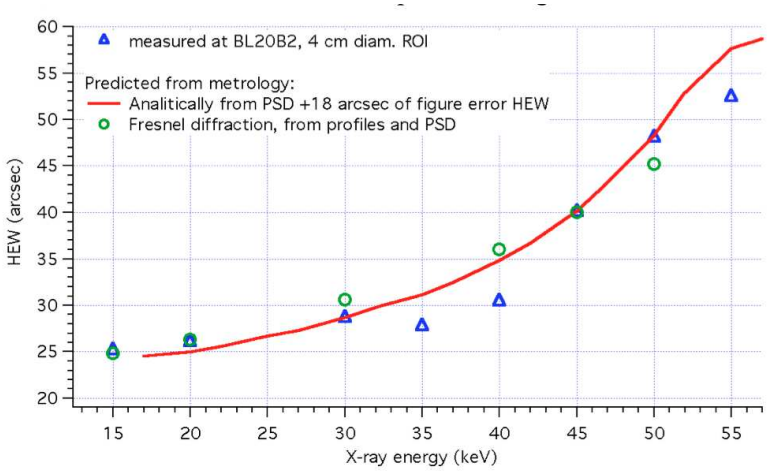

Figure 9.21: MS297 HEW trend as measured at SPring-8, compared with the results of the analytical computation (line) and the HEW consistently computed from the Fresnel diffraction theory (circles: see also the PSFs in Fig. 9.22)

Finally, in Fig. 9.22, we display the simulated PSFs computed from measured profiles and PSD at 20 keV, 30 keV, and 50 keV respectively. The PSFs were obtained by superposing a rough profile, simulated from the PSD (Fig. 9.19), to each one of the SPR measurements (Fig. 9.17), and applying the formulae reported in section 7 (Raimondi & Spiga 2011) to the resulting profile. The 6 PSFs were then averaged among them and normalized over a 4 cm wide region, the same lateral size of the detector used to reconstruct the PSFs (Fig. 9.15). Exactly the same procedure was applied to the same metrology dataset, at the X-ray energies mentioned above. The simulations accurately match the measured PSFs computed from the SPring-8 measurement dataset. Consequently, also the HEW values computed from the simulated PSFs are in good accord with the measured values (Fig. 9.21) to within a couple of arcseconds. The remaining discrepancies might be caused by the small number of profiles measured with the SPR, which might not be fully representative of the figure of all the tested sectors at SPring-8.

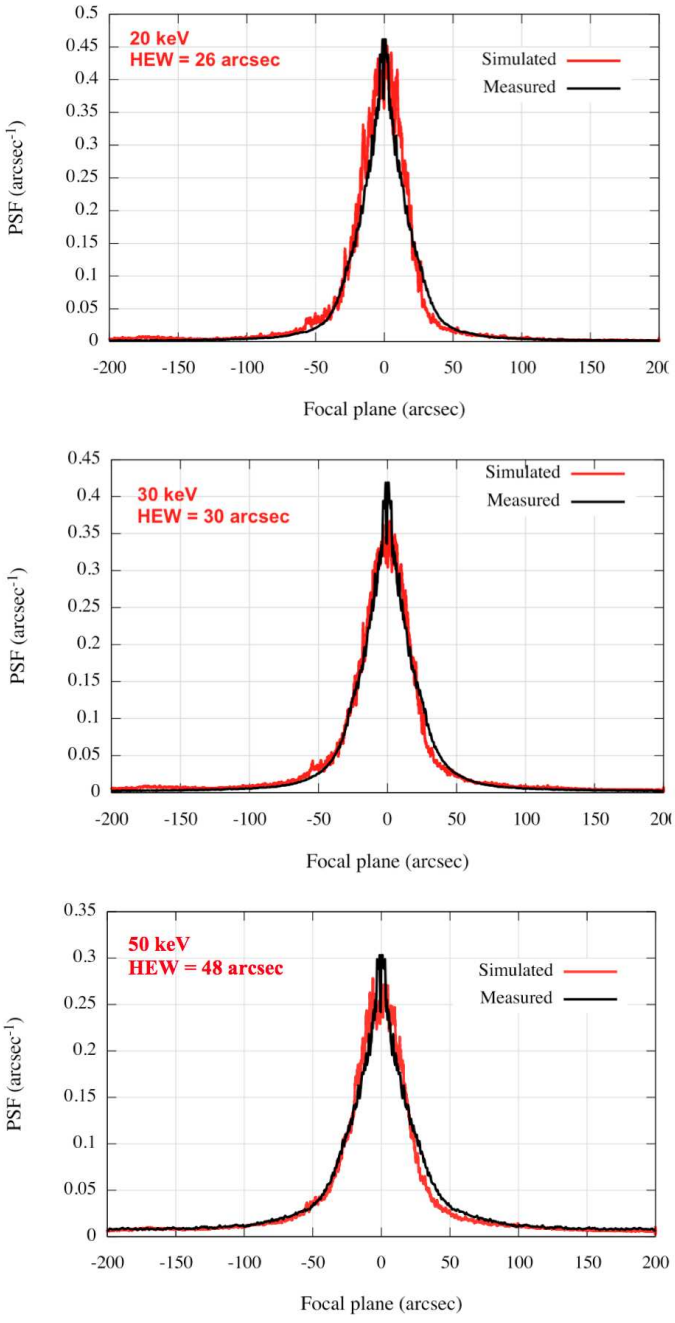

Figure 9.22: Simulated PSF from measured profiles and roughness, at 20, 30, 50keV respectively, using the Fresnel diffraction approach. The experimental PSFs are reproduced accurately.

9.6 Conclusions

The angular resolution measurements of a hard X-ray Wolter-I optic prototype for NHXM, performed at Spring-8, BL20B2, have made possible an extension of the characterizations, usually performed at PANTER, to higher energies, not far from the upper limit of the energy range of NHXM (80 keV, in the baseline design). The measurement campaign also allowed us overcoming the problem of effective area loss due to the source at finite distance. The measured HEW in pencil beam setup, after a reconstruction of the PSF, is in substantial agreement with the measurements achieved at PANTER (Basso et al. 2011) at lower energies. In particular, the HEW at 30 keV is close to, although not compliant yet with, the NHXM target of 20 arcsec. The measured HEW increases with the X-ray energy in good agreement with the metrology of profiles and surface roughness, under the condition that the HEWs related to the figure errors and scattering can be added linearly, not in quadrature as initially supposed. *Finally, the PSF in hard X-rays can be correctly predicted by analyzing in a self-consistent way the profile and the roughness using the Fresnel diffraction approach. Therefore, measurements performed at SPring-8 provided an independent confirmation not only of the metrology characterization but also of the method adopted to derive the PSF from the metrology dataset.*

10 Conclusions

My PhD activity is included in the mission project *NHXM* financed by ASI and in the development of X-ray mirrors for *ATHENA* mission project financed by ESA. The first part of my PhD project has been therefore aimed at the *characterization of microroughness and reflectivity of the mirrors*, at INAF/OAB. The second part of the project was instead dedicated to the *development of a self-consistent general method*, based on physical optics, to compute the PSF of X-ray mirrors from their profile metrology. In the third part, I performed *calibration tests of Technical Demonstrator Models for NHXM optics*. These last measurements have also demonstrated the correctness of the Fresnel diffraction method. A comparison between the measured PSF and the simulated one perfectly agree. In the following I summarize the main conclusions of my research work.

- *X-ray characterization and analysis of multilayer samples for the NHXM project*, with the BEDE-D1 X-ray diffractometer, the AFM and the LTP operated at INAF-OAB. The multilayers are deposited using the dedicated facility at MLT for coating with multilayers the mirror shells.

  The characterizations I performed have provided a complete diagnostic of the W/Si and Pt/C multilayer deposition process, enabling a fine tuning of the process parameter set, until the coating reflectance reached an optimal level and the coating structure matched accurately the stack design. Such a detailed feedback, and consequently the coating development, would have been impossible without direct XRR tests and the accurate analysis dealt with them via the PPM program.

- *Improvement of mirror shell substrate roughness by reduction of the Gold thickness*. Studying the Bragg peaks breadth I obtained an estimate of the size of the gold crystallites as a function of the thickness in a non-destructive way. The larger are the crystallites, the higher is the value of the microroughness. The conclusion is that the more the gold layer is thick, the larger are

the crystallites and *larger crystallites lead microroughness increase*. This has provided a strong evidence that, in order to reduce the increasing roughness we had to reduce the gold layer thickness from the standard < 200 nm to 50 nm, the minimum thickness needed to detach the shell from mandrel, with apparent gain in terms of mirror microroughness.

- *I developed a new method for PSF computation of real X-ray mirrors based on Fresnel-Huygens principle*. I demonstrated how the Point Spread Function of a focusing X-ray mirror with imperfections can be computed at *any* monochromatic energy along with the Huygens-Fresnel principle, applied to meridional profiles of the mirrors. This can be done regardless of any distinction between figure errors and microroughness, also accounting for the aperture diffraction effects. From this viewpoint, the classical distinction between figure errors and microroughness is unessential to the aim of computing the PSF: this treatment does not require setting any boundary.

- *The Fresnel diffraction method was extended to double reflection Wolter-I systems*. I implemented the self-consistent method based on the Huygens-Fresnel principle to compute the PSF to the double-reflection X-ray mirror (e.g. Wolter-I system). This formalism solves the long-standing problem of setting adequate tolerances of profile and roughness for X-ray mirrors. The PSF of a mirror can now be computed from metrology in a completely consistent way. The PSF computation reproduces the ray-tracing results wherever the geometrical optics may be applied. In hard X-rays, the single- and double-reflection results are consistent with the prediction of the analytical model, when it is applicable.

- *Glass characterization for the IXO/ATHENA X-ray telescope and application of Fresnel diffraction method to interpret the metrology results*.

  – I performed XRS measurements in high-resolution setup that allow, after a proper alignment of the sample and the analyser, a direct measurement of the PSF of the slumped and integrated glass, at an X-ray energy and incidence angle that approximately reproduces the operational condition of the grazing incidence mirror at 1.5 keV. The simulation of the PSF using the profiles from CUP and the measured roughness PSD, along with the self-consistent computation à la Fresnel, correctly reproduces the measured PSFs.

  – I also dealt with an quantitative evaluation of the interaction between the incidence wavelength and the different spatial wavelengths. Given the complete surface metrology of a mirror and all its boundary conditions as the incidence angle and the incidence wave energy, it is possible to know the impact of the spatial wavelengths on the PSF enlargement and the

spectral range where a particular care to the surface smoothness should be taken.

- I performed *optical module calibration and test at PANTER and Spring-8 and application of Fresnel diffraction simulations*. The angular resolution measurements of a hard X-ray Wolter-I optic prototype for NHXM, performed at Spring-8, BL20B2, have made possible an extension of the characterizations, usually performed at PANTER, to higher energies, not far from the upper limit of the energy range of NHXM (80 keV), in the baseline design. *Finally, the PSF in hard X-rays can be correctly predicted by analyzing in a self-consistent way the profile and the roughness using the Fresnel diffraction approach. Therefore, measurements performed at SPring-8 provided not only an independent confirmation of the metrology characterization but also an experimental proof of the method adopted to derive the PSF from the metrology dataset*.

Bibliography

Allaria E., Callegari C., Cocco D., Fawley W. M., Kiskinova M., Masciovecchio C., Parmigiani F., 2010, New Journal of Physics, 12, 075002

Aschenbach B., 2005, in O. Citterio & S. L. O'Dell ed., Society of Photo-Optical Instrumentation Engineers (SPIE) Conference Series Vol. 5900 of Society of Photo-Optical Instrumentation Engineers (SPIE) Conference Series, Boundary between geometric and wave optical treatment of x-ray mirrors. pp 92–98

Barcons X., Mateos S., Ceballos M. T., 2000, MNRAS, 316, L13

Basso S., Pareschi G., Citterio O., Spiga D., Tagliaferri G., Raimondi L., Sironi G., Cotroneo V., Salmaso B., Negri B., Attinà P., Borghi G., Orlandi A., Vernani D., Valsecchi G., Binda R., 2011, in Society of Photo-Optical Instrumentation Engineers (SPIE) Conference Series Vol. 8147 of Society of Photo-Optical Instrumentation Engineers (SPIE) Conference Series, The optics system of the New Hard X-ray Mission: status report

Basso S., Spiga D., Pareschi G., Citterio O., Malaguti G., Burkert W., Freyberg M., 2007, in Society of Photo-Optical Instrumentation Engineers (SPIE) Conference Series Vol. 6688 of Society of Photo-Optical Instrumentation Engineers (SPIE) Conference Series, SIMBOL-X: the problem of the calibrating a 0.5-80 keV 20m focal length focussing telescope

Burrows D. N., Hill J. E., Nousek J. A., Wells A. A., Short A. T., Ambrosi R. M., Chincarini G., Citterio O., Tagliaferri G., 2003, in J. E. Truemper & H. D. Tananbaum ed., Society of Photo-Optical Instrumentation Engineers (SPIE) Conference Series Vol. 4851 of Society of Photo-Optical Instrumentation Engineers (SPIE) Conference Series, Swift x-ray telescope (XRT). pp 1320–1325

Christensen F. E., Hornstrup A., Schnopper H. W., 1988, Appl. Opt., 27, 1548

Churazov E., Sunyaev R., Revnivtsev M., Sazonov S., Molkov S., Grebenev S., Winkler C., Parmar A., Bazzano A., Falanga M., Gros A., Lebrun F., Natalucci L., 2007, A&A, 467, 529

Church E. L., 1979, in M. Weisskopf ed., Society of Photo-Optical Instrumentation Engineers (SPIE) Conference Series Vol. 184 of Society of Photo-Optical Instrumentation Engineers (SPIE) Conference Series, Role of surface topography in X-ray scattering. pp 196–202

Church E. L., 1988, Appl. Opt., 27, 1518

Church E. L., Takacs P. Z., 1986, in J. F. Osantowski & L. van Speybroeck ed., Society of Photo-Optical Instrumentation Engineers (SPIE) Conference Series Vol. 640 of Society of Photo-Optical Instrumentation Engineers (SPIE) Conference Series, The interpretation of glancing incidence scattering measurements. pp 126–133

Civitani M., Basso S., Bavdaz M., Citterio O., Conconi P., Gallieni D., Ghigo M., Martelli F., Pagano G., Pareschi G., Parodi G., Proserpio L., Salmaso B., Spiga D., Tagliaferri G., Tintori M., Zambra A., 2010, in Society of Photo-Optical Instrumentation Engineers (SPIE) Conference Series Vol. 7732 of Society of Photo-Optical Instrumentation Engineers (SPIE) Conference Series, IXO x-ray mirrors based on slumped glass segments with reinforcing ribs: optical and mechanical design, image error budget, and optics unit integration process

Conconi P., Campana S., 2001, A&A, 372, 1088

Conconi P., Campana S., Tagliaferri G., Pareschi G., Citterio O., Cotroneo V., Proserpio L., Civitani M., 2010, MNRAS, 405, 877

de Chambure D., Lainé R., van Katwijk K., Kletzkine P., 1999, ESA Bulletin, 100, 30

de Korte P. A. J., Giralt R., Coste J. N., Ernu C., Frindel S., Flamand J., Contet J. J., 1981, Appl. Opt., 20, 1080

Engelhaupt D. E., Rood R. W., Fawcett S. C., Griffith C., 1994, in R. B. Hoover & A. B. Walker ed., Society of Photo-Optical Instrumentation Engineers (SPIE) Conference Series Vol. 2279 of Society of Photo-Optical Instrumentation Engineers (SPIE) Conference Series, Replication of Wolter I x-ray mirrors by electroforming techniques. pp 56–65

Eriksen K. A., Hughes J. P., Badenes C., Fesen R., Ghavamian P., Moffett D., Plucinksy P. P., Rakowski C. E., Reynoso E. M., Slane P., 2011, ApJ, 728, L28

Ferrando P., Arnaud M., Briel U., Citterio O., Clédassou R., Duchon P., Fiore F., Giommi P., Goldwurm A., Malaguti G., Mereghetti S., Micela G., Pareschi G., Rio Y., Roques J. P., Strüder L., Tagliaferri G., 2006, in Society of Photo-Optical Instrumentation Engineers (SPIE) Conference Series Vol. 6266 of Society of Photo-Optical Instrumentation Engineers (SPIE) Conference Series, Simbol-X: mission overview

Freyberg M. J., Bräuninger H., Burkert W., Hartner G. D., Citterio O., Mazzoleni F., Pareschi G., Spiga D., Romaine S., Gorenstein P., Ramsey B. D., 2005, Experimental Astronomy, 20, 405

Frontera F., Orlandini M., Landi R., Comastri A., Fiore F., Setti G., Amati L., Costa E., Masetti N., Palazzi E., 2007, ApJ, 666, 86

Garoli D., Boscolo Marchi E., Mattarello V., Bertoli J., Salmaso G., Kools J., Spiga D., Tagliaferri G., Pareschi G., 2009, in Society of Photo-Optical Instrumentation Engineers (SPIE) Conference Series Vol. 7360 of Society of Photo-Optical Instru-

mentation Engineers (SPIE) Conference Series, Enabling deposition of hard x-ray reflective coatings as an industrial manufacturing process

George I. M., Fabian A. C., 1991, MNRAS, 249, 352

Giacconi R., Bechtold J., Branduardi G., Forman W., Henry J. P., Jones C., Kellogg E., van der Laan H., Liller W., Marshall H., Murray S. S., Pye J., Schreier E., Sargent W. L. W., Seward F., Tananbaum H., 1979, ApJ, 234, L1

Giacconi R., Gursky H., Paolini F. R., Rossi B. B., 1962, Physical Review Letters, 9, 439

Harvey J. E., Moran E. C., Zmek W. P., 1988, Appl. Opt., 27, 1527

Hasinger G., Altieri B., Arnaud M., Barcons X., Bergeron J., Brunner H., Dadina M., Dennerl K., Ferrando P., Finoguenov A., Griffiths R. E., Hashimoto Y., Jansen F. A., Lumb D. H., Mason K. O., Mateos S., 2001, A&A, 365, L45

Joensen K. D., Voutov P., Szentgyorgyi A., Roll J., Gorenstein P., Høghøj P., Christensen F. E., 1995, Appl. Opt., 34, 7935

Kirkpatrick P., Baez A. V., 1948, Journal of the Optical Society of America (1917-1983), 38, 766

Marshall F. E., Boldt E. A., Holt S. S., Miller R. B., Mushotzky R. F., Rose L. A., Rothschild R. E., Serlemitsos P. J., 1980, ApJ, 235, 4

Matt G., Perola G. C., Piro L., 1991, A&A, 247, 25

McHardy I. M., Koerding E., Knigge C., Uttley P., Fender R. P., 2006, Nature, 444, 730

Merloni A., Heinz S., di Matteo T., 2003, MNRAS, 345, 1057

Miyazawa T., Furuzawa A., Kanou Y., Matsuda K., Sakai M., Yamane N., Ishida Y., Hara S., Miyata Y., Sakanobe K., Haba Y., Matsumoto H., Tawara Y., Kunieda H., Mori H., 2010, in Society of Photo-Optical Instrumentation Engineers (SPIE) Conference Series Vol. 7732 of Society of Photo-Optical Instrumentation Engineers (SPIE) Conference Series, Current status of hard x-ray characterization of ASTRO-H HXT at SPring-8

Miyazawa T., Furuzawa A., Kanou Y., Matsuda K., Sakai M., Yamane N., Kato H., Miyata Y., Sakanobe K., Haba Y., Ishibashi K., Matsumoto H., Tawara Y., 2011, in Society of Photo-Optical Instrumentation Engineers (SPIE) Conference Series Vol. 8147 of Society of Photo-Optical Instrumentation Engineers (SPIE) Conference Series, The current status of reflector production and hard x-ray characterization for ASTRO-H/HXT

Miyazawa T., Furuzawa A., Mori H., Haba Y., Kanou Y., Matsuda K., Sakai M., Tawara Y., Kunieda H., Ishida M., Maeda Y., Awaki H., Okajima T., 2010, in AAS/High Energy Astrophysics Division #11 Vol. 42 of Bulletin of the American Astronomical Society, The Current Status of ASTRO-H/HXT. p. 724

Miyazawa T., Ogasaka Y., Iwahara T., Kanou Y., Sasaki N., Makinae Y., Sasaya S., Inukai Y., Furuzawa A., Haba Y., Kunieda H., Yamashita K., Uesugi K., Suzuki Y.,

Tamura K., Maeda Y., Ishida M., Okajima T., 2008, in Society of Photo-Optical Instrumentation Engineers (SPIE) Conference Series Vol. 7011 of Society of Photo-Optical Instrumentation Engineers (SPIE) Conference Series, Hard x-ray characterization of the NeXT hard x-ray telescopes at SPring-8

Moretti A., Campana S., Lazzati D., Tagliaferri G., 2003, ApJ, 588, 696

Moretti A., Campana S., Tagliaferri G., Abbey A. F., Ambrosi R. M., Angelini L., Beardmore A. P., Bräuninger H. W., Burkert W., Burrows D. N., Capalbi D. J., Wells A. A., 2004, in K. A. Flanagan & O. H. W. Siegmund ed., Society of Photo-Optical Instrumentation Engineers (SPIE) Conference Series Vol. 5165 of Society of Photo-Optical Instrumentation Engineers (SPIE) Conference Series, SWIFT XRT point spread function measured at the Panter end-to-end tests. pp 232–240

O'dell S. L., Elsner R. F., Kolodziejeczak J. J., Weisskopf M. C., Hughes J. P., van Speybroeck L. P., 1993, in R. B. Hoover & A. B. C. Walker Jr. ed., Society of Photo-Optical Instrumentation Engineers (SPIE) Conference Series Vol. 1742 of Society of Photo-Optical Instrumentation Engineers (SPIE) Conference Series, X-ray evidence for particulate contamination on the AXAF VETA-1 mirrors. pp 171–182

Ogasaka Y., Tamura K., Shibata R., Furuzawa A., Miyazawa T., Shimoda K., Fukaya Y., Iwahara T., Nakamura T., Naitou M., Kanou Y., Sasaki N., Ueno D., Okajima T., Miyata E., Tawa N., Mukai K., Ikegami K., 2008, Japanese Journal of Applied Physics, 47, 5743

Orlandi A., Basso S., Borghi G., Binda R., Citterio O., Grisoni G., Kools J., Marioni F., Missaglia N., Negri B., Negri R., Pareschi G., Raimondi L., Salmaso B., 2011, in Society of Photo-Optical Instrumentation Engineers (SPIE) Conference Series Vol. 8076 of Society of Photo-Optical Instrumentation Engineers (SPIE) Conference Series, Technologies for manufacturing of high angular resolution multilayer coated optics for the New Hard X-ray Mission

Pareschi G., Basso S., Bavdaz M., Citterio O., Civitani M. M., Conconi P., Gallieni D., Ghigo M., Martelli F., Parodi G., Proserpio L., Sironi G., Spiga D., Tagliaferri G., Tintori M., Wille E., Zambra A., 2011, in Society of Photo-Optical Instrumentation Engineers (SPIE) Conference Series Vol. 8147 of Society of Photo-Optical Instrumentation Engineers (SPIE) Conference Series, IXO glass mirrors development in Europe

Proserpio L., Ghigo M., Basso S., Conconi P., Citterio O., Civitani M., Negri R., Pagano G., Pareschi G., Salmaso B., Spiga D., Tagliaferri G., Terzi L., Zambra A., Parodi G., Martelli F., Bavdaz M., Wille E., 2011, in Society of Photo-Optical Instrumentation Engineers (SPIE) Conference Series Vol. 8147 of Society of Photo-Optical Instrumentation Engineers (SPIE) Conference Series, Production of the IXO glass segmented mirrors by hot slumping with pressure assistance: tests and results

Raimondi L., Spiga D., 2010, in Society of Photo-Optical Instrumentation Engineers (SPIE) Conference Series Vol. 7732 of Society of Photo-Optical Instrumentation Engineers (SPIE) Conference Series, Self-consistent computation of x-ray mirror point spread functions from surface profile and roughness

Raimondi L., Spiga D., 2011, in Society of Photo-Optical Instrumentation Engineers (SPIE) Conference Series Vol. 8147 of Society of Photo-Optical Instrumentation Engineers (SPIE) Conference Series, Point spread function of real Wolter-I X-ray mirrors: computation by means of the Huygens-Fresnel principle

Romaine S., Gorenstein P., Bruni R., Pareschi G., Citterio O., Ghigo M., Mazzoleni F., Spiga D., Basso S., Conti G., Ramsey B., Gubarev M., O'Dell S., Speegle C., Engelhaupt D., Freyberg M., Burkert W., Hartner G., 2005, in American Astronomical Society Meeting Abstracts Vol. 37 of Bulletin of the American Astronomical Society, Development of Prototype Nickel Optic for the Constellation-X Hard X-Ray Telescope. p. 1172

Salmaso B., Spiga D., Canestrari R., Raimondi L., 2011, in Society of Photo-Optical Instrumentation Engineers (SPIE) Conference Series Vol. 8147 of Society of Photo-Optical Instrumentation Engineers (SPIE) Conference Series, Accurate modeling of periodic and graded multilayer x-ray scattering from surface microroughness characterization

Setti G., Woltjer L., 1989, A&A, 224, L21

Sironi G., Citterio O., Pareschi G., 2011, in Society of Photo-Optical Instrumentation Engineers (SPIE) Conference Series Vol. 8141 of Society of Photo-Optical Instrumentation Engineers (SPIE) Conference Series, X-ray optics shape error evaluation: synergy between innovative shape metrology and the TraceIT 3D ray-tracing

Sironi G., Spiga D., Pareschi G., Missaglia N., Paganini L., 2009, in Society of Photo-Optical Instrumentation Engineers (SPIE) Conference Series Vol. 7437 of Society of Photo-Optical Instrumentation Engineers (SPIE) Conference Series, Thin gold layer in Ni electroforming process: optical surface characterization

Sironi G., Spiga D., Raimondi L., Pareschi G., Orlandi A., Borghi G., Missaglia N., Negri B., 2010, in Society of Photo-Optical Instrumentation Engineers (SPIE) Conference Series Vol. 7732 of Society of Photo-Optical Instrumentation Engineers (SPIE) Conference Series, Thin gold layer in NiCo and Ni electroforming process: optical surface characterization

Soong Y., Serlemitsos P. J., Okajima T., Hahne D., 2011, in Society of Photo-Optical Instrumentation Engineers (SPIE) Conference Series Vol. 8147 of Society of Photo-Optical Instrumentation Engineers (SPIE) Conference Series, ASTRO-H Soft X-ray Telescope (SXT)

Spiga D., 2007, A&A, 468, 775

Spiga D., 2011, A&A, 529, A18

Spiga D., Cotroneo V., Basso S., Conconi P., 2009, A&A, 505, 373

Spiga D., Mirone A., Pareschi G., Canestrari R., Cotroneo V., Ferrari C., Ferrero C., Lazzarini L., Vernani D., 2006, in Society of Photo-Optical Instrumentation Engineers (SPIE) Conference Series Vol. 6266 of Society of Photo-Optical Instrumentation Engineers (SPIE) Conference Series, Characterization of multilayer stack parameters from x-ray reflectivity data using the PPM program: measurements and comparison with TEM results

Spiller E., 1996, Optics & Photonics News, 7, 60

Stover J. C., 1995, Optical scattering. Measurement and analysis

Tagliaferri G., Hornstrup A., Huovelin J., Reglero V., Romaine S., Rozanska A., Santangelo A., Stewart G., 2011, Experimental Astronomy, p. 98

van Speybroeck L. P., Chase R. C., 1972, Appl. Opt., 11, 440

Vecchi A., Molendi S., Guainazzi M., Fiore F., Parmar A. N., 1999, A&A, 349, L73

von Bieren K., 1982, Journal of the Optical Society of America (1917-1983), 72, 1771

Weisskopf M. C., 1999, ArXiv Astrophysics e-prints

Willingale R., 1988, Appl. Opt., 27, 1423

Windt D. L., Waskiewicz W. K., Griffith J. E., 1994, Appl. Opt., 33, 2025

Zhao P., Van Speybroeck L. P., 2003, in J. E. Truemper & H. D. Tananbaum ed., Society of Photo-Optical Instrumentation Engineers (SPIE) Conference Series Vol. 4851 of Society of Photo-Optical Instrumentation Engineers (SPIE) Conference Series, A new method to model x-ray scattering from random rough surfaces. pp 124–139

List of publications

- *The NHXM observatory*, Tagliaferri, G., Hornstrup, A., Huovelin, J., Reglero, V., Romaine, S., Rozanska, A., Santangelo, A., Stewart, G., et Al., Experimental Astronomy, ExA, 98T, (2011)

- *Accurate modeling of the x-ray multilayer scattering from surface microroughness characterization*, Salmaso B., Spiga D., Canestrari R., **Raimondi L.**, SPIE, Volume 8147-65, (2011)

- *Point Spread Function of real Wolter-I X-ray mirrors: computation by means of the Huygens-Fresnel principle*, **Raimondi L.**, Spiga D., SPIE, Volume 8147-33, (2011)

- *Production of the IXO glass segmented mirrors by hot slumping with pressure assistance: tests and results*, Mauro Ghigo, Laura Proserpio, Stefano Basso, Marcos Bavdaz, Oberto Citterio, Marta M. Civitani, Paolo Conconi, Francesco Martelli, Riccardo Negri, Giuseppe Pagano, Giovanni Pareschi, Giancarlo Parodi, Daniele Spiga, **Lorenzo Raimondi**, et Al., SPIE, Volume 8147-20, (2011)

- *Angular resolution measurements of a hard x-ray optic for the New Hard X-ray Mission at SPring-8*, Daniele Spiga, **Lorenzo Raimondi**, et Al., SPIE, Volume 8147-8, (2011)

- *The optics system of the New Hard X-ray Mission: status report* , Stefano Basso, Giovanni Pareschi, Oberto Citterio, Gianpiero Tagliaferri, Daniele Spiga, **Lorenzo Raimondi**, et Al., SPIE, Volume 8147-7, (2011)

- *Technologies for manufacturing of high angular resolution multilayer coated optics for the New Hard X-ray Mission*, Orlandi, A., Basso, S., Borghi, G., Binda, R., Citterio, O., Grisoni, G., Kools, J., Marioni, F., Missaglia, N., Negri, B., Negri, R., Pareschi, G.,**Raimondi L.**, et Al., SPIE, Volume 8076, (2011)

- *High-resolution X-ray scattering measurement of slumped glasses*, Spiga, D. , **Raimondi, L.** , Salmaso, B., 2011, INAF/OAB Internal Report 04/2011

- *IXO slumped glasses D5 and D7: analysis of spatial wavelength impact on the Point Spread Function by means of the Fresnel diffraction*, **Raimondi L.**, Spiga D., Salmaso B., 2011, INAF/OAB Internal Report 03/2011

- *Hard X-ray mirrors for NHXM: reflectivity and roughness characterization of mirror shell samples*, Salmaso B., **Raimondi L.**, Negri R., Spiga D., Binda R., Orlandi A., Valsecchi G., 2011, INAF/OAB Internal Report 02/2011

- *Thin gold layer in NiCo and Ni electroforming process: optical surface characterization*, Sironi G., Spiga D., **Raimondi L.**, Pareschi G., Orlandi A., Borghi G., Missaglia N., Negri B., SPIE, Volume 7732, pp. 77322R-77322R-8 (2010)

- *The optics system of the New Hard X-ray Mission: design and development*, Basso S., Pareschi G., Citterio O., Spiga D., Tagliaferri G., Civitani M., **Raimondi L.**, Sironi G., Cotroneo V., Negri B., et al., SPIE, Volume 7732, pp. 773218-773218-11 (2010)

- *Technologies for manufacturing of high angular resolution multilayer coated optics for the New hard X-ray Mission*, Orlandi A., Basso S., Borghi G., Binda R., Citterio O., Grisoni G., Kools J., Marioni F., Missaglia N., Negri B., **Raimondi L.**, et al., SPIE Vol. 8076, 807606 (2010)

- *Self-consistent computation of X-ray mirror Point Spread Functions from surface profile and roughness*, **Raimondi L.**, Spiga D., SPIE, Volume 7732, pp. 77322Q-77322Q-12 (2010)

- *X-ray tests at PANTER on the TDM2 optic prototype for the New Hard X-ray Mission*, Spiga D., **Raimondi L.**, Salmaso B., Valsecchi G., Orlandi A., Borghi G., Binda R., Basso S., Borrelli D., Marioni F., et al., 2010, INAF/OAB Internal Report 06/2010

- *X-ray tests at PANTER on the TDM1 optic prototype for the New Hard X-ray Mission*, Spiga D., **Raimondi L.**, Valsecchi G., Orlandi A., Borghi G., Salmaso G., Marchi E. B., Binda R., Basso S., Marioni F., et al., 2010, INAF/OAB Internal Report 05/2010

- *Slumped glasses for the IXO X-ray telescope: PSF simulations by application of the Fresnel diffraction*, **Raimondi L.**, Spiga D., 2010, INAF/OAB Internal Report 04/2010

- *Reflectivity and stress characterization of W/Si and Pt/C multilayer samples for the New Hard X-ray Mission phase B development*, Spiga D., **Raimondi L.**, Salmaso B., Negri R., 2010, INAF/OAB Internal Report 03/2010

- *Powerful Radio Galaxies with Simbol-X: Lobes and Hot Spots*, Migliori G., Grandi P., Angelini L., **Raimondi L.**, Torresi E., Palumbo G. G. C., 2009, AIPC, 1126, 156
- *Simbol-X Telescope Scientific Calibrations: Requirements and Plans*, Malaguti G., Angelini L., **Raimondi L.**, Moretti A., Trifoglio M., 2009, AIPC, 1126, 85
- *The Galactic Center View with Simbol-X*, **Raimondi L.**, Malaguti G., Angelini L., Cappi M., Grandi P., Palumbo G. G. C., Puccetti S., 2009, AIPC, 1126, 153
- *Simbol−X, a formation flight, focusing, broad-band X-ray telescope: calibrations and simulations critical issues*, **Raimondi L.**, Internal Report *INAF/IASF-Bologna*, n. 520/2008
- *Il telescopio Simbol−X: note per l'uso del simulatore ASI/ASDC*, **Raimondi L.**, Internal Report *INAF/IASF-Bologna*, n. 519/2008

Acknowledgments

I thank *INAF/Brera Astronomical Observatory* for hosting my Ph.D activity in these three years and for financial support. I thank in particular *Giovanni Pareschi* for giving me an opportunity to work in his group, *Gianpiero Tagliaferri* for involving me in the NHXM project and financial support, *Daniele Spiga* for being a guide to me and *Bianca Salmaso* for all her questions and answers.

I thank *Università degli studi dell'Insubria* and in particular the coordinator of the Ph.D. course in Astronomy and Astrophysics, Prof. *Aldo Treves*.

I also thank *INAF/IASF-BO* for financial support. I especially thank *Pino Malaguti* for trusting me and giving me the opportunity to undertake this project.

I thank *PANTER facility MPE* for all collaborations and for the always perfect assistance. I thank in particular the PANTER team: *V. Burwitz, M. Freyberg, W. Burkert, G. Hartner, and B. Budau*.

I thank the *Japan Synchrotron Radiation Research Institute Spring-8* for the excellent work done together and the impeccable support they gave me. I thank especially *A. Furuzawa, H. Kunieda, H. Matsumoto, H. Mori, T. Miyazawa* from University of Nagoya. The synchrotron radiation experiments were performed at the BL20B2 of Spring-8 with the approval of the Japan Synchrotron Radiation Research Institute (JASRI) (Proposal No. 2010B1551).

ASI (the Italian space agency) is acknowledged to support the missions for my training activities.

I also thank *Media-Lario s.r.l.* for the fruitful collaboration and the possibility to work at a high level of technology.

I am also grateful to all people who were close by and helped me to go through with it and to go one step further.

Qui auget scientiam, auget et dolorem.
Qui auget dolorem, auget et scientiam.

– Arthur Schopenhauer –